Blister Formation Using Ultrafast Laser Pulses

Alan Godfrey

A thesis submitted in partial fulfillment of the requirements for the Doctorate in Philosophy degree in Physics

Department of Physics
Faculty of Sciences
University of Ottawa

Abstract

Ultrafast laser pulses are frequently used for machining and structuration of materials. They provide superior localization of energy deposition compared to nanosecond pulses and continuous-wave lasers. Additionally, the inherent high intensities of ultrafast laser pulses provide access to nonlinear absorption processes, which enable laser machining at scales below the diffraction limit.

This thesis explores nonlinear absorption of ultrafast laser pulses in laser-induced blister formation. In this process, laser pulses are focussed through a transparent substrate and deposit energy beneath a film, giving rise to intact protrusions known as blisters. In the past, laser-induced blisters were used for indirect laser transfer of materials by imparting momentum to material placed on top of the film, and are often noticed as a pre-ablation phase of solid materials irradiated by pulsed lasers.

We first demonstrate that nonlinear absorption of single tightly-focussed femtosecond pulses can create polymer blisters below the diffraction limit (400 nm full-width at half-maximum), a factor of 10 smaller than previous polymer blisters and a factor of 2 smaller than previous blisters in glass films. We model the energy deposition process and observe a linear relationship between the deposited energy and the resulting blister volume.

We then characterize blister-patterned polymer films using a variety of microscopy and spectroscopy techniques. We provide direct confirmation that laser modification is confined entirely below the film surface and that the chemistry of the film surface is left unchanged. We demonstrate that blister patterning of polymer films adds purely morphological changes that increase hydrophobicity.

We introduce a multilayer film for blister formation consisting of a reflective metal layer sandwiched between two layers of polymer, for application in laser transfer of materials. The metal layer ensures that a material to be transferred (which is placed on top of the multilayer stack, opposite the laser) is not exposed to the laser directly, preventing modification, while allowing high intensities to drive nonlinear absorption in the multilayer film.

Lastly, we explore laser-induced blister formation as a method of microlens fabrication. We fabricate arrays of blisters in a polymer film and characterize the resulting focussing properties. We find that blisters act as meniscus lenses with positive focal lengths for sufficiently large blister curvatures.

This thesis demonstrates new possibilities of laser-induced blister formation. Nanoscale laser-induced blisters using tightly-focussed ultrafast pulses could enable laser transfer of materials at sizes below the diffraction limit, and can structure films while preserving surface chemistry. Blister formation in multilayer films may be useful for material transfer below the diffraction limit, and could also be used in existing micrometer- and millimeter-scale transfer processes. Laser-induced blister formation further provides an on-demand single-pulse microlens fabrication method with no post-processing steps required.

Acknowledgements

When I started my graduate studies at University of Ottawa in September 2016, I could not foresee how many brilliant and supportive people would be involved in shaping my thesis work. It has been a privilege to work with my supervisor, Prof. Paul B. Corkum. Paul is an exceptional scientist with equally exceptional kindness and patience. I am thankful for the guidance, encouragement and many opportunities he has given me during my degree.

Science is a team sport. I acknowledge Deepak Kallepalli, who was my close colleague, mentor and friend over the last several years. Working with him, I learned much about research and about life. I cannot thank him enough for his contributions to the scientist that I am today. I also acknowledge the effort of two students I worked with earlier in the project, Jesse Ratté and Janiya Khassenova, who were a pleasure to work with and mentor. I acknowledge Martin Chiasson, Tyler Clancy and Yu-Hsuan Wang for their early contributions to the experimental setup that I developed during this work. I thank Mathew Britton and Zhengyan Li for generously giving their time to train me in the lab. I acknowledge Chunmei Zhang, Donghyuk Ko and Shawn Sederberg for their management of the lab. I am thankful for collaboration and support from André Staudte, Søren Møller, and Aleksey Korobenko, three scientists I admire greatly. I thank my fellow Ph.D. candidates Mathew Britton, Graham Brown, Fanqi Kong, Guilmot Ernotte, Zack Dube and Tian Wang for setting a high standard of excellence that I strove to match throughout my degree. I thank all members of the group as well for countless helpful discussions and for their unique contributions in making our research group a welcoming and supportive community.

I am also thankful to many collaborators outside of the group who generously lent their expertise. I acknowledge Dr. Maohui Chen for generously sharing his atomic force microscopy knowledge and instrumentation. I acknowledge Sabaa Rashid and Dr. Choloong Hahn for lending their world-class abilities with focussed ion beams to my work. I would like to thank the staff of Prof. Pierre Berini's Nanofab facility for their training in a number of fabrication and characterization techniques that were used in this thesis. I acknowledge Dr. Zygmunt J. Jakubek for sharing his wealth of knowledge about polymer chemistry. I thank Andrew Ochalski for his assistance with optical microscopy experiments. I would also like to thank our collaborators Sasha Loboda, Adam Carew and Daaf Sandkuijl from Standard BioTools, from whom I gained expertise and experience in laser-ionization mass spectrometry.

I am thankful to University of Ottawa Physics Department for many excellent graduate courses and the collaborative environment that enabled the research in this thesis. I treasure the friendships I have made during my degree, especially those made while serving the Physics Graduate Student Association and the Optica-SPIE Student Chapter.

I would like to acknowledge Søren Møller, Mathew Britton, Fanqi Kong, Graham Brown, and Benoit Vanus, who generously gave their time to provide feedback on my writing.

Lastly, I'd like to thank the people in my life outside of research. My partner Kira Hillier has provided much support, happiness and love over the past decade. I look forward to our future chapters together with our wonderful dogs Sophie and Hank. It is a rare experience to be a twin, and even rarer to study the same discipline. I'd like to thank James Godfrey for many interesting discussions about experimental optics and providing healthy competition. And of course, none of this would have been possible without my parents, who have always encouraged me to follow my passions and have provided so much in order for me to do so.

List of Publications

I contributed to the following peer-reviewed publications during my graduate studies at University of Ottawa.

1. **Alan T.K. Godfrey**, Deepak L.N. Kallepalli, Jesse Ratté, Chunmei Zhang, P.B. Corkum. Femtosecond-Laser-Induced Nanoscale Blisters in Polyimide Thin Films through Nonlinear Absorption. Physical Review Applied **14**, 044057 (2020). **Appears in Section 3.1.**

2. **Alan T.K. Godfrey**, Deepak L.N. Kallepalli, Sabaa Rashid, Jesse Ratté, Chunmei Zhang, P.B. Corkum. Blister formation in dynamic release mirror structures using femtosecond laser pulses. Optics Express **30**, 39922-39931 (2022). **Appears in Section 5.3.**

3. Deepak L. N. Kallepalli, **Alan T.K. Godfrey**, Jaspreet Walia, Fabio Variola, André Staudte, Chunmei Zhang, Zygmunt J. Jakubek, P. B. Corkum. Multiphoton laser-induced confined chemical changes in polymer films. Optics Express **28**, 11267-11279 (2020). **Appears in Section 4.1.**

4. Deepak L. N. Kallepalli, **Alan T.K. Godfrey**, Jesse Ratté, André Staudte, Chunmei Zhang, P. B. Corkum. Surface adhesion of back-illuminated ultrafast laser-treated polymers. Physical Review Materials **5**, 045201 (2021). **Appears in Section 4.2.**

5. A. Korobenko, S. Saha, **A. T. K. Godfrey**, M. Gertsvolf, A. Yu. Naumov, D. M. Villeneuve, A. Boltasseva, V. M. Shalaev, P. B. Corkum. High-harmonic generation in metallic titanium nitride. Nature Communications **12**, 4981 (2021).

Statement of Personal Contributions to the Publications

In Publication 1, I was the lead author. I co-wrote this paper with the second author. I designed and performed laser-induced blister formation experiments with assistance from the

second and third authors. I fabricated all samples and conducted all atomic force microscopy (AFM) measurements. Along with the second author, I collected linear absorption data. I performed all calculations and analysis.

In Publication 2, I was the lead author. I co-wrote this paper with the second author. I designed and performed laser-induced blister formation experiments with assistance from the second and fourth authors. I fabricated all samples and conducted all AFM measurements. I was involved in collecting focussed ion beam (FIB) measurements with the third author. I performed all calculations and analysis.

In Publication 3, I was the second author. I co-wrote this paper with the lead author. I designed and performed laser-induced blister formation experiments with assistance from the lead author. I fabricated all samples and conducted all AFM measurements. I assisted the lead author in analyzing the spectroscopy and microscopy data. I was involved in collecting FIB measurements along with the lead author and an expert instrument operator who was acknowledged in the publication.

In Publication 4, I was the second author. I co-wrote this paper with the lead author. I designed and performed laser-induced blister formation experiments with assistance from the third author and the lead author. I fabricated all samples and conducted all AFM measurements and analysis. I assisted the lead author in collecting water drop goniometry measurements. I was involved in collecting FIB measurements along with the lead author and an expert instrument operator who was acknowledged in the publication.

In Publication 5, I was the third author. I conducted AFM measurements, assisted the lead author in analyzing the AFM data and contributed to writing the manuscript.

Contents

List of Figures

Chapter 1

Introduction

Light-based technologies are essential to our society today and continue to increase in prevalence due to the rich variety of physical processes that can be achieved with light. Light is the cornerstone of many large industries, such as optical data storage [1], telecommunications [2], lithography for chip manufacturing [3], solar power [4], laser welding in manufacturing [5], and laser eye surgery [6]. Light also carries a great deal of scientific and research interest. Scientific applications include (but are not limited to) linear and nonlinear optical microscopy [7–9], optical spectroscopy [10], high harmonic generation [11], remote sensing by laser-induced breakdown spectroscopy [12], mass spectrometry (such as matrix-assisted laser desorption ionization and laser ablation techniques) [13, 14], laser-based material printing [15, 16], and laser-induced micro- and nano-structuration of surfaces [17, 18].

Many of these applications rely on the fact that light energy can be absorbed in materials. As will be developed in Chapter 2, laser pulses with femtosecond durations are particularly useful for confined energy in deposition in the smallest possible volumes. This is owing to their high typical intensities leading to nonlinear absorption, confining the absorption region, as well as the lack of thermal diffusion over the duration of the pulse (i.e. the energy stays where it is absorbed).

This thesis focusses on the deposition of energy from intense, tightly-focussed femtosecond pulses. For a thin polymer film on a glass substrate, it is possible to focus individual laser

pulses through the glass onto the underside of the polymer. The laser energy deposited under the polymer film results in the formation of micro- and nanostructures.

1.1 Thesis Outline

Chapters 2, 6 and 7 of this thesis follow a monograph format. Chapters 3 to 5 follow a thesis-by-articles format, consisting of 4 peer-reviewed articles. Each paper is preceded by an introduction section, and figures and references are self-contained within each paper.

- Chapter 2 provides relevant background in the origin of intense femtosecond laser pulses, laser machining and Laser-Induced Forward Transfer (LIFT) of materials, tight focussing of laser pulses, and confined energy deposition through nonlinear absorption. It also covers the experimental setup, fabrication and characterization techniques used in the work comprising this thesis.

- Chapter 3 discusses further background on intact 'blister' microstructures. We then show how we use the confined energy deposition of tightly focussed femtosecond pulses to generate the smallest intact laser-induced blister structures in a thin polymer film to date (700 nm base width, 400 nm FWHM).

- Chapter 4 explores resulting changes to the optical and chemical properties of polymer films when structured with laser-induced blisters. By overlapping structures made by single pulses, we create surface textures that greatly modify the surface adhesion, as shown through measurements of water drop contact angles. We also show that during this process, chemical modification by the laser is trapped entirely under the film, and many changes to the optical properties of the polymer had also occurred.

- Chapter 5 identifies potential drawbacks for using a homogenous polymer film (shown in Chapter 3) for nonlinear absorption in a Laser-Induced Forward Transfer process. We introduce a new approach using a multilayer film combining polymer and metal films which remedies this problem by preventing transmission of intensities below the

nonlinear absorption threshold. We then study the blister formation process in this context and identify the roles of the polymer and metal layers in this process.

- Chapter 6 demonstrates a new application of laser-induced blister formation: single-pulse writing of microlenses into a polymer film. We fabricate arrays of blister microlenses for various pulse energies and laser focal spot sizes and characterize their focussing behaviour using optical microscopy.

- Chapter 7 presents our outlook on the advances made in this thesis, and the next steps to be taken. We propose that femtosecond pulses can be used in imaging mass cytometry, for fast imaging of biological tissue sections with sub-cellular detail. With this, we can provide direct insight into biology and medicine.

Chapter 2

Background and Experimental Details

This chapter provides the required background knowledge in optics, sample fabrication and characterization for this thesis. Before delving into ultrafast optics, we must first cover the relevant historical background and knowledge of Gaussian optics. I will then explain how we generate small laser focal spots of extremely high intensities. We use these high intensities to drive nonlinear absorption, a nonlinear optical effect that helps us to further confine the region of energy deposition. Additionally, employing laser pulses with durations shorter than the thermal relaxation time of a material, which is typically $<10\,\mathrm{ps}$ for dielectrics [19], prevents heat diffusion during energy deposition. These effects enable smaller laser-induced structures and ablation spots than what would be possible with linear absorption of nanosecond pulses, which is the method favoured in previous works on polymer blister formation.

Chapters 3 to 5 follow a condensed thesis-by-articles format, so this chapter will also explain the relevant details of our optical setup, sample fabrication, and sample characterization.

2.1 Optics

2.1.1 A Brief History of Laser Sources, Laser Machining and Laser-Induced Forward Transfer

In August of 1960, the field of optics changed forever when Theodore Maiman published results of the first solid-state laser using a ruby crystal [20]. Since then, numerous long-pulse and continuous-wave lasers have been developed and integrated into modern technologies, such as data storage, fiber-optic communications, microscopy, and laser welding. Lasers are useful because they are monochromatic[1] and coherent; the waves produced all add constructively and have a well-defined polarization direction. This produces high peak powers that increase as the duration of the pulse decreases. Shortly after Maiman, McClung and Hellwarth demonstrated the first high-peak-power nanosecond laser pulse using Q-switching to extract pulses from a highly efficient ruby laser cavity [22, 23]. In 1968, E.B. Treacy noted that short pulses had a small range of wavelengths dispersed over time, and could be made even shorter (down to hundreds of femtoseconds) by using a pair of diffraction gratings to reduce this 'chirp' [24, 25]. At this point, laser technology was limited by optical damage in the laser cavity. Strickland and Mourou solved this problem by introducing chirped-pulse amplification in 1985 [26] which earned them the 2018 Nobel Prize in Physics. This technique is the basis of most high-energy femtosecond laser systems in use today. By condensing laser energy in space (tight focussing) and time (pulse compression), femtosecond laser pulses routinely reach intensities around 10^{12} – 10^{15} W/cm^2, which is billions of times greater than the intensity of sunlight at the Earth's surface, confined to the scale of micrometers. This intensity is sufficient for driving nonlinear absorption in glass, polymers and metals. Nonlinear

[1] Monochromaticity is relative. CW lasers are nearly monochromatic, with typical bandwidths below 1 nm. When lasers are pulsed, the frequencies in the pulse now modulate the pulse (i.e. turning the pulse 'on' and 'off' in time). As a result, the pulse must have more frequency components as a basic consequence of the Fourier transform between time and frequency domains. The transform limit (see, for example, Chapter 3 of Weiner's *Ultrafast Optics* [21]) determines the shortest possible pulse duration for a given linewidth. For the scenarios in this thesis, laser pulses are referred to by their *central* wavelength, and the bandwidths of the pulses ($\sim$ 25 nm) are small relative to broad polymer absorption bands and the specifications of our optics. The lack of strict monochromaticity is always an experimental consideration for ultrafast pulses.

absorption will be discussed in 2.1.4.

Picosecond and femtosecond pulses are particularly advantageous for micromachining and other similar kinds of work as compared to nanosecond pulses. Their peak intensities are typically much higher that nanosecond pulses due to their shorter pulse durations, which in turn provides easier access to nonlinear absorption. These nonlinear absorption processes are threshold-like and allow of deterministic machining at and below the micrometer scale [27–29]. Also, picosecond and femtosecond pulses provide rapid energy deposition without significant thermal diffusion for pulse durations up to the thermal relaxation time of the material [19]. This leads to clean non-thermal ablation without significant melting of the surroundings, as in the case of nanosecond pulse machining [30].

A wide variety of microstructures and nanostructures are achievable using pulsed lasers, especially for femtosecond lasers, in metals, dielectrics and semiconductors [28, 31–36]. Historically, there is an emphasis on using lasers to modify and/or remove material from bulk or a thin film on a substrate. However, lasers can also be used to transfer material and additively build objects, as in the technique of Laser-Induced Forward Transfer (LIFT) [15, 16]. In LIFT, a laser pulse is sent through a transparent substrate and interacts with a material of interest on the far side. The material is propelled by the laser (either by direct interaction or by thrust generated from an intermediate absorbing film) and ejected from the substrate to be received on another surface. LIFT has a wide range of applications in electronics (organic LEDs, organic thin-film transistors, metallic nanoparticle ink or paste "wires", microcapacitors and microbatteries), printing biological material (DNA strands, cells for building tissue), and step-by-step building of 3D metal structures [15, 16].

Many variations of LIFT are possible, as reviewed in Ref. [16] and further summarized here. In direct LIFT, the transfer material absorbs laser pulses directly. Solid materials can undergo melting and then transfer as ejected liquid. This has potential to create nanoparticle droplets. Additionally, materials in liquid phase can be transferred directly as liquid jets. Multiple laser pulses can be used on solid donor films to achieve incremental delamination and transfer without a significant phase change. However, direct LIFT has the obvious drawback

of potentially modifying the material that one hopes to transfer, since absorption in the transfer material is unavoidable. Intermediate absorbing layers called dynamic release layers (DRLs) can also be employed, to absorb the laser and promote successful material transfer. Thin metal DRLs absorb and uniformize the deposited energy, though elevated temperatures may still affect the transfer material, and contamination of the transfer material from metal film fragments occurs [37]. Polymer DRLs protect the transfer material from both optical and thermal damage. One possible choice of polymer DRL is triazine, which cleanly undergoes photodecomposition when irradiated by UV light. However, it is not commercially available and can have the deleterious effect of shockwave formation from vaporization, which can disrupt transfer material. A different choice of polymer, such as polyimide, can result in intact plastic deformation driven by laser vaporization of part of the film, rather than full photodecomposition. Blister formation is discussed in greater detail in Chapter 3.

Blister-based LIFT has been shown to be successful even for thermally and mechanically sensitive materials, such as gold-coated nanoparticles, carbon nanotubes and monolayer transition metal dichalcogenide crystals [38]. Further, using the enhanced energy confinement of nonlinear absorption (discussed in Section 2.1.2), thin blister-forming polymer DRLs may allow for improved resolution of LIFT for a wide variety of transfer materials.

2.1.2 Focussing of a Gaussian Laser Beam

Gaussian optics describes how light is focussed to a spot of finite size. This is used to determine intensity and fluence (peak power and energy, respectively, per unit area), which is critical to this work. Fortunately, these topics are well understood and developed in many texts and resources [39–44]. They will be summarized here briefly.

Laser beams are frequently idealized as being circularly symmetric and Gaussian in their radial intensity profiles. For a perfectly collimated Gaussian beam, the intensity profile is unchanged as it propagates (along the z-axis, which is conventional in optics). The equation for the intensity profile is

$$I(r) = I_0 \cdot e^{-2r^2/\omega^2} \tag{2.1}$$

where r is the distance from the axis, I_0 is the peak intensity at $r = 0$, and ω is the radius of the beam at $1/e^2$ of the peak intensity. Since this thesis deals with phenomena that depend on intensity (power-over-area) and fluence (energy-over-area), we do not need to get into details about the electric field which is rapidly time-varying.

The radius of the laser spot at any point along the axis of a focussed monochromatic Gaussian laser beam is described by

$$\omega(z) = \omega_0 \sqrt{1 + \left(\frac{\lambda z}{\pi \omega_0^2}\right)^2} \tag{2.2}$$

where z is the location along the optic axis, $\omega_0 \equiv \omega(0)$ is the radius at the beam waist located at $z = 0$, and λ is the wavelength of the light. The value of z can be negative (describing a being beam focussed) or positive (describing the divergence of the beam after the focus), and has even symmetry about $z = 0$. Figure 2.1 illustrates this symmetry. Combining Equations 2.1 and 2.2, the intensity of the focussed Gaussian beam in space is

$$I(r, z) = I_0 \cdot \left(\frac{\omega_0^2}{\omega^2(z)}\right) \cdot e^{-2r^2/\omega^2} \tag{2.3}$$

where $I_0 \equiv I(0, 0)$ is the peak intensity on axis at the location of the beam waist, and the factor of $\omega_0^2/\omega^2(z)$ allows for the peak intensity on axis to scale by an appropriate factor of beam area.

The quality of the laser beam, particularly how much it differs from a perfect Gaussian beam, can affect the resultant beam focussing. Fortunately, accounting for this change in focussing behaviour is simple for a circularly-symmetric beam. Using Siegman's metric of M^2, which is based on second-moment beam diameter measurements, an imperfect beam will give a focal spot a factor of M wider than a perfect Gaussian beam with a limiting value of $M^2 = 1$ [45]. As we find in Section 2.2, the laser used in this thesis work had a beam profile with $M^2 = 1.08$, so our beam quality was very close to an ideal Gaussian beam.

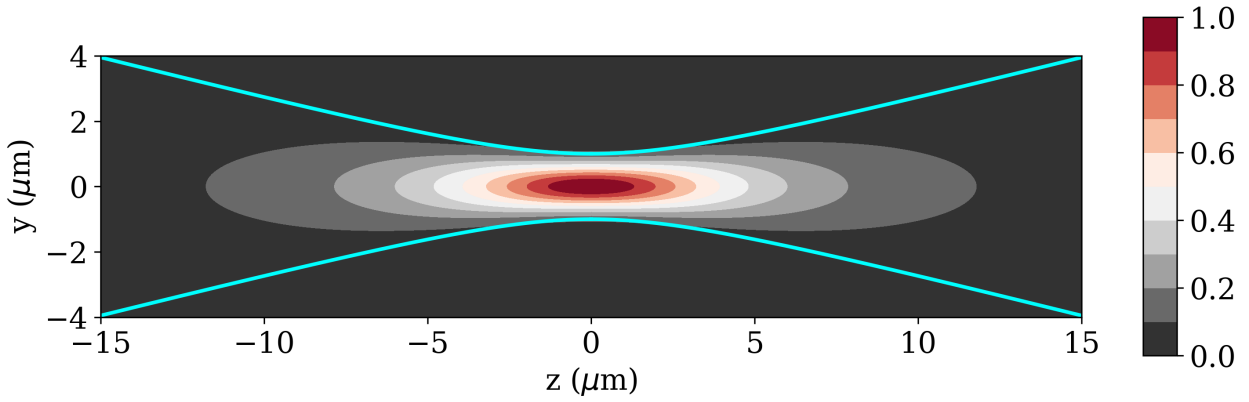

Figure 2.1: An illustration of a focussed Gaussian beam based on Equation 2.3. In this example, the radius of the beam was chosen to be $\omega_0 = 1$ µm and the peak intensity is normalized to $I_0 = 1$ (unitless). The cyan lines denote the beam diameter 2ω at each z-position. Note that this is a yz-view of the beam for $x = 0$, and $r = \sqrt{x^2 + y^2}$.

2.1.3 Spatiotemporal Description of a Focussed Laser Pulse

Microscope objectives, which are compound optics created from several optical elements, are a common tool used for tightly focussing laser beams. They are typically well-corrected for spherical aberration, which occurs when rays further from the optic axis are focussed at a different distance than on-axis rays, and for chromatic aberration, which occurs when different wavelengths of light are focussed at different distances.

Microscope objectives are characterized most commonly by their image magnification and their numerical aperture (NA). The NA determines the diffraction-limited laser spot size at the beam waist in the following well-known way (see, for example, Zalloum *et al.* [46]):

$$2\omega_0 = \frac{1.22\lambda}{NA} \tag{2.4}$$

where $2\omega_0$ is the full diameter of the beam waist and NA is the numerical aperture. At high NA, the estimate of the spot size may be inaccurate if the focussing conditions are nonparaxial; however, for typical values in this work ($\omega_0 \approx 1\mu$m, $\lambda = 800$ nm), paraxial estimates are still valid [47]. Our high-NA objectives were underfilled, which reduced the effective NA and increased the spot size, resulting in paraxial-like conditions. Equation 2.4 can then be used with Equations 2.2 and 2.3 to provide a simple model of the focal volume

for a Gaussian laser pulse focussed by a microscope objective. The effective axial extent of the focus is described by the Rayleigh length z_R, which is the distance between the beam waist and the position where the beam has expanded to $\omega(z_R) = \sqrt{2}\omega_0$:

$$z_R = \frac{\pi\omega_0^2}{\lambda} \tag{2.5}$$

When a laser pulse is focussed precisely onto a thin film of material (i.e. the beam waist is positioned on the surface of interest to within a fraction of the Rayleigh length), the beam waist size can be used to estimate the peak intensity and fluence involved in the laser interaction. The power profile of a Gaussian temporal pulse is typically expressed as [48]:

$$P(t) = P_0 \cdot 2^{-(2t/\tau)^2} \tag{2.6}$$

where P_0 is the peak power of the pulse, t is time, and τ is the intensity full-width at half-maximum of the pulse. Since the power integrated over all times must give the total energy of the pulse, then it is easily shown that

$$P_0 = 2\sqrt{\frac{\ln(2)}{\pi}}\left(\frac{E_{pulse}}{\tau}\right) \approx 0.94\frac{E_{pulse}}{\tau} \tag{2.7}$$

where E_{pulse} is the total energy of the laser pulse (see Appendix A). A simpler pulse profile that is sometimes used is a square temporal pulse with width τ. In this case, the peak power is constant over the pulse and is simply:

$$P_{0,square} = \frac{E_{pulse}}{\tau} \tag{2.8}$$

In this thesis, it is noted explicitly whichever temporal profile is chosen for calculations; the Gaussian profile is generally preferred due to better accuracy in describing the pulses produced by our laser and in subsequent intensity-dependant interactions such as ionization.

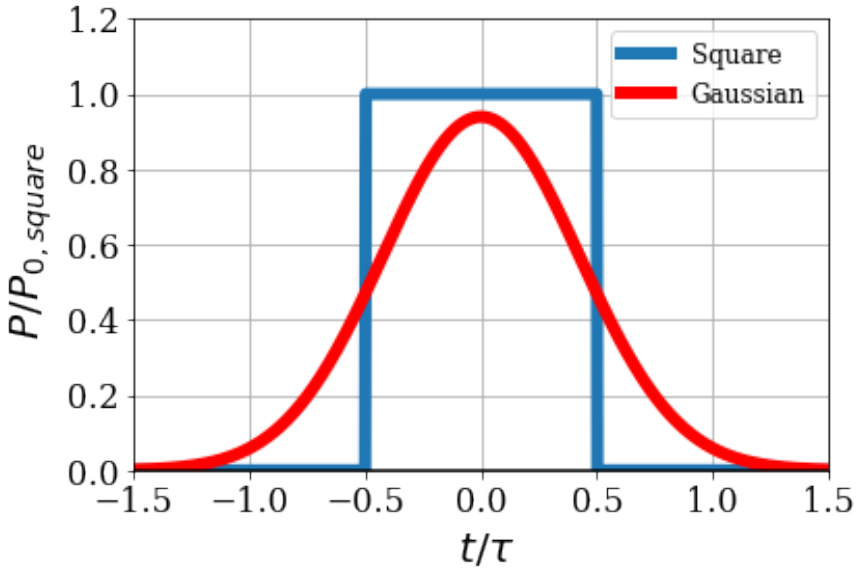

Figure 2.2: A comparison of temporal pulse shapes. The horizontal axis is normalized to pulse duration, τ, and the vertical axis is normalized to the peak power in the square pulse, $P_{0,square}$. Both curves have the same area beneath them; temporal pulses with each profile would carry the same pulse energy.

The peak intensity of the Gaussian spatial profile of the focus is then given by [42, 43]:

$$I_0 = \frac{2P_0}{\pi\omega_0^2} \tag{2.9}$$

Equation 2.9 can be used with Equation 2.3 (with $z = 0$) to model the intensity profile at the beam waist (effectively reducing to Equation 2.1), and further used with Equations 2.2 and 2.3 to provide a simple estimate of the three-dimensional intensity profile for a laser pulse focussed by a microscope objective with a given NA. It is important to ensure that temporal broadening of the laser pulses in glass is accounted for; our methods for ensuring laser pulses are optimally short in experiment are described in Section 2.2.

2.1.4 Nonlinear Absorption

Optical absorption is everywhere in our daily life. Many colours we see are a direct result of optical absorption as light scatters from objects on the way to our eyes. If the sun shines too brightly, we put on our tinted sunglasses to absorb excessive visible and UV light. These are

examples of linear absorption. Linear absorption is always 'on', and leads to the exponential decay of intensity represented by the Beer-Lambert Law as light propagates through an absorbing material (see, for example, [49]). This is expressed as:

$$I(z) = I_0 e^{-\alpha z} \tag{2.10}$$

where $I(z)$ is the light intensity at distance z from the starting point $z = 0$, I_0 is the initial intensity, and α is the linear absorption coefficient of the material. The absorption is 'linear' in that it depends linearly on the instantaneous photon flux in the material. More explicitly, $\frac{dI}{dz} \propto I$, which yields the exponential function in the previous equation. In Boyd's *Nonlinear Optics, 3rd Edition*, it is noted that standard linear absorption corresponds to a one-photon transition between two states with the following rate [41]:

$$R = \frac{\sigma I}{\hbar \omega'} \tag{2.11}$$

where R is the atomic transition rate, σ is the absorption cross-section describing the likelihood of absorption events, $\hbar$ is the reduced Planck constant and ω' is the optical frequency of the light. (The primed notation has been chosen to avoid ambiguity with Section 2.1.2) This gives us a quantized perspective with which to understand absorption. The absorption cross-section σ is a constant in linear absorption, meaning that the absorption rate is linear with incident intensity as expected.

However, at higher intensities, photons with insufficient energy for excitation alone can drive nonlinear or multiphoton absorption. It is simplest to understand multiphoton absorption as simultaneous absorption of multiple photons. Figure 2.3 shows a visual comparison between linear and two-photon absorption.

The 'nonlinear' part of the phenomenon refers to the fact that the absorption rate is no longer linear (i.e. the absorption cross-section is no longer constant with respect to intensity) during this kind of absorption. In the lowest order of multiphoton absorption, two-photon

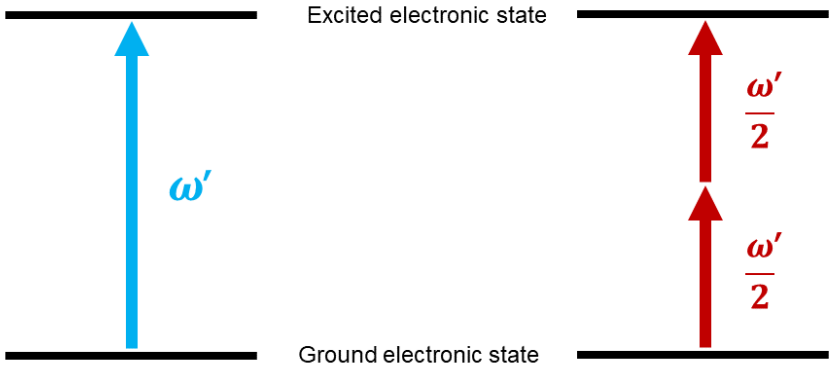

Figure 2.3: A comparison between linear (left) and two-photon absorption (right) in a two-level system. The levels have an energy gap corresponding to one photon of angular frequency $\omega' = 2\pi c/\lambda$. Under sufficiently high light intensity, two photons of half the frequency ($\omega'/2$) can be absorbed 'nearly simultaneously' as though they were a single photon promoting an electron to the excited state.

absorption, the total absorption cross-section depends linearly on intensity, which can be described by:

$$\sigma = \sigma_2 I \tag{2.12}$$

where σ_2 is the constant two-photon absorption cross-section for the material, and we have neglected simultaneous linear absorption for simplicity. Thus, the total transition rate in the case of two-photon absorption is proportional to I^2. In general, multiphoton absorption of N photons scales with I^N. However, this breaks down once the intensity is high enough to invalidate the underlying assumption that electron motion is perturbative, or if saturation occurs [50].

The first consequence of this intensity scaling is that nonlinear absorption does not occur until intensities are exceedingly high ($> 10^{12}$ W/cm^2 in this thesis). Fortunately, laser pulses with durations in the nanosecond to femtosecond range carry high enough peak powers to reach the required intensities quite easily. The result of strong intensity scaling is that nonlinear absorption processes have a characteristic intensity threshold with an onset much sharper than in linear absorption. We approximate this onset as a step-like function of intensity.

The second consequence follows from the first. For a focussed laser beam (as in Figure

2.1), the intensity is highest around the beam waist. As can be seen in Figure 2.4, higher orders of intensity dependence will lead to energy deposition in successively smaller volumes (both laterally and along the axis). This is the resolution advantage of nonlinear absorption that is exploited widely in various optical techniques, such as nonlinear optical microscopies [51, 52] and laser ablation below the diffraction limit [53]. In the context of this thesis, confinement along the optical axis is beneficial for reducing laser penetration into a thin film, while the lateral confinement imposes the ultimate resolution limit for creating intact laser-induced structures in our films. This idea is emphasized in Chapter 3. In scenarios where trains of several pulses are used for material processing, plasma shielding can limit the penetration into the film even further [54]. However, in the case of single femtosecond pulses, plasma can only be generated long after the laser energy is deposited and hence does not play a role.

It is worth noting that we use many molecular materials in this work such as polymers and glass. These contain many bonded atoms with numerous vibrational states. Rather than having sharply defined energy levels, the two 'levels' of the system are each a broad continuum of states (bands). However, it is still generally regarded as sufficient to describe dielectrics and semiconductors as having a single well-defined band gap, and so the ideas from this section are still reasonable.

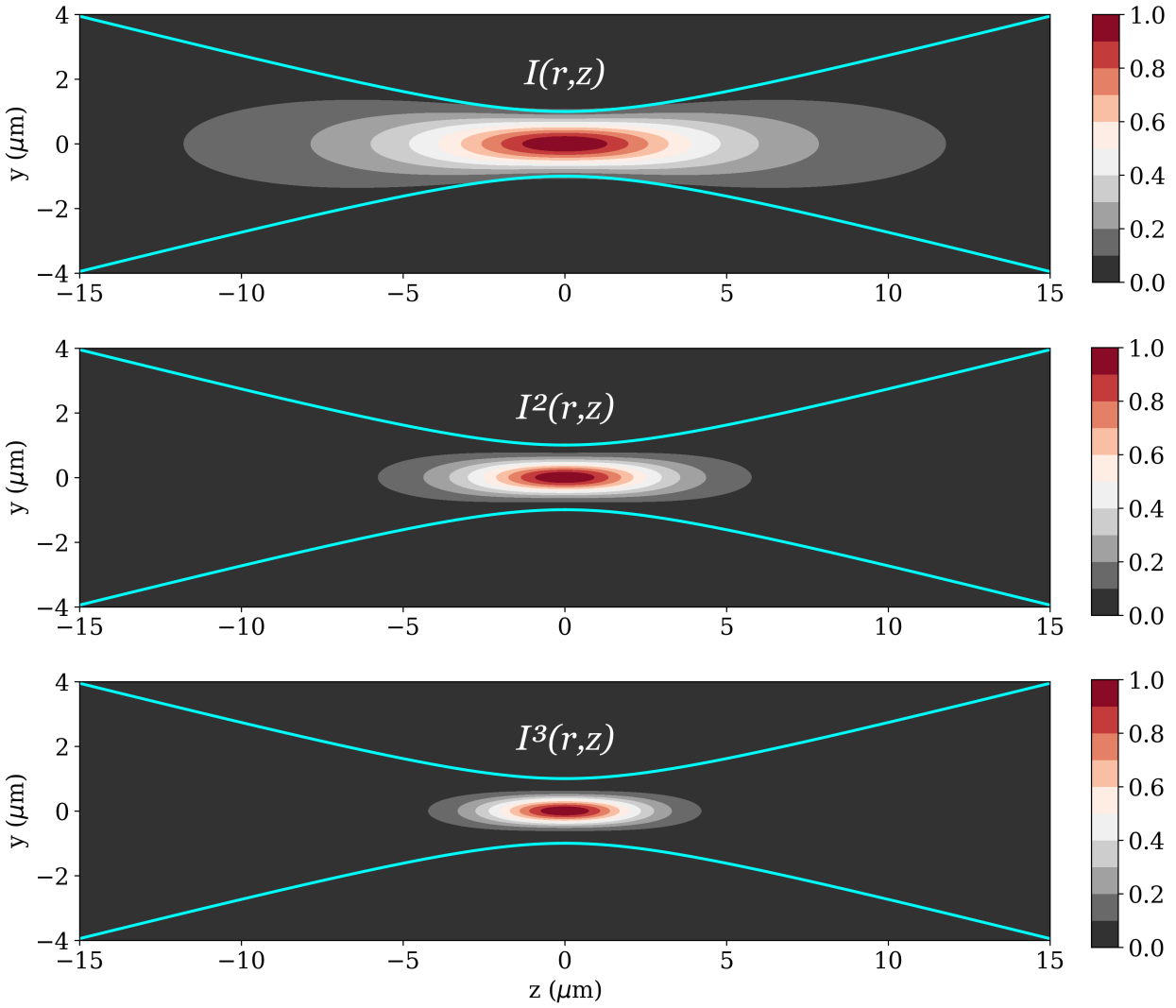

Figure 2.4: A comparison of various powers of intensity, which represent intensity dependences in linear and nonlinear absorption processes, for the Gaussian beam shown in Figure 2.1. Top: $I(r,z)$, middle: $I^2(r,z)$, bottom: $I^3(r,z)$. Powers of intensity are normalized to a peak value of 1 (unitless).The greater spatial confinement of the absorbed energy (proportional to these powers of intensity) leads to smaller scale energy deposition than what is possible from linear absorption.

2.2 Experimental Methods

This section is a detailed summary of the experimental setup that was developed for the work in Chapters 3 to 6. While the setup is described in the papers and drafts comprising these chapters, some technical details were left out for brevity. This section will fill in those details to give the reader a full understanding of how these experiments were built and performed.

The laser source for the system is a Coherent RegA 9040, producing laser pulses with a duration of 45 fs (as measured by frequency-resolved optical gating [55]) and a central wavelength of 800 nm. The pulse energy delivered from the laser was 6 µJ directly in front of the output aperture of the laser, with a shot-to-shot energy fluctuation of 1%. The repetition rate was adjustable between 500 Hz and 500 kHz through the synchronized delay generator in the system. The delay generator could be operated in single-shot mode, yielding single pulses on demand. The system contains an adjustable grating compressor, allowing for the chirp of the pulses to be adjusted to pre-compensate for dispersion of the optics in the experimental setup. This provides the shortest possible laser pulse, and thus the highest possible intensity, at the sample.

The layout of the experiment is shown in Fig. 2.5. We implemented a spatial filter to improve the quality of the beam profile. The initial quality of the beam was poor, and spatial noise in the beam profile must be filtered out to prevent it from being mapped onto the resulting laser modification. The spatial filter functions by focussing the laser using a plano-convex lens (f = 750 mm) through a 150 µm diamond pinhole from Advanced Wire Die Ltd. mounted in a two-axis translation mount to position the pinhole around the beam axis. The mounted pinhole was then placed onto a manual translation stage, to adjust the axial position so that the pinhole was placed at the beam waist. The pinhole position was selected by optimizing the power of the transmitted laser beam, then further by measuring the spatial profile on a Dataray WinCamD UCD12 imaging beam profiler and optimizing the circular symmetry of the beam. The filtered beam was collimated by a second plano-convex lens (f = 500 mm) also placed on a translation stage aligned with the beam axis. The position of the collimating lens was adjusted along the axis to ensure the beam size remained constant after propagating several meters. We used a Thorlabs MTS50-Z8 motorized translation stage to scan the Dataray beam profiler through the focus of a plano-convex lens with f = 100 mm. By fitting measurements of beam radius through the focus, we obtained a beam quality factor of $M^2 = 1.08 \pm 0.02$ [45].

After spatial filtering, the beam was sent through a variable attenuator. This consisted

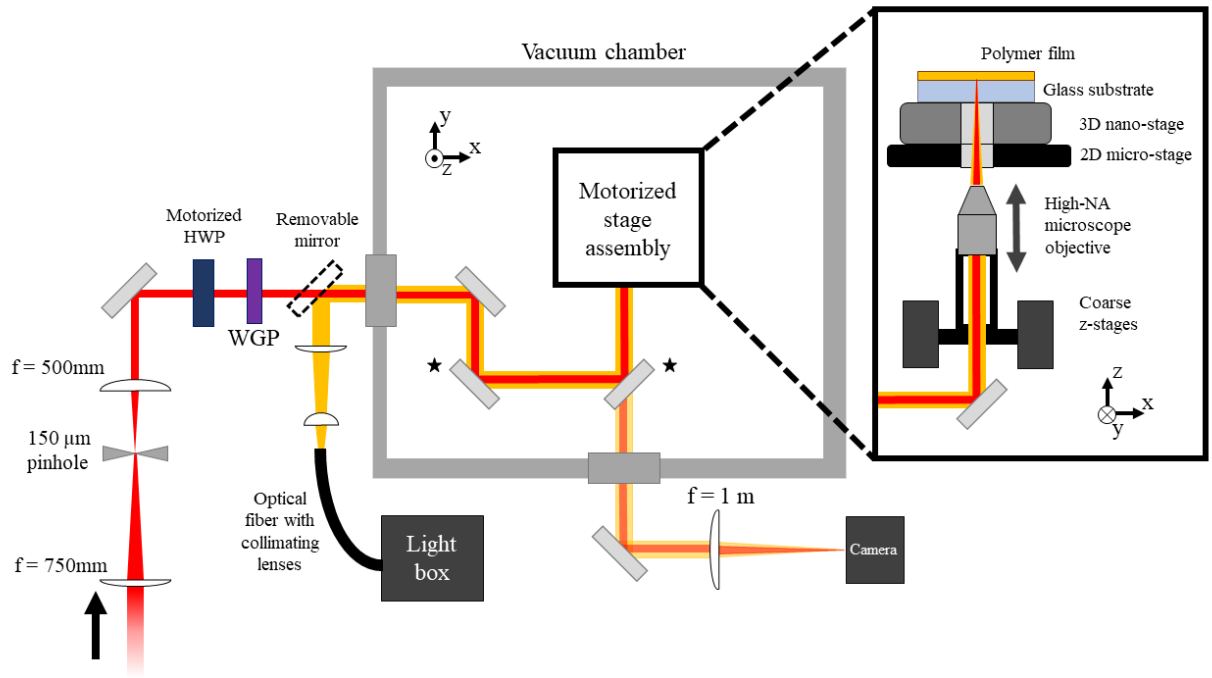

Figure 2.5: A diagram of the experimental setup used for laser micro- and nano-structuring experiments in Chapters 3 to 6. The beam is first spatially filtered using a diamond pinhole. The power is adjusted using a half-wave plate (HWP) in a motorized mount followed by a wire grid polarizer (WGP). The beam is then transmitted through a quartz window into the vacuum chamber and sent under the motorized stage assembly (right). The white light illumination path is shown collinear to the laser beam; however, the white light beam could only be used when blocking the laser with a removable mirror. Mirrors denoted by stars were used for aligning though the motorized stage assembly. A small amount of laser light and white light could be reflected from the sample, partially transmitted through one mirror, and used to image the laser focus and sample respectively. Objects not drawn to scale.

of an 800 nm half-wave plate in a Thorlabs PRM1Z8 motorized rotation mount and a Thorlabs WP25M-VIS broadband wire grid polarizer fixed to transmit the vertical polarization component of the laser beam. The beam was then sent through a quartz vacuum chamber window into the imaging mass spectrometry system which was the basis of Martin Chiasson's 2016 thesis [56]. While it was designed to be a vacuum system for mass spectrometry, it could also be used to perform laser micro- and nano-structuring experiments at ambient pressures under dry air flow without running the mass spectrometer. The beam is directed through the chamber using 3 steering mirrors that bring the beam towards the sample stage and provide the necessary degrees of freedom for alignment. Prior to the vacuum window,

we also placed a mirror on a removable magnetic mount for coupling in white light for in situ widefield imaging of the sample surface. The white light was generated by an Edmund Optics MI-150 High-Intensity Illuminator light box coupled into a Thorlabs M35L02 (0.39 NA, 1 mm core diameter) multimode optical fiber and then loosely collimated using a sequence of plano-convex lenses.

The beam is then reflected off a mirror mounted at a 45° incline, directing the beam upward into the through the sample stage assembly. We used high-NA microscope objective lenses mounted at the end of an SM1-threaded tube, which was screwed into a baseplate connecting two motorized translation stages working in tandem along the z-axis (i.e. along the beam axis). We used 10× 0.2NA, 20× 0.4 NA, 40× 0.75 NA and 80× 0.95 NA objectives; the specific objective used in each study is specified as needed in Chapters 3 to 6. This provided coarse adjustment of the focus on the sample with a 5 µm error or greater in repeatability. Above the objective, the sample was mounted on a holder that was inserted into a 3D translation stage assembly. This assembly consists of a micro-precision 2D xy stage (i.e. motion orthogonal to the beam axis) with a motion range of 10 mm on both axes and a 3D nano-precision stage with motion ranges of 100 µm on all three axes. The nano-precision stages had motion accuracy and repeatability better than 500 nm.

Once the beam reached the sample, a small portion of the laser light leaked back through one of the chamber mirrors and coupled out of the chamber through another vacuum window. Since our microscope objectives were infinity-corrected, the objective will re-collimate the reflection of a collimated laser beam focussed precisely on the sample. We then use a planoconvex lens (f = 1 m) to focus the reflected beam onto a Basler acA1300-200uc CMOS camera to re-image the laser focal spot from the sample. By coupling in white light instead of the laser, we can also generate a widefield image of the surface.

Since microscope objectives are tightly-focussing compound optics, correct alignment is critical for a high-quality laser focus. To ensure this, we placed threaded adjustable irises at each end of the tube and used two adjustable mirrors (starred in Figure 2.5) to align the beam through the center of each iris. We also used many glass optics in the setup, which

introduce dispersion on our laser pulses and increase their duration. To correct for this effect, we used the simple setup shown in Figure 2.6 to minimize the pulse duration at the sample. Inside of the vacuum chamber, we passed pulses through a coverslip to match the amount of glass during the experiment and then focussed them into a beta barium borate (BBO) crystal to generate second harmonic light centered around 400 nm. Residual 800 nm light was filtered out using two Thorlabs FGB37 absorbing bandpass filters, and the power of the 400 nm light was measured on a Thorlabs S170C power sensor. The grating compressor in the RegA 9040 laser system was adjusted to maximize the second harmonic signal. Since second-harmonic generation is a nonlinear process proportional to the square of the intensity in the perturbative regime (see for example, Boyd's *Nonlinear Optics, 3rd Edition* [41]), this procedure ensures the shortest, most intense pulse possible on the far side of our glass coverslip where we perform our experiments.

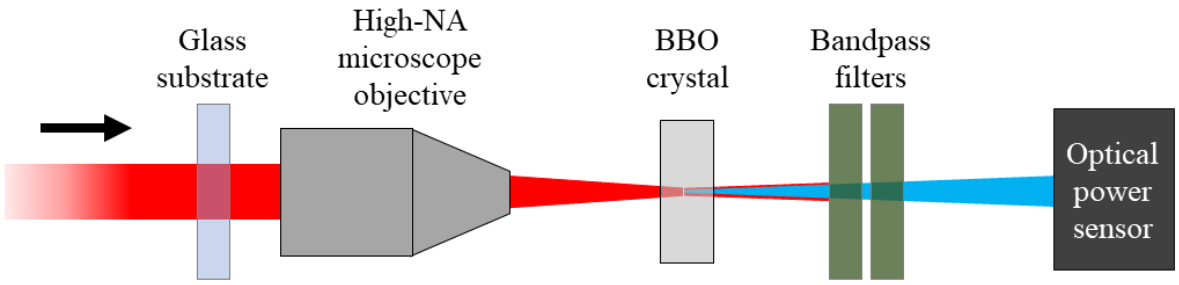

Figure 2.6: A diagram of the simple setup used to obtain the shortest pulse duration for our experiments. The beam is passed through the coverslip to be used in the experiment, then through the objective into a second-harmonic beta barium borate (BBO) crystal. Two bandpass filters were used to ensure all remaining 800 nm light was removed before measuring the optical power of the second-harmonic beam at 400 nm. The grating compressor in the laser system was adjusted to obtain the maximum second harmonic yield. Objects not drawn to scale.

For such tight-focussing optics, it is also critical to ensure that the laser is focussed precisely on the surface, as the Rayleigh lengths for these objectives are on the order of micrometers. This is particularly important, as a factor of 2 in intensity over the Rayleigh length is enormous in the context of nonlinear phenomena (scaling as 2^N for an N-photon process). The method of imaging the laser focus on the camera is sensitive to the sample

position, but it also depends on the collimation of the beam before the objective and the distance between the camera and the imaging lens. To determine the optimal focus position to an accuracy of 1 µm or better, we performed single-shot optical damage tests at various positions near the apparent focus determined by imaging. For numerous z-positions of the sample set using the nano-precision stage, single laser pulses of decreasing energy were fired at pristine regions of the polymer until laser modification was no longer visible. Since the intensity and fluence of the laser beam are highest at the beam waist, the optimal focus position is the one with the minimum pulse energy needed to modify the polymer. Unless otherwise noted, each blister fabrication experiment in this thesis was done at room pressure while flowing dry air out through a hinged porthole on the chamber. From preliminary observations, we noticed little difference between blisters formed at room pressure and blisters formed at 10^{-3} to 10^{-6} Torr. Slight changes to the focal distance of high-NA microscope objectives were accounted for in any experiments done under vacuum.

The motorized stages and operation of the laser were controlled primarily through LabVIEW for the work in this thesis. To efficiently integrate the stages and laser while keeping the control code general and scalable, the main LabVIEW control code was designed to receive individual instructions (such as stage motion, fire laser, set laser pulse energy, etc.) from an input text file. These input files were generated in Python, which allowed for efficient control of experiments with tens of thousands of operations. Laser pulse energy calibrations were collected using LabVIEW and fed into the main control code as a text file. Pulse energies were selected by interpolating the calibration data with a spline fit.

2.3 Fabrication and Characterization Techniques

This section presents a summary of the various techniques used in this thesis.

- We performed **polymer film fabrication** (polyimide and PMMA) by spin-coating using a Laurell WS-650-23 spin processor [57]. In this technique, a pre-cleaned substrate is mounted to a vacuum chuck. A small volume of liquid polymer precursor is dispensed

onto the substrate, and the sample is rotationally accelerated and then held at a fixed speed to disperse the polymer precursor evenly over the surface. The polymer film is placed on a hot plate at the recommended temperature to cure the film and bake out the solvent in the precursor. Specific film recipes are mentioned as needed throughout this work.

- **Metal film fabrication** was done using two techniques: sputter coating and vapor deposition. Sputter coating was performed using a Quorum 150R sputtering system [58]. A current is passed through a sacrificial electrode disk of the material to be coated, which sits over top of the substrate in a small vacuum chamber. The current generates a metal plasma which causes particles of the metal to be ejected and distributed on the substrate. Vapor deposition was performed using an Angstrom Nexdep evaporator [59]. The substrate was mounted at the top of the evaporator, and a crucible containing the desired metal at the bottom of the evaporator was irradiated with an electron beam to eject material and coat the substrate. In both techniques, a witness sample containing lithographed structures in a polymer film was also mounted and coated, then developed in isopropyl alcohol and measured using atomic force microscope (see later in this section) to verify the film thickness.

- **Profilometry** was performed using a Bruker DektakXT stylus profilometer [60]. This technique was used to determine spin-coated polymer film thicknesses. A scalpel was used to create a small scratch in the film, which removed material without affecting the glass substrate. The profilometer scans a sharply-pointed stylus across the scratch, which provides a height map of the scratch and therefore a measurement of the thickness of the film. The minimum measurable step height of the DektakXT was less than 10 nm according to manufacturer specifications.

- **Atomic force microscopy** (AFM) was used for surface characterization measurements with nanoscale accuracy throughout this thesis. Two instruments were used in the results of this works, a Bruker Dimension Icon AFM [61] and a JPK Nanowizard

II AFM. The instrument used will be specified in each chapter. Measurements were performed in contact mode. In this technique, a flexible cantilever with a sharp tip is scanned across the sample surface using a piezoelectric actuator with a constant force applied to keep the tip in contact with the surface [62]. As the height of the surface changes, the flexible cantilever responds to the surface morphology by bending. A laser beam is reflected from the top of the cantilever onto a position-sensitive photodiode (PSPD). The deflection of the laser beam measured by the PSPD maps the surface height. While AFM has been used for atomic-scale surface imaging since the late 80's [63–65], it is also useful for imaging micro- and nano-structures, which does not require this level of resolution. Contact AFM has been used throughout this thesis for characterizing large areas (up to 1000s of μm^2), which contain laser-induced structures, as well as measuring natural surface roughness over a few μm^2 prior to laser modification.

- **Focussed Ion Beam** (FIB) characterization was performed using a Zeiss ORION Nanofab **helium ion microscope** (which uses a helium FIB) equipped with a gallium FIB for characterizing the interior of laser-induced microstructures [66]. The gallium FIB is capable of rapidly machining away material with a resolution better than 3 nm, and was used to mill away half of a microstructure. The helium ion beam was used to image inside of the remaining half of the structure from the side.

- **Contact angle goniometry** was used to characterize the surface adhesion of water to textured polymer surfaces. In this technique, a small water droplet (volume ~1 µL) is placed on a surface and then viewed from the side with a camera. The water droplet sits intact on the surface, and the angle at which the water droplet meets the surface is determined using a contour generated by the instrument software. Since the sample surface is flat, the differences between contact angles on either side of the droplet image was small and the average was taken. The contact angle is a measure of the hydrophobicity or hydrophilicity of the surface, which is the tendency to repel or draw in water. As discussed in Chapter 4, hydrophobicity (or more generally, surface

adhesion) is closely related to two inherent properties of the surface: its roughness and its chemical composition. The instrument we used was a VCA Optima Series goniometer by AST Products Inc. with a contact angle resolution of 0.5°.

- **Absorption spectrometry** was performed on polymer samples using an Agilent Cary 5000 UV-vis-NIR spectrophotometer in a transmission geometry to determine their linear absorption properties. As described earlier in this chapter, the absorption spectrum indicates the bandgap of the material, and this gives information about the possible nonlinear absorption processes in materials. We found our polymer films to be transparent at our laser wavelength under low-intensity lamp illumination. However, strong absorption at 400 nm indicates that two-photon absorption of 800 nm is possible, and strong absorption of 267 nm light indicates three-photon absorption of 800 nm is possible.

- **Confocal micro-Raman Spectroscopy** was performed on polymer samples using a Witec Alpha a300 confocal Raman microscope. This technique combines point-scanning optical microscopy with Raman spectroscopy. The Raman spectroscopic signal, as discussed in Chapter 4, provides information about vibrational states in a material by laser excitation. This provides more detailed information than conventional absorption and fluorescence spectroscopy techniques, which only provide bandgap information. We carried out these measurements to understand the chemical nature of the material changes after laser irradiation in our work. However, the material showed fluorescence that obscured the Raman signal at all 4 excitation wavelengths, since Raman scattering typically has a much smaller cross-section than strong fluorescence excitation processes.

- **Confocal fluorescence microscopy** was also performed using the Witec Alpha a300 confocal Raman microscope. Our polymer material did not display strong fluorescence originally, and so fluorescence was further evidence of the chemical change induced in our polymer film samples.

- **Bulk fluorescence** and **fluorescence polarization anisotropy** measurements were both performed using a Horiba Jobin Yvon Fluorolog Tau-3 Lifetime System in constant excitation mode. Bulk fluorescence measurements reveal the total fluorescence spectrum over a large area. In fluorescence polarization anisotropy measurements, rotating polarizers are added in front of both the excitation and sample emission paths to select specific polarization components of each. As presented in Chapter 4, by analyzing the polarization components of these beams, we can determine how the polarization direction of the incoming laser creates oriented structures (aggregates) in the material.

- **Reflection-absorption infrared spectroscopy** (RAIRS) measurements were performed using a Thermo Nicolet Nexus 870 FTIR spectrometer. Because the wavelength is in the infrared (5—12 µm) in our RAIRS measurements, the infrared spectroscopy technique allows us to access low-energy stretching and bending modes of bonds. This allows us to probe the creation and/or destruction of bonds in the polymer when the laser induces chemical change. We carried out these infrared absorption measurements to provide information on bond structure, since Raman spectroscopy measurements were obscured by background fluorescence and could not provide this information.

- **X-ray photoelectron spectroscopy** (XPS) was used to obtain surface measurements that are confined to less that 10 nm of depth into the surface of our polymer films. In this technique, the surface is irradiated with a high energy X-ray source (in our case, aluminum Kα X-rays at 1486 eV of photon energy) to liberate electrons from atoms through the photoelectric effect [67]. These measurements were used in Chapter 4 to confirm that the chemical composition of polymer films had not changed at the surface after irradiation, which is further evidence that chemical change is fully confined beneath the film.

Chapter 3

Nanoscale Blister Formation Using Femtosecond Pulses

In Chapter 2, we showed that multiphoton absorption depends nonlinearly on light intensity. Multiphoton absorption in a dielectric requires high intensities (in this thesis, $> 10^{12}$ W/cm^2) but also results in superior confinement of the resulting energy deposition, as illustrated in Figure 2.4. In this chapter, we use the confined energy deposition of multiphoton absorption for laser-induced blister formation, where an intense laser pulse is used to form a protruding microstructure in a thin film of material.

Laser-induced blister formation occurs in an experimental configuration shown in Figure 3.1. A laser pulse is focussed through a transparent substrate onto the underside of a coated film (in our case, a polymer film on glass). In this geometry, the laser pulse deposits energy under the film, locally heating and/or vaporizing a portion of the film [16, 68–70]. The heated portion expands against the unmodified remainder of the film, pushing up an intact 'blister' structure which is still connected to the film.

Blistering (often called a bulging phase of the material) is a common occurrence in the dynamics of thin-film laser ablation, before the material shears and/or disintegrates [71–75]. This can potentially leave intact blister structures on surfaces if the ablation is incomplete. As demonstrated in these works, for example, blister formation does not strictly require

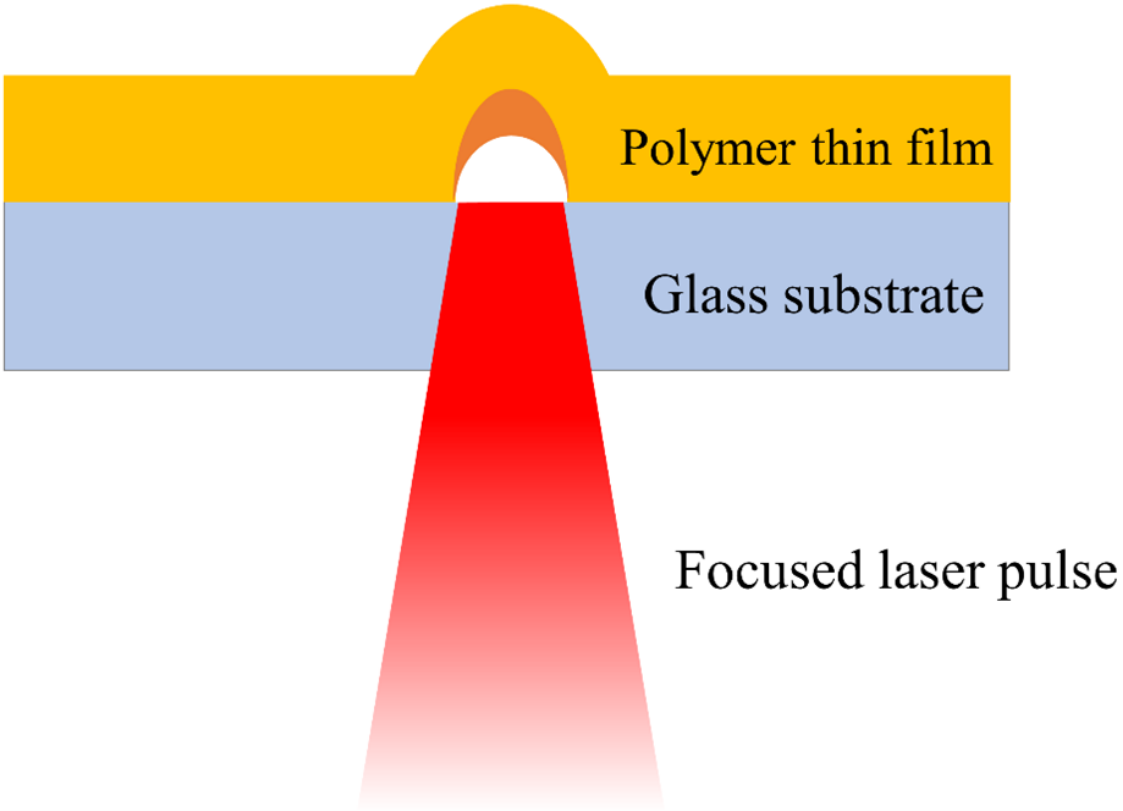

Figure 3.1: A schematic of the blister formation process for a polymer thin film on a glass substrate, with the laser pulse incident from the bottom of the figure. The laser pulse is focussed through the glass substrate and undergoes multiphoton absorption in the polymer film (yellow). In this illustration, the polymer film is left intact at the top of the blister, and modified polymer (orange) and a hollow void (white) are confined under the film.

back-illumination with a laser, but does require some form of energy deposition causing delamination of a film. Studies of film delamination over large length scales (millimetres down to several 100s of micrometers) have been performed in detail. Some such studies rely on laser-based delamination [76–78]. Other studies examined delamination by mechanical effects on the substrate [79], thermomechanical stress [80] or by chemical means [81].

Previous work has been done on microscale laser-induced blister formation in SiO_2 and SiN_x films on silicon substrates. Serrano and Cahill used nanosecond pulses to achieve intact glass blisters on silicon down to diameters of approximately 1 μm [82]. They used film thicknesses of 25 and 50 nm, and the laser pulse energy was deposited into the opaque substrate by front illumination through the transparent film to cause delamination. McDonald *et al.*

made a similar demonstration in SiO_2 films using femtosecond laser pulses, though the work did not focus on the smallest blister sizes that could be obtained; diameters 15 μm or larger were achieved [83]. Several more recent studies by the Herman group explored interferometric processing of SiO_2 and SiN_x on silicon substrates [84–86]. In these studies, the energy of the laser was deposited directly in the glass film because of standing-wave interference created by reflection from the substrate. Ablation was mostly seen, though Kumar *et al.* achieved intact blisters of 2 μm diameter and smaller features that showed evidence of a blister phase before ablating [84]. Since these studies all relied on front illumination of films on opaque substrates, this scheme would be impractical for realizing a generalized LIFT process for sensitive materials.

In our work, we extend blister formation to even smaller scales, in a configuration that may enable laser-based printing of sensitive materials with unprecedented resolution. We first motivate the use of nonlinear absorption processes for restricting absorption in a thin film, which enables the formation of smaller intact blister microstructures. We show a simple model of how various orders of absorption cause heating in a polymer film; higher absorption orders confine the absorption in both width and depth. This was done using a square temporal pulse, but is sufficiently above the absorption threshold in the chosen examples such that similar amounts of energy would be deposited for a Gaussian temporal pulse. Then, we experimentally demonstrate the use of tightly-focussed femtosecond pulses to create laser-induced blisters through confined nonlinear absorption in a polyimide film. We achieve the smallest laser-induced blisters to date to the best of our knowledge (400 nm FWHM, 700 nm full width at $1/e^2$), owing to the nonlinear absorption process as well as the pulse duration being short enough to avoid thermal diffusion. This represents a factor-of-2 improvement on what was achieved in glass films on silicon, and a factor-of-10 improvement on what had been shown for back-illuminated polymer films on glass which are more relevant to LIFT applications. This work also led us to consider other uses for blisters outside of LIFT, such as direct structuring of surfaces to control surface adhesion in Chapter 4, and laser-induced blister microlenses shown in Chapter 6.

In the experimental conditions of the following paper, it was also important to consider high intensities in the substrate before the pulse reaches the polymer film. Intensities around 10^{13} W/cm^2 generate absorbing free electrons in glass, which attenuates a pulse as it is focussed though the glass [87]. In this process, to a good approximation, intensities above the ionization threshold of glass are removed from the beam profile without otherwise affecting the pulse. This is a scenario that had not be addressed in any previous laser-induced blister formation or LIFT work to our knowledge.

3.1 Experimental Demonstration of Nanoscale Laser-Induced Blisters

Femtosecond-Laser-Induced Nanoscale Blisters in Polyimide Thin Films through Nonlinear Absorption

Alan T.K. Godfrey,* Deepak L.N. Kallepalli, Jesse Ratté, Chunmei Zhang,† and P.B. Corkum
Joint Attosecond Science Laboratory, University of Ottawa and National Research Council of Canada, 25 Templeton Street, Ottawa K1N 6N5, Canada

(Received 20 April 2020; revised 17 September 2020; accepted 18 September 2020; published 29 October 2020)

Nonlinear absorption of femtosecond laser pulses provides a unique opportunity to confine energy deposition in any medium to a region that is below the focal diameter of a pulse. Illumination of a polymer film through a transparent high-band-gap material such as glass, followed by nonlinear absorption of 800-nm light in polymers, allows us to further restrict absorption to a very thin layer along the propagation direction. We demonstrate this confinement by simulating femtosecond-laser-induced polymer modification by linear, two-photon, and three-photon absorption, and discuss the control over energy absorption in polymers that multiphoton processes offer. Energy deposited in a thin polymer film induces a protruding blister. We present experimental results for blister diameter and height scaling with variation of pulse energy. Using pulse energies of 20–200 nJ and 0.4-NA focusing, we fabricate blisters with diameters of 1–5.5 μm and heights of 75 nm to 2 μm. Using 0.95-NA focusing, we obtain laser-induced blisters with diameters as small as 700 nm, suggesting blister-based laser-induced forward transfer is possible on and below the 1-μm scale. Submicrometer blister formation with use of femtosecond lasers also offers a method of direct, precise laser writing of microstructures on films with single laser pulses. This method is a possible alternative to lithography, laser milling, and laser-based additive machining.

DOI: 10.1103/PhysRevApplied.14.044057

I. INTRODUCTION

When a femtosecond light pulse irradiates a material, one can easily exceed the ablation threshold of the material, leading to material removal long before heat transport becomes important [1–3]. This enables, for example, deterministic machining, sub-focal-spot machining, and nanoscale fabrication [4–6].

A similar situation can arise for irradiation of a low-band-gap material by light that has passed through a high-band-gap medium. For example, a femtosecond pulse containing approximately 1.3×10^{13} W/cm^2 can pass through a thick borosilicate glass plate before free-carrier generation in the medium is great enough to significantly attenuate the beam [7]. A few-cycle pulse in fused silica can even reach approximately 10^{14} W/cm^2 [8]. If high intensities are reached while Kerr-induced self-focusing is avoided (by use of tight focusing [9] or a sufficiently thin medium), a polymer film on glass can experience high-order multiphoton absorption of a well-controlled beam. Furthermore, with a modest increase of intensity above the threshold for free-carrier generation, the primary influence of the glass medium is to cap the intensity but leave the pulse otherwise unchanged in space and time [10].

We study the light-polymer interaction under these conditions. When an intense laser pulse is focused through a substrate onto a coated film, it can create a pocket of superheated material beneath the surface of the film that expands into a protruding blister. Blisters have been used to achieve laser-induced forward transfer, where they impart thrust on an object or material on the surface, thereby desorbing it while avoiding direct laser exposure [11].

Both polymers and metals have been explored as sacrificial laser-absorbing layers for laser-induced-forward-transfer applications, with pulse durations ranging from nanoseconds to femtoseconds [11–16]. Polymer films are ideal for preserving the chemical purity of the transferred material; metals are prone to degradation from thermal and chemical damage, leading to contamination of the transferred material [17]. Arnold and coworkers [11,13,16] demonstrated blister formation by linear absorption of nanosecond lasers in polyimide films. The underlying physics of polymer-blister formation in the nanosecond-pulse regime was addressed for blisters with a width of of 10–100 μm. However, no thorough studies regarding femtosecond lasers and nonlinear-absorption processes have been performed to our knowledge. Blisters on the few-micrometer and submicrometer scales have also not been explored. Nonlinear absorption of femtosecond pulses

*XXXXXXXXXXXXXXX
†XXXXXXXXXXXXXXX

leads to confined energy deposition due to thresholdlike absorption behavior and lack of heat dissipation over the timescale of the pulse.

In this paper, we demonstrate the advantages of nonlinear absorption of femtosecond pulses to create polymer blisters. We calculate material breakdown induced by single femtosecond pulses in laboratory conditions to illustrate the confinement of energy deposition. We then show blisters fabricated in polyimide films with use of single femtosecond pulses. We examine the effects of laser pulse energy on the resulting blister size, and show a linear relationship between the energy deposited into the polymer and the resulting blister volume.

This work establishes a method for direct and precise laser writing of microstructures on films using single laser pulses, which is an alternative to lithography, laser milling, and laser-based additive machining. Since the laser energy is deposited beneath the film, morphological changes are achieved while preserving the surface chemistry [18].

II. EXPERIMENTAL AND CALCULATION DETAILS

A. Experiment

A schematic of the femtosecond-laser-induced-blister-formation experiment is shown in Fig. 1(a). We use a Coherent RegA 9040 Ti:sapphire laser producing transform-limited pulses with a duration of 45 fs (FWHM, measured via frequency-resolved optical gating [19] by a MesaPhotonics MP002 FROGscan instrument) at a central wavelength of 800 nm. The beam is passed through a spatial filter and the spatial profile is verified to be Gaussian with a beam profiler (DataRay WinCamD UCD12); we measure the beam to have $M^2 = 1.08 \pm 0.02$. We adjust the pulse energy using a rotatable half-wave plate followed by a linear polarizer. The laser beam is focused by a 0.4-NA microscope objective (Edmund Optics DIN

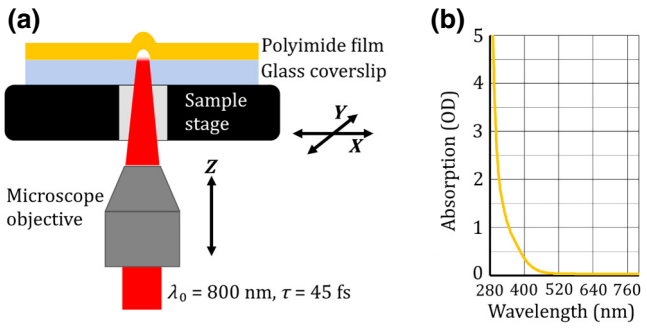

FIG. 1. (a) Experimental configuration. Single femtosecond pulses are focused through a coverslip substrate onto the underside of a polyimide film. (b) Visible linear-absorption spectrum of polyimide film with a thickness of 1.3 μm. No linear absorption is seen for visible wavelengths longer than 500 nm.

20× 0.4-NA achromatic objective, corrected for 170-μm coverslips, stock no. 33-438), which is mounted into a vertical motor stage for adjustment of focal-spot placement. The 6-mm aperture of the objective is filled with a 4-mm-diameter beam; therefore, the $1/e^2$ focal-spot diameter is estimated to be $2\omega_0 = (6\,\text{mm}/4\,\text{mm})(1.22\lambda/\eta) \approx 3.7\,\mu$m, where η is the NA of the objective [20,21]. We adjust the chirp using a grating compressor to maximize the intensity after the objective, indicated by second-harmonic yield from a β-barium borate crystal. In one instance, a 0.95-NA objective (Leitz Wetzlar 80× 0.95-NA PL objective, stock no. 48728) with a 10-mm entrance aperture is also used, resulting in an estimated focal-spot diameter of 2.6 μm. This objective is not coverslip corrected, resulting in spherical aberration that stretches the focus axially and reduces the peak intensity at the focus [22]. Reduced intensity from spherical aberration effects and chirp from additional glass in the 0.95-NA objective is compensated by increasing the pulse energy.

We use polyimide films on no. 1.5 Fisherbrand borosilicate glass coverslips (0.16–0.19 mm in thickness) as substrates, which are prerinsed in acetone, isopropyl alcohol, and deionized water and dried on a hotplate. We calculate the critical power for self-focusing of borosilicate glass at 800 nm to be 2.5 MW [23]; for our 50-fs pulse, this corresponds to a pulse energy of 180 nJ. Focused to a 3-μm spot size, the light intensity before self-focusing in the substrate occurs can reach 3×10^{13} W/cm^2 in the absence of nonlinear absorption by the substrate. Films are spin-coated with use of PI-2555 precursor purchased from HD Microsystems at a spin speed of 6000 revolutions/min for 60 s. This yields a film thickness of 1.31 ± 0.05 μm as determined with a Bruker Dektak XT contact profilometer. We measure the linear-absorption spectra of polyimide films from 280 to 800 nm using an Agilent Cary 5000 UV–vis-near-IR spectrophotometer, shown in Fig. 1(b). The films are transparent to wavelengths above 500 nm, indicating that 800-nm light can be absorbed only through two-photon absorption and higher-order processes. The absorption spectra of the polyimide film match the literature and the absorption is ascribed to an $n \rightarrow \pi^*$ transition [24,25].

Above the lens stage, samples are mounted onto a two-axis horizontal stage. Samples are oriented film side up, so that the laser is focused through the coverslip onto the underside of the polyimide film. A dichroic mirror is used before the objective in a coaxial geometry, allowing a small fraction of laser light to be reflected from the sample, recollimated through the objective, and exit to an imaging line for *in situ* laser-spot monitoring. Coupling in white light and changing the position of the objective also allows *in situ* white-light microscopy. We use *in situ* imaging to find the optimal position of the laser focus on the sample. By using pulse energies near the polymer damage threshold at various focal positions, we find that the optimal focal

position corresponds to the blister made with the lowest pulse energy. We rely on optical contrast *in situ*, which is consistent with *ex situ* optical microscope and atomic force microscope (AFM) measurements.

The laser is used in single-shot mode to generate individual blister structures in polyimide films. We characterize the resulting blisters using a JPK Nanowizard II BioAFM instrument in contact mode. From the AFM data, we determine the height, base diameter, and volume of each blister. The blister height is defined as the difference between the local maximum and minimum heights, and the diameter is defined as the effective circular diameter of the base area for each blister. The blister volume is defined as the volume between the elevated surface of a blister and the plane of the flat surroundings at the top surface of the film.

B. Calculations

To gain a qualitative understanding of the light-polymer interaction, we consider the energy absorption profile when a femtosecond pulse causes laser-induced breakdown through linear, two-photon, and three-photon absorption in a polymer film. Treating each order of absorption separately, we highlight their main features. We assume that the film has the physical characteristics of polyimide ($\rho = 1.42$ g/cm^3, $c = 1.09$ J/g K, $T_{\mathrm{decomp}} = 550\,^{\circ}$C) [26,27]. We choose the linear-absorption coefficient to match values used in previous studies on blister formation in polyimide through linear absorption of nanosecond pulses, for comparison with nonlinear absorption [11]. While the heat capacity will not be constant over the temperature range the polymer will experience, we treat it as constant in our qualitative model. Since nonlinear-absorption coefficients of undoped polymers are not reported, we chose two-photon-absorption and three-photon-absorption cross sections to be those of zinc oxide [28]—a material with a similar band gap. We also assume that the laser pulse has a Gaussian temporal profile, with $\tau = 50$ fs being the $1/e$ full width of the intensity in time, and a Gaussian spatial profile with $2\omega_0 = 3$ μm, where $2\omega_0$ is the $1/e$ full width of the electric field in space. See Supplemental Material [29] for further details of this calculation.

III. RESULTS AND DISCUSSION

In Fig. 2, we show the calculated temperature profile due to each of the three absorption mechanisms. Pulse energies are chosen such that the peak temperature in the material reaches 10 000 K in all cases. This is the temperature of cold-dense plasmas [30] which is accessible, at least briefly, under normal laboratory conditions. At this temperature we expect molecular dissociation and ionization. Thus, within this assumption, we heat the polymer near the interface (a breakdown depth of approximately 100 nm in the three-photon calculation) until it forms a plasma, transforming its chemical state [18,31–34] in the process.

Figure 2 shows that the heat-deposition region is smaller in all directions for nonlinear absorption. Most notably, the depth of energy deposition is more than 20 times shallower in the case of the three-photon absorption compared with linear absorption, and is approximately two thirds of the diameter. The pulse energy used in this case is also an order of magnitude lower; this is due to the high intensities of tightly focused femtosecond pulses and the cubic intensity dependence of three-photon absorption. Figure 2 also illustrates more general characteristics

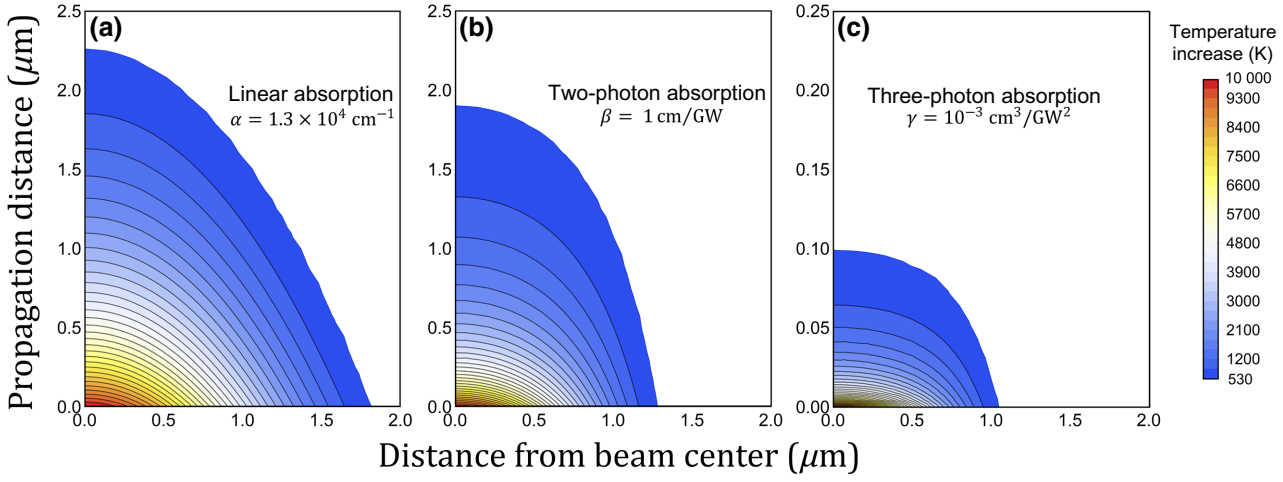

FIG. 2. Calculated temperature distributions induced by a 50-fs laser pulse focused to a 1.5-μm radius in materials with (a) linear- (polyimide-like) absorption, (b) two-photon- (ZnO-like) absorption, and (c) three-photon- (ZnO-like) absorption mechanisms. Pulse energies of (a) 42 nJ, (b) 31 nJ, and (c) 2.5 nJ are chosen to set the peak temperature to 10 000 K in all cases. The vertical axis for (c) is stretched by a factor of 10.

of energy deposition through high-order nonlinear absorption. After the third-order term dominates (for intensities above 10^{12} W/cm^2), most of the beam energy is deposited within a very small volume. The penetration depth is very shallow (approximately 100 nm), thereby resulting in precise energy deposition within a thin film. Higher intensity, which leads to higher orders of absorption, will accentuate this trend without changing the overall conclusion. These characteristics should be important for blister-based laser-induced forward transfer of sensitive materials on the nanoscale; energy must be deposited with both lateral and axial confinement to create a nanoscale blister without penetrating and rupturing the film.

Now we move to the experiment. We show that once we exceed an intensity of 3×10^{12} W/cm^2 (where three-photon absorption dominates in our model), we create blisters with volumes that grow linearly with intensity. For even higher input intensity, this growth slows since intensities above the ionization threshold of the substrate are now attenuated before reaching the polymer [10]. However, we show that by estimating the energy deposited in both the dielectric and the polymer, the linear growth of the blister volume with the energy absorbed by the polymer remains valid.

We first examine the dependence of blister height and diameter on pulse energy. Figure 3 shows AFM scans of blisters created near the blister-formation threshold obtained with a 0.4-NA objective. Along the X direction, four blisters are made at a fixed pulse energy to assess the repeatability of the blister-formation process. Along the Y direction, the pulse energy is varied. We account for losses due to Fresnel reflections from the sample (air-glass and glass-polyimide interfaces) [35]; the net transmission of the sample is 0.954. We observe the blister-formation threshold to be approximately 18 nJ of pulse energy (peak fluence of 0.09 J/cm^2, peak intensity of 4×10^{12} W/cm^2) as measured after losses from the microscope objective. This pulse energy results in a blister of 75-nm height and 1.2-μm diameter. In our qualitative calculation, a peak temperature of 10 000 K is reached at 3.5×10^{11} W/cm^2 for three-photon absorption, more than an order of magnitude less intensity than in the two-photon case. The peak intensity at the experimental blister-formation threshold is approximately 20 times that of the three-photon-absorption calculation; at this intensity, three-photon and higher-order processes will dominate over two-photon absorption. Thus, three-photon absorption or higher-order processes are the dominant mechanisms in these experiments.

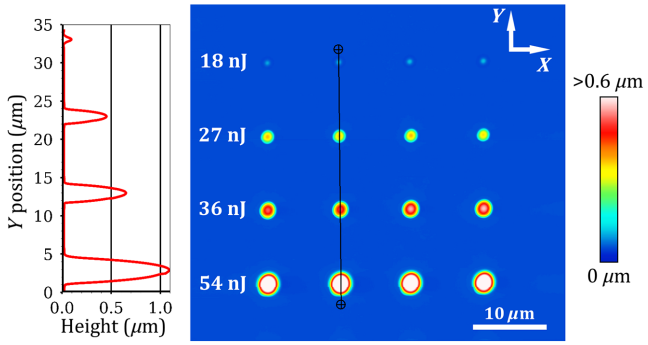

FIG. 3. An AFM image of blisters fabricated in 1.3-μm polyimide with a 0.4-NA objective with pulse energies near the damage threshold. The AFM line profile displayed (left) corresponds to the cross section denoted by the black line in the two-dimensional image. The blister-formation threshold is seen at a pulse energy of 19 nJ (peak intensity of 4×10^{12} W/cm^2). Near the threshold, small changes in pulse energy create drastic changes in blister height and diameter.

At low energies, blisters scale strongly in both height and diameter with pulse energy. For example, pulse energies 3 times higher than the threshold result in blisters of 1-μm height and 3.9-μm diameter. Figure 4 shows blisters formed in the same conditions but with increased pulse energies. In this regime, blisters have a weaker, linearlike scaling in both height and diameter compared with the strong nonlinear scaling near the threshold. In the rightmost column in Fig. 4, pulse energies of approximately 11 times the threshold energy yield blisters with heights of 2 μm and base diameters of 5.5 μm. At such energies, outer parts of the spatial profile of the laser pulses exceed the threshold intensity for blister formation. Some asymmetry in the outer portion of the beam (less than 10% of the peak intensity) is not fully corrected by the spatial filter, resulting in slight but increasing blister asymmetry with increasing pulse energies, as seen in the lower-right portion of blisters in Fig. 4. As the pulse energy is increased above

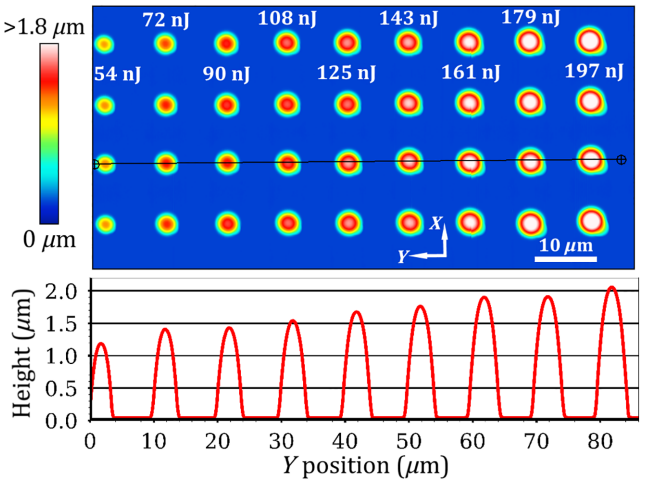

FIG. 4. An AFM image of blisters fabricated in 1.3-μm polyimide with a 0.4-NA objective with increased pulse energies. The AFM line profile displayed (bottom) corresponds to the cross section denoted by the black line in the two-dimensional image. For intermediate pulse energies, blister heights and diameters scale less steeply with pulse energy.

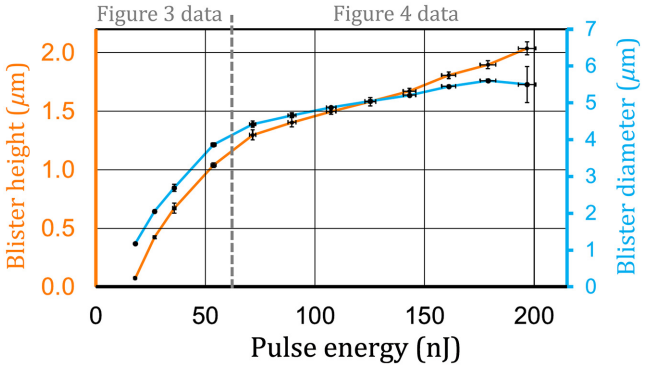

FIG. 5. Dependence of blister height and diameter on pulse energy. As seen in Fig. 3, near-threshold scaling of the height and diameter is nonlinear. At the higher energies shown in Fig. 4, the trend becomes linear until the onset of blister rupture. The horizontal error bars represent pulse-energy variations of the laser.

200 nJ, blisters rupture due to excessive pressure built up beneath the film; they are no longer left intact, showing cracking, diminished height, and removal of material. See Supplemental Material [29] for further details on blister rupture.

Height and diameter scaling for intact blisters in these experiments is summarized in Fig. 5. As also seen directly through AFM images, both scaling curves have two distinct regimes: (i) nonlinear scaling from the threshold pulse energy to 72 nJ and (ii) linearlike scaling onward until the onset of rupture. The monotonic increase of blister height and diameter with pulse energy is consistent with the literature, and is due to increased temperatures and pressures of the material confined beneath the film [16].

Since the laser pulses in these experiments are often intense enough to cause substrate breakdown, we must account for energy lost to the substrate before a pulse reaches the polymer. In these situations, any intensity exceeding the breakdown threshold of the medium is simply removed from the beam to a reasonable approximation [10]. We adopt this model for a Gaussian pulse in both space and time. We estimate the intensity threshold for blister formation as the peak intensity in time at the edge of a blister formed with the threshold pulse energy ($I_{\mathrm{peak}} \approx 3 \times 10^{12}$ W/cm^2). We then calculate the energy absorbed in the polymer as a function of the pulse energy used. This decouples the effects of nonlinear optical interactions in glass and polyimide from the expansion process of polyimide blisters.

Figure 6 shows the dependence of blister volume, height, and diameter on energy absorbed in the film, accounting for absorption losses in the substrate. The resulting blister volumes (V) shown in Fig. 6(a) are linear with the amount of energy absorbed in the film (E_{abs}). Figure 6(b) shows that the height (H) and diameter (D) scale approximately with the square root and the fourth root, respectively, of the absorbed pulse energy. Considering that a conical-like volume is proportional to the base area (approximately $\frac{1}{4}\pi D^2$) times the height, the sum of these powers is consistent with the linear trend seen for the blister volume.

We propose a physical reason for the linear trend between blister volume and energy absorbed in the film. Since the laser-induced transition from a solid to a dense plasma is well established at intensities above 3×10^{12} W/cm^2, from our calculations, we can estimate that most of the pulse energy is used to create the plasma and transport heat. This dense plasma contains many

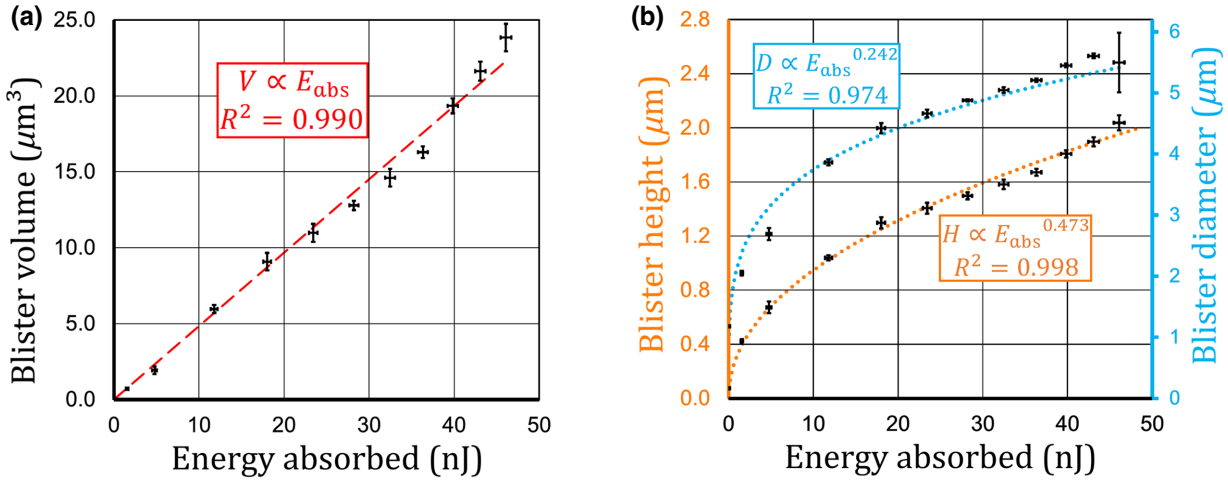

FIG. 6. Dependence of (a) blister volume (V) and (b) blister height (H) and blister diameter (D) on pulse energy absorbed in a 1.3-μm polyimide film with use of a 0.4-NA objective. The horizontal error bars represent variations in absorbed energy due to pulse-energy variations of the laser. The coefficients of determination ($R^2 \sim 1$) show excellent agreement with the linear fit in (a) and power fits in (b).

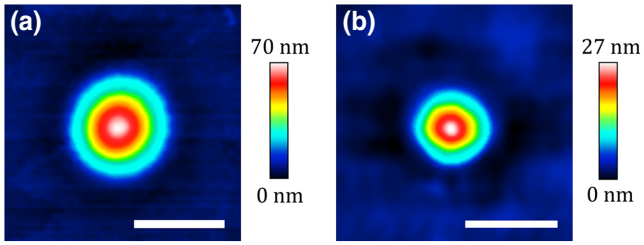

FIG. 7. (a) An AFM image of the smallest observed blister fabricated with a 0.4-NA objective. The $1/e^2$ diameter of the blister is 1.01 μm, which is 28% of the focal-spot diameter. (b) An AFM image of the smallest observed blister fabricated with a 0.95-NA objective. The $1/e^2$ diameter is 710 nm, which is 28% of the Gaussian focal-spot diameter. The scale bars are 1 μm wide in both images.

dissociated products, and will also thermally break down the neighboring polymer. Through these processes, many new products are created, some of which are gaseous. As we add more energy, we break proportionally more bonds, which creates proportionally more gas. The gas we create will be at an elevated temperature and pressure but very small in volume. This is followed by rapid isothermal expansion, converting the generated pressure-volume work into a final volume at ambient pressure ($V_F = P_I V_I / P_F$). The linear trend between volume and absorbed energy is consistent with similar experiments involving femtosecond-laser fabrication of voids in fused silica [36]. Since we know the volume of gas created, it should be possible to estimate the time-dependent pressure and therefore the surface motion, which is a measurable quantity.

A powerful consequence of nonlinear absorption is the possibility of energy deposition at scales below the diffraction limit. To understand the resolution advantage of forming blisters through nonlinear absorption, we closely examine AFM images of the smallest blisters formed with 18 nJ of pulse energy and a 0.4-NA objective (as shown in Fig. 3). The smallest of these is shown in Fig. 7(a). The resulting blisters have $1/e^2$ diameters of 1.02 ± 0.1 μm, which is 28% of the focal-spot diameter. The $1/e^2$-diameter definition is used because blister structures have smooth curvature and no distinct cutoff, like the intensity distribution of the Gaussian focal spot used to create them. We also examine the smallest blister made with 160 nJ of pulse energy and a 0.95-NA objective, shown in Fig. 7(b). In this case, a diameter of 710 nm is achieved, which is again 28% of the focal-spot diameter, and is smaller than the laser wavelength.

Looking forward, even smaller structures should be possible. Beyond traditional geometric optics, a key consideration is the thickness of the irradiated film; the resolution limit in subwavelength desorption of thin films decreases significantly with decreasing film thickness [37]. We have calculated, and experimentally shown through helium-ion microscopy and x-ray photoelectron spectroscopy, that the penetration depth into the film becomes very small for high-order nonlinear absorption, which will aid in creating intact blisters in thinner films [18]. Higher orders of nonlinear absorption could also be used to further restrict energy deposition.

IV. CONCLUSION

Femtosecond laser pulses provide a unique opportunity to deposit energy in a highly controlled manner, through the choice of the absorption mechanism, pulse energy, pulse duration, and substrate mediation via intensity and material choice. Through our calculations, we illustrate the advantage of femtosecond pulses for confining energy deposition in a thin film. We demonstrate this advantage by achieving laser-induced blisters smaller than the laser wavelength. Blister formation at these scales is highly tunable, with resulting blister volumes that scale linearly with the energy deposited in the material.

Further steps could be taken to refine the blister-formation process. For example, a composite film with stacked layers of different materials could be used to control energy deposition and expansion separately, and we could use high-speed surface interferometry to measure the height and velocity of a blister as it expands. In addition, energy deposition will scale linearly with pulse duration for a fixed peak intensity, providing further control over the expansion rate. These techniques would be a convenient way to tailor blister-based laser-induced forward transfer of sensitive materials, where ejection speed is critical.

Precise fabrication of laser-induced blisters could impact several fields. This approach could lead to nanoscale blister-based laser-induced forward transfer of arbitrarily sensitive materials. Blisters on the few-micrometer and submicrometer scales can also be used for direct surface texturing and patterning of materials. Precise microtexturing and perturbation of surfaces can be achieved without lithography, laser milling, or laser-based additive machining. No external processes are used to add or remove materials, and the surface composition remains unchanged since the energy is confined beneath the film [18]. Blister microstructuring of surfaces could find interesting applications in chemically-stable-superhydrophobic-surface patterning and rapid microlens-array fabrication. Blisters may also be used to create metamaterials by directly writing subwavelength surface structures.

ACKNOWLEDGMENTS

We acknowledge Dr. Maohui Chen for training in atomic force microscopy and Tony Olivieri for training related to polyimide-film fabrication. We are also pleased

to acknowledge the support of laboratory engineers Yu-Hsuan Wang and Tyler Clancy from the University of Ottawa throughout this work. We acknowledge funding from Natural Sciences and Engineering Research Council of Canada (NSERC) Engage (Grant No. EGP 523138-18) and Discovery (Grant No. RGPIN-2019-04603) grants, the Ontario Centres of Excellence Voucher for Innovation and Productivity I Program (Grant No. 29119), Fluidigm Canada, and the Canada Foundation for Innovation. A.T.K.G. acknowledges financial support from the NSERC's Postgraduate Scholarship – Doctoral and the University of Ottawa's Excellence Scholarship.

[1] B. N. Chichkov, C. Momma, S. Nolte, F. von Alvensleben, and A. Tünnermann, Femtosecond, picosecond and nanosecond laser ablation of solids, Appl. Phys. A **63**, 109 (1996).
[2] K. Sugioka and Y. Cheng, Ultrafast lasers-reliable tools for advanced materials processing, Light: Sci. Appl. **3**, e149 (2014).
[3] M. Malinauskas, A. Žukauskas, S. Hasegawa, Y. Hayasaki, V. Mizeikis, R. Buividas, and S. Juodkazis, Ultrafast laser processing of materials: From science to industry, Light: Sci. Appl. **5**, e16133 (2016).
[4] A. Joglekar, H. Liu, G. Spooner, E. Meyhfer, G. Mourou, and A. Hunt, A study of the deterministic character of optical damage by femtosecond laser pulses and applications to nanomachining, Appl. Phys. B **77**, 25 (2003).
[5] P. P. Pronko, S. K. Dutta, J. Squier, J. V. Rudd, D. Du, and G. Mourou, Machining of sub-micron holes using a femtosecond laser at 800 nm, Opt. Commun. **114**, 106 (1995).
[6] K. Sugioka and Y. Cheng, Femtosecond laser three-dimensional micro- and nanofabrication, Appl. Phys. Rev. **1**, 041303 (2014).
[7] A. Ben-Yakar and R. L. Byer, Femtosecond laser ablation properties of borosilicate glass, J. Appl. Phys. **96**, 5316 (2004).
[8] M. Lenzner, J. Krüger, S. Sartania, Z. Cheng, C. Spielmann, G. Mourou, W. Kautek, and F. Krausz, Femtosecond Optical Breakdown in Dielectrics, Phys. Rev. Lett. **80**, 4076 (1998).
[9] N. T. Nguyen, A. Saliminia, W. Liu, S. L. Chin, and R. Valle, Optical breakdown versus filamentation in fused silica by use of femtosecond infrared laser pulses, Opt. Lett. **28**, 1591 (2003).
[10] D. M. Rayner, A. Naumov, and P. B. Corkum, Ultrashort pulse non-linear optical absorption in transparent media, Opt. Express **13**, 3208 (2005).
[11] N. T. Kattamis, P. E. Purnick, R. Weiss, and C. B. Arnold, Thick film laser induced forward transfer for deposition of thermally and mechanically sensitive materials, Appl. Phys. Lett. **91**, 171120 (2007).
[12] P. Delaporte and A.-P. Alloncle, Laser-induced forward transfer: A high resolution additive manufacturing technology, Opt. Laser Technol. **78**, 33 (2016).
[13] M. S. Brown, C. F. Brasz, Y. Ventikos, and C. B. Arnold, Impulsively actuated jets from thin liquid films for high-resolution printing applications, J. Fluid Mech. **709**, 341 (2012).
[14] N. T. Goodfriend, S. Y. Heng, O. A. Nerushev, A. V. Gromov, A. V. Bulgakov, M. Okada, W. Xu, R. Kitaura, J. Warner, H. Shinohara, and E. E. B. Campbell, Blister-based-laser-induced-forward-transfer: A non-contact, dry laser-based transfer method for nanomaterials, Nanotechnology **29**, 385301 (2018).
[15] A. Piqué, H. Kim, and C. B. Arnold, in *Laser Ablation and its Applications*, Springer Series in Optical Sciences, edited by C. Phipps (Springer, US, Boston, MA, 2007), p. 339.
[16] M. S. Brown, N. T. Kattamis, and C. B. Arnold, Time-resolved study of polyimide absorption layers for blister-actuated laser-induced forward transfer, J. Appl. Phys. **107**, 083103 (2010).
[17] N. T. Kattamis, N. D. McDaniel, S. Bernhard, and C. B. Arnold, Laser direct write printing of sensitive and robust light emitting organic molecules, Appl. Phys. Lett. **94**, 103306 (2009).
[18] D. L. N. Kallepalli, A. T. K. Godfrey, J. Walia, F. Variola, A. Staudte, C. Zhang, Z. J. Jakubek, and P. B. Corkum, Multiphoton laser-induced confined chemical changes in polymer films, Opt. Express **28**, 11267 (2020).
[19] R. Trebino, K. W. DeLong, D. N. Fittinghoff, J. N. Sweetser, M. A. Krumbgel, B. A. Richman, and D. J. Kane, Measuring ultrashort laser pulses in the time-frequency domain using frequency-resolved optical gating, Rev. Sci. Instrum. **68**, 3277 (1997).
[20] O. H. Y. Zalloum, M. Parrish, A. Terekhov, and W. Hofmeister, On femtosecond micromachining of HPHT single-crystal diamond with direct laser writing using tight focusing, Opt. Express **18**, 13122 (2010).
[21] K. Sugioka, Progress in ultrafast laser processing and future prospects, Nanophotonics **6**, 393 (2016).
[22] L. Capuano, R. Pohl, R. M. Tiggelaar, J. W. Berenschot, J. G. E. Gardeniers, and G. R. B. E. Römer, Morphology of single picosecond pulse subsurface laser-induced modifications of sapphire and subsequent selective etching, Opt. Express **26**, 29283 (2018).
[23] C. B. Schaffer, A. Brodeur, and E. Mazur, Laser-induced breakdown and damage in bulk transparent materials induced by tightly focused femtosecond laser pulses, Meas. Sci. Technol. **12**, 1784 (2001).
[24] M. Nishikawa, B. Taheri, and J. L. West, Mechanism of unidirectional liquid-crystal alignment on polyimides with linearly polarized ultraviolet light exposure, Appl. Phys. Lett. **72**, 2403 (1998).
[25] B. Li, T. He, and M. Ding, Tuning the aggregation of polyimide thin films by modification of their molecular interactions, Polym. Int. **49**, 395 (2000).
[26] DuPont Kapton – Summary of Properties.
[27] PRODUCT BULLETIN – PI 2525, PI 2555 & PI 2574 (2012).
[28] M. G. Vivas, T. Shih, T. Voss, E. Mazur, and C. R. Mendonca, Nonlinear spectra of ZnO: Reverse saturable, two- and three-photon absorption, Opt. Express **18**, 9628 (2010).
[29] See Supplemental Material at http://link.aps.org/supplemental/10.1103/PhysRevApplied.14.044057 for further

details on blister-rupture and temperature-distribution calculations.

[30] S. H. Glenzer, O. L. Landen, P. Neumayer, R. W. Lee, K. Widmann, S. W. Pollaine, R. J. Wallace, G. Gregori, A. Höll, T. Bornath, R. Thiele, V. Schwarz, W.-D. Kraeft, and R. Redmer, Observations of Plasmons in Warm Dense Matter, Phys. Rev. Lett. **98**, 065002 (2007).

[31] D. L. N. Kallepalli, A. M. Alshehri, D. T. Marquez, L. Andrzejewski, J. C. Scaiano, and R. Bhardwaj, Ultra-high density optical data storage in common transparent plastics, Sci. Rep. **6**, 26163 (2016).

[32] K. L. N. Deepak, R. Kuladeep, S. Venugopal Rao, and D. Narayana Rao, Luminescent microstructures in bulk and thin films of PMMA, PDMS, PVA, and PS fabricated using femtosecond direct writing technique, Chem. Phys. Lett. **503**, 57 (2011).

[33] Z. Nie, H. Lee, H. Yoo, Y. Lee, Y. Kim, K.-S. Lim, and M. Lee, Multilayered optical bit memory with a high signal-to-noise ratio in fluorescent polymethylmethacrylate, Appl. Phys. Lett. **94**, 111912 (2009).

[34] A. M. Alshehri, K. L. N. Deepak, D. T. Marquez, S. Desgreniers, and V. R. Bhardwaj, Localized nanoclusters formation in PDMS upon irradiation with femtosecond laser, Opt. Mater. Express **5**, 858 (2015).

[35] T. J.-Y. Derrien, R. Koter, J. Krüger, S. Höhm, A. Rosenfeld, and J. Bonse, Plasmonic formation mechanism of periodic 100-nm-structures upon femtosecond laser irradiation of silicon in water, J. Appl. Phys. **116**, 074902 (2014).

[36] E. G. Gamaly, L. Rapp, V. Roppo, S. Juodkazis, and A. V. Rode, Generation of high energy density by fs-laser-induced confined microexplosion, New J. Phys. **15**, 025018 (2013).

[37] V. Sametoglu, V. T. K. Sauer, and Y. Y. Tsui, Production of 70-nm Cr dots by laser-induced forward transfer, Opt. Express **21**, 18525 (2013).

Femtosecond-Laser-Induced Nanoscale Blisters in Polyimide Thin Films through Nonlinear Absorption: Supplementary

Alan T. K. Godfrey [1,*] Deepak L. N. Kallepalli [1] Jesse Ratté [1] Chunmei Zhang [1,*] and P. B. Corkum [1]

[1] *Joint Attosecond Science Laboratory, University of Ottawa and National Research Council of Canada, 25 Templeton St., Ottawa K1N 6N5, Canada*

I. DERIVATION & FULL SUMMARY OF CALCULATION

This section provides the complete details and set of parameters used for the calculations shown in the main paper. These calculations were performed using Mathematica version 11.1. The advantages of using femtosecond lasers to induce material breakdown are two-fold. Femtosecond pulses deposit energy with minimal heat dissipation, and because amplified femtosecond pulses are extremely intense, nonlinear absorption processes are easily accessible. These two factors, when combined, lead to deposition of energy with much greater confinement than other methods.

We demonstrate this in the following calculation of femtosecond-laser-induced breakdown through linear, two-photon, and three-photon absorption (henceforth 1PA, 2PA, and 3PA) in a polymer film. Each mechanism was considered separately, as is typical by material selection in LIFT experiments using polymer films, and which naturally highlights the main features of energy deposition from each absorption order. We model the film to have the density, heat capacity and decomposition temperature of polyimide [1, 2]. The linear absorption coefficient was chosen to match experiments involving blister formation through linear absorption of 355 nm light in polyimide [3]. Since nonlinear absorption coefficients of undoped polymers are not reported, we chose two- and three-photon absorption cross sections to be those reported for zinc oxide, a material with a similar band gap [4]. In all three scenarios, laser pulses were taken to have durations of $\tau = 50$ fs with square envelopes and Gaussian spatial intensity profiles with focal spot diameters of $2\omega_0 = 3$ µm at their waists. These values are summarized in **Table I**. The focal spot was placed at the surface of the modelled polymer films in all cases; this is equivalent to focussing on the underside of a polymer film in our experimental conditions.

Since femtosecond pulses are much shorter than timescales of heat dissipation, absorption is approximated to be instantaneous. Thus, pulse intensities incident on the polymer are taken to be $I_0(r) = I_{peak} \cdot \exp\left(-2r^2/\omega_0^2\right)$ where peak intensity in space and time is defined as $I_{peak} = \left(2/\pi\omega_0^2\right)(E_{pulse}/\tau)$. Pulse energies were chosen separately for the cases of 1PA, 2PA, and 3PA, such that the peak temperature in the material reached 10000K in all cases; these pulse energy values were 42 nJ, 31 nJ, and 2.5 nJ respectively. This was done to compare the confinement of similar levels of breakdown for each absorption order. The intensity attenuation from each absorption mechanism was calculated and converted into energy deposition proportional to $-dI/dz$ where z is the direction of propagation into the polymer film. Circular symmetry was used to simplify these calculations. In particular, the energy absorbed within a small annular cylinder of thickness with an inner radius of r, outer radius of $r + \Delta r$, and a height of Δz at a distance z into the film is given by the equation below.

$$E_{abs}(z,\Delta z, r, \Delta r) = 2\pi\tau \int_r^{r+\Delta r} r' \cdot [I(z,r') - I(z+\Delta z, r')]dr' \quad (1)$$

The function $I(z,r)$ represents the intensity at each point in the material, given by the below equations in the cases of 1PA, 2PA, and 3PA.

$$I(z,r) = I_0(r) \cdot \begin{cases} e^{-\alpha z} & \text{for 1PA} \\ (1+\beta \cdot I_0(r) \cdot z)^{-1} & \text{for 2PA} \\ (1+2\gamma \cdot I_0^2(r) \cdot z)^{-1/2} & \text{for 3PA} \end{cases} \quad (2)$$

To obtain local temperature increase ΔT, we equated the energy absorbed to heat energy as given by $Q = c\rho V \Delta T$ where $V = \pi \Delta z \Delta r[2r + \Delta r]$ is the volume of each annular cylindrical region. Therefore, the local temperature increase is given by:

$$\Delta T(z, \Delta z, r, \Delta r) = \frac{E_{abs}(z, \Delta z, r, \Delta r)}{c\rho \Delta z \Delta r[2r + \Delta r]} \quad (3)$$

Using Equation (3), we generated plots of the temperature distributions induced by 1PA, 2PA, and 3PA respectively. These plots are shown in **Fig. 1** of the main paper.

* xxxxxxxxxxxxxxxxxxxxxxxxxxxxxxxxxxxxxx

Symbol	*Definition*	*Value*	*Reference*
ρ	Density of polyimide	1.42 g cm^{-3}	[1]
c	Specific heat capacity of polyimide	1.09 J g^{-1} K^{-1}	[2]
T_{decomp}	Decomposition temperature of polyimide	550°C	[2]
α	1PA absorption coefficient of polyimide at $\lambda = 355$ nm	1.3×10^4 cm^{-1}	[3]
β	2PA absorption coefficient of ZnO at $\lambda \sim 550$–750 nm	∼1 cm/GW	[4]
γ	3PA absorption coefficient of ZnO at $\lambda \sim 850$–950 nm	$\sim10^{-3}$ cm^3/GW^2	[4]
τ	Duration of pulse, square envelope	50 fs	chosen
ω_0	Radius of beam waist	1.5 µm	chosen
E_{pulse}	Pulse energies used in each case (1PA, 2PA, 3PA)	42, 31, 2.5 nJ	chosen

TABLE I. Summary of simulated polymer and laser parameters used in calculation. 'Chosen' denotes parameters that were selected to model typical values in experiment.

II. BLISTER RUPTURE AT HIGH PULSE ENERGIES

In blister fabrication experiments, excessive pulse energies result in mechanical failure of the film. This is caused by excessive laser penetration into the film and/or pressure built up beneath the film. AFM data of ruptured blisters in a 1.3 µm polyimide film are shown in **Figure 1**. Between 215 nJ and 360 nJ of pulse energy, blisters were no longer left intact; rupture was seen as infrequent cracking and reduction in blister height. At higher energies, blisters show consistent cracking and in extreme cases, partial removal of the film. As seen in Fig. 4 of the main paper, blisters made with large pulse energies show slight asymmetry from the outer low-intensity portions of the pulse profile.

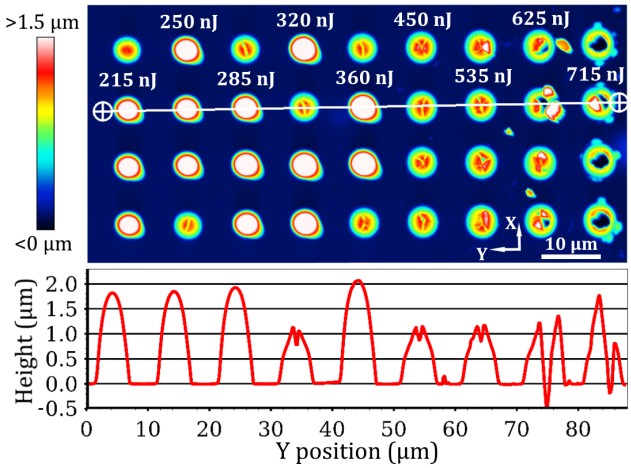

FIG. 1. (color online) An AFM image of blisters fabricated in 1.3 µm polyimide using a 0.4 NA objective with excessive pulse energies. The AFM line profile displayed (bottom) corresponds to the cross-section denoted by the black line in the 2D image. From 215 nJ to 360 nJ, structures show occasional cracking and diminished height. As pulse energy is increased further, blisters show consistent cracking of material, and then material removal.

[1] DuPont Kapton – Summary of Properties.

[2] PRODUCT BULLETIN - PI 2525, PI 2555 & PI 2574 (2012).

[3] N. T. Kattamis, P. E. Purnick, R. Weiss, and C. B. Arnold, Thick film laser induced forward transfer for deposition of thermally and mechanically sensitive materials, Applied Physics Letters **91**, 171120 (2007).

[4] M. G. Vivas, T. Shih, T. Voss, E. Mazur, and C. R. Mendonca, Nonlinear spectra of ZnO: reverse saturable, two- and three-photon absorption, Optics Express **18**, 9628 (2010).

3.2 Bandgap of Polyimide Films

The bandgap of polyimide depends greatly on its preparation. Various works on polyimide have reported bandgaps between approximately 1.7 eV and 3.3 eV [88–91]. By Tauc plot analysis [92], shown in Figure 3.2, we determined from our linear absorption data that the bandgap of our polyimide film was 2.56 eV. This further confirms that our 800-nm laser pulses, with photon energies of 1.55 eV, cannot undergo linear absorption in polyimide but can undergo two-photon absorption.

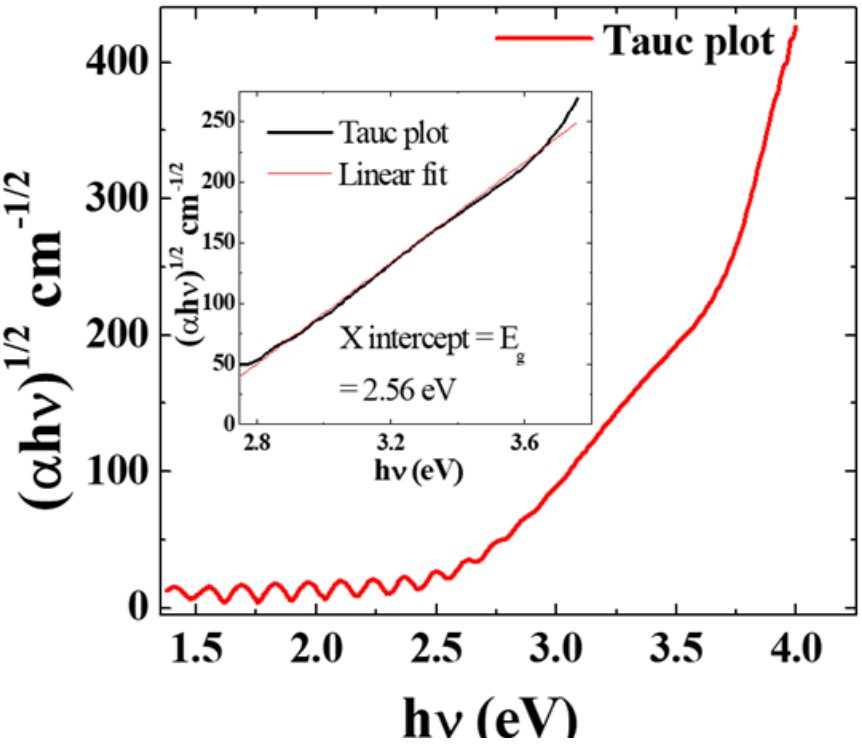

Figure 3.2: Tauc plot analysis [92] of our polyimide film to determine the band gap. The inset shows the partial linear fit used to determine the bandgap value of 2.56 eV at the x-intercept. The undulations at lower photon energies are due to thin-film interference effects causing small variations in overall light transmission of the film on glass, depending on wavelength.

Chapter 4

Confined Optical and Chemical Changes from Blister Formation in Polymers

So far, we have seen the fabrication of laser-induced polymer blisters on the micro- and nanoscale using single femtosecond laser pulses. Since polymer blisters were used entirely as a means for Laser-Induced Forward Transfer (LIFT) in the past, their optical and chemical properties were not studied. In this chapter, we show two papers exploring the optical and chemical properties of femtosecond-laser induced blisters and the resulting changes to adhesion between the polymer surface and external media (such as a water droplet) when patterning a large area of film with these structures.

In Section 4.1, we present a manuscript focussed on optical measurements and focussed ion beam measurements of laser-fabricated blisters. We explore the structure of blisters with nanoscale accuracy by using gallium and helium focussed ion beams (FIB) to mill away material and image the interior of structures. Through image contrast analysis, these measurements suggest that laser-induced changes to the polymer's chemistry are contained beneath the film. We characterize the laser-induced chemical changes to the film using infrared spectroscopy and X-ray photoelectron spectroscopy (XPS) (see Section 2.3). We then

examine bulk fluorescence and fluorescence polarization anisotropy behaviour to determine the types of new ordered polymer aggregates that are formed by the laser. We also attempt to measure the Raman spectrum of the modified polymer (see Section 2.3), but discover that the Raman scattering signal is obscured by significant and broad fluorescence at all available excitation wavelengths. In summary, XPS and FIB measurements show that the chemistry of the polymer at the film's surface is not changed, while the optical spectroscopy measurements (in addition to FIB) indicate significant chemical changes are confined beneath the film.

Section 4.2 uses the results from Section 4.1 to create controlled changes to the roughness of a surface, thereby changing its surface adhesion as measured through water drop goniometry (see Section 2.3). In this work, large areas on the polymer film are patterned using laser-induced blisters with varying widths, heights, and degrees of overlap between structures. We discover that adding surface textures using blister patterns greatly increases the hydrophobicity of the surface. An advantage to using blisters for surface texturing is that the changes are purely textural, leaving the chemical composition of the surface essentially unchanged. Polymers experience strain during blister formation and can undergo strain-induced crystallization, which could potentially affect the orientation of interlinked polymers at the surface [93, 94]. However, we expect this effect (with a size scale on the order of molecular chains) to be a minimal contribution as compared to the natural roughness of the polymer surface (several nm) and the overall blister surface structuration (a few hundreds of nm).

As discussed in Section 4.2, if a flat surface is initially hydrophobic due to its chemical composition, structuring said surface will only increase its hydrophobicity provided the chemistry remains the same. Other work involving laser-induced changes to hydrophobicity or hydrophilicity in the past involved irradiation the surface and changing the chemical structure in addition to the morphology [95–103]. Other works use different fabrication methods such as spray, spin or dip-coating, plasma etching, chemical etching, vapor deposition, thermal deposition or various lithography techniques [104]. Our work decouples changes to chemical structure and surface morphology in the context of laser-induced hydrophobicity.

Wenzel and Cassie-Baxter state equations [105], which are used to predict the water

contact angle based on surface structure, require purely morphological changes to a surface. However, in previous works involving laser-induced changes to surface adhesion by direct laser irradiation, the resulting surface changes were both morphological and chemical [95–103]. Thus, these equations could not be used in earlier works. We, however, can make valid use of the Cassie-Baxter equation to estimate the liquid contact area fraction of water droplets on the structured surfaces since our analysis indicates the chemical composition of our samples is unchanged. This work demonstrates how the implementation of hydrophobic surfaces using existing polymers can be made more convenient and flexible, since a polymer with high hydrophobicity can be selected initially and its hydrophobicity can only improve with surface structuration.

For explanations of each characterization tool and its operating principles, please refer to Section 2.3.

4.1 Optical Study of Confined Chemical Changes in Femtosecond-Laser-Induced Blisters

Please note that the following paper mentions a thermodynamical model which estimates ~10000 K peak temperatures; this is the same model presented in the paper from Chapter 3 [106].

Research Article | Vol. 28, No. 8 / 13 April 2020 / Optics Express 11267
Optics EXPRESS

Multiphoton laser-induced confined chemical changes in polymer films

DEEPAK L. N. KALLEPALLI,[1] ALAN T. K. GODFREY,[1] JASPREET WALIA,[2] FABIO VARIOLA,[3] ANDRÉ STAUDTE,[1] CHUNMEI ZHANG,[1] ZYGMUNT J. JAKUBEK,[4] AND P. B. CORKUM[1,*]

[1]*Joint Attosecond Science Laboratory, University of Ottawa and National Research Council of Canada, 100 Sussex Dr., Ottawa K1N 5A2, Canada*

[2]*Center for Research in Photonics, School of Electrical Engineering and Computer Science, University of Ottawa, Ottawa K1N 6N5, Canada*

[3]*Department of Mechanical Engineering, 161 Louis Pasteur, Colonel By Hall, University of Ottawa, Ottawa K1N 6N5, Canada*

[4]*Metrology Research Center, National Research Council Canada, 100 Sussex Dr., Ottawa, K1N 5A2, Canada*

[*]*XXXXXXXXXXXXXXXXXX*

Abstract: We report ultrafast-laser-induced photochemical, structural, and morphological changes in a polyimide film irradiated at the polymer-glass interface in back-incident geometry. Back-illumination creates locally hot material at the interface leading to a confined photochemical change at the interface and a morphological change through a blister formation. The laser-induced photochemical changes in polyimide resulted in new absorption and luminescence properties in the visible region. The laser-treated polyimide exhibited photoluminescence anisotropy resulting from formation of ordered polymer upon irradiation by linearly polarized ultrashort laser pulses. Confocal fluorescence microscopy resulted in similar observations to the bulk. Reflection-absorption infrared spectroscopy and X-ray photoelectron spectroscopy together indicated confinement of laser-induced chemical changes at the interface.

1. Introduction

Back-illumination of a low bandgap polymer through a high bandgap glass substrate with an ultrafast laser pulse leads to energy deposition at the interface and thereby creates hot material confined at the substrate-polymer interface. The deposited energy results in a localized expanding plasma which induces a protruding blister on the film's surface and a photochemical change confined near the interface [1–7]. The photochemical changes induced by the laser pulse are limited to its penetration depth. In contrast, front illumination creates surface voids and cracks [8,9]. Such high intensities and extreme temperature will result in chemical changes in the polymer such as bond scission followed by rearrangement. The photochemical modification of the polymer results in changes in light absorption and luminescence properties. One potential application of laser-induced fluorescence is 3D optical data storage, where data can be read with laser-induced fluorescence at multiple grey levels [10–13]. We expect the laser-induced fluorescence intensity to scale with absorbed energy [10,12,13].

We investigate the chemical changes induced by an ultrafast laser through back-illumination. We demonstrate the confinement of photochemical changes by imaging the cross-sections of irradiated regions using a focused ion beam (FIB) technique. We also report the nature of chemical changes using fluorescence, confocal micro-Raman (and fluorescence), reflection-absorption Infrared (RAIRS), and X-ray photoelectron spectroscopy (XPS) techniques. This study is related to our work on ultrafast laser-induced blister formation in polyimide films [14].

#389215 https://doi.org/10.1364/OE.389215
Journal © 2020 Received 27 Jan 2020; revised 12 Mar 2020; accepted 23 Mar 2020; published 1 Apr 2020

Optics EXPRESS

2. Experimental

We prepared polyimide films on #1.5 Fisherbrand borosilicate glass coverslips. The coverslips were rinsed with acetone, isopropanol, and deionized water to remove any contaminants and dried on a hotplate. Polyimide films were made using PI-2525 and PI-2555 precursors from HD Microsystems following the recommended spin curves and baking conditions. We used a Ti:sapphire laser (Coherent model RegA 9040) producing a near Gaussian pulse in space and time with a duration of ~ 50-fs duration at a central wavelength of 800 nm. The laser pulse energy was controlled using a motorized half-wave plate followed by a polarizing beam-splitter cube. The laser beam was focused using microscope objectives (10x 0.2 NA, 20x 0.4 NA) mounted into a vertical motor stage (PI M-112, Germany) with a travel range of 25 mm for adjusting the placement of the focal spot on the sample. Since polyimide is transparent for 800 nm (1.55 eV) wavelength, the modification is due to a nonlinear absorption mechanism with a minimum of two photons.

Above the vertical stage, polyimide-on-glass coverslips were mounted onto a 5-axis piezo nano-precision stage (PI, Germany) assembled on top of a micro-precision horizontal XY stage (MICOS MS-4, USA). The nano-precision stage was used for fine adjustment of the focal position. The laser was focused through the glass substrate onto the polymer-glass interface ("back-incidence" geometry). A dichroic mirror was used before the microscope objective in a coaxial geometry, allowing a small portion of the focused laser light to back-reflect from the sample, re-collimate through the objective, and travel to an imaging line for in-situ laser spot monitoring. Coupling in white light and changing the position of the objective also allows for in-situ white-light microscopy. We used a white-light microscope to find the optimal position of the laser focus on the sample, by firing pulses with energies near the damage threshold while adjusting the position of the focal spot. The details on the characterization techniques used in our study are given in Appendix A.

3. Results and discussion

It is known that the maximum laser intensity transmitted to the far side of glass substrate is self-limited by the nonlinear interactions within the glass [15,16]. The intensity leaving the material is, at maximum, equal to the absorption threshold. In our experiments, the substrate is borosilicate glass, whose absorption threshold is ~ 1.3×10^{13} W/cm^2 [17]. The actual intensity delivered to polyimide (our case study) is the lower of the incident intensity or ~ 1.3×10^{13} W/cm^2. In our experiments, the transmission losses of the microscope objective are taken into account. The volume of blisters increases with the pulse energy delivered to the polymer (after transmission and substrate losses are corrected for) [14].

We characterized the surface topography using atomic force microscopy (AFM) before and after irradiation experiments. Since FIB characterization requires metal coating, we carried out the FIB analysis after completion of all spectroscopy analysis. The following subsections are organized by the characterization techniques and spectroscopy tools employed in our investigation.

3.1. Focused ion beam diagnostics

First, we fabricated individual blisters at 320 nJ energy (vacuum intensity ~ 1.4×10^{14} W/cm^2) using a 20x 0.4 Numerical Aperture (NA) microscope objective yielding a focal spot of 3 μm diameter. We focused an ultrafast laser pulse at the glass-polymer interface as shown in schematic Fig. 1(a). The polymer nonlinearly absorbs the laser energy, assuming a constant specific heat (a very coarse assumption), the polymer temperature rapidly reaches ~ 10,000 K. At this temperature, the polymer locally melts and vaporizes forming a protruding blister as shown in Fig. 1(b). For our calculations, we used a simple thermodynamic model considering an ultrashort laser pulse with 50 fs duration and a peak intensity of ~ 10^{13} W/cm^2 focused to a 3

Optics EXPRESS

μm spot. Since, we used a Gaussian pulse, the temperature induced by the pulse is not uniform, leading to vaporization of material in the center and melting on the edges [14].

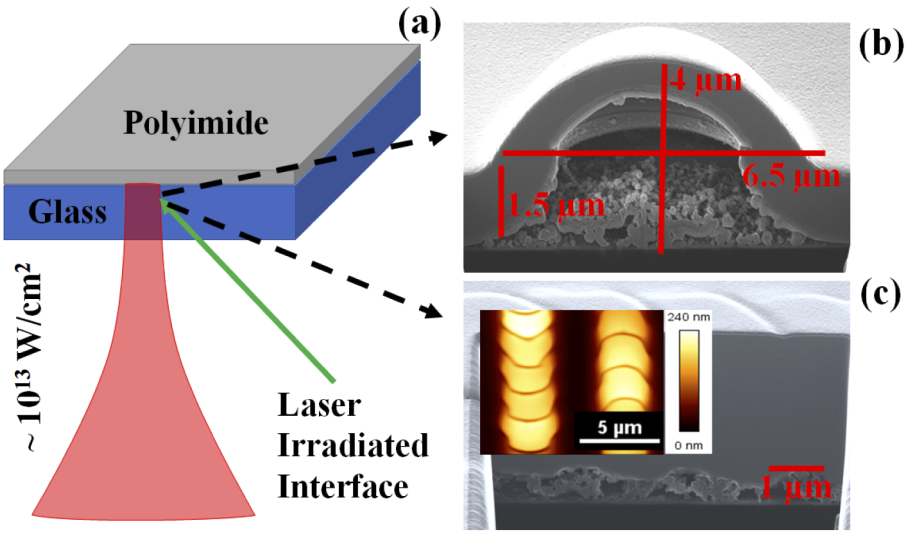

Fig. 1. (color online) **(a)** A schematic showing the interaction of a single laser pulse (a central wavelength of 800 nm with peak intensity ~ 10^{13} W/cm^2) focused at the glass-polymer interface as shown by the green arrow. This results in formation of a confined plasma leading to chemical change at the interface (Fig. 1(b)) and a blister. **(b)** FIB image showing interior of a 1.5 μm polyimide blister fabricated at 320 nJ pulse energy using 20x 0.4 NA objective (vacuum intensity ~ 1.4 $\times 10^{14}$ W/cm^2). The height and diameter of the blister are approximately ~ 2.5 μm and 6.5 μm, respectively. With our 0.4 NA objective, we do not observe rupture even with 650 nJ incident energy (vacuum intensity ~ 7 $\times 10^{13}$ W/cm^2). **(c)** FIB image of laser-treated polyimide fabricated at a pulse energy of 650 nJ with an effective no.of 2-shots per site using a 10x 0.2 NA objective. Inset shows an AFM image of the same. Oriented crescent contours are seen in both AFM and FIB images. Blisters are approximately ~ 240 nm in height and ~ 4 μm in diameter.

We used focused gallium (Ga) and helium (He) ion beams to dissect and image the interior of blister as shown in Fig. 1(b). The dissected blister showed formation of a hollow bubble underneath the chemically intact surface. Further, the FIB image showed an embedded layer (marked in Fig. 1(a)) underneath the intact surface with a contrast from the surrounding unmodified polymer. The thin embedded layer underwent chemical transformation due to nonlinear absorption of 800 nm light. The penetration depth for photochemical modification via nonlinear absorption at laser wavelength of 800 nm is far less than 0.73 μm reported for single-photon modification at 400 nm [1]. However, at the intensities that we use in this experiment, high order absorption will dominate [14].

From the FIB image, it is evident that the ultrafast laser creates a confined chemical change followed by a morphological change (blister) at the glass-polymer interface. We also observed solidified molten material underneath the blister, some of which settled on the underlying glass (as shown in Fig. 1(b)); both with same phase contrast. Since the local temperature generated in polyimide exceeds the melting point, the interaction region melts, cools and re-solidifies. The chemical properties of these melted regions are completely different from pristine polyimide. Though similar experiments involving blister formation for thin films of polyimide and titanium using 355 nm and 800 nm excitation wavelengths have been reported, these experiments lack the direct evidence of confined photochemical modification followed by deformation of the intact

Optics EXPRESS

polymer caused by a bubble underneath [1,7,18,19]. We report direct experimental evidence for confinement of chemical changes only at the interface using FIB diagnostic. It is not reported by others involving blister-actuated and dynamic release layer Laser-induced forward transfer (LIFT) experiments [1–4,18,20–31].

To determine the nature of the chemical changes at the glass-polymer interface, we created blister patterns on 3.5 μm thick polyimide films. The patterned surface areas of polyimide were matched with excitation beam sizes ($\sim$ cm^2) in a conventional fluorimeter and RAIRS to obtain a reasonable signal for spectroscopy analysis (later sections). Polyimide film was patterned using laser pulse energy of 650 nJ with a 10x (0.2 NA) microscope objective at scan speed of 4 mm/s (vacuum intensity $\sim 7 \times 10^{13}$ W/cm^2) . The repetition rate of the laser was 2 kHz with a line spacing (on the sample) of 6 μm. The effective no. of shots per focal spot is 2 with these conditions.

Figure 1(c) shows an FIB image of a dissected overlapped blisters with effective no. of 2-shots per focal spot. The interior portions contained a series of hollow regions with crescent orientation along the scan direction. Inset shows AFM image of blistered surface. The AFM image of the blistered surface clearly shows oriented crescent contours of blisters in the writing direction of laser beam. When a laser pulse is incident, it imprints a circular contour. Since the sample effectively has 2 shots for each focal spot, the second shot imprints its contour on half of the modified region affected by the first shot while the sample is under motion.

In addition to FIB, we also carried out indirect measurements to study the extent (depth) of photochemical modification using reflection-absorption infrared spectroscopy (RAIRS) and X-ray Photoelectron (XPS) spectroscopy [32,33]. We did not coat polyimide thin films on a metal substrate as required and hence, the IR radiation interacted with the entire film and reflected by the glass substrate. Because of this, we could observe the photochemical changes which occurred beneath the film. The details of the RAIRS spectra recorded are given in Appendix B. We also carried out XPS characterization on these samples. X-rays are confined to the surface of material, with a sampling depth as small as 7.5 nm [32]. We did not observe any changes with XPS because the surface was intact in our case. Together, these spectroscopy techniques indicated the confinement of chemical modification at the polymer-glass interface, which coincided with observations from FIB diagnostics. We have also used other polymers such as polymethyl methacrylate (PMMA) and observed similar photochemical and morphological changes.

3.2. *Photo chemistry: bulk fluorescence*

We performed fluorescence (excitation-emission) measurements to study chemical changes induced by an ultrafast intense laser pulse. We recorded fluorescence (emission) spectra for pristine and laser-modified polyimide (as shown in Fig. 2). Fluorescence spectra were acquired with 300-550 nm excitation in steps of 5 nm. These spectra showed maximum fluorescence intensity in the blue and green regions for the laser-modified polyimide and almost negligible fluorescence in the visible spectrum for pristine polyimide, except fluorescence [34,35] from the polymer backbone (inset of Fig. 2). The fluorescence intensities for pristine and laser-treated polyimide samples were compared and scaled. Their relative intensities are shown in the color scale.

To comprehend the nature of fluorescence, we compared the fluorescence from laser-altered polyimide with carbon dots [36]. Laser-treated polyimide showed fluorescence bands at 547 nm (at 425 nm excitation wavelength), 416 nm, and 436 nm (both at 350 nm excitation wavelength), which are consistent with violet, blue, and green carbon dots. We compared the fluorescence spectra with carbon dots because polymers are carbon rich materials and can be transformed into carbon clusters/carbon dust upon laser irradiation [13,37–43]. It is possible that the observed spectrum could be caused by either carbon dots and/or polymer aggregates resulted from polymer chain scission followed by rearrangement [44].

Optics EXPRESS

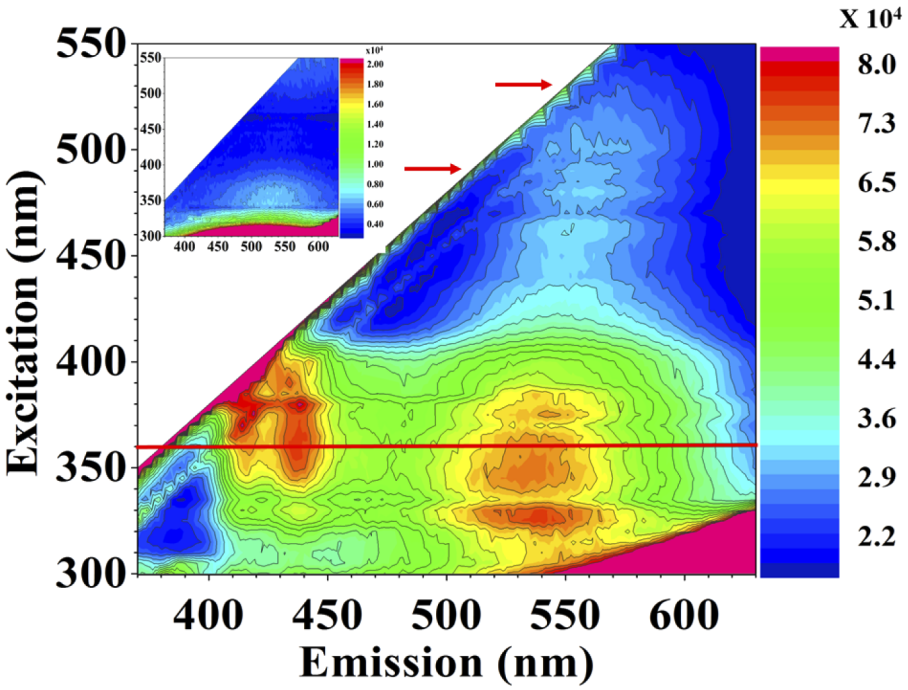

Fig. 2. (color online) Fluorescence spectra of laser-modified polyimide. Inset shows the background fluorescence of pristine polyimide. The fluorescence intensity of laser-modified polyimide is scaled relative to the pristine material and is shown in the color scale. The maximum fluorescence was obtained at 360 nm excitation shown with a red line. Laser-modified polyimide showed fluorescence bands at 552 nm and 572 nm at excitation wavelengths of 490 nm and 530 nm. Both excitation wavelengths are marked with red arrows. Not shown, we have also compared the spectrum of laser-modified borosilicate glass with the laser-modified polyimide to rule out its contribution.

We also studied the fluorescence properties of laser-modified polyimide above 425 nm excitation. We chose two excitation wavelengths at 490 nm and 530 nm (shown by red arrows in Fig. 2) to compare the fluorescence with confocal fluorescence measurements in section 3.4. When corrected for detector sensitivity, the fluorescence spectra in Fig. 2 at both the excitation wavelengths (490 nm and 530 nm) match the confocal fluorescence measurements in Fig. 4. Both measurements reveal that the peak shifts relative to their pristine counterparts indicating a distorted polymer matrix.

When a fs laser pulse is focused at the glass-polyimide interface, it forms a hot plasma. When the plasma expands outwards, a temperature gradient is formed. It is possible that the material in the focal volume is vaporized and collects on the interface, resulting in carbon dots. The material that is not vaporized, but melted due to the temperature gradient, forms an underside layer of polyimide as seen in FIB image (Fig. 1(b)). The heated, non-vaporized polymer remains attached to the expanding, unmodified polyimide material resulting in a distorted matrix.

Since the experiments involved high peak intensities in the substrate, fluorescence from laser-modified glass should be investigated to rule out its contribution. For this, we recorded fluorescence spectra for laser-modified borosilicate glass under similar excitation conditions. The recorded spectra were completely different from those of laser-modified polyimide which confirm that significant modification was only done to the polymer. However, we could not obtain fluorescent images of these modified regions using the fluorimeter.

Optics EXPRESS

3.3. Nature of fluorescence: polarization anisotropy studies

Several carbon-rich materials including carbon dots, polymers, and biological macromolecules have shown polarization anisotropy of fluorescence [35,36,45]. In these studies, linearly polarized light preferentially excites molecules or particles with transition dipole moments parallel to the polarization, leading to polarized emission. Thus, amorphous polymers tend to show less anisotropy, since molecular chains are randomly distributed. In the past, it was shown that a linearly polarized femtosecond laser beam can align polymer chains inducing formation of ordered aggregates, for example via π-π stacking [46–48] in spin-cast films. Fig. 3(a) shows the fluorescence spectra for pristine and laser-treated polyimide samples at 360 nm excitation, where both samples have significant absorption. The laser-induced fluorescence for the patterned sample had two partially resolved bands and a shoulder with an intensity pattern resembling a spectrum of H-type aggregates. Spectral characteristics of ordered polymer aggregates are well described by HJ-aggregate model developed by Spano et al. [49–51]. In short, for J-type aggregates or a single planarized chain, the highest energy (shortest wavelength) fluorescence peak, I_{00} peak is the strongest, while for H-type aggregates such as π-π stacked multiple chains the I_{00} peak is only weakly allowed and the I_{01} peak carries the most intensity. Pristine polyimide spectrum did not show any ordered aggregate signature due to a random distrbution of polymer chains.

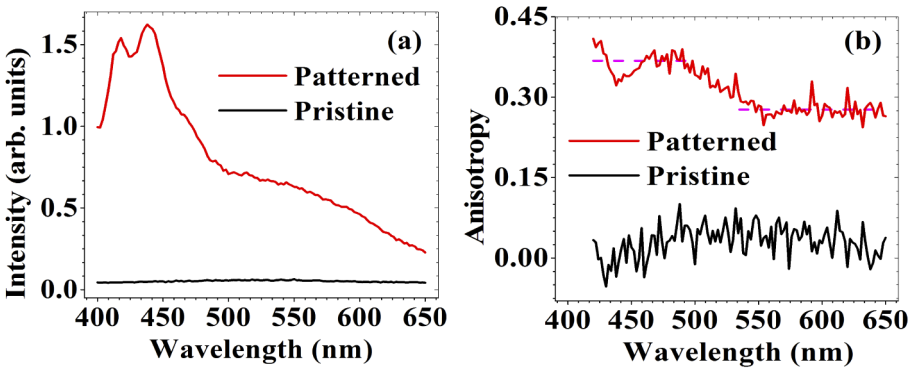

Fig. 3. (color online) **(a)** Fluorescence spectra of pristine (black) and laser-modified polyimide (red) excited at 360 nm. **(b)** Polarization anisotropy of fluorescence for pristine (black) and laser-modified polyimide (red). Laser-modified polyimide showed anisotropy around 0.4 in the blue region and 0.3 in the green region. Both are indicated with dashed lines.

To confirm the formation of HJ-aggregates, we performed studies on polarization anisotropy of fluorescence. Molecules aligned along a given linear polarization are excited most strongly and the maximum fluorescence signal is obtained with a parallel analyzer. We acquired fluorescence spectra using 360 nm excitation for four combinations of parallel and perpendicular polarizer-analyzer orientations. Polarization anisotropy is determined from these spectra using the equation (1).

$$r = \frac{I_{VV} - GI_{VH}}{I_{VV} + 2GI_{VH}} \tag{1}$$

The fluorescence intensities are represented by a letter I followed by two subscripts. The first subscript denotes the excitation polarization and the second represents the fluorescence polarization. H and V represent horizontal and vertical polarization components. G is an instrumental factor related to the preference of the emission optics for the vertical polarization (I_{HV}) to the horizontal polarization (I_{HH}) and r is fluorescence anisotropy [52]. Fig. 3(b) shows polarization anisotropy curves for pristine (black) and laser-patterned polyimide (red) samples.

Optics EXPRESS

We observed maximum fluorescence when the laser-irradiated sample was oriented so that the polarization of the writing laser was perpendicular to the excitation polarization of the fluorimeter. In these experiments, induced polarization anisotropy of fluorescence could be understood in two ways; (i) an ultrafast laser induces dipole moments parallel or perpendicular to its polarization depending upon net dipole moment along or perpendicular to a backbone axis which exerts a force that aligns molecules [53], and/or (ii) the laser selectively breaks molecular chains aligned with its polarization direction. Considering the peak intensity of the pulses used ($\sim 10^{14}$ W/cm^2, far above the damage threshold of 1.3×10^{13} W/cm^2), the latter case is likely, though it has not been reported. In either case, the overall fluorescence is from specific molecular chains only.

3.4. Photo chemistry on micron scale

We collected Raman spectra from a confocal micro-Raman instrument to study photochemical modification on the scale of individual blisters. The black curve in Fig. 4(a) shows a characteristic Raman spectrum for pristine polyimide excited with a 532 nm continuous wave (CW) laser. Six main peaks are easily resolved. Spectral signatures appearing at 1776 cm^{-1} corresponds to C=O stretching, and the two peaks at 1620 cm^{-1} and 1666 cm^{-1} correspond to C=C stretching in ring and double ring structures respectively. The peaks at 1419 cm^{-1}, 1377 cm^{-1}, and 1131 cm^{-1} represent C-N, C-C stretches, and a ring breathing mode [54,55].

A Raman scattering spectrum was recorded from a single blister fabricated using an ultrafast laser at 258 nJ energy with a 0.4 NA objective. Considering the substrate-mediated absorption that onsets for I > $10^{12} W/cm^2$, the remaining intensity $I_{abs} \approx 10^{13} W/cm^2$ is delivered to the polymer. Blisters exhibited strong photoluminescence (fluorescence) as can be seen in Fig. 4(a) (increased background for red curve), making detection of Raman-scattered photons difficult. We attempted to record Raman signals at other excitation wavelengths but could not succeed due to overwhelming background fluorescence. In the literature, intensity ratios between D (disorder $\approx$ 1350 cm^{-1}) and G (graphite $\approx$ 1580 cm^{-1}) bands are used to indicate carbonization due to ultrafast laser treatment [56]. In our case, we could not compare these intensities accurately since these bands were masked by strong background fluorescence.

To compare ultrafast-laser-induced photoluminescence with standard CW laser treatment, pristine polyimide was irradiated through a NA = 0.9 lens by 32 mW of CW excitation from a 532 nm laser for 60 s, and a Raman spectrum of the region was recorded (blue curve in Fig. 4(a)). The CW laser (I = 8×10^6 W/cm^2) modification did not show any fluorescence, but showed D and G bands indicating carbonization of polyimide [50]. The nature of photochemical modification with ultrafast laser pulses is distinct from that of CW lasers.

Since we observed photoluminescence masking the Raman signal, we acquired fluorescence spectra to compare with our earlier bulk measurements reported in Section 2. We recorded fluorescence at four different excitation wavelengths (488 nm, 532 nm, 632 nm, and 785 nm) for pristine and blistered polyimide using a confocal micro-Raman instrument. Point-wise fluorescence spectra were integrated over individual blisters. Fig. 4(b) shows integrated fluorescence spectra for polyimide blisters and pristine polyimide at two different excitation wavelengths (488 nm and 532 nm). Polyimide blisters have shown significant increases in fluorescence intensity. Also, fluorescence intensity decreased with increasing excitation wavelength, indicating that the ultrafast laser-induced defect states were formed in the UV region. This agrees with trend seen in bulk fluorescence measurements shown in Fig. 2. Fig. 4(c) shows fluorescence maps of a single blister for each excitation wavelength.

We noticed that the fluorescence intensity was always lower at the center than at the edges of a blister. This may be due to (i) the intensity of the Gaussian pulse at the center is maximum, inducing maximum pressure at the center resulting in deposition of modified material at the edges and/or (ii) the local temperature in the material at the center of Gaussian pulse results in more vapor formation. This leaves less modified material at the center than surroundings. In

Optics EXPRESS

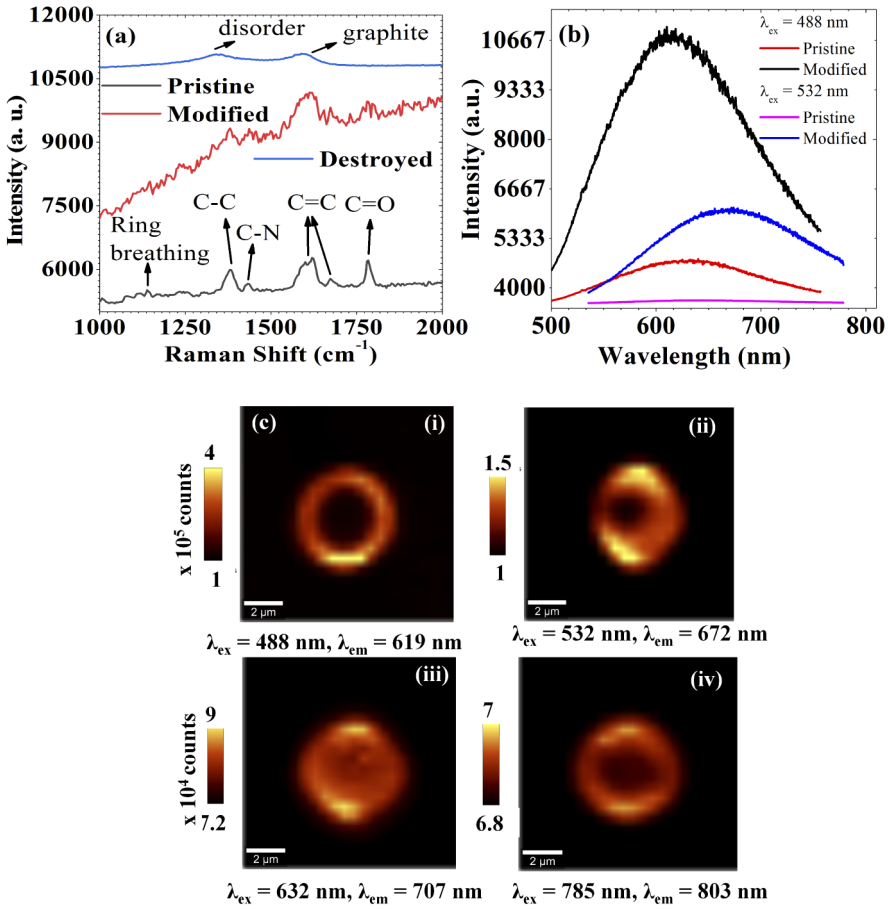

Fig. 4. (color online) **(a)** Raman spectra for pristine (black), an individual polyimide blister fabricated at 258 nJ pulse energy (red) using 0.4 NA (vacuum intensity ~ 1.1 $\times 10^{14}$ W/cm^2) , and a CW laser-modified polyimide (blue). Raman excitation wavelength was fixed at 532 nm. **(b)** Integrated photoluminescence of a blister at different excitations. As marked by red arrows in Fig. 2, the fluorescence spectra close to the excitation wavelengths of 490 nm and 530 nm are compared. **(c)**Fluorescence from blisters at various excitation wavelengths with 1 mW power. The fluorescence at 488 nm (i) and 532 nm (ii) excitations showed an order of magnitude (10^5 counts) more than that of fluorescence at excitation wavelengths of 632 nm (iii) and 785 nm (iv).

either case, the local fluorescence at the center is different from its surroundings due to the extent of laser-induced pressure or temperature.

4. Conclusion

Illumination of a polymer through a glass substrate creates a thin and modified polymer layer. Confined beneath the surface, chemical changes to the polymer are inevitable. We have studied these changes using different spectroscopic methods. To observe physical changes, we have focused an ion beam to cut open and then image a blister created by a 320 nJ (vacuum intensity ~ 1.4 $\times 10^{14}$ W/cm^2) , 45-fs pulse focused to a full width at half maximum diameter of 6.5 μm. While some of the pulse energy is deposited in the substrate [14], a great deal is used to create

Optics EXPRESS

the hollow region that we observe, partially filled with debris, which localized at the interface. We also see evidence of modified polymer at the hollow region-polymer interface.

To observe chemical changes, we have measured bulk and locally excited fluorescence (using confocal micro-Raman) from the modified polymer. We see fluorescence signals that were not previously present. These changes are evidence of chemical changes to the material. By imaging the fluorescence we find that it comes mainly from the periphery of the bubble suggesting that it arises from material that has been liquefied or vaporized and then deposited at the outer edges of the blister. We also observe that the fluorescence is polarized and depends on the relative polarization of the writing and exciting beams.

The nonuniform chemical modification of this study is not a limitation to laser-induced forwards transfer (LIFT). We have demonstrated that the chemical changes induced by an ultrafast laser are confined to glass-polymer interface. The thrust generated in the mechanical deformation of the film deposits the material. Our study suggests femtosecond pulse irradiation of polymers through a glass substrate could be also important for applications in (i) contaminant-free LIFT, since heat and chemical changes are localized far from the polymer-vacuum interface, (ii) the nonuniformity may be helpful for producing high-quality micro lenses through the refractive index change confined to the interface and/or morphological change, (iii) data storage since laser-induced photochemical changes and anisotropy allow high storage capacity, and (iv) generating high harmonics in gases and solids since ionizing materials are the source of high-harmonic radiation [57,58].

Appendix A: characterization details

The interior modification confined to the interface was studied using focused ion beam (FIB) technique. Zeiss's ORION NanoFab multi-column (GFIS, and Gallium-FIB) Helium Ion Microscope (HIM) and Focused Ion Beam (Gallium- FIB) were used to study the blistered samples. Gallium ions were used to dissect the blisters and Helium ions were used to image. Prior to performing dissection, the samples were coated with 30 nm Aluminium to protect from damage due to ion beam irradiation. Steady state and polarization-dependent fluorescence measurements were all performed with a Horiba Jobin Yvon Fluorolog Tau-3 Lifetime System. PI-2525 thin films were used for fluorescence measurements.

Raman spectroscopic data was recorded using a Witec Alpha a300 system (confocal micro-Raman) in the back scattering configuration using a 600 groove/mm grating at a resolution of 4.6 cm^{-1}. An excitation laser operating at a wavelength of 532 nm, with a total power of 1 mW focussed through a 20x 0.4 N.A. objective, was used to excite Raman scattering in the polyimide samples. Each spectrum was recorded using 10 accumulations and an integration time of 15 s. Photoluminescence (fluorescence) imaging was performed using the same confocal micro-Raman instrument, with excitation wavelengths of 488 nm, 532 nm, 632 nm, and 785 nm. Images were acquired using a 100x 0.9 NA objective. To maximize the detectable spectral range, a 300 groove/mm grating was used, providing a spectral resolution of 0.27 nm. Images with dimensions of 15 μm by 15 μm were realized by recording 30 spectra per line and 30 lines per image. Each fluorescence spectrum was recorded using a single accumulation with an integration time of 0.5 s.

All AFM images were taken using the Nanowizard II BioAFM (Bruker, JPK Instruments, Berlin, Germany) mounted on an Olympus IX81 inverted microscope, operating in contact mode. Silicon nitride cantilevers (DNP-S, Veeco, CA) were used in contact mode imaging. Reflection-absorption infrared spectroscopy (RAIRS) measurements were performed on a Thermo Nicolet Nexus 870 FTIR spectrometer with the incident light beam hitting the surface of the sample at 80°. Each spectrum is the average result of 256 accumulations recorded at a spectral resolution of 0.4 cm^{-1}, taken from a region approximately 0.5 cm^2 in size. A clean borosilicate coverslip was used for background correction. The excitation source was an Everglo IR source

Optics EXPRESS

covering the 4000 cm^{-1} to 400 cm^{-1} spectral range. XPS measurements were performed using Al Kα as an excitation source with energy of 1,486 eV. Both confocal micro-Raman and RAIRS measurements were carried out on PI-2555 thin films.

Appendix B: reflection-absorption infrared spectroscopy (RAIRS) studies

We used the laser-treated polyimide sample (used in fluorescence studies) for comparison with pristine polyimide in RAIRS studies. Fig. 5 shows the RAIRS spectra for pristine (black) and laser-modified polyimide (red). The absorbed IR intensity is plotted against the Y-axis in arbitrary units as the IR spectrum for pristine polyimide was vertically shifted for comparison. A clear change in the shape of the RAIRS spectrum for laser-modified sample was observed. Since these experiments were carried out on two different samples, there could be variations in thicknesses of coverslips and polyimide thin films. Hence their intensities cannot be directly compared. However, the relative intensities for each of these vibrational modes in both the spectra can be compared with respect to a fixed vibrational mode. Absorption spectra were normalized to account for different film thicknesses.

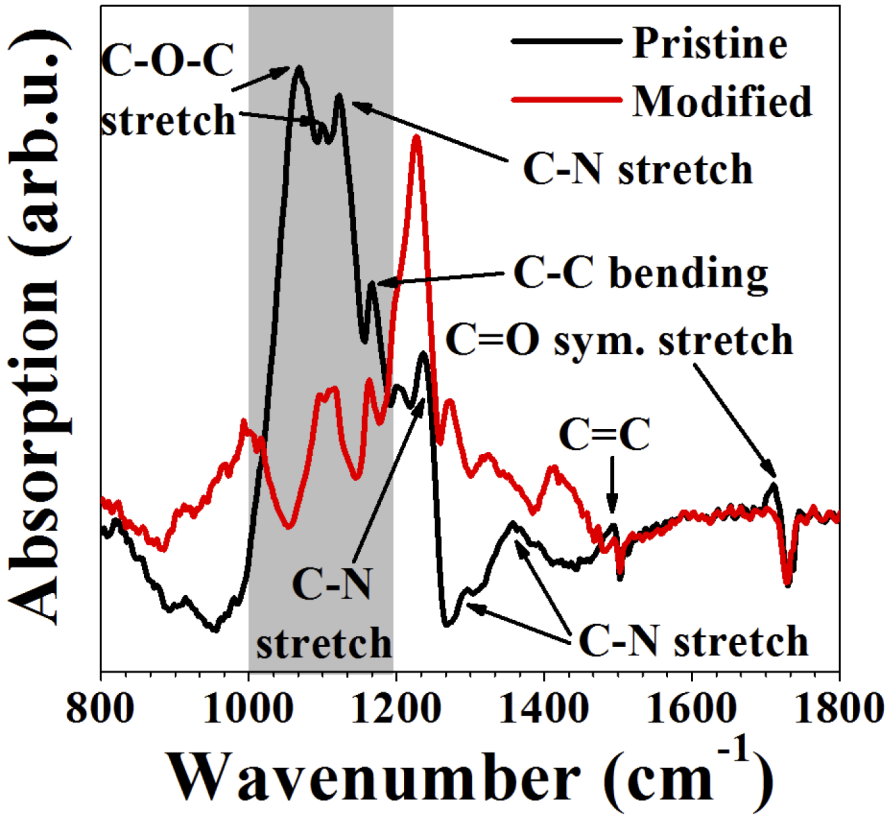

Fig. 5. (color online) RAIRS spectra of pristine (black) and laser-modified (red) polyimide.

We assigned bands for pristine polyimide from the Refs. [59–61]. Bands close to 1068 cm^{-1}, 1167 cm^{-1}, and 1236 cm^{-1} were assigned to C-O-C stretching, C-C bending, and C-N stretching [59]. Bands at 1358 cm^{-1}, 1493 cm^{-1}, and 1711 cm^{-1} are assigned to C-N stretching of the aromatic ring, C=C stretching, and C=O symmetric stretching [60]. The bands close to 1099 cm^{-1} and 1122 cm^{-1} correspond to C-N imide and 1296 cm^{-1} correspond to C-N stretching modes [61]. These bands correspond to vibrational modes of different groups of polyimide.

Optics EXPRESS

From Fig. 5, the pristine polyimide had less absorption in the region above 1200 cm^{-1} compared to laser-modified polyimide. However, this trend was different in the highlighted region shown in the plot in between 1000-1200 cm^{-1}. There are a few changes in peak positions of C-N stretching in the region 1300-1400 cm^{-1}.

The vibrational modes for laser-modified polyimide shifted to 1097 cm^{-1}, 1226 cm^{-1}, and 1411 cm^{-1} compared to the corresponding vibrational modes of pristine polyimide at 1068 cm^{-1}, 1236 cm^{-1}, and 1358 cm^{-1}, respectively. These studies together with relative intensity differences between laser-modified and pristine polyimide indicate that the laser-modified polyimide underwent photochemical and structural changes. These results agreed with earlier reports on UV exposed polyimide [61]. Oxygen containing groups on polymer surfaces such as C-O, C=O, and O-C=O are responsible for surface hydrophobicity and hydrophilicity of polymers [62] (though the role of surface roughness cannot be ignored). In our case, the absorption of C-O-C stretching (highlighted region) for laser-modified polyimide decreased indicating that the laser-treated polyimide transformed to hydrophobic. We performed hydrophobicity tests on these laser-modified polyimide surfaces and found that the results were in agreement with RAIRS studies reported earlier [62].

Funding

Natural Sciences and Engineering Research Council of Canada (Engage EGP 523138- 18, Discovery RGPIN-2019-04603); Ontario Centres of Excellence (VIP1 Program 29119); National Research Council Canada (Ideation Project A1-015007).

Acknowledgments

All authors acknowledge financial support from Natural Sciences and Engineering Research Council of Canada (NSERC), Ontario Centres of Excellence (OCE). Alan T. K. Godfrey acknowledges financial support from NSERC's Postgraduate Scholarship - Doctoral and University of Ottawa's Scholarship. Zygmunt J. Jakubek and Paul B Corkum acknowledge NRC Canada Ideation project (A1-015007) on Hybrid crystalline films for polymer electronics applications. We acknowledge Maohui Chen for training in atomic force microscopy, Choloong Hahn for FIB measurements, Tony Olivieri for training related to polyimide film fabrication, and Alexander Sander for acquiring XPS spectra.

Disclosures

The authors declare no conflicts of interest.

References

1. N. T. Kattamis, P. E. Purnick, R. Weiss, and C. B. Arnold, "Thick film laser induced forward transfer for deposition of thermally and mechanically sensitive materials," Appl. Phys. Lett. **91**(17), 171120 (2007).
2. M. S. Brown, N. T. Kattamis, and C. B. Arnold, "Time-resolved study of polyimide absorption layers for blister-actuated laser-induced forward transfer," J. Appl. Phys. **107**(8), 083103 (2010).
3. M. S. Brown, C. F. Brasz, Y. Ventikos, and C. B. Arnold, "Impulsively actuated jets from thin liquid films for high-resolution printing applications," J. Fluid Mech. **709**, 341–370 (2012).
4. N. T. Kattamis, M. S. Brown, and C. B. Arnold, "Finite element analysis of blister formation in laser-induced forward transfer," J. Mater. Res. **26**(18), 2438–2449 (2011).
5. J. P. McDonald, V. R. Mistry, K. E. Ray, S. M. Yalisove, J. A. Nees, and N. R. Moody, "Femtosecond-laser-induced delamination and blister formation in thermal oxide films on silicon (100)," Appl. Phys. Lett. **88**(15), 153121 (2006).
6. J. R. Serrano and D. G. Cahill, "Laser-Induced Blistering of Thin SiO2 on Si," Microscale Thermophys. Eng. **9**(2), 155–164 (2005).
7. N. T. Goodfriend, S. V. Starinskiy, O. A. Nerushev, N. M. Bulgakova, A. V. Bulgakov, and E. E. B. Campbell, "Laser pulse duration dependence of blister formation on back-radiated Ti thin films for BB-LIFT," Appl. Phys. A **122**(3), 154 (2016).
8. M. Forster, W. Kautek, N. Faure, E. Audouard, and R. Stoian, "Periodic nanoscale structures on polyimide surfaces generated by temporally tailored femtosecond laser pulses," Phys. Chem. Chem. Phys. **13**(9), 4155–4158 (2011).

Optics EXPRESS

9. C. De Marco, S. M. Eaton, R. Suriano, S. Turri, M. Levi, R. Ramponi, G. Cerullo, and R. Osellame, "Surface Properties of Femtosecond Laser Ablated PMMA," ACS Appl. Mater. & Interfaces **2**(8), 2377–2384 (2010).
10. D. L. N. Kallepalli, A. M. Alshehri, D. T. Marquez, L. Andrzejewski, J. C. Scaiano, and R. Bhardwaj, "Ultra-high density optical data storage in common transparent plastics," Sci. Rep. **6**(1), 26163 (2016).
11. D. L. N. Kallepalli, R. Kuladeep, S. V. Rao, and D. N. Rao, "Luminescent microstructures in bulk and thin films of PMMA, PDMS, PVA, and PS fabricated using femtosecond direct writing technique," Chem. Phys. Lett. **503**(1-3), 57–60 (2011).
12. Z. Nie, H. Lee, H. Yoo, Y. Lee, Y. Kim, K.-S. Lim, and M. Lee, "Multilayered optical bit memory with a high signal-to-noise ratio in fluorescent polymethylmethacrylate," Appl. Phys. Lett. **94**(11), 111912 (2009).
13. A. M. Alshehri, K. L. N. Deepak, D. T. Marquez, S. Desgreniers, and V. R. Bhardwaj, "Localized nanoclusters formation in PDMS upon irradiation with femtosecond laser," Opt. Mater. Express **5**(4), 858–869 (2015).
14. A. T. K. Godfrey, D. L. N. Kallepalli, J. Ratte, and P. B. Corkum, Ultrafast laser-induced blister formation in polyimide films (unpublished data).
15. D. M. Rayner, A. Naumov, and P. B. Corkum, "Ultrashort pulse non-linear optical absorption in transparent media," Opt. Express **13**(9), 3208–3217 (2005).
16. L. Mercadier, D. M. Rayner, and P. B. Corkum, "Control of Femtosecond Laser Ablation of Thin Films from a Dielectric Surface by Nonlinear Interaction with the Substrate," Phys. Rev. Appl. **2**(3), 034001 (2014).
17. A. Ben-Yakar and R. L. Byer, "Femtosecond laser ablation properties of borosilicate glass," J. Appl. Phys. **96**(9), 5316–5323 (2004).
18. C. B. Arnold, P. Serra, and A. Piqué, "Laser Direct-Write Techniques for Printing of Complex Materials," MRS Bull. **32**(1), 23–31 (2007).
19. G. Heise, M. Domke, J. Konrad, S. Sarrach, J. Sotrop, and H. P. Huber, "Laser lift-off initiated by direct induced ablation of different metal thin films with ultra-short laser pulses," J. Phys. D: Appl. Phys. **45**(31), 315303 (2012).
20. P. Delaporte and A.-P. Alloncle, "Laser-induced forward transfer: A high resolution additive manufacturing technology," Opt. & Laser Technol. **78**, 33–41 (2016).
21. N. R. Schiele, D. T. Corr, Y. Huang, N. A. Raof, Y. Xie, and D. B. Chrisey, "Laser-based direct-write techniques for cell printing," Biofabrication **2**(3), 032001 (2010).
22. G. Jing, Y. Wang, T. Zhou, S. F. Perry, M. T. Grimes, and S. Tatic-Lucic, "Cell patterning using molecular vapor deposition of self-assembled monolayers and lift-off technique," Acta Biomater. **7**(3), 1094–1103 (2011).
23. M. Gruene, A. Deiwick, L. Koch, S. Schlie, C. Unger, N. Hofmann, I. Bernemann, B. Glasmacher, and B. Chichkov, "Laser Printing of Stem Cells for Biofabrication of Scaffold-Free Autologous Grafts," Tissue Eng. Part C: Methods **17**(1), 79–87 (2011).
24. L. Koch, S. Kuhn, H. Sorg, M. Gruene, S. Schlie, R. Gaebel, B. Polchow, K. Reimers, S. Stoelting, N. Ma, P. M. Vogt, G. Steinhoff, and B. Chichkov, "Laser Printing of Skin Cells and Human Stem Cells," Tissue Eng. Part C: Methods **16**(5), 847–854 (2010).
25. A. Palla-Papavlu, V. Dinca, C. Luculescu, J. Shaw-Stewart, M. Nagel, T. Lippert, and M. Dinescu, "Laser induced forward transfer of soft materials," J. Opt. **12**(12), 124014 (2010).
26. P. Serra, M. Colina, J. M. Fernández-Pradas, L. Sevilla, and J. L. Morenza, "Preparation of functional DNA microarrays through laser-induced forward transfer," Appl. Phys. Lett. **85**(9), 1639–1641 (2004).
27. B. Hopp, T. Smausz, Z. Antal, N. Kresz, Z. Bor, and D. Chrisey, "Absorbing film assisted laser induced forward transfer of fungi (Trichoderma conidia)," J. Appl. Phys. **96**(6), 3478–3481 (2004).
28. J. Barron, P. Wu, H. Ladouceur, and B. Ringeisen, "Biological Laser Printing: A Novel Technique for Creating Heterogeneous 3-dimensional Cell Patterns," Biomed. Microdevices **6**(2), 139–147 (2004).
29. J. Xu, J. Liu, D. Cui, M. Gerhold, A. Y. Wang, M. Nagel, and T. K. Lippert, "Laser-assisted forward transfer of multi-spectral nanocrystal quantum dot emitters," Nanotechnology **18**(2), 025403 (2007).
30. R. Fardel, M. Nagel, F. Nüesch, T. Lippert, and A. Wokaun, "Fabrication of organic light-emitting diode pixels by laser-assisted forward transfer," Appl. Phys. Lett. **91**(6), 061103 (2007).
31. D. P. Banks, K. Kaur, R. Gazia, R. Fardel, M. Nagel, T. Lippert, and R. W. Eason, "Triazene photopolymer dynamic release layer-assisted femtosecond laser-induced forward transfer with an active carrier substrate," EPL **83**(3), 38003 (2008).
32. J. Yarwood, "Fourier Transform Infrared Reflection Spectroscopy for Surface Analysis," Anal. Proc. **30**, 6 (1993).
33. C. M. Chan and L.-T. Weng, "Surface Characterization of Polymer Blends by XPS and ToF-SIMS," Materials **9**(8), 655 (2016).
34. K. Kanosue, R. Augulis, D. Peckus, R. Karpicz, T. Tamulevicius, S. Tamulevicius, V. Gulbinas, and S. Ando, "Polyimide and Imide Compound Exhibiting Bright Red Fluorescence with Very Large Stokes Shifts via Excited-State Intramolecular Proton Transfer II. Ultrafast Proton Transfer Dynamics in the Excited State," Macromolecules **49**(5), 1848–1857 (2016).
35. E. D. Wachsman and C. W. Frank, "Effect of cure history on the morphology of polyimide: Fluorescence spectroscopy as a method for determining the degree of cure," Polymer **29**(7), 1191–1197 (1988).
36. M. O. Dekaliuk, O. Viagin, Y. V. Malyukin, and A. P. Demchenko, "Fluorescent carbon nanomaterials: "quantum dots" or nanoclusters?" Phys. Chem. Chem. Phys. **16**(30), 16075–16084 (2014).
37. S. Hayashi, M. Kataoka, and K. Yamamoto, "Photoluminescence Spectra of Carbon Clusters Embedded in SiO2," Jpn. J. Appl. Phys. **32**(Part 2, No. 2B), L274–L276 (1993).

Optics EXPRESS

38. W. Krätschmer, K. Fostiropoulos, and D. R. Huffman, "The infrared and ultraviolet absorption spectra of laboratory-produced carbon dust: evidence for the presence of the C60 molecule," Chem. Phys. Lett. **170**(2-3), 167–170 (1990).
39. D. Fink, W. H. Chung, R. Klett, A. Schmoldt, J. Cardoso, R. Montiel, M. H. Vazquez, L. Wang, F. Hosoi, H. Omichi, and P. Goppelt-Langer, "Carbonaceous clusters in irradiated polymers as revealed by UV-Vis spectrometry," Radiat. Eff. Defects Solids **133**(3), 193–208 (1995).
40. D. Fink, R. Klett, L. T. Chadderton, J. Cardoso, R. Montiel, H. Vazquez, and A. A. Karanovich, "Carbonaceous clusters in irradiated polymers as revealed by small angle X-ray scattering and ESR," Nucl. Instruments Methods Phys. Res. Sect. B: Beam Interactions with Mater. Atoms **111**(3-4), 303–314 (1996).
41. S. Gupta, D. Choudhary, and A. Sarma, "Study of carbonaceous clusters in irradiated polycarbonate with UV-vis spectroscopy," J. Polym. Sci. Part B: Polym. Phys. **38**(12), 1589–1594 (2000).
42. E. Despagnet-Ayoub, W. W. Kramer, W. Sattler, A. Sattler, P. J. LaBeaume, J. W. Thackeray, J. F. Cameron, T. Cardolaccia, A. A. Rachford, J. R. Winkler, and H. B. Gray, "Triphenylsulfonium topophotochemistry," Photochem. Photobiol. Sci. **17**(1), 27–34 (2018).
43. U. Mahilny, A. Trofimova, S. Nazarov, A. Tolstik, R. Heintzmann, and E. Tolstik, "Highly concentrated phenanthrenequinone polymethylmethacrylate composite for thick reflection holograms recording at 532 nm," Opt. Mater. Express **6**(11), 3427–3437 (2016).
44. T. Wang, A. Wang, R. Wang, Z. Liu, Y. Sun, G. Shan, Y. Chen, and Y. Liu, "Carbon dots with molecular fluorescence and their application as a "turn-off" fluorescent probe for ferricyanide detection," Sci. Rep. **9**(1), 10723 (2019).
45. D. M. Jameson and J. A. Ross, "Fluorescence Polarization/Anisotropy in Diagnostics and Imaging," Chem. Rev. **110**(5), 2685–2708 (2010).
46. S. Chae, K. H. Jo, S. W. Lee, H.-S. Keum, H. J. Kim, J. Choi, and H. H. Lee, "Selective Chain Alignment of Conducting Polymer Blend Films by an Ultrafast Laser," Macromol. Chem. Phys. **217**(4), 537–542 (2016).
47. A. Moliton and R. C. Hiorns, "Review of electronic and optical properties of semiconducting π-conjugated polymers: applications in optoelectronics," Polym. Int. **53**(10), 1397–1412 (2004).
48. Y. Martinez-Rubi, Z. J. Jakubek, M. B. Jakubinek, K. S. Kim, F. Cheng, M. Couillard, C. Kingston, and B. Simard, "Self-Assembly and Visualization of Poly(3-hexyl-thiophene) Chain Alignment along Boron Nitride Nanotubes," J. Phys. Chem. C **119**(47), 26605–26610 (2015).
49. H. Yamagata and F. C. Spano, "Interplay between intrachain and interchain interactions in semiconducting polymer assemblies: The HJ-aggregate model," J. Chem. Phys. **136**(18), 184901 (2012).
50. F. C. Spano and C. Silva, "H- and J-Aggregate Behavior in Polymeric Semiconductors," Annu. Rev. Phys. Chem. **65**(1), 477–500 (2014).
51. T. Eder, T. Stangl, M. Gmelch, K. Remmerssen, D. Laux, S. Höger, J. M. Lupton, and J. Vogelsang, "Switching between H- and J-type electronic coupling in single conjugated polymer aggregates," Nat. Commun. **8**(1), 1641 (2017).
52. J. R. Lakowicz and B. R. Masters, "Principles of Fluorescence Spectroscopy, Third Edition," J. Biomed. Opt. **13**(2), 029901 (2008).
53. M. Nishikawa, B. Taheri, and J. L. West, "Mechanism of unidirectional liquid-crystal alignment on polyimides with linearly polarized ultraviolet light exposure," Appl. Phys. Lett. **72**(19), 2403–2405 (1998).
54. X. J. Gu, "Raman spectroscopy and the effects of ultraviolet irradiation on polyimide film," Appl. Phys. Lett. **62**(13), 1568–1570 (1993).
55. A. K. Shukla, V. M. Yadav, A. Kumar, I. A. Palani, and A. Manivannan, "Investigations on effect of laser-induced self-assembled patterning on optical properties of flexible polyimide substrates for solar cell applications," J. Phys. D: Appl. Phys. **51**(4), 045502 (2018).
56. C. Cheng, S. Wang, J. Wu, Y. Yu, R. Li, S. Eda, J. Chen, G. Feng, B. Lawrie, and A. Hu, "Bisphenol A Sensors on Polyimide Fabricated by Laser Direct Writing for Onsite River Water Monitoring at Attomolar Concentration," ACS Appl. Mater. & Interfaces **8**(28), 17784–17792 (2016).
57. M. Hentschel, R. Kienberger, C. Spielmann, G. A. Reider, N. Milosevic, T. Brabec, P. Corkum, U. Heinzmann, M. Drescher, and F. Krausz, "Attosecond metrology," Nature **414**(6863), 509–513 (2001).
58. G. Vampa, T. J. Hammond, N. Thiré, B. E. Schmidt, F. Légaré, C. R. McDonald, T. Brabec, and P. B. Corkum, "Linking high harmonics from gases and solids," Nature **522**(7557), 462–464 (2015).
59. M. Garg and J. K. Quamara, "FTIR analysis of high energy heavy ion irradiated kapton-H polyimide," (2007).
60. Y.-K. Xu, M.-S. Zhan, and K. Wang, "Structure and properties of polyimide films during a far-infrared-induced imidization process," J. Polym. Sci. Part B: Polym. Phys. **42**(13), 2490–2501 (2004).
61. K. P. Adhi, R. L. Owings, T. A. Railkar, W. D. Brown, and A. P. Malshe, "Chemical modifications in femtosecond ultraviolet (248 nm) excimer laser radiation-processed polyimide," Appl. Surf. Sci. **225**(1-4), 324–331 (2004).
62. C. Qu, J. Hu, X. Liu, Z. Li, and Y. Ding, "Morphology and Mechanical Properties of Polyimide Films: The Effects of UV Irradiation on Microscale Surface," Mater. (Basel) **10**(11), 1329 (2017).

4.2 Controlling Surface Adhesion Using Femtosecond-Laser-Induced Blister Patterns

Surface adhesion of back-illuminated ultrafast laser-treated polymers

Deepak L. N. Kallepalli,* Alan T. K. Godfrey, Jesse Ratté, André Staudte, Chunmei Zhang, and P. B. Corkum†
Joint Attosecond Science Laboratory, University of Ottawa and the National Research Council of Canada, 100 Sussex Dr., Ottawa, Canada K1N 6N5

(Received 31 August 2020; revised 16 February 2021; accepted 6 April 2021; published 28 April 2021)

We report a decreased surface wettability when polymer films on a glass substrate are treated by ultrafast laser pulses in a back-illumination geometry. We propose that back illumination through the substrate confines chemical changes beneath the surface of polymer films, leaving the surface blistered but chemically intact. To confirm this hypothesis, we measure the phase contrast of the polymer when imaged with a focused ion beam. We observe a void at the polymer-quartz interface that results from the expansion of an ultrafast laser-induced plasma. A modified polymer layer surrounds the void, but otherwise the film seems unmodified. We also use x-ray photoelectron spectroscopy to confirm that there is no chemical change to the surface. When patterned with partially overlapping blisters, our polymer surface shows increased hydrophobicity. The increased hydrophobicity of back-illuminated surfaces can only result from the morphological change. This contrasts with the combined chemical and morphological changes of the polymer surface caused by a front-illumination geometry.

DOI: 10.1103/PhysRevMaterials.5.045201

I. INTRODUCTION

The use of ultrafast pulses for local energy deposition in materials has several applications in 3D optical data storage [1,2], integrated optics [3–5], and laser-induced forward transfer (LIFT) [6–11]. In contaminant-free LIFT, the nonlinear interaction of an ultrafast pulse with the polymer film (often called a dynamic release layer) between a glass substrate and transfer material ensures the confinement of the energy deposition to the glass-polymer interface, leaving the transfer material chemically intact [12]. When an ultrafast femtosecond pulse interacts with a polymer film at the interface, it creates a localized hot plasma [13,14]. The hot plasma expands, leading to formation of a blister.

The adhesive properties of materials are altered by both front and back illumination. However, front illumination induces both morphological and chemical changes to the surface [15,16]. Front-illuminated surfaces can lead to hydrophilic, hydrophobic, and superhydrophobic states in addition to chemical changes [17–25]. Thus, changes to surface adhesion are often attributed to an interplay between surface chemistry and morphology, in particular for front-illuminated surfaces. To the best of our knowledge there have been no reports of changes to adhesion induced by an ultrafast laser in a back-illuminated geometry.

We report an increase in hydrophobicity of a polyimide film induced by an ultrafast laser in a back-illumination geometry. Using focused ion beam (FIB) microscope and x-ray photoelectron spectroscopy (XPS), we find that these changes are strictly morphological at the interface of the film. This observation is consistent with our previous spectroscopic measurements, which showed that laser-induced chemical changes are confined to the glass-polyimide interface [12]. We confirm the increased hydrophobicity by measuring the contact angle of water droplets on laser-modified surfaces, and we find that the contact angle increases with laser fluence.

II. EXPERIMENT

We prepared polyimide films on two different substrates: (1) on #1.5 Fisherbrand borosilicate glass coverslips (for FIB and contact angle measurements) and (2) on 500 μm fused silica discs for our XPS measurements. Both were rinsed with acetone, isopropanol, and deionized water to remove contaminants and dried on a hotplate. Polyimide films were made using PI-2525 (for thicker films) and PI-2555 (for thinner films $\leqslant$1.4 μm) precursors from HD Microsystems following the recommended spin curves and baking conditions.

We used a Ti:Sapphire laser (Coherent RegA 9040) producing pulses of 50-fs duration at a central wavelength of 800 nm. The laser pulse energy was controlled using a motorized half-wave plate followed by a polarizing beam-splitter cube. The laser beam was focused using microscope objectives (10×0.2 NA, 20×0.4 NA) mounted into a vertical motor stage (PI M-112) with a travel range of 25 mm for adjusting the focal spot on the sample. Since polyimide is transparent at a wavelength of 800 nm (1.55 eV), any modification is due to nonlinear absorption (Supplemental Material Sec. I [26]).

We mounted polyimide-on-glass coverslips onto a five-axis piezo nanoprecision stage (PI) assembled on top of a microprecision horizontal XY stage (MICOS MS-4). The nanoprecision stage was used for fine adjustment of the focal position. The laser was focused through the glass substrate onto the glass-polymer interface (back-illumination geometry). A dichroic mirror was used before the microscope objective in a coaxial geometry, allowing a small portion of

*XXXXXXXXXXXXXXXXX
†XXXXXXXXXXXXXXXXX

2475-9953/2021/5(4)/045201(7)

the focused laser light to back-reflect from the sample, recollimate through the objective, and travel to an imaging line for *in situ* laser spot monitoring. Coupling in white light and changing the position of the objective also allows for *in situ* white-light microscopy. We used this to find the optimal position of the laser focus on the sample, by firing pulses with energies near the damage threshold while adjusting the position of the focal spot. A schematic of our experimental setup and characterization details are in Supplemental Material Secs. II and III [26].

III. RESULTS AND DISCUSSION

The self-focusing threshold in the substrate is P=2.8 MW, and for a 50-fs pulse this corresponds to 140 nJ energy. Despite the losses in the substrate, the remaining energy delivered to the polymer film at the interface leads to a blister formation. Increasing the energy, especially for a low NA lens, will lead to continuum generation and breakdown in the substrate, in addition to blister formation [13]. Here, we accounted for the substrate-mediated absorption in glass using the lawn-mower model published in our earlier work [13,14]. In this section, we report pulse energies delivered through the substrate accounting for the nonlinear absorption in the substrate. The minimum number of photons required for modification in polymer is 2 (see absorption spectrum of pristine polymer in Supplemental Material Sec. I [26]).

We carried out laser irradiation experiments using thin polyimide films on glass and examined the changes in chemical composition and morphology at the glass-polymer interface and the surface. Contaminant-free LIFT requires confinement of chemical changes near the glass-polyimide interface while the polymer surface undergoes a morphological change through blister formation. Since polymers possess lower surface energies (∼40 mJ/m^2 for polyimide) compared to metals (∼J/m^2), we chose a test polymer and carried out studies on chemical composition and morphology [27–29]. We used FIB and XPS measurements to study the morphology and chemical composition. We show hydrophobicity test results on laser-irradiated polyimide surfaces to demonstrate its relevance to the LIFT technique and other applications.

A. Chemical composition of the surface

In this section, we present results from FIB measurements that image changes near the interface, followed by XPS measurements. For FIB analysis, we fabricated a series of individual blisters with ≈130 nJ of pulse energy focused by a 0.4 NA microscope objective reaching an intensity of 5.3 × 10^{13} W/cm^2 at the interface. All laser-irradiation experiments were carried out by focusing pulses at the glass-polyimide interface.

We used focused gallium and helium ion beams to dissect and image the interior of blisters, respectively, as shown in Fig. 1(a). The dissected blister showed a thin embedded layer of modification underneath the unmodified polymer in the blister. The image contrast indicates that only a very thin layer on the underside of the blister has undergone chemical transformation. In addition, a void is present beneath the

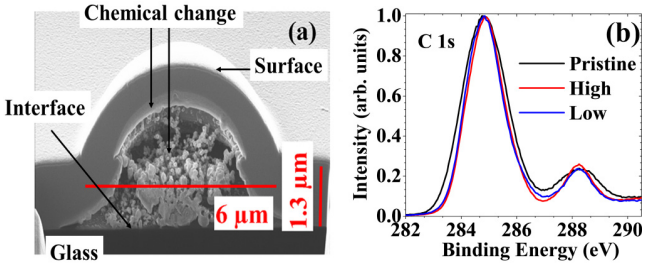

FIG. 1. (a) FIB image of a blister fabricated with ∼130 nJ pulse energy focused by a 0.4 NA objective (∼2.8 J/cm^2). The height and diameter of the blister are 1.6 μm and 6 μm, respectively. Glass (substrate), interface, and unmodified surface are indicated with black arrows. The chemical changes are apparent in the different brightness compared to the surrounding material. (b) XPS of the carbon (1s) absorption edge for pristine (black) and laser-modified polyimide (red and blue). The laser-modified polyimide was subjected to a low dose of ∼1.8 J/cm^2 (blue curve) and a high dose of ∼4.7 J/cm^2 (red curve). Normalized intensity for 284.85 eV peak is plotted on the Y axis for comparison.

embedded layer. It is partially filled with molten material that has solidified.

This observation is consistent with what we expect. When an ultrafast laser pulse is focused into the material interface, it forms a plasma [13]. At the temperature that we achieve, the material vaporizes and undergoes a chemical change creating the embedded layer and the solidified material on glass, as seen in Fig. 1(a). Earlier reports involving blister formation in thin films of polyimide and titanium using 355 nm and 800 nm laser wavelengths lack the direct experimental evidence of confined chemical changes at the interface [5,11,30,31]. Our observation of confined chemical changes provides direct experimental evidence for confinement of chemical changes only at the interface induced by an ultrafast laser [5–8,30–42].

XPS is a surface characterization technique with a typical sampling depth of 7.5 nm [43,44]. Hence, we chose XPS to study any chemical changes that occurred to the front surface in back-illuminated experiments on polyimide. Conventional spectroscopic techniques, such as absorption and fluorescence, are not useful in studying local changes occurring at specific depths as these measurements result in a combined spectrum of pristine polymer surface, modified polymer at the interface, and glass [12].

In our earlier report, we recorded local photoluminescence changes using confocal micro-Raman and fluorescence techniques [12]. We observed photoluminescence changes more confined to the edges than the center of these individual blisters when excited at different wavelengths using a 0.9 NA objective. However, this technique cannot resolve the modified polymer at the interface from the film surface, due to the limited depth resolution (axial resolution of 1.5–2.3 μm). Therefore, we chose XPS characterization for this study as x rays offer better depth resolution compared to these techniques. XPS measurements provided isolated information about the chemistry of the film surface.

Since XPS characterization requires a large, patterned surface area, we patterned 2 mm×3 mm areas on 1.3 μm thin

films of PI-2555 by overlapping the individual blisters in back-illumination geometry. Two regions were modified with ~4.7 J/cm^2 (high irradiation dose) and ~1.8 J/cm^2 (low irradiation dose). The calculation of energy densities and irradiation details can be found in Supplemental Material Secs. IV and V [26].

Figure 1(b) shows the carbon (1s) absorption edge for pristine and laser-irradiated samples (black, red, and blue for high and low irradiation dosed polyimide). For pristine polyimide, the carbon absorption edge [black curve in Fig. 1(b)] consists of two peaks at 288.35 eV and 284.85 eV corresponding to C=O and C-C/C-H, respectively. The XPS spectra recorded for laser-modified polyimide surfaces [red and blue curves in Fig. 1(b)] were corrected for energy shifts due to charge compensation (≈2 eV) and plotted to compare with pristine polyimide [24]. There were no peak shifts and/or new peaks observed, indicating that the surface is chemically intact after the laser treatment. We also compared the intensity ratios of peaks at 284.85 eV (C-C/C-H) and 288.35 eV (C=O) for laser-modified polyimide samples (blue and red curves) with the pristine polyimide. Since the morphology of the surface is altered after the laser treatment, the resulting number of photoelectrons generated also changes. Hence, intensity ratios of peaks are compared rather than their individual intensities [45]. The normalized intensity ratios of peaks for laser-modified samples were nearly equal when compared with the pristine polyimide (nearly 4). From this, we conclude that the carbon bonds at the surface of film were not altered. We also compared O(1s) and N(1s) envelopes for a laser modified with pristine polyimide and did not observe any peaks shift or any significant changes in the intensity ratios (details are in Supplemental Material Sec. V [26]), further confirming that the surface chemistry was not altered.

B. Role of surface morphology on adhesion

Having determined that back-illuminated ultrafast laser-treated polymers leave the chemical composition of the polymer intact, we next turn to the role of surface morphology (roughness ratio) on surface adhesion. It is known that surface adhesion is influenced by both chemistry and morphology. When a water droplet is placed on a flat surface (zero roughness), it shows a contact angle known as Young's angle (Θ_0) illustrated in Fig. 2(a). The contact angle results from a balanced surface force between three interfaces: air-solid, solid-liquid, and liquid-air.

The initial chemical state of a polymer surface depends on the baking conditions (such as temperature or time). When polymers are baked for a long time or at higher temperatures, hydrophilic groups are removed resulting in enhanced hydrophobicity. Figures 2(b) and 2(c) show the contact angles of 110°(±0.5°) and 82°(±0.5°) for water droplets placed on polyimide thin films, which were prepared by baking at 300 °C and 180 °C for 30 mins, respectively.

When surface texture is added to any substrate in back illumination, it increases its initial hydrophilic or hydrophobic state. Since our experiments are carried out in back-illumination geometry on polymers prepared at 300 °C, the addition of surface texture enhances hydrophobicity as shown in Fig. 2(d). In experiments, the surface texture

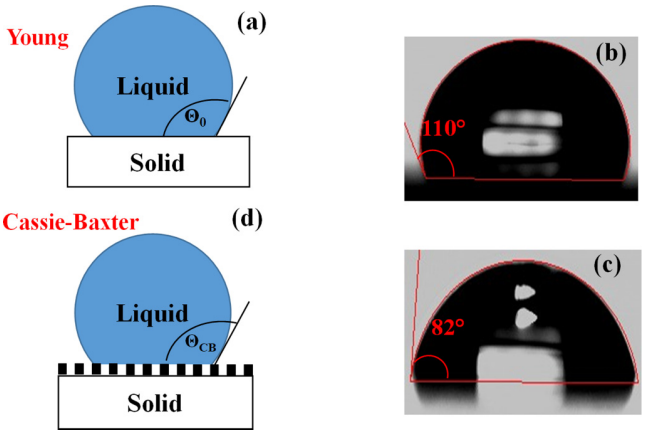

FIG. 2. (a) A flat substrate showing Young's contact angle (Θ_0). (b) and (c) show contact angles of 110° (±0.5°) and 82° (±0.5°) of pristine polyimide films baked at 300 °C and 180 °C for 30 mins. (d) Young's contact angle (Θ_0) transforms to Cassie-Baxter angle (Θ_{CB}) for hydrophobic surfaces upon addition of surface texture. Additional surface texture increases its initial hydrophobicity ($\Theta_{CB} > \Theta_0$).

induced by an ultrafast laser is pointlike due to the intensity distribution of the pulse (blisters which are pointlike objects), in contrast to the uniform surface texture (periodically placed pillars), shown in Fig. 2(d).

Since a 1 μL water droplet requires a ~mm^2 surface area for a hydrophobicity measurement, we patterned surface areas of 2 mm×3 mm under a 10^{-3} Torr vacuum (to avoid interaction with atmospheric oxygen [24]). We patterned surfaces with 1, 2, and 4 shots per focal spot diameter on average (N), by varying scan speed (v), laser repetition rate (L), and line spacing (ΔX) (details in Supplemental Material Sec. VI). AFM topographies of the patterned surfaces are shown in Fig. 3. In AFM related studies, the average surface roughness (R) is defined as the arithmetic mean of the absolute values of the roughness profile ordinates. In our case, the pristine polyimide had an average surface roughness (R) of 0.2 nm and a surface height of 8 nm. Patterned surfaces with $N = 1$, 2, and 4 had average roughnesses of 225 nm, 125 nm, and 59 nm with surface heights of 1.2 μm, 800 nm, and 350 nm, respectively. The maximum patterned surface heights for $N = 4$ and 2 were less than the maximum heights for $N = 1$. The energy (E) used to pattern these surfaces was varied with N to avoid rupture of the film.

If laser-induced surface texture is added to an initially flat surface in back illumination, it changes only the adhesive properties (preserving the surface chemistry) by minimizing the contact area fraction via pointlike blister formation [13]. When large surface areas are patterned using an ultrafast laser, the laser-induced surface texture contains complex rough patterns (in 3D) causing a locally increased hydrophobicity due to an increase in the density of air pockets. Hence, the wettability (measured by the liquid contact area fraction) exhibited by such surfaces depends directly on the nature of the laser-induced surface texture that includes the properties of blisters (diameter, height, line spacing, overlap in scan direction, and the shape).

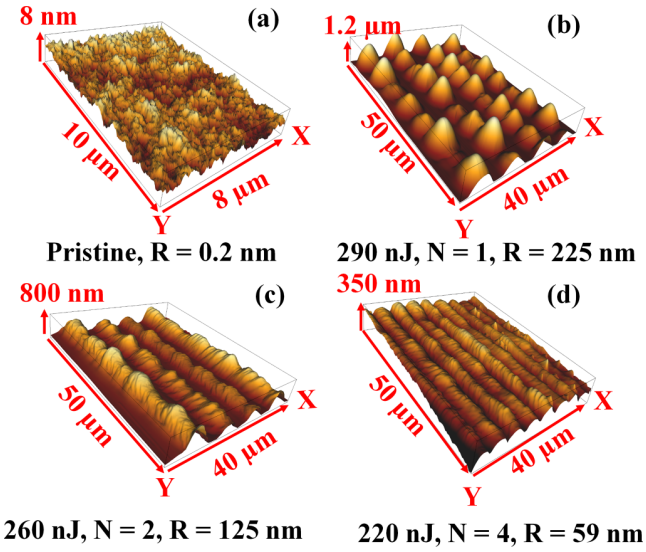

FIG. 3. (a) AFM image of a pristine polyimide surface with average roughness of 0.2 nm with a maximum surface height of 8 nm. Surface topographies shown in (b), (c), and (d) are laser-patterned surfaces of polyimide fabricated with different energies (E), no. of shots (N), average surface roughness (R), at line spacings (ΔX) of 10 μm, 9 μm, and 5 μm, respectively.

The addition of laser-induced surface texture to an existing hydrophobic surface [Fig. 4(a)] in back illumination transforms it into a superhydrophobic surface by minimizing the liquid contact area fraction (f) given by the Cassie-Baxter equation $\cos(\Theta_{CB}) = f(1 + r\cos(\Theta_0)) - 1$ [46] [equation (17) in Ref. [46]], where r is the ratio of the actual surface to the geometric surface. The liquid contact area fraction (f) is a dimensionless number (unlike the average surface roughness measured by AFM) and is defined as the ratio of the textured surface area in contact with the liquid droplet and the flat surface before texturing [46].

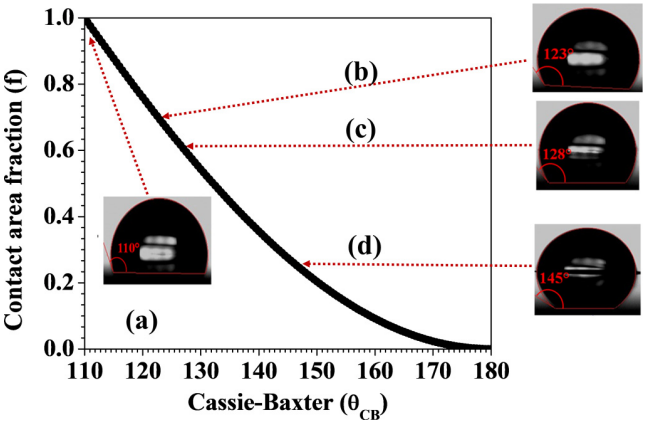

FIG. 4. Plot of liquid contact area fraction (f) dependence on the Cassie-Baxter angle (Θ_{CB}). The curve was obtained under the assumption of our initial polyimide surfaces to be flat. The accuracy of the goniometer was $\pm 0.5^\circ$. The acquisition software automatically added the contour shown in red and provided the contact angles. Water contact angle measurement of (a) pristine polyimide ($110^\circ \pm 0.5^\circ$). Here, both the Cassie-Baxter and Young's contact angle are equal ($\Theta_{CB} = \Theta_0$). Laser-patterned surface with (b) $N = 1$ ($123^\circ \pm 0.5^\circ$), (c) $N = 2$ ($128^\circ \pm 0.5^\circ$), and (d) $N = 4$ ($145^\circ \pm 0.5^\circ$).

To estimate the role of properties of blisters on the liquid contact area fraction (f), we define the laser shot density per unit surface (S) as $S = \frac{L}{v \cdot \Delta X}$. Here, L and v together provide the total number of laser shots along the scan direction, and ΔX in the orthogonal direction. The parameters (L, v, ΔX) for the laser-patterned surfaces of $N = 1$, 2, and 4 shots per focal spot are (500 Hz, 3 mm/s, 10 μm), (500 Hz, 0.5 mm/s, 9 μm), and (2 kHz, 1 mm/s, 5 μm), respectively. From this, we calculated the laser shot densities for the laser-patterned surfaces of $N = 1$, 2, and 4 shots/spot to be 0.017 shots/μm^2, 0.11 shots/μm^2, and 0.4 shots/μm^2, respectively. These calculations showed that the laser-patterned surface with $N = 4$ shots/spot had the maximum laser shot density per unit surface (S) and had the maximum contact angle (145°) shown in Fig. 4(d).

We note that the shape of the nanoscale structure of the blisters also plays a key role. Complex rough patterns such as triangular and fractal-like structures were shown to be superhydrophobic [47]. In the overlapped regions of the laser shots, we observed complex rough patterns involving substructures for each of these individual structures (details are in Supplemental Material Sec. VIII [26]). From AFM line scan profiles (shown in Supplemental Material Sec. VIII [26]), we found that the one-shot surface had smooth structures compared to two-shot and four-shot surfaces which had nanoscale substructures (fractal-like spikes on blisters). The presence of these substructures, caused by increasing the laser shot density per surface, plays a major role in minimizing the overall contact area fraction leading to increased contact angles.

Since the characterization of such complex surfaces involving multiscale roughness is difficult, we indirectly estimated the liquid contact area fractions (f) from the experimental values of Θ_0 and Θ_{CB} (details are in Supplemental Material Sec. VII [26]) and indicated them in Fig. 4. This formula is valid for a surface that is flat and chemically homogeneous. The angle Θ_0 (Young's angle) corresponds to the contact angle shown by a water droplet, which is 110° for pristine surfaces of polyimide. Since we used the same pristine polyimide surface for laser-texturing experiments, we set Θ_0 to be 110° (as reference) and obtained the contact area fraction (f) curve for various contact angles greater than 110°, owing to the fact that the addition of laser-induced surface texture increases contact angle of a surface. The calculated contact area fractions are mapped to the measured contact angles in Fig. 4.

Thus, the addition of the laser-induced surface texture in back illumination creates structures and substructures, minimizing the contact area fraction (f). The smaller the contact area fraction, the higher the air pocket density that gives rise to the superhydrophobic behavior. Figure 4(b) shows a contact angle of 123° ($\pm 0.5^\circ$) for a laser-patterned surface with $N = 1$ at 290 nJ energy ($\sim$6.2 J/cm^2) . The increase in contact angle by 13° is due to the increased surface texture caused by the formation of blisters. Since the film thickness was 1.3 μm, we lowered the energy to avoid rupturing of the film [13]. We decreased the energy to 260 nJ ($\sim$5.6 J/cm^2) for $N = 2$ and 220 nJ ($\sim$4.7 J/cm^2) for $N = 4$. These surfaces showed contact angles of 128° ($\pm 0.5^\circ$) and 145° ($\pm 0.5^\circ$) [Figs. 4(c)

and 4(d)], due to creation of both structures and substructures. The same experiment could be carried out at lower energy, say 220 nJ ($\sim$4.7 J/cm^2), but in this case, the diameter of blisters is smaller. Thus, a smaller pitch would be required to overlap blisters.

These results clearly indicate that the increase in hydrophobicity in polymers when irradiated in back illumination is due to the creation of complex surfaces (involving substructures along with micro/nanostructures, similar to fractal-type structures in Ref. [47]). Although the surface roughness, as measured by an AFM, for the patterned surface of $N = 1$ was higher than that of $N = 2$, the density of air pockets $N = 1$ was slightly lower than for $N = 2$ due to a change in pitch. The pitch for $N = 1$ and $N = 2$ surfaces were 10 μm and 9 μm, respectively. The higher the pitch, the lower the surface structural density and thereby the density of air pockets. For the patterned surface of $N = 4$, the density of air pockets was even higher when the pitch was reduced to half ($\Delta X = 5$ μm). These quantitative results clearly indicate that the adhesive properties of a polymer surface can be controlled by adding a texture in back illumination.

Based on our surface studies and related contact angle measurements, we propose a two-step LIFT procedure (considering the initial surface to be hydrophobic) to obtain a contaminant-free transfer of sensitive materials such as cells and organelles. In the first step, we would add only a texture to the surface in back illumination (preserving the surface chemistry) to minimize the surface adhesion. In the second step, we would irradiate the transformed surface with another laser pulse for a gentle desorption of the sensitive materials from the surface.

IV. CONCLUSIONS

We studied ultrafast-laser-induced photochemical and morphological changes in polyimide thin films using FIB, XPS, AFM, and water contact angle measurements. Upon nonlinear interaction of ultrafast light with a polyimide film at the interface, the thin film was locally transformed and delaminated from the substrate, leading to formation of a blister and an embedded modified layer with a different phase contrast beneath the film. Both XPS and FIB measurements show that the chemical changes are confined to the glass-polyimide interface. The morphological change due to blister formation is evident through FIB measurements. Blister-patterned surfaces show increased contact angle of water droplets due to increased surface texture and therefore, increased hydrophobicity. By isolating morphological changes from chemical modification, we show that the addition of surface texture increases hydrophobicity and thereby decreases surface adhesion. We have demonstrated that back-illuminated surfaces preserve the surface chemistry and the resulting adhesion arises only from morphological changes.

The reduced adhesion that we have observed may be useful for contaminant-free LIFT since laser-induced chemical changes can be confined near the glass-polymer interface while morphological changes can help materials to gently desorb. In addition, confining the region of chemical change is essential for 3D optical data storage based on laser-induced fluorescence from polymers while isolated morphological changes may help create water repellent surfaces for applications in de-icing and defrosting.

ACKNOWLEDGMENTS

All authors acknowledge financial support from Natural Sciences and Engineering Research Council of Canada (NSERC) Engage (Grant No. EGP523138-18) and Discovery (Grant No. RGPIN-2019-04603), Ontario Centres of Excellence Voucher for innovation and Productivity I Program (Grant No. 29119), the Joint Centre for Extreme Photonics (JCEP) of the University of Ottawa and the National Research Council, and Fluidigm Canada, Markham, Ontario. Alan T. K. Godfrey acknowledges financial support from NSERC's Postgraduate Scholarship–Doctoral and University of Ottawa's Excellence Scholarship. We acknowledge Dr. Maohui Chen for training in atomic force microscopy, Dr. Choloong Hahn for FIB measurements, Tony Olivieri for training related to polyimide film fabrication, and Dr. Alexander Sander for acquiring XPS spectra. We acknowledge Dr. Zygmunt J. Jakubek for helping us to acquire absorption spectra for pristine and laser-modified polyimide (Supplemental Material [26]). We acknowledge the help received from Charbel Atallah, Ph.D. student, Department of Chemical and Biological Engineering, University of Ottawa for water drop contact angle measurements. We acknowledge help received from laboratory engineer Yu-Hsuan Wang.

[1] D. L. N. Kallepalli, A. M. Alshehri, D. T. Marquez, L. Andrzejewski, J. C. Scaiano, and R. Bhardwaj, Ultra-high density optical data storage in common transparent plastics, Sci. Rep. **6**, 26163 (2016).

[2] D. L. N. Kallepalli, R. Kuladeep, S. V. Rao, and D. N. Rao, Luminescent microstructures in bulk and thin films of PMMA, PDMS, PVA, and PS fabricated using femtosecond direct writing technique, Chem. Phys. Lett. **503**, 57 (2011).

[3] S. Nolte, M. Will, J. Burghoff, and A. Tuennermann, Femtosecond waveguide writing: A new avenue to three-dimensional integrated optics, Appl. Phys. A **77**, 109 (2003).

[4] Y. Bellouard, A. A. Said, and P. Bado, Integrating optics and micro-mechanics in a single substrate: A step toward monolithic integration in fused silica, Opt. Express **13**, 6635 (2005).

[5] N. T. Kattamis, P. E. Purnick, R. Weiss, and C. B. Arnold, Thick film laser induced forward transfer for deposition of thermally and mechanically sensitive materials, Appl. Phys. Lett. **91**, 171120 (2007).

[6] M. S. Brown, N. T. Kattamis, and C. B. Arnold, Time-resolved study of polyimide absorption layers for blister-actuated laser-induced forward transfer, J. Appl. Phys. **107**, 083103 (2010).

[7] M. S. Brown, C. F. Brasz, Y. Ventikos, and C. B. Arnold, Impulsively actuated jets from thin liquid films for high-resolution printing applications, J. Fluid Mech. **709**, 341 (2012).

[8] N. T. Kattamis, M. S. Brown, and C. B. Arnold, Finite element analysis of blister formation in laser-induced forward transfer, J. Mater. Res. **26**, 2438 (2011).

[9] J. P. McDonald, V. R. Mistry, K. E. Ray, S. M. Yalisove, J. A. Nees, and N. R. Moody, Femtosecond-laser-induced delamination and blister formation in thermal oxide films on silicon (100), Appl. Phys. Lett. **88**, 153121 (2006).

[10] J. R. Serranoand D. G. Cahill, Laser-induced blistering of thin SiO_2 on Si, Microscale Thermophys. Eng. **9**, 155 (2005).

[11] N. T. Goodfriend, S. V. Starinskiy, O. A. Nerushev, N. M. Bulgakova, A. V. Bulgakov, and E. E. B. Campbell, Laser pulse duration dependence of blister formation on back-radiated Ti thin films for BB-LIFT, Appl. Phys. A **122**, 154 (2016).

[12] D. L. N. Kallepalli, A. T. K. Godfrey, J. Walia, F. Variola, A. Staudte, C. Zhang, Z. J. Jakubek, and P. B. Corkum, Multiphoton laser-induced confined chemical changes in polymer films, Opt. Express **28**, 11267 (2020).

[13] A. T. K. Godfrey, D. L. N. Kallepalli, J. Ratté, C. Zhang, and P. B. Corkum, Femtosecond-Laser-Induced Nanoscale Blisters in Polyimide Thin Films through Nonlinear Absorption, Phys. Rev. Appl. **14**, 044057 (2020).

[14] D. M. Rayner, A. Naumov, and P. B. Corkum, Ultrashort pulse non-linear optical absorption in transparent media, Opt. Express **13**, 3208 (2005).

[15] M. Forster, W. Kautek, N. Faure, E. Audouard, and R. Stoian, Periodic nanoscale structures on polyimide surfaces generated by temporally tailored femtosecond laser pulses, Phys. Chem. Chem. Phys. **13**, 4155 (2011).

[16] C. De Marco, S. M. Eaton, R. Suriano, S. Turri, M. Levi, R. Ramponi, G. Cerullo, and R. Osellame, Surface properties of femtosecond laser ablated PMMA, ACS Appl. Mater. Interfaces **2**, 2377 (2010).

[17] C. Cheng, S. Wang, J. Wu, Y. Yu, R. Li, S. Eda, J. Chen, G. Feng, B. Lawrie, and A. Hu, Bisphenol a sensors on polyimide fabricated by laser direct writing for onsite river water monitoring at attomolar concentration, ACS Appl. Mater. Interfaces **8**, 17784 (2016).

[18] M. Tang, Laser ablation of metal substrates for superhydrophobic effect, J. Laser Micro/Nanoeng. **6**, 6 (2011).

[19] J. Long, P. Fan, D. Gong, D. Jiang, H. Zhang, L. Li, and M. Zhong, Superhydrophobic surfaces fabricated by femtosecond laser with tunable water adhesion: From lotus leaf to rose petal, ACS Appl. Mater. Interfaces **7**, 9858 (2015).

[20] S. Moradi, S. Kamal, P. Englezos, and S. G. Hatzikiriakos, Femtosecond laser irradiation of metallic surfaces: Effects of laser parameters on superhydrophobicity, Nanotechnology **24**, 415302 (2013).

[21] U. Hermens, S. V. Kirner, C. Emonts, P. Comanns, E. Skoulas, A. Mimidis, H. Mescheder, K. Winands, J. Krüger, E. Stratakis, and J. Bonse, Mimicking lizard-like surface structures upon ultrashort laser pulse irradiation of inorganic materials, Appl. Surf. Sci. **418**, 499 (2017).

[22] B. E. J. Lee, H. Exir, A. Weck, and K. Grandfield, Characterization and evaluation of femtosecond laser-induced sub-micron periodic structures generated on titanium to improve osseointegration of implants, Appl. Surf. Sci. **441**, 1034 (2018).

[23] M. Zuo, T. Takeichi, A. Matsumoto, and K. Tsutsumi, Surface characterization of polyimide films, Colloid Polym. Sci. **276**, 555 (1998).

[24] Z. K. Wang, H. Y. Zheng, C. P. Lim, and Y. C. Lam, Polymer hydrophilicity and hydrophobicity induced by femtosecond laser direct irradiation, Appl. Phys. Lett. **95**, 111110 (2009).

[25] A. M. Alshehri, S. Hadjiantoniou, R. J. Hickey, Z. Al-Rekabi, J. L. Harden, A. E. Pelling, and V. R. Bhardwaj, Selective cell adhesion on femtosecond laser-microstructured polydimethylsiloxane, Biomed. Mater. **11**, 015014 (2016).

[26] See Supplemental Material at http://link.aps.org/supplemental/10.1103/PhysRevMaterials.5.045201 for the absorption spectrum of pristine polyimide in Fig. S1 indicated no linear absorption in the visible region from 450 nm to 800 nm. Therefore, any absorption at 800 nm requires a minimum of 2 photons to be absorbed for modification.

[27] A. Kozbial, Z. Li, C. Conaway, R. McGinley, S. Dhingra, V. Vahdat, F. Zhou, B. D'Urso, H. Liu, and L. Li, Study on the surface energy of graphene by contact angle measurements, Langmuir **30**, 8598 (2014).

[28] T.-S. Wong, S. H. Kang, S. K. Y. Tang, E. J. Smythe, B. D. Hatton, A. Grinthal, and J. Aizenberg, Bioinspired self-repairing slippery surfaces with pressure-stable omniphobicity, Nature (London) **477**, 443 (2011).

[29] W. Zheng, Surface wetting characteristics of rubbed polyimide thin films, in *Polymer Thin Films*, edited by A. A. Hashim (IntechOpen Limited, Rijeka, Croatia, 2010).

[30] R. Fardel, M. Nagel, F. Nüesch, T. Lippert, and A. Wokaun, Fabrication of organic light-emitting diode pixels by laser-assisted forward transfer, Appl. Phys. Lett. **91**, 061103 (2007).

[31] D. P. Banks, K. Kaur, R. Gazia, R. Fardel, M. Nagel, T. Lippert, and R. W. Eason, Triazene photopolymer dynamic release layer-assisted femtosecond laser-induced forward transfer with an active carrier substrate, Europhys. Lett. **83**, 38003 (2008).

[32] P. Delaporte and A.-P. Alloncle, Laser-induced forward transfer: A high resolution additive manufacturing technology, Opt. Laser Technol. **78**, 33 (2016).

[33] N. R. Schiele, D. T. Corr, Y. Huang, N. A. Raof, Y. Xie, and D. B. Chrisey, Laser-based direct-write techniques for cell printing, Biofabrication **2**, 032001 (2010).

[34] C. B. Arnold, P. Serra, and A. Piqué, Laser direct-write techniques for printing of complex materials, MRS Bull. **32**, 23 (2007).

[35] G. Jing, Y. Wang, T. Zhou, S. F. Perry, M. T. Grimes, and S. Tatic-Lucic, Cell patterning using molecular vapor deposition of self-assembled monolayers and lift-off technique, Acta Biomater. **7**, 1094 (2011).

[36] M. Gruene, A. Deiwick, L. Koch, S. Schlie, C. Unger, N. Hofmann, I. Bernemann, B. Glasmacher, and B. Chichkov, Laser printing of stem cells for biofabrication of scaffold-free autologous grafts, Tissue Eng. Part C: Methods **17**, 79 (2010).

[37] L. Koch, S. Kuhn, H. Sorg, M. Gruene, S. Schlie, R. Gaebel, B. Polchow, K. Reimers, S. Stoelting, N. Ma, P. M. Vogt, G. Steinhoff, and B. Chichkov, Laser printing of skin cells and human stem cells, Tissue Eng. Part C: Methods **16**, 847 (2009).

[38] A. Palla-Papavlu, V. Dinca, C. Luculescu, J. Shaw-Stewart, M. Nagel, T. Lippert, and M. Dinescu, Laser induced forward transfer of soft materials, J. Opt. **12**, 124014 (2010).

[39] P. Serra, M. Colina, J. M. Fernández-Pradas, L. Sevilla, and J. L. Morenza, Preparation of functional DNA microarrays

through laser-induced forward transfer, Appl. Phys. Lett. **85**, 1639 (2004).

[40] B. Hopp, T. Smausz, Z. Antal, N. Kresz, Z. Bor, and D. Chrisey, Absorbing film assisted laser induced forward transfer of fungi (Trichoderma conidia), J. Appl. Phys. **96**, 3478 (2004).

[41] J. Barron, P. Wu, H. Ladouceur, and B. Ringeisen, Biological laser printing: A novel technique for creating heterogeneous 3-dimensional cell patterns, Biomed. Microdev. **6**, 139 (2004).

[42] J. Xu, J. Liu, D. Cui, M. Gerhold, A. Y. Wang, M. Nagel, and T. K. Lippert, Laser-assisted forward transfer of multi-spectral nanocrystal quantum dot emitters, Nanotechnology **18**, 025403 (2006).

[43] C. M. Chan and L.-T. Weng, Surface characterization of polymer blends by XPS and ToF-SIMS, Materials **9**, 655 (2016).

[44] D. Zeng, K. Yung, and C. Xie, Xps investigation of the chemical characteristics of kapton films ablated by a pulsed TEA CO_2 laser, Surf. Coat. Technol. **153**, 210 (2002).

[45] http://www.casaxps.com/help_manual/manual_updates/Basics_Quantification_of_XPS_Spectra.pdf.

[46] B. Wang, Y. Zhang, L. Shi, J. Li, and Z. Guo, Advances in the theory of superhydrophobic surfaces, J. Mater. Chem. **22**, 20112 (2012).

[47] Q. Zheng and C. Lü, Size effects of surface roughness to superhydrophobicity, Proc. IUTAM **10**, 462 (2014).

Surface adhesion of back-illuminated ultrafast laser-treated polymers: Supplemental

Deepak L. N. Kallepalli*, Alan T. K. Godfrey, Jesse Ratté, André Staudte, Chunmei Zhang, and P. B. Corkum*

Joint Attosecond Science Laboratory, University of Ottawa and National Research Council of Canada, 100 Sussex Dr., Ottawa K1N 6N5, Canada

I. *Absorption studies:*

We recorded absorption spectra for pristine and laser-patterned polyimide as shown in **Fig. S1** using an Agilent Cary 5000 UV-vis-NIR spectrophotometer in transmission mode. The polyimide was patterned in back-illumination geometry using 350 nJ pulse energy with a 0.2NA focussing, a fluence of ~2J/cm^2 and N=2 shots per focal spot. This resulted in blisters in the laser modified film of 240 nm height and 4 μm in diameter.

The absorption spectrum of pristine polyimide indicated no linear absorption in the visible region from 450-800 nm; the absorption below 400 nm can be attributed to $\pi \rightarrow \pi^*$ transitions within various groups containing benzene rings [1-4]. From the absorption spectrum of pristine polyimide, the minimum no. of 800 nm photons required for modification is 2. The absorption spectrum for laser-modified polyimide is shown for comparison. The interaction with the laser increases the absorption across the visible spectrum by approximately a factor of three compared to the pristine polyimide. Since we recorded the absorption spectra in transmission mode, the changes in absorption are from the unmodified polymer surface, modified polymer at the interface, and glass.

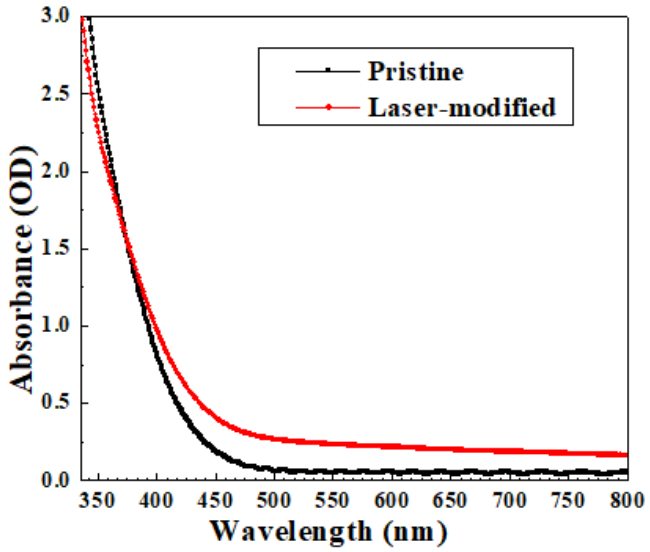

Fig. S1: Absorption spectra of pristine and laser-modified polyimide (thickness of 3.5 μm on a borosilicate coverslip).

II. Schematic of experimental setup:

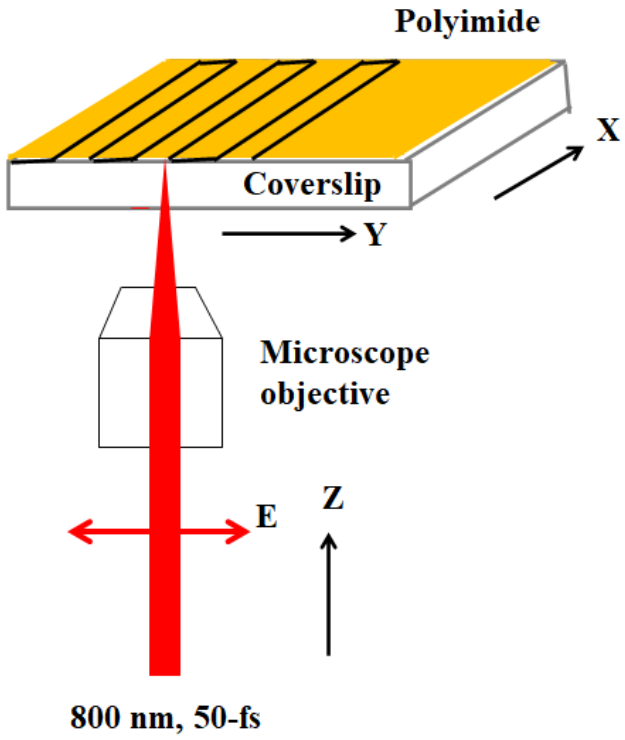

Fig. S2: Schematic of the experimental setup

As shown in the schematic (Fig. S2), we focused the horizontally polarized light (along Y) from RegA Ti:Sapphire laser with a central wavelength of 800 nm and pulse duration of 50 fs through a glass coverslip onto a thin film of polyimide. The substrate was translated along X and Y directions in a raster scan pattern as marked in the schematic.

III. Characterization details:

The interior modification confined beneath the film was studied using focused ion beam (FIB) measurements. Zeiss's ORION NanoFab multi-column Helium Ion Microscope and Gallium-Focused Ion Beam were used to study the blistered samples. Gallium ions were used to dissect the blisters and Helium ions were used to image their cross-sections. Prior to performing dissection, the samples were coated with 30 nm of aluminium to protect from excessive damage due to gallium ion exposure.

All AFM images were taken using the Nanowizard® II BioAFM (JPK Instruments, Berlin, Germany) mounted on an Olympus IX81 inverted confocal microscope, operating in contact mode. Silicon nitride cantilevers (DNP-S, Veeco, CA) were used in contact mode imaging.

XPS measurements were performed using Al Kα as an excitation source with energy of 1,486 eV.

Wettability tests were performed with a goniometer (VCA Optima AST Products Inc.). The instrument had an in-line camera arranged with a syringe for dispensing water. Our measurements were performed with a 1 µL droplet. The laser-patterned surfaces were placed underneath the syringe; the patterned surface was slowly moved up manually and monitored through the camera viewing window of the software until it touched the droplet hanging from the syringe. The contour in red shown in contact angle measurements was produced by the analysis software automatically. The accuracy of the instrument used was 0.5°.

IV. Calculation of energy density:

The estimated spot size (ω_0) is given by $\omega_0 = {}^{(1.22\lambda)}/_{NA}$, where λ is the wavelength of the laser (800 nm) and NA is the numerical aperture of the microscope objective [5]. We used a 0.4 NA objective for FIB measurements and a 0.2 NA objective for XPS measurements. The calculated spot sizes for these two objectives are 2.4 µm and 4.8 µm, respectively. In our experiments, we calculated energy densities using the formula $F = {}^{E}/_{(\pi \times 0.25 \times \omega_0^2)}$.

V. ***XPS Analysis for O (1s) and N (1s) Envelopes:***

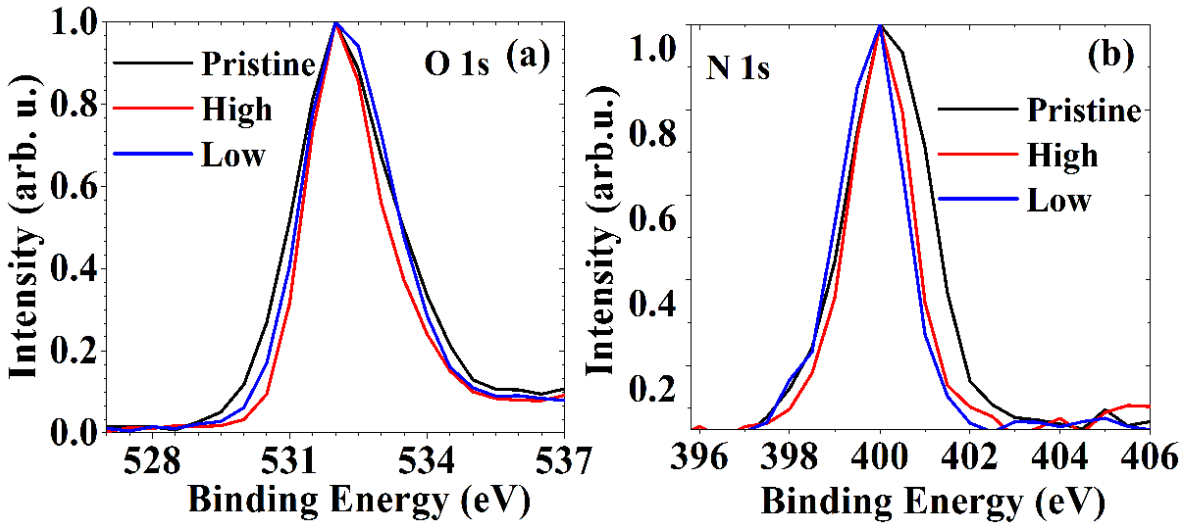

Fig. S3: XPS spectra for O (1s) and N (1s) envelopes for pristine and laser-modified polyimide samples. Blue for low irradiation dose at ~ 1.8 J/cm^2 and red curves for high irradiation dose at ~ 4.7 J/cm^2. Normalized intensity is plotted on Y-axis for comparison.

Two regions were modified with 870 nJ (high irradiation dose ~ 4.7 J/cm^2) and 330 nJ (low irradiation dose ~ 1.8 J/cm^2) pulse energies focused by a 0.2 NA objective at a fixed laser repetition rate (L) of 500 Hz. The scan speeds and line spacing (v, ΔX) for these regions were (4.5 mm/s, 12µm) and (3 mm/s, 8µm), respectively. The films experienced delamination and breakage at energies exceeding 500 nJ, corresponding to 2.7 J/cm^2 with a line spacing of less than 12 µm.

Figure S3(a) and **Figure S3(b)** show the XPS spectra for O(1s) and N (1s) envelopes for pristine (black) and laser-irradiated polyimide samples (blue and red). The O(1s) and N(1s) envelopes showed peaks at 532 eV and 400 eV (black curves in **Fig. S3(a),** and **Fig. S3(b)**), respectively [6]. The laser-modified polyimide surfaces were corrected for charge compensation and compared with pristine. We did not observe any new bands and peak shifts, indicating that the back-illuminated laser-irradiated polyimide did not undergo any chemical changes on its surface.

VI. *Calculation of number of shots/focal spot diameter (N):*

Here, we calculated the nonlinear spot size (ω_{NL}), given by $\omega_{NL} = {}^{1.22\lambda}/_{NA\sqrt{n}}$, where λ is the wavelength of the laser (800 nm), NA is the numerical aperture of the microscope objective (0.4), and n is the minimum number of photons required for nonlinear absorption (2 for polyimide) [5, 7]. For contact angle measurements, we used a 0.4 NA objective to pattern the surfaces in back-illumination. With these parameters, the estimated spot size (ω_{NL}) is 1.8 μm for a 0.4 NA objective. For laser-texturing experiments, we varied the speed of the translation stage and the pulse energy at laser repetition rates of 500 Hz and 2 kHz to fabricate equivalent single-shot and overlapped blister patterns. The number of equivalent laser shots (N) per focal spot of diameter (ω_{NL}) and at scan speed (v) is given by the equation $N = \frac{\omega_{NL} \times L}{v}$, where L is the repetition rate of the laser.

VII. *Estimation of contact area fraction (f):*

If a droplet of liquid (water) is placed on a solid surface, the liquid and solid surfaces come together under equilibrium at a characteristic angle called Young's angle (Θ_0). This angle is defined for an ideal solid surface where the influence of roughness is neglected. The contact angle shown by a water droplet on a heterogeneous interface (gas, liquid, and solid) is given by $\cos\Theta_{CB} = f(1 + r\cos\Theta_0) - 1$, where Θ_{CB} is the Cassie-Baxter angle for a rough surface and Θ_0 is the contact angle for an ideal solid surface [8-9]. Here, r is defined as the roughness factor which is a ratio of actual surface area to geometric surface area (shape of the structures is considered) [7].

We assume that our initial surfaces (average roughness measured by AFM was very small R ~ 0.2 nm) are flat (r = 1). Under this assumption, the equation becomes $\cos\Theta_{CB} = f(1 + \cos\Theta_0) - 1$. From contact angle measurements, pristine surfaces that we approximated to flat surfaces have shown a contact angle of 110°. By inserting the value of Θ_0 = 110°, we obtain the contact area fraction, f = 1.52 (1+cos Θ_{CB}).

Using the modified Cassie-Baxter equation, we plotted a curve, shown in Fig. 4(a) (in the manuscript file) for a range of Θ_{CB} values greater than 110°. This purely gives a theoretical curve for contact area fraction when laser-induced surface texture is added.

VIII. AFM line scan profiles of textured surfaces:

The line scan profiles for the patterned surfaces of N =1, 2, and 4 were obtained from the AFM images.

Patterned surface of N = 1: The AFM image below corresponds to the **Fig. 3(b)**. The line scans (red, green, and blue) across the series of blisters show a smooth regular blister pattern (almost no substructures) with a minimum laser shot density of 0.017 μm^{-2}.

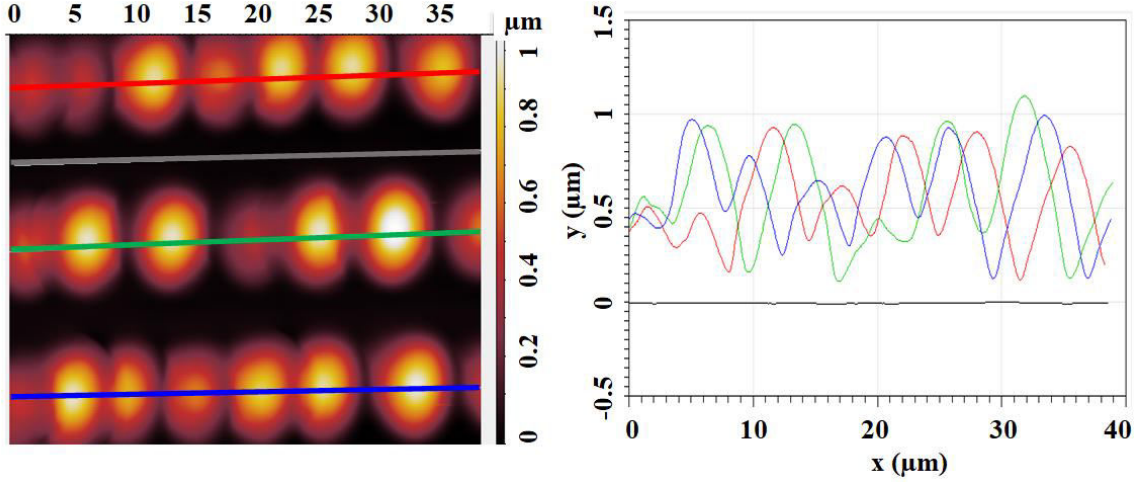

Fig. S4 (a): AFM line scan profile of patterned surface of N = 1.

Patterned surface of N = 2: The following AFM image corresponds to **Fig. 3(c)**. The line scans show the presence of substructures on each of the blisters with a higher laser shot density than in **Fig. 3(b)**.

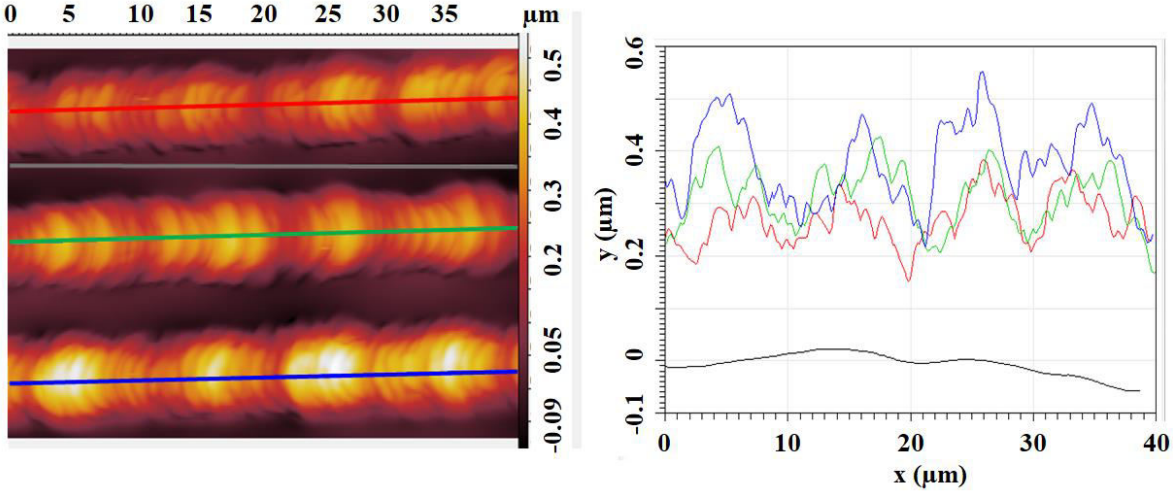

Fig. S4 (b): AFM line scan profile of patterned surface of N = 2.

Patterned surface of N = 4: The following AFM image corresponds to **Fig. 3(d).** The line scan profiles are complex as shown in **Fig. 3(c)**, with the highest laser shot density (almost zero pristine parts of the surface in between lines).

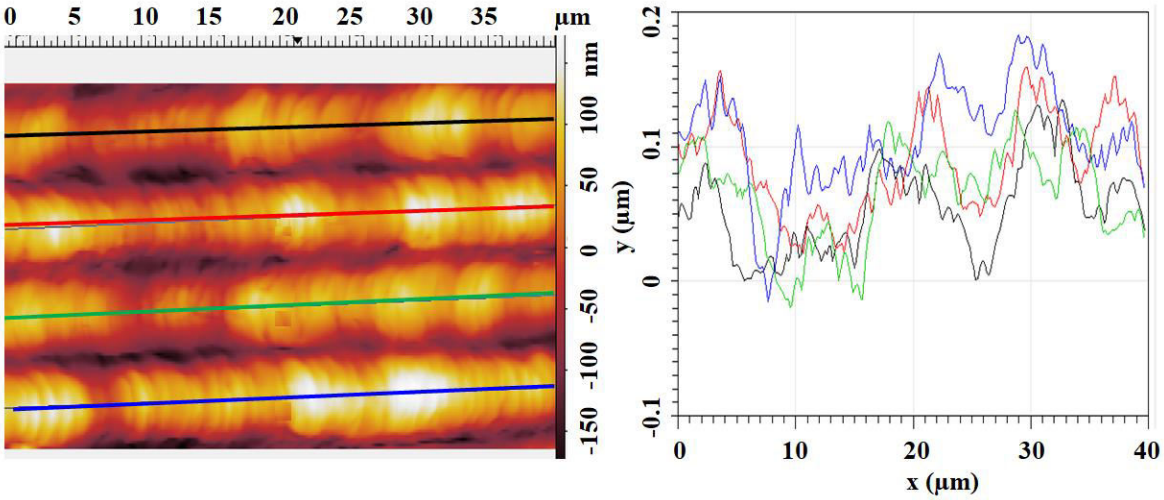

Fig. S4 (c): AFM line scan profile of patterned surface of N = 4.

References:

[1] M. Nishikawa, B. Taheri, and J. L. West, Mechanism of unidirectional liquid-crystal alignment on polyimides with linearly polarized ultraviolet light exposure, Appl. Phys. Lett. **72**, 19, 2403 (1998).

[2] B. Li, T. He, and M. Ding, Tuning the aggregation of polyimide thin films by modification of their molecular interactions, Polym. Int. **49**, 395 (2000).

[3] N. S. Shcheblanov, and M. E. Povarnitsyn, Bond-breaking mechanism of vitreous silica densification by IR femtosecond laser pulses, Eur. Phys. Lett. **114**, 26004 (2016).

[4] X. Xie, E. Lötstedt, S. Roither, M. Schöffler, D. Kartashov, K. Midorikawa, A. Baltuška, K. Yamanouchi, and M. Kitzlerb, Duration of an intense laser pulse can determine the breakage of multiple chemical bonds, Sci. Rep. **5**, 12877 (2015).

[5] O. H. Y. Zalloum, M. Parrish, A. Terekhov, and W. Hofmeister, on femtosecond micromachining of HPHT single-crystal diamond with direct laser writing using tight focusing, Opt. Express **18**, 13122 (2010).

[6] Z. K. Wang, H. Y. Zheng, C. P. Lim, and Y. C. Lam, Polymer hydrophilicity and hydrophobicity induced by femtosecond laser direct irradiation, Appl. Phys. Lett. **95**, 111110 (2009).

[7] K. Sugioka, Progress in ultrafast laser processing and future prospects, Nanophotonics **6**, 393 (2016).

[8] B. Wang, Y. Zhang, L. Shi, J. Li, and Z. Guo, Advances in the theory of superhydrophobic surfaces, J. Mater.Chem.22, 20112 (2012)

[9] Y. C. Jung and B. Bhushan, Contact angle, adhesion and friction properties of micro-and nanopatterned polymers for superhydrophobicity, Nanotechnology17, 4970(2006).

Chapter 5

A Multilayer Approach to Blister Formation

In Chapter 3, we created laser-induced blisters with sizes as small as 700 nm in full base width (400 nm full width at half maximum), which are the smallest to date that we are aware of. We also established that polymers are a versatile choice of dynamic release layer (DRL) which allows for contamination-free transfer, unlike metal DRLs or Laser-Induced Forward Transfer (LIFT) without a DRL. A natural next step is to apply polymer blister formation on this scale to LIFT to explore the resolution advantage that can be obtaining in this flexible material printing technique. As we will see, there are complications to overcome before applying nonlinear-absorption-based polymer blister formation to LIFT for two reasons:

- As mentioned in Chapter 2, nonlinear absorption only occurs at sufficiently high intensities beyond a characteristic threshold. Below this threshold, nonlinear absorption does not occur and, if the material is otherwise transparent, the remaining light passes through it.

- Materials can have drastically different nonlinear absorption and ablation thresholds. If the light passing through the blister-forming polymer layer is intense enough, a low-threshold material after the polymer can then be affected by the transmitted intensity.

These points are demonstrated by the following preliminary experiment, where we aimed to use a polyimide film to LIFT gold. Although this experiment was performed using > 20-µm-wide desorption areas, these results still illustrate the two problems described above, and why an altered approach is needed. This led us to implement a multilayer approach to blister formation based on intense nonlinear absorption, which is discussed in Sections 5.2 and 5.3.

5.1 Trial LIFT Experiment using Femtosecond-Pulse-Induced Polyimide Blisters

LIFT involves removing a piece of material from a source sample (called the "donor") that is transferred some distance to another surface (called the "receiver") [16]. We set up the trial LIFT experiment as follows.

Using our experimental setup shown in Figure 2.5, we selected a 10× 0.2 NA microscope objective for this experiment and followed the procedures outlined in Section 2.2. The sample was configured as shown in Figure 5.1. We spin-coated a 1.3-µm-thick film of polyimide onto a #1.5 borosilicate coverslip and deposited 40 nm of gold on top of the polyimide film via sputter coating. This coated coverslip acted as the donor. We then placed another #1.5 borosilicate coverslip on top of the donor, to act as the receiver, with two pieces of 12-µm-thick aluminum foil between the donor and receiver to provide adequate separation. The experiment chamber was pumped down to a vacuum pressure of 5×10^{-5} Torr to minimize the possibility of material breakup in the atmosphere, which can occur during LIFT at atmospheric pressures when the ejection speed is supersonic [16, 107]. Breakup in the atmosphere is a known limitation of some LIFT techniques, but is beyond the scope of this work.

The laser pulse energy was fixed at 300 nJ after the objective, and the laser intensity and fluence were varied by moving the focus of the beam to increase the size of the focal spot at the polyimide film. Four separated shots were taken for each lens position to assess repeatability, spaced adequately to ensure that any transferred material was separated on the receiver. The entrance aperture of the objective was 10 mm and the collimated laser beam diameter was

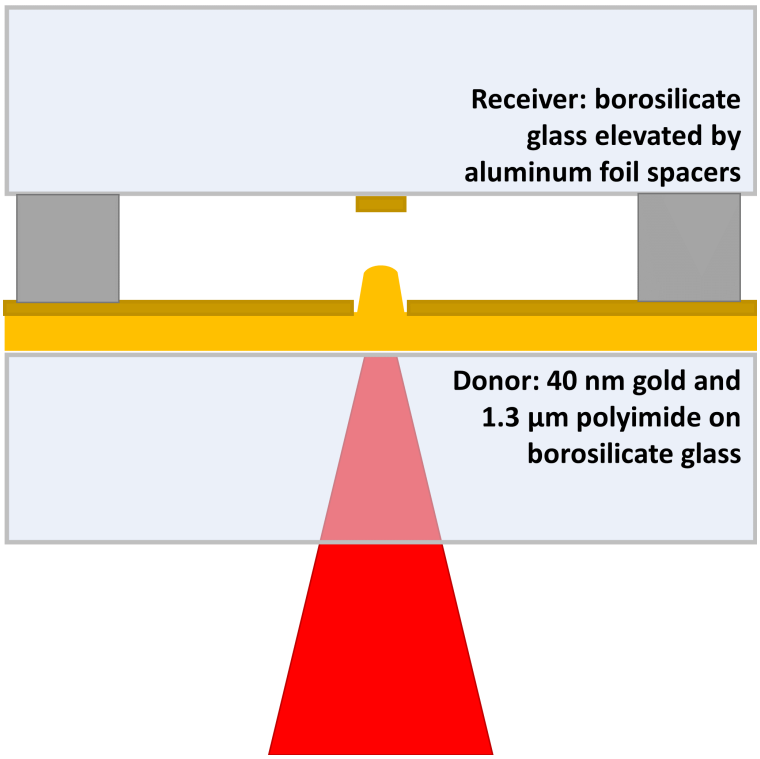

Figure 5.1: Schematic for the gold LIFT trial experiment. Dimensions of materials and laser beam not to scale. Polyimide was used to form blisters, with the objective of transferring gold in blister-based LIFT.

4 mm, which resulted in an estimated beam waist diameter of 12 µm. The peak intensity of 1.1×10^{13} W/cm^2 is below the ionization threshold for borosilicate glass [108]; therefore, even though the laser is focussed through the glass in this experiment, nonlinear absorption in the substrate (as covered in Chapter 3) would not occur here. The peak fluence at the beam waist was approximately 0.5 J/cm^2. This experiment is informative from a qualitative perspective, so, while modelling the beam and determining intensities and fluences would be diligent, this example is illustrative even without performing deeper analysis.

Figure 5.2 shows a microscope image of the receiver after the experiment was performed. There was very little transfer at high intensities (i.e. no transfer or incomplete transfer was seen for off-focus distances from 0 to 120 µm, or intensities of 1.1×10^{13} W/cm^2 down to 6×10^{12} W/cm^2). At intermediate intensities (i.e. focus offset of 170 to 370 µm or intensities of 5×10^{12} W/cm^2 down to 3×10^{12} W/cm^2), homogenous transfer of the gold film was observed. For larger focus offsets, the transfer degraded in uniformity likely due to the reduced laser

fluence being insufficient for driving the material transfer.

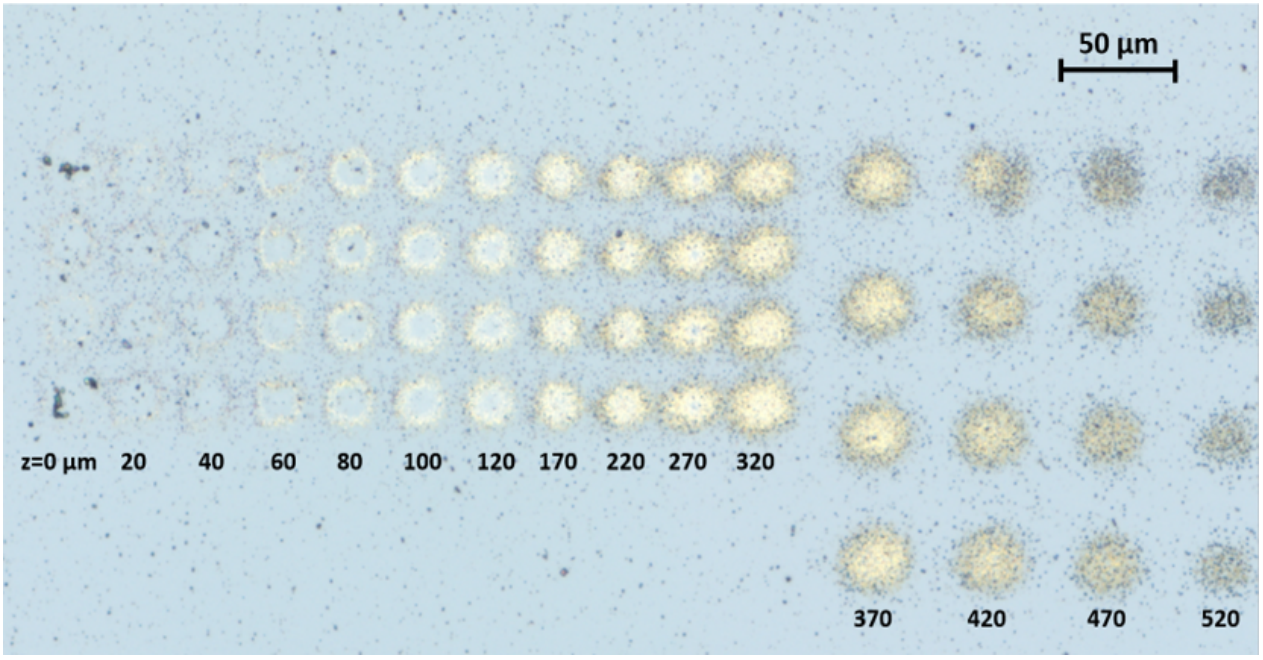

Figure 5.2: Optical microscope image of the receiver after the trial LIFT experiment. The pulse energy was fixed at 300 nJ after the 0.2 NA microscope objective, and the position of the laser focus was moved away from the sample (positive z values, as labeled) to adjust the laser intensity and fluence at the polyimide film. Gold transfer was homogenous for focus offsets of 170 to 370 µm.

To determine the transfer mechanism, we used atomic force microscopy (AFM) to examine the sites of laser irradiation on the donor film. Figure 5.3 shows an AFM image of the donor sample where material was removed using relatively large focus offsets of 370 µm (bottom) and 420 µm (top). In this case, we observed clean gold film removal with a step height of 40 nm, which corresponds to the thickness of the gold layer, and large steps on edge of the film from the ablation process. No blisters were observed. Therefore, the transfer must have occurred due to direct laser interaction with the gold. Figure 5.4 shows AFM images of material removal for higher intensities and fluences. In this case, clean removal of the gold film is observed again, but blisters appear in the center of the removal sites that cover only a small fraction of the gold removal area.

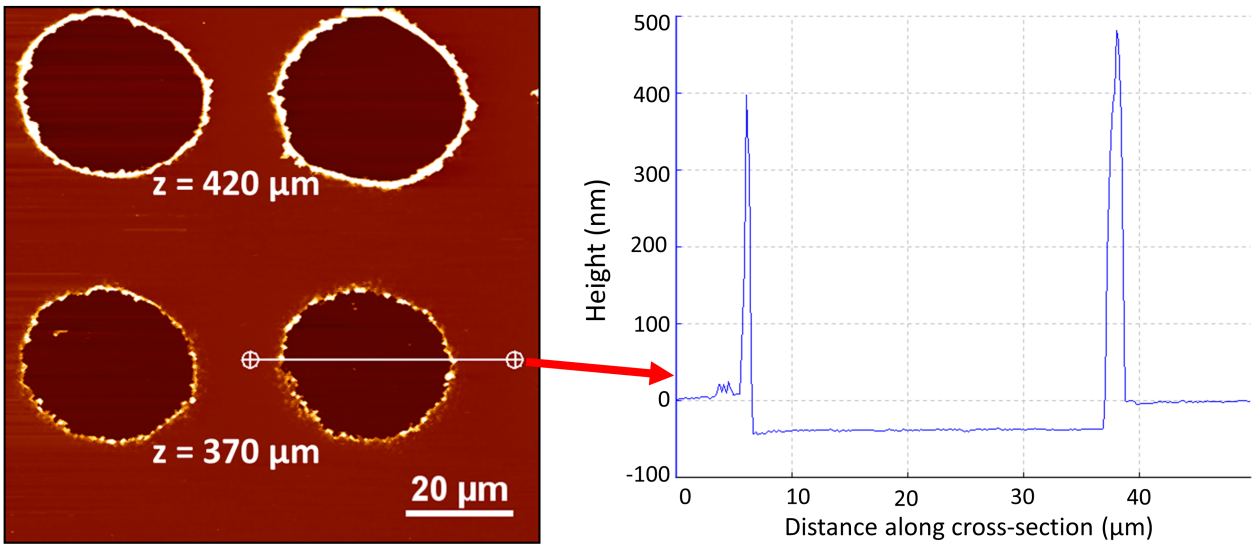

Figure 5.3: AFM image of material removal sites (left) and height profile of one site (right) on the donor. Each row is labelled with the corresponding focus offset used. A step of 40 nm is seen, corresponding to the thickness of the gold film.

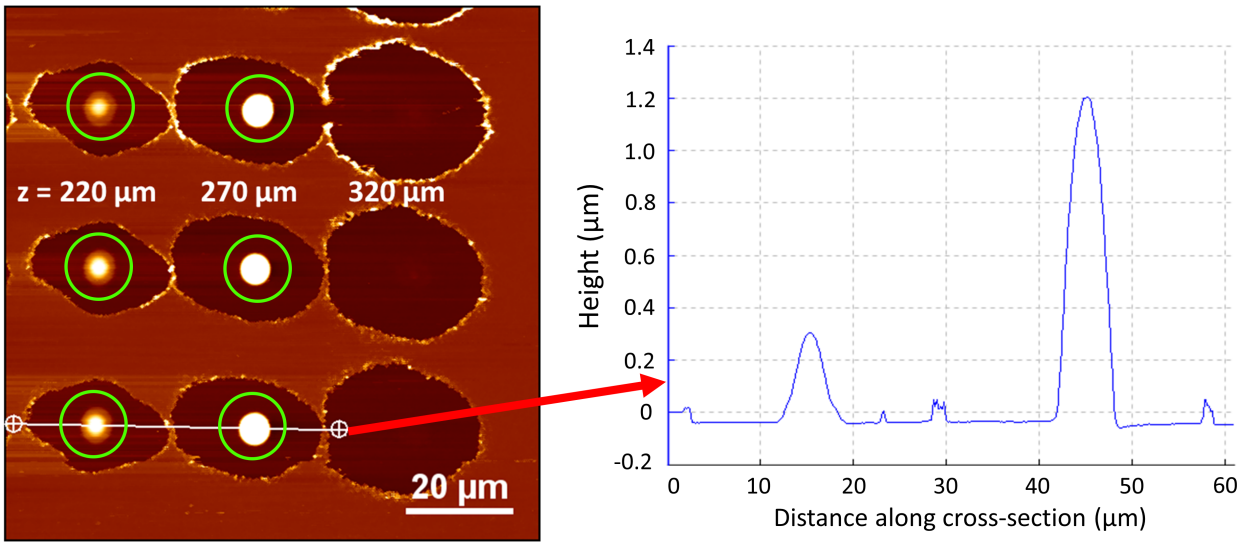

Figure 5.4: AFM image of material removal sites (left) and height profile of two sites (right) on the donor. Each column is labelled with the corresponding focus offset used; the AFM scan orientation is perpendicular to that of Figure 5.3. In addition to clean gold removal, blisters are now visible at the center of material removal sites for higher fluences (lower values of z) circled in green.

5.2 Developing the Multilayer Approach for Blister Formation

The experiment in Section 5.1 showed that, while material transfer was possible, blister formation was completely independent from gold transfer. This is because the threshold for nonlinear absorption leading to blister formation in polyimide is higher than the ablation threshold for a thin gold film. Below the nonlinear absorption threshold, the polyimide film is effectively transparent to the 800 nm laser pulse, allowing it to pass through and interact with the gold film.

More generally, many sensitive materials we hope to LIFT may have a damage threshold or ablation threshold at a lower fluence than the threshold for blister formation in the polymer. Simultaneously, a high-order nonlinear interaction in the blister-forming polymer layer requires very high intensity. Pure metal DRLs are useful for this problem, as they have very low penetration depths and high opacity, but they have the drawbacks of chemical contamination and thermal damage to the transfer material [37].

With all this in mind, we conceived the novel approach of combining layers of polymer and metal into a dynamic release mirror structure (DRMS). This approach to blister formation can realize the benefits of both materials while mitigating their individual drawbacks. In Section 5.3, we present a draft manuscript that investigates laser-induced blister formation in multilayer films of gold and PMMA using intense femtosecond pulses. The sample configuration is summarized in Figure 5.5.

Each film layer in Figure 5.5(a) provides different functions in the blister formation process. The bottom polymer layer can be used for absorption and subsequent expansion to drive the blister formation process. The intermediate gold layer may prevent transmission of the laser to a sensitive material, and it may also reflect incoming pulses to allow constructive self-interference of the laser pulse within the bottom polymer layer. The first constructive interference node, which is one-quarter of the wavelength in the medium ($\frac{\lambda}{4n} \approx \frac{800\text{nm}}{4(1.5)} \approx 130\text{nm}$) could increase the local intensity by up to a factor of 4. For example, the small polyimide

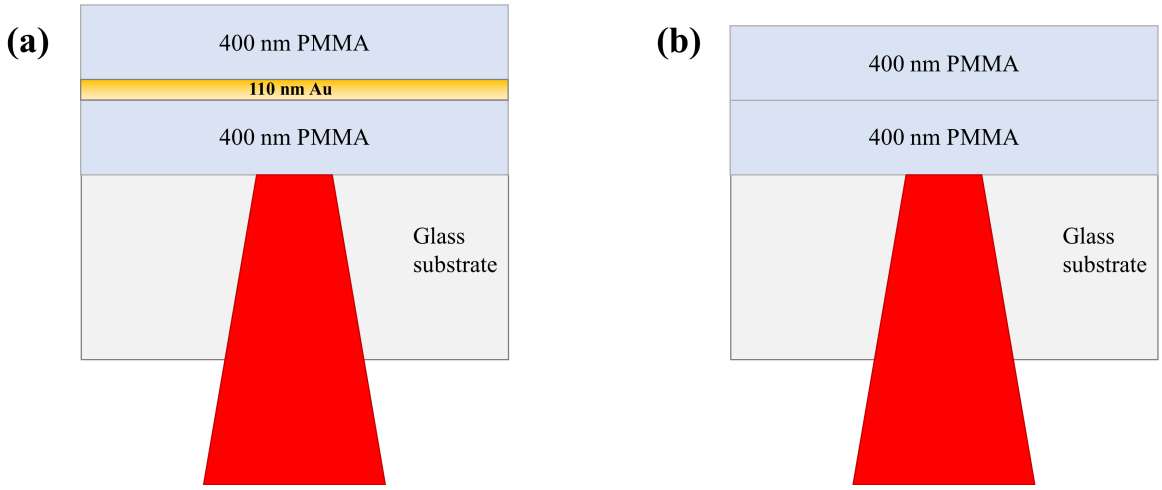

Figure 5.5: Configuration of films used for the study in Section 5.3. The PMMA-gold DRMS in (a) was the main film of interest and was compared with a PMMA-only version of the film in (b) as a control sample. Laser beam and substrate dimensions are not to scale.

blisters seen in Figure 5.4 may have been a result of such constructive interference occurring after reflection from the 40 nm gold layer. Laser pulses can also potentially interact with the gold film directly. The top polymer layer is used as a capping layer to contain any vaporized or melted material and provide thermal insulation to preserve the transfer material. This would guarantee clean desorption of a transfer material without alteration or contamination while still allowing intense nonlinear interactions to drive a blister formation process.

In this work, it was also important to revisit the idea of the substrate interaction. The work in previous chapters only considered intensity thresholds, which is useful due to its simplicity. However, material ablation and modification processes depend more directly on the laser fluence. Intensity and fluence correspond to different physical processes; ionization is the fast response of the electrons to the laser intensity, and ablation and heating are related to the total amount of energy deposited in a region (over a timescale much shorter than thermal relaxation time of the material).

Additionally, in this work, intensities leading to substrate ionization are reached before the bulk PMMA ablation fluence threshold. In such cases, we must reassess the intensity threshold modelling that was used in earlier work. When the film ablation fluence threshold is

met at intensities well below the substrate ionization threshold, the earlier model is sufficiently accurate. However, in this scenario, the ablation threshold for the bottom PMMA layer in the DRMS is only met at intensities causing nonlinear absorption in the substrate. Therefore, the substrate and film interactions must be thought about in sequence since intensity and fluence are no longer linearly related.

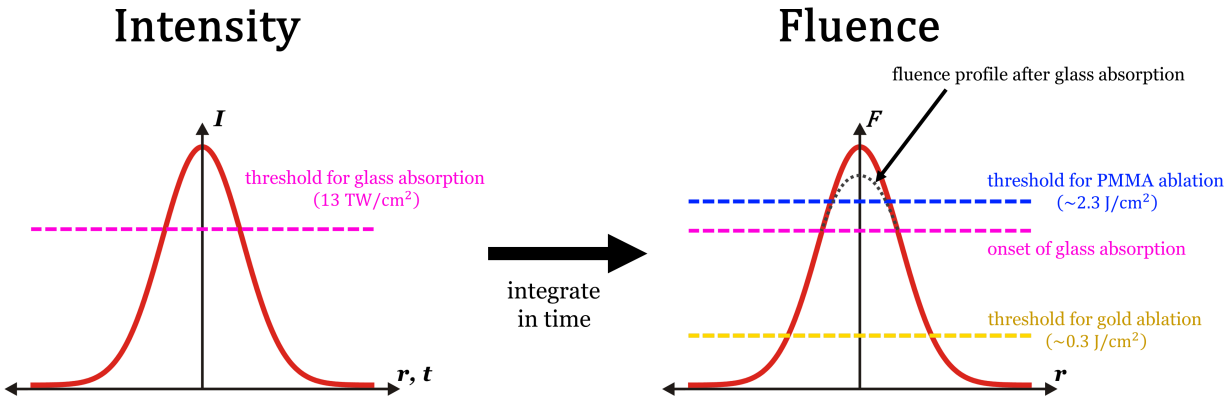

Figure 5.6: Threshold model for the various interactions in the multilayer film blister formation experiment. First, a pulse with a Gaussian intensity profile in space and time passes though the borosilicate glass substrate (ionization threshold shown in magenta [108]). In order to consider the fluence of the pulse relative to the ablation threshold fluences of gold [109] and PMMA [110, 111] shown in gold and blue, respectively, the pulse intensity is integrated in time to give a spatial fluence profile. The pulse fluence after glass absorption, shown by the dotted black line, is the result of time integration. The fluence corresponding to the onset of glass ionization (which depends nonlinearly on intensity) is also shown in magenta.

In our manuscript, we find that the absorption in the gold layer is dominant in our configuration, though there is also evidence of absorption in the polymer at higher fluences. Absorption of ultrafast pulses in noble metal films can result in interband and/or intraband absorption. Chan *et al.* studied this in detail and found nonlinear absorption was considerable above peak fluences of 0.25 J/cm^2 for pulse durations of 140 fs or greater [112]. As shown in the paper ahead, our pulses were 45 fs in duration, with minimum fluences of 0.3–0.5 J/cm^2 and reached up to 1.0–1.1 J/cm^2 (i.e. intensities ~3 to 10 times higher). For gold in particular, Cheng *et al.* notes the importance of d-band absorption in experiments using 50 fs, 800 nm pulses, and that it is a two-photon absorption process in these circumstances [113].

Thus, the absorption in gold is still multiphoton and hence threshold-like, so we see localized energy deposition leading to small blisters. Upon focussed ion beam (FIB) characterization of the blisters, we noticed droplet formation in the gold similar to works on laser-induced gold film spallation [74] and direct LIFT of particles formed by irradiating solid films with femtosecond pulses [114]. This mechanism can drive an underlying blister formation process while being contained by the top polymer layer. For use in LIFT, a transfer material would need to be placed on top of the DRMS. Experimental verification would also be needed to ensure enough thrust was generated to overcome the inertia of the transfer material and its adhesion to the DRMS.

In the future, materials could be chosen so either a two-layer (polymer on metal) or three-layer DRMS (as shown) could be used. The bottom polymer layer in this case should be selected to undergo absorption at a lower fluence than significant absorption in the metal. The top polymer layer should also be optimized for tensile strength and minimum thickness; for example, a thin polyimide coating or elastomer-doped PMMA. This work has shown that either approach would be feasible.

It would also be interesting to apply this approach to more traditional LIFT scenarios relying on nanosecond and picosecond pulses and on larger length scales. While our work focussed on structures on and near the nanoscale, the DRMS approach should be equally valid at larger scales. For future work on the nanoscale, it may be of interest to study the use of longer femtosecond pulses and few-picosecond pulses (as long as they are still much shorter than the thermal diffusion time in the blister-forming material) to mitigate interaction with the glass substrate. Choosing a substrate material with a higher damage threshold, such as fused silica or quartz, would also be beneficial. For work on larger scales, using intensities above the nonlinear absorption threshold of the substrate could achieve flat-top-like fluence profiles at the blister-forming film without the use of beam-shaping optics. The use of substrate absorption to limit the beam intensity has been shown to improve repeatability in femtosecond pulse laser ablation of polymer films [115]. Flat-top beams were used in other blister formation work to provide uniform laser penetration into the film across the laser

focal spot, though they were generated before being focussed onto samples rather than being generated in the substrate during focussing [69, 93, 116].

5.3 Experimental Study of Blister Formation using a Dynamic Release Mirror Structure

Blister Formation in Dynamic Release Mirror Structures using Femtosecond Laser Pulses

Alan T. K. Godfrey,[1] Deepak L. N. Kallepalli,[1] Sabaa Rashid,[2] Jesse Ratté,[1] Chunmei Zhang,[1] and P. B. Corkum[1]

[1] *Joint Attosecond Science Laboratory, University of Ottawa and National Research Council of Canada, 25 Templeton St., Ottawa K1N 6N5, Canada*

[2] *Centre for Research in Photonics, University of Ottawa, 25 Templeton St., Ottawa K1N 6N5, Canada*

Blister formation occurs when a laser pulse interacts with the underside of a polymer film on a glass substrate and is fundamental in Laser-Induced Forward Transfer (LIFT). We present a novel method of controlling blister formation using a thin metal film situated between two thin polymer films. This enables a wide range of laser pulse energies by limiting the laser penetration in the film, which allows us to push past the diffraction limit by exploiting nonlinear interactions without transmitting high intensities that may destroy a transfer material. We study blisters using a helium ion microscope, which images their interiors, and find that laser energy deposition is primarily in the metal layer and the top polymer layer remains intact. Blister expansion is driven by laser-induced ablation/spallation of the gold film. Our work shows that this technique could be a viable platform for contaminant-free LIFT using nonlinear absorption beyond the diffraction limit.

I. INTRODUCTION

Laser-Induced Forward Transfer (LIFT) has received a great deal of attention due to its versatility, simplicity, and its potential to deposit materials over length scales ranging from nanometers to millimeters [1–3]. LIFT involves focusing a laser pulse through a transparent support substrate onto the rear side of a thin film of the material to be transferred, which is called the donor. Another substrate, which is called the receiver, is placed on the donor material with or without a spacer to accept the transfer material [3–11].

There has been a transition from using a continuous-wave laser, as in the case of Laser-Induced Thermal Imaging (LITI), to nanosecond, picosecond, and femtosecond laser pulses in LIFT processes [12–14]. Advanced versions of LIFT use a dynamic release layer (DRL) between the donor and support substrate to minimise the contamination of the donor from direct interaction with the laser. The DRL absorbs laser light and provides thrust either by vaporizing fully, such as for a triazine film [2, 3, 14], or by partial heating or vaporization resulting in blister formation [4–6, 10–12]. Ultrafast lasers with femtosecond pulse durations are preferred in achieving contaminant-free transfer as the energy deposition occurs with minimal thermal diffusion.

In addition to using femtosecond lasers, nonlinear absorption of light in materials plays an important role in small-scale material transfer at or below the diffraction limit. Work on polyimide blisters with 45-fs pulses using nonlinear absorption of 800 nm light showed submicrometer blister diameters (∼700 nm full width at $1/e^2$) [15]. Similar work using 15-ns pulses at a wavelength of 355 nm in the linear absorption regime achieved blister sizes as small as 10 m, which was approximately the size of the laser spot [5]. Further, we demonstrated that the chemical changes induced by an ultrafast laser are confined below the polymer surface, leaving the surface chemically intact, as shown through focused ion beam and X-ray photoelectron spectroscopy techniques [16, 17]. The size of laser-induced structures decreases with decreasing thickness [18], but thinner films are more prone to rupture [5]. Therefore, minimizing the depth and width of laser energy deposition will enable thinner DRLs and thus smaller transfer sizes. Metal films have also been used as DRLs [10, 11, 19, 20]. While these films have much smaller absorption depths, they can lead to contamination by fragments of metal in the transfer material [21].

We report a DRL called a dynamic release mirror structure (DRMS) that consists of a metal layer sandwiched between two polymer layers. It is capable of contaminant-free LIFT, since chemical changes are confined to the glass-polymer interface below the metal layer. It may also enhance the laser intensity and fluence inside of the film by forming a standing wave in the polymer below the metal layer that promotes formation of intact blisters below the threshold energy for a similar polymer film without a metal layer. The central metal layer may also absorb laser light and reflect excessive intensities which would otherwise be transmitted by a single nonlinearly absorbing polymer film and damage the donor. Additionally, the technique can be used from ultraviolet to near-infrared wavelengths and for all pulse durations since metals tend to be highly reflective and opaque over a broad range of wavelengths. The DRMS configuration combines the advantages of metals and polymers for DRL-based LIFT.

Fig. 1 shows a schematic of our experimental setup. First, an ultrafast laser pulse at 800 nm wavelength is focused onto the DRMS. At sufficiently high intensities, the borosilicate glass substrate may absorb 3 photons of 800 nm light based on its ∼4 eV bandgap [22]. The remaining energy in the pulse reaches the DRMS. The first layer in the DRMS is a 400-nm-thick PMMA layer that may undergo nonlinear absorption to drive the expansion of a protruding blister. The energy left over is then reflected from the central metal layer, which may allow for

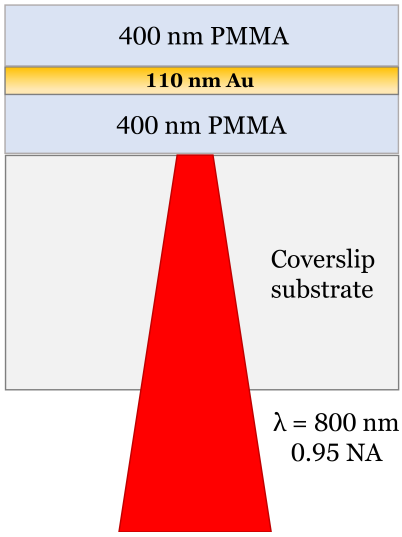

FIG. 1. A schematic showing a focussed laser pulse incident on the DRMS sample.

the laser pulse to interfere with itself and enhance the intensity and fluence in regions of constructive interference. In cases where the initial pulse intensity and fluence is below the polymer absorption threshold, nonlinear absorption driven by standing-wave interference may dominate. PMMA has a similar bandgap to borosilicate glass [23, 24]. In this case it will undergo three-photon absorption as well. Absorption may also happen directly in the gold layer. The top layer is another 400-nm-thick PMMA layer which is not exposed to the laser. It acts as a 'cap' on the DRMS to control the expansion and prevent film rupture that would contaminate a transfer material. In this paper, we assess the contributions of each layer to the blister formation process.

II. EXPERIMENTAL DETAILS

We used the femtosecond-laser-induced blister formation experiment setup as shown in ref. [15]. A Coherent RegA 9040 Ti:sapphire laser produces pulses with a duration of 45 fs FWHM, as measured by a MesaPhotonics MP002 FROGscan instrument, at a central wavelength of 800 nm. The beam passes through a spatial filter and the spatial profile is verified to be Gaussian with a beam profiler (DataRay WinCamD UCD12); we measure the beam to have $M^2 = 1.08 \pm 0.02$. We adjust the pulse energy using a rotatable half-wave plate followed by a linear polarizer. The laser beam is focused by a 0.95-NA microscope objective (Leitz Wetzlar 80× 0.95-NA objective, stock no. 48728), which is mounted into a vertical motor stage to adjust the focal spot placement. The collimated beam diameter at the objective was 4 mm, which underfilled the 10-mm entrance aperture and resulted in an estimated focal spot diameter of 2.6 µm. We measured the objective transmission to be 65.1% and estimate the net reflectivity of the sample to be 4.3% following Derrien *et al.* [25]. Pulse energies are given as measured before the microscope objective; losses are factored into all intensity and fluence values.

For sample fabrication, we use PMMA films on no. 1.5 Fisherbrand borosilicate glass coverslips (0.16—0.19 mm in thickness) as substrates. Substrates are prerinsed in acetone, isopropyl alcohol, and deionized water and dried on a hotplate. PMMA films are spin-coated with Microchem 495 PMMA A6 precursor at a spin speed of 2000 revolutions/min for 30 s. This yielded a film thickness of 400±50 nm for each layer of PMMA as determined with a Bruker Dektak XT contact profilometer. The gold layer in the DRMS was coated by thermal vapor deposition, and its thickness was determined to be 110±5 nm by using a JPK Nanowizard II BioAFM atomic force microscope in contact mode. We use the same method to characterize the surface morphology of laser-induced blisters after fabrication. We determined the net transmission of the DRMS to be 13% by passing the collimated laser beam through the sample.

We used a Zeiss ORION Nanofab helium ion microscope for characterizing the interior of blisters. The sample was mounted normal to the focused gallium ion source, which was used to mill away half of each blister before imaging from a 45° angle using the helium ion beam. Prior to this, the sample was coated with 30 nm of aluminum to protect the film from damage from excessive gallium beam exposure.

III. RESULTS & DISCUSSION

First, we fabricated blisters on the PMMA and DRMS samples in a back-illumination geometry as shown in **Fig. 1**. The laser pulse energy was adjusted from 40 nJ to 1.5 µJ. **Fig. 2** shows the AFM scan profiles of height and diameter of the blisters for the DRMS sample.

We plot blister height and radius as a function of laser pulse energy in **Fig. 3**. The height of blisters should depend on how far the laser energy deposition penetrates the film and how much material remains to support the intact expansion of a blister. Under the given experimental conditions, we achieved blisters with heights of 350 nm at 200 nJ of pulse energy. Further increase in energy beyond 200 nJ caused blisters rupture. Figure 3 indicates an increasing trend of height and diameter with pulse energy, and saturation of these values at energies near 200 nJ, before rupture occurs.

We compare these results with the 800-nm-thick PMMA sample. **Fig. 4** shows AFM scans of the laser-induced structures in the film. We did not observe any modification below 250 nJ of pulse energy. At 250 nJ, which is the energy threshold for modification (visual and morphological), we immediately saw film rupture which continued for all higher energies used. This comparison shows how an embedded metal layer in a polymer film greatly improves control of blister formation.

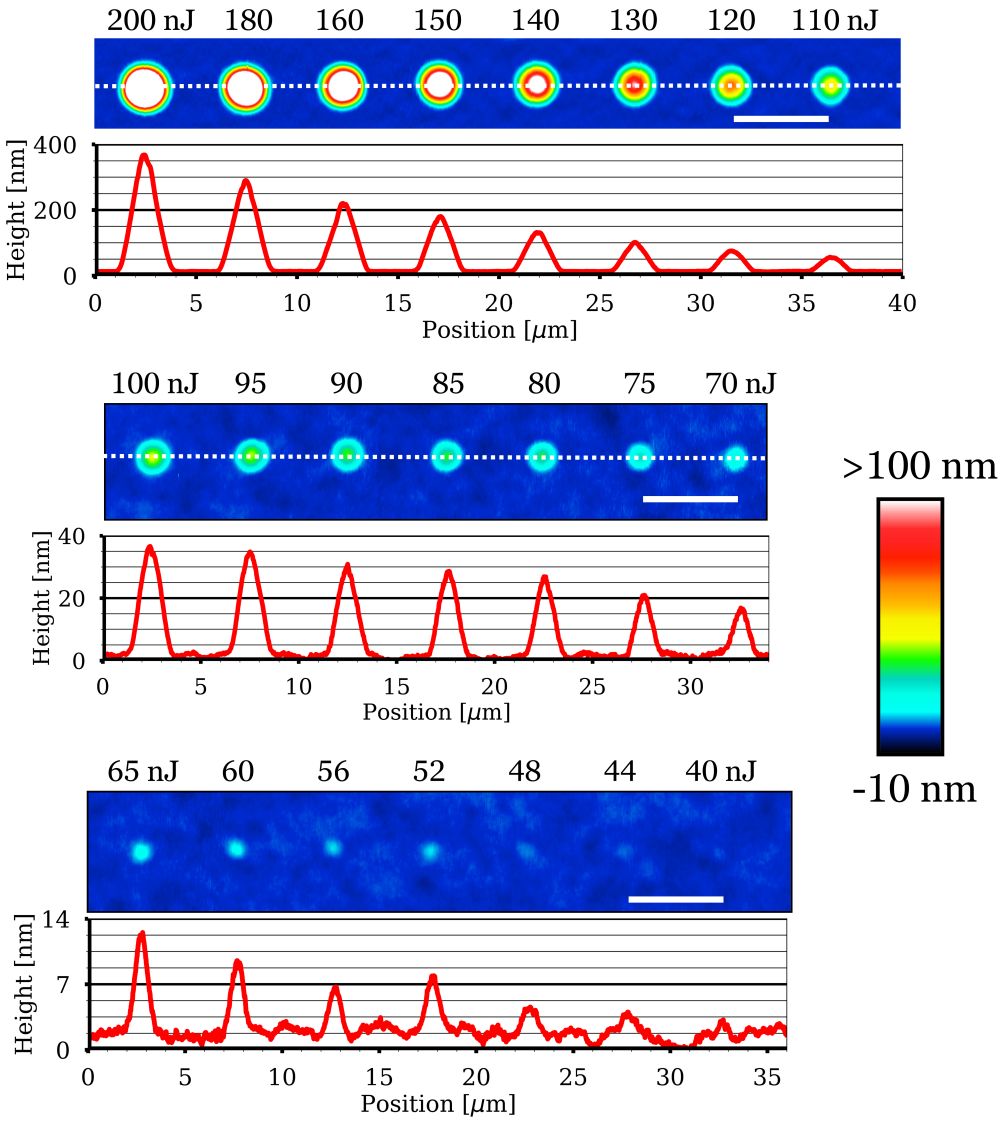

FIG. 2. AFM images and cross-sectional profiles of blisters created in the DRMS sample at different pulse energies. Scalebars are 5 µm in length.

We examined blisters using the helium ion microscope. **Fig. 5(a)** shows a cross-sectional view blister made with a pulse energy of 300 nJ. This image was generated after a single pass with the gallium milling beam. However, there was considerable material redeposition, evidenced by the lack of a sharp boundary between PMMA and the glass substrate. This was addressed by following with a second gallium beam cut using the same parameters but made over a smaller area to prevent redeposition. The image after the second gallium beam cut is shown in **Fig. 5(b)**. The second cut greatly enhanced the contrast between each material but resulted in milling of small pockets from both PMMA layers. These pockets should not be confused with the initial laser modification.

In **Fig. 5(a)** and **5(b)**, we see the gold layer has been disrupted, and resolidified gold has collected in the top layer of PMMA. The PMMA close to the melted gold has also been modified, as seen by its phase contrast. In the center of the structure, there is a small ablated region in the bottom PMMA layer. The ablated region could be due to increased fluence due to standing-wave interference caused by reflection from the gold layer. We expect the highest fluence enhancement from this effect at the first constructive interference node ~ 130 nm ($\lambda/4$ in the medium) away from the gold film. Gold is highly reflective, but ultrafast changes to gold reflectivity should be considered. In the work by Apalkov and Stockman, the reflectivity of metal nanofilms was reduced by a factor of ~ 3 at an electric field strength of 3 V/Å[26]. In our work, the breakdown intensity of borosilicate glass limits the field strength to ~ 0.8 V/Å, and the film thickness is several times the skin depth, so total reflectivity should

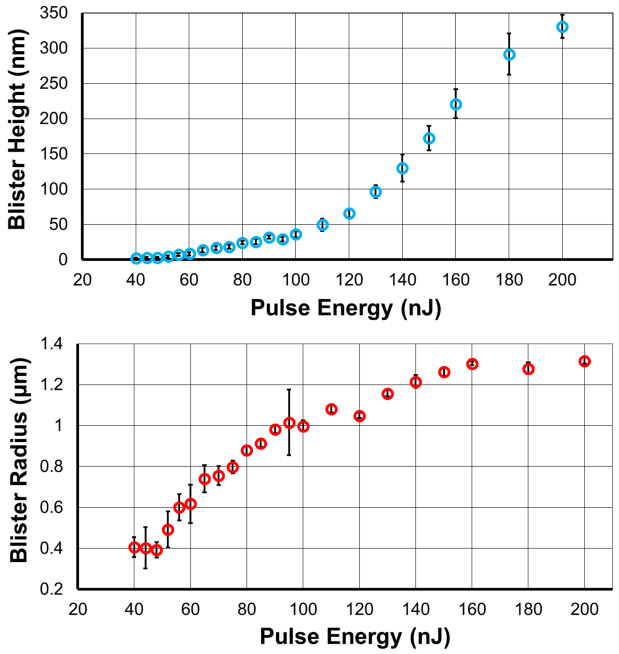

FIG. 3. Trends in blister height (above) and blister diameter (below) with pulse energy. Near the threshold pulse energy of 40 nJ, blister heights are on the scale of the surface roughness. Beyond 200 nJ of pulse energy, blisters were not left intact and showed rupture.

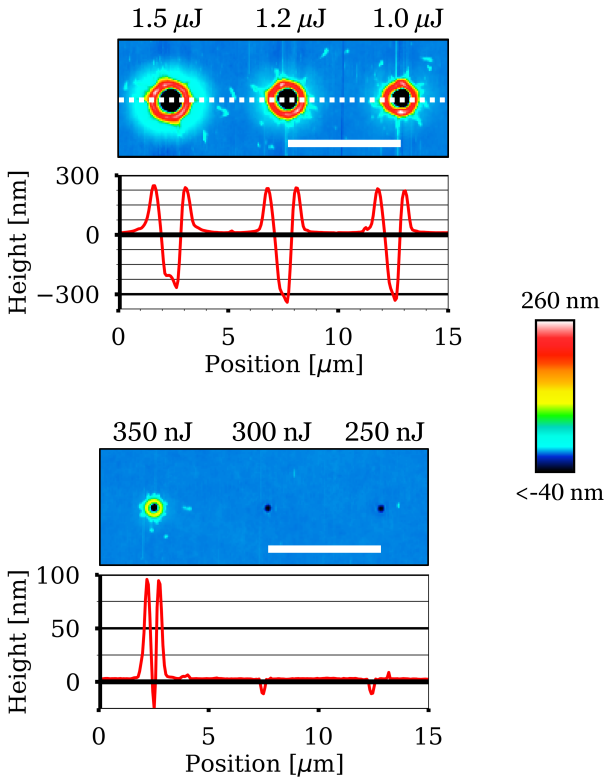

FIG. 4. AFM images of ablation spots on the PMMA sample at different pulse energies. No intact blister formation was seen. Scalebars are 5 μm in length.

not be greatly affected. Lastly, a small crack in the top PMMA layer is visible, where the aluminum coating has entered. We have observed similar cracks in polyimide blisters with excessive pulse energies [15]. Still higher pulse energies lead to rupture of the structures.

Fig. 5(c) and **5(d)** show the same measurements performed for a blister made with 180 nJ of pulse energy. Similar features are seen, but at this energy we see laser-modified gold layer forms an intact ball of gold that stays partially connected to the underlying film. Similar observations of ultrafast laser spallation of ultrathin gold films on glass have been reported for front illumination, where pulses of moderate energy allow the melted gold to cool and become trapped due to surface tension [27]. It should be noted that the characteristic two-temperature heating length of gold was 120 nm, which is approximately the thickness of our gold film; hence the results for front and back incidence are analogous. Similar droplet formation has also been observed in laser-based printing of silicon nanoparticles using femtosecond pulses [28].

We now consider the intensities and fluences leading to the blister formation and PMMA ablation in this experiment. Intensity is the key quantity for multiphoton ionization, whereas fluence is the key quantity for ablation and similar processes [14, 29–31]. The spherical aberration of our objective causes axial stretching of the focus resulting in reduced intensity in the focus [32]. Also, as established by Rayner *et al.* [33], an intense pulse focussed through glass can be attenuated by ionization of the medium, which limits the peak intensity of the pulse. In our case, intensities above 13 TW/cm^2 will break down borosilicate glass and be lost to the medium before reaching film [34]. The peak intensity is strictly limited, but the peak fluence of a Gaussian pulse (determined by integrating over the temporal extent of the pulse) may still increase.

Fig. 6 shows modelled values for peak fluences under experimental conditions, accounting for nonlinear absorption in the substrate. We estimate that, with an aberration-based axial stretch of the focus by a factor of 2.0 to 3.1 (which decreases the laser intensity and fluence), the resulting fluence thresholds for blister formation range from 0.30–0.47 J/cm^2 at an input pulse energy of 40 nJ. This estimate was made by scaling the peak intensity and fluence by a constant factor to match known threshold values for femtosecond laser ablation of ultrathin gold films. For a film of approximately 100 nm thickness, the fluence threshold for ablation is approximately 0.3–0.5 J/cm^2 (31). Absorption in the glass did not occur at the DRMS blister formation threshold, since the peak intensity was too low to ionize borosilicate glass (<10 TW/cm^2 at maximum).

In the case of the PMMA-only film, the onset of damage occurred at approximately 1.0–1.1 J/cm^2, which is approximately one-third of the fluence in vacuum due to

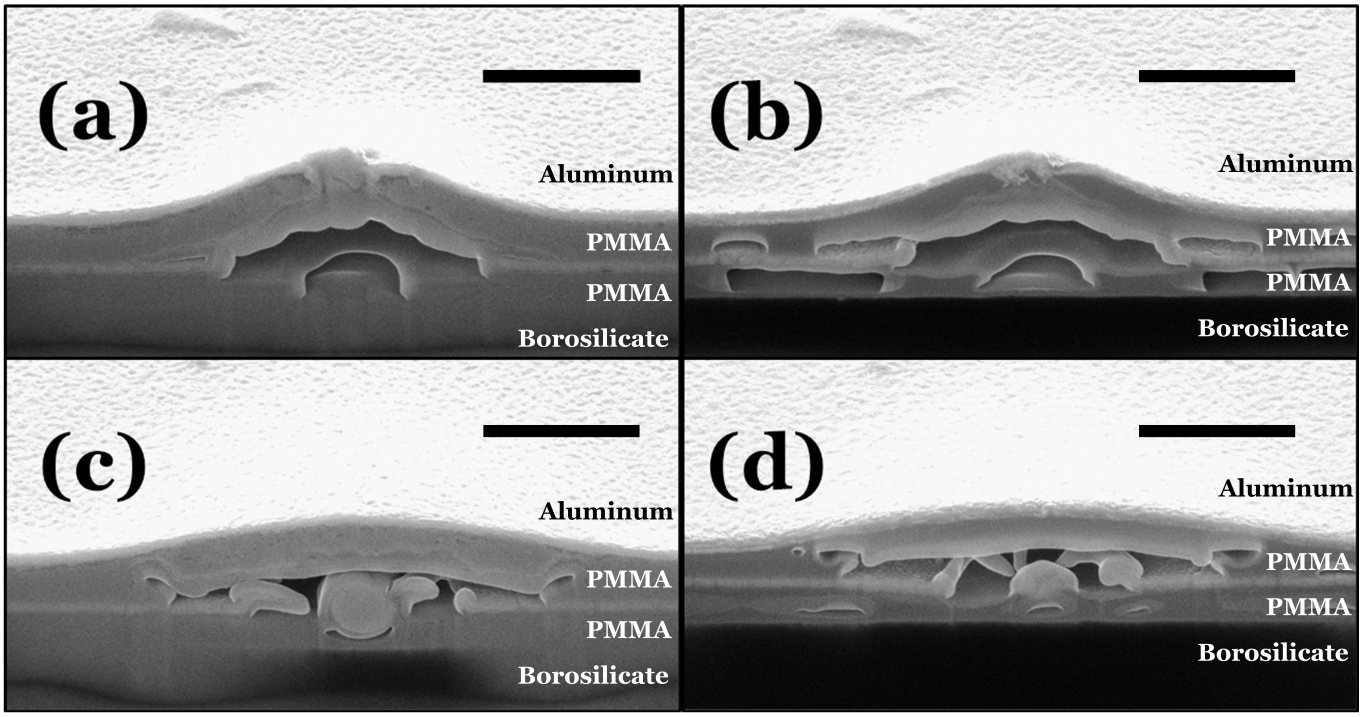

FIG. 5. Helium ion microscope images of blisters in the DRMS sample that have been sectioned by a gallium beam. Scalebars are 1 µm in length. A blister made using 300 nJ of pulse energy is shown **(a)** after 1 pass of the gallium beam and **(b)** after a second pass to remove redeposited material which obscures material boundaries in the image. The process was repeated in **(c)** and **(d)** for a blister made using 180 nJ of pulse energy. The central gold layer, unmodified and modified PMMA, borosilicate glass substrate and aluminum protective layer are all resolvable by phase contrast.

attenuation by the glass substrate. Even without the aberration (axial stretch factor of 1), the peak fluence would only reach 1.3 J/cm^2. Given a refractive index of 1.49 at 800 nm [35], the normal incidence reflectance of the PMMA-air interface is 0.039, which would lead to a standing-wave intensity and fluence increase of 43% [36]. Even then, our fluences are lower than the literature values for ablation of bulk PMMA with similar laser parameters, 2.3–2.9 J/cm^2 [30, 37]. The high NA and spherical aberration may result in light rays that are no longer normal to the PMMA-air interface everywhere in the focus. Deviation from normal incidence would increase the reflectivity and hence may further enhance the local intensity and fluence due to a standing wave.

Our results indicate that the driving mechanism of blister expansion is laser spallation of the gold film. However, the top polymer layer confined the molten gold, which would allow contaminant-free LIFT using this scheme. Additionally, the thickness of the polymer layer provides a way to selectively dampen the expansion process independent of the metal layer. The bottom layer of polymer played a small role in the experiment, but the nonlinear interaction could be enhanced by selection of a substrate such as fused silica with a much higher bandgap ($\sim$ 9 eV) [22]. Alternately, it could be accessed by lengthening the femtosecond pulse, reducing the intensity for a given fluence, or by reducing the bandgap of the polymer by material selection.

IV. CONCLUSION

We have developed a multilayer configuration for blister formation that offers comparable spatial resolution to our previous work [15] with the added advantages of reduced intensity at the donor material and more parameters for optimization of the blister formation process. We studied the high-intensity interaction with the multilayer film and substrate and determined that the interaction with the gold layer drives blister formation, owing to its low damage threshold compared to PMMA. Nonlinear interaction with the polymer also occurs but was suppressed due to nonlinear absorption in the substrate. When the metal film gives rise to laser-induced blister formation, the ultimate spatial resolution limit should depend on the heat diffusion length in the metal layer. This could be improved by choosing a metal with lower thermal conductivity such as chromium, nickel, steel or titanium.

The multilayer approach to blister formation provides access to nonlinear interactions in thin films of metal and polymer without risking damage or contamination to a transfer material in LIFT. It combines the advantages of polymers and metals as dynamic release layers

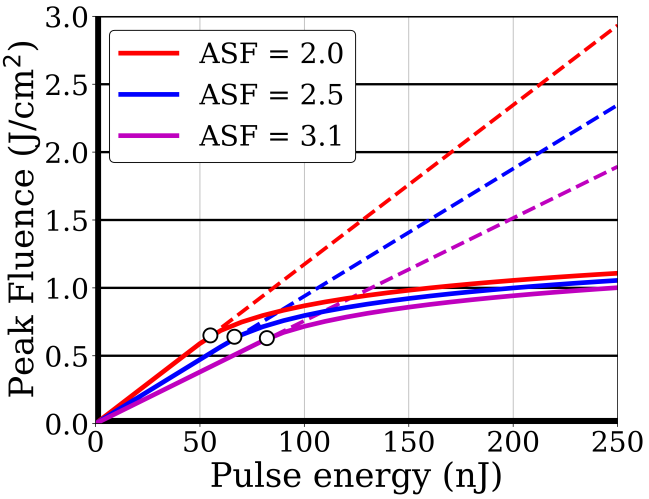

FIG. 6. Modelled peak fluence of laser pulses after passing through the borosilicate glass substrate. ASF = axial stretch factor. Pulse energy is given before transmission losses and nonlinear absorption by the glass. The dashed lines indicate the peak fluence in vacuum conditions. The white breakpoints on each line indicate when the intensity reaches the breakdown threshold for borosilicate glass.

while also mitigating the drawbacks of using each material separately. It can be used for improving resolution of blister-based LIFT, but it could also be used in existing microscale applications for enhanced control and flexibility. While our work has focussed on using intense nonlinear interactions on scales near the diffraction limit, the DRMS approach may also be interesting to apply in the linear regime with nanosecond pulses.

FUNDING

We acknowledge funding from the following sources: Natural Sciences and Engineering Research Council of Canada (NSERC) Engage (EGP 523138-18); and Discovery (RGPIN-2019-04603) grants; Ontario Centres of Excellence (OCE) Voucher for Innovation and Productivity (VIP1) Program (29119); Fluidigm Canada and the Canada Foundation for Innovation. Alan T. K. Godfrey acknowledges financial support from NSERC's Postgraduate Scholarship - Doctoral and University of Ottawa's Excellence Scholarship.

ACKNOWLEDGEMENTS

We acknowledge funding from Natural Sciences and Engineering Research Council of Canada (NSERC) Engage (Grant No. EGP 523138-18) and Discovery (Grant No. RGPIN-2019- 04603) grants, the Ontario Centres of Excellence Voucher for Innovation and Productivity I Program (Grant No. 29119), Fluidigm Canada, and the Canada Foundation for Innovation. A.T.K.G. acknowledges financial support from the NSERC's Postgraduate Scholarship – Doctoral and the University of Ottawa's Excellence Scholarship.

DISCLOSURES

The authors declare no conflicts of interest.

[1] J. Bohandy, B. F. Kim, and F. J. Adrian, Metal deposition from a supported metal film using an excimer laser, Journal of Applied Physics **60**, 1538 (1986), publisher: American Institute of Physics.

[2] D. P. Banks, C. Grivas, J. D. Mills, R. W. Eason, and I. Zergioti, Nanodroplets deposited in microarrays by femtosecond Ti:sapphire laser-induced forward transfer, Appl. Phys. Lett. **89**, 193107 (2006).

[3] D. P. Banks, K. Kaur, R. Gazia, R. Fardel, M. Nagel, T. Lippert, and R. W. Eason, Triazene photopolymer dynamic release layer-assisted femtosecond laser-induced forward transfer with an active carrier substrate, EPL (Europhysics Letters) **83**, 38003 (2008).

[4] N. T. Kattamis, P. E. Purnick, R. Weiss, and C. B. Arnold, Thick film laser induced forward transfer for deposition of thermally and mechanically sensitive materials, Appl. Phys. Lett. **91**, 171120 (2007).

[5] M. S. Brown, N. T. Kattamis, and C. B. Arnold, Time-resolved study of polyimide absorption layers for blister-actuated laser-induced forward transfer, Journal of Applied Physics **107**, 083103 (2010).

[6] M. S. Brown, C. F. Brasz, Y. Ventikos, and C. B. Arnold, Impulsively actuated jets from thin liquid films for high-resolution printing applications, Journal of Fluid Mechanics **709**, 341 (2012).

[7] N. T. Kattamis, M. S. Brown, and C. B. Arnold, Finite element analysis of blister formation in laser-induced forward transfer, Journal of Materials Research **26**, 2438 (2011).

[8] J. P. McDonald, V. R. Mistry, K. E. Ray, S. M. Yalisove, J. A. Nees, and N. R. Moody, Femtosecond-laser-induced delamination and blister formation in thermal oxide films on silicon (100), Appl. Phys. Lett. **88**, 153121 (2006), publisher: American Institute of Physics.

[9] J. R. Serranoand D. G. Cahill, Laser-Induced Blistering of Thin SiO2 on Si, Microscale Thermophysical Engineering **9**, 155 (2005).

[10] N. T. Goodfriend, S. V. Starinskiy, O. A. Nerushev, N. M. Bulgakova, A. V. Bulgakov, and E. E. B. Campbell, Laser pulse duration dependence of blister formation on back-radiated Ti thin films for BB-LIFT, Applied Physics A **122**, 10.1007/s00339-016-9666-x (2016).

[11] N. T. Goodfriend, S. Y. Heng, O. A. Nerushev, A. V. Gromov, A. V. Bulgakov, M. Okada, W. Xu, R. Kitaura, J. Warner, H. Shinohara, and E. E. B. Campbell, Blister-based-laser-induced-forward-transfer: a non-contact, dry laser-based transfer method for nanomaterials, Nanotechnology **29**, 385301 (2018).

[12] L. Rapp, A. P. Alloncle, A. K. Diallo, S. Nénon, C. Videlot-Ackermann, F. Fages, and P. Delaporte, Pulsed-Laser Printing Process for Organic Thin Film Transistors Fabrication, AIP Conference Proceedings **1278**, 824 (2010).

[13] Laser thermal patterning of OLED materials.

[14] K. S. Kaur, R. Fardel, T. C. May-Smith, M. Nagel, D. P. Banks, C. Grivas, T. Lippert, and R. W. Eason, Shadowgraphic studies of triazene assisted laser-induced forward transfer of ceramic thin films, Journal of Applied Physics **105**, 113119 (2009), publisher: American Institute of Physics.

[15] A. T. Godfrey, D. L. Kallepalli, J. Ratté, C. Zhang, and P. Corkum, Femtosecond-Laser-Induced Nanoscale Blisters in Polyimide Thin Films through Nonlinear Absorption, Phys. Rev. Applied **14**, 044057 (2020), publisher: American Physical Society.

[16] D. L. N. Kallepalli, A. T. K. Godfrey, J. Walia, F. Variola, A. Staudte, C. Zhang, Z. J. Jakubek, and P. B. Corkum, Multiphoton laser-induced confined chemical changes in polymer films, Opt. Express, OE **28**, 11267 (2020), publisher: Optical Society of America.

[17] D. L. N. Kallepalli, A. T. K. Godfrey, J. Ratté, A. Staudte, C. Zhang, and P. B. Corkum, Surface adhesion of back-illuminated ultrafast laser-treated polymers, Phys. Rev. Materials **5**, 045201 (2021), publisher: American Physical Society.

[18] V. Sametoglu, V. T. K. Sauer, and Y. Y. Tsui, Production of 70-nm Cr dots by laser-induced forward transfer, Opt. Express, OE **21**, 18525 (2013).

[19] J. M. Fitz-Gerald, A. Piqué, D. B. Chrisey, P. D. Rack, M. Zeleznik, R. C. Y. Auyeung, and S. Lakeou, Laser direct writing of phosphor screens for high-definition displays, Appl. Phys. Lett. **76**, 1386 (2000), publisher: American Institute of Physics.

[20] B. Hopp, T. Smausz, Z. Antal, N. Kresz, Z. Bor, and D. Chrisey, Absorbing film assisted laser induced forward transfer of fungi (Trichoderma conidia), Journal of Applied Physics **96**, 3478 (2004), publisher: American Institute of Physics.

[21] N. T. Kattamis, N. D. McDaniel, S. Bernhard, and C. B. Arnold, Laser direct write printing of sensitive and robust light emitting organic molecules, Appl. Phys. Lett. **94**, 103306 (2009), publisher: American Institute of Physics.

[22] M. Lenzner, J. Krüger, S. Sartania, Z. Cheng, C. Spielmann, G. Mourou, W. Kautek, and F. Krausz, Femtosecond Optical Breakdown in Dielectrics, Phys. Rev. Lett. **80**, 4076 (1998), publisher: American Physical Society.

[23] S. B. Aziz, O. G. Abdullah, A. M. Hussein, and H. M. Ahmed, From Insulating PMMA Polymer to Conjugated Double Bond Behavior: Green Chemistry as a Novel Approach to Fabricate Small Band Gap Polymers, Polymers (Basel) **9**, 626 (2017).

[24] Q. M. Al-Bataineh, A. A. Ahmad, A. M. Alsaad, and A. D. Telfah, Optical characterizations of PMMA/metal oxide nanoparticles thin films: bandgap engineering using a novel derived model, Heliyon **7**, e05952 (2021).

[25] T. J.-Y. Derrien, R. Koter, J. Krüger, S. Höhm, A. Rosenfeld, and J. Bonse, Plasmonic formation mechanism of periodic 100-nm-structures upon femtosecond laser irradiation of silicon in water, Journal of Applied Physics **116**, 074902 (2014), publisher: American Institute of Physics.

[26] V. Apalkovand M. I. Stockman, Metal nanofilm in strong ultrafast optical fields, Phys. Rev. B **88**, 245438 (2013), publisher: American Physical Society.

[27] N. Inogamov, V. Zhakhovsky, and K. Migdal, Laser-induced spalling of thin metal film from silica substrate followed by inflation of microbump, Applied Physics A **122**, 10.1007/s00339-016-9942-9 (2016).

[28] U. Zywietz, T. Fischer, A. Evlyukhin, C. Reinhardt, and B. Chichkov, Laser Printing of Nanoparticles, in Laser Printing of Functional Materials (John Wiley & Sons, Ltd, 2018) pp. 251–268.

[29] D. P. Banks, K. Kaur, and R. W. Eason, Influence of optical standing waves on the femtosecond laser-induced forward transfer of transparent thin films, Appl. Opt. **48**, 2058 (2009).

[30] J.-M. Guay, A. Villafranca, F. Baset, K. Popov, L. Ramunno, and V. R. Bhardwaj, Polarization-dependent femtosecond laser ablation of poly-methyl methacrylate, New J. Phys. **14**, 085010 (2012), publisher: IOP Publishing.

[31] J. Krüger, D. Dufft, R. Koter, and A. Hertwig, Femtosecond laser-induced damage of gold films, Applied Surface Science Photon-Assisted Synthesis and Processing of Functional Materials, **253**, 7815 (2007).

[32] L. Capuano, R. Pohl, R. M. Tiggelaar, J. W. Berenschot, J. G. E. Gardeniers, and G. R. B. E. Römer, Morphology of single picosecond pulse subsurface laser-induced modifications of sapphire and subsequent selective etching, Opt. Express, OE **26**, 29283 (2018), publisher: Optical Society of America.

[33] D. M. Rayner, A. Naumov, and P. B. Corkum, Ultrashort pulse non-linear optical absorption in transparent media, Opt. Express, OE **13**, 3208 (2005).

[34] A. Ben-Yakarand R. L. Byer, Femtosecond laser ablation properties of borosilicate glass, Journal of Applied Physics **96**, 5316 (2004).

[35] N. Sultanova, S. Kasarova, and I. Nikolov, Dispersion Properties of Optical Polymers, Acta Phys. Pol. A **116**, 585 (2009).

[36] This is calculated by the standard equation for intensity/fluence of an interfering wave. In terms of intensity, $I_{total} = I_1 + I_2 + 2\sqrt{I_1 I_2}\sin\phi$ where I_1 is the incident intensity, I_2 is the intensity of the reflected light, and ϕ is the phase difference between the incident and reflected light at some location in space. The enhancement factor is found by setting $I_2 = RI_1$ where R is the reflectance of the PMMA, and taking $\sin\phi = 1$ for fully constructive interference at a node.

[37] S. Baudach, J. Bonse, J. Krüger, and W. Kautek, Ultrashort pulse laser ablation of polycarbonate and polymethylmethacrylate, Applied Surface Science **154-155**, 555 (2000).

Chapter 6

Application of Laser-Induced Blisters as Microlenses

Blisters have not generally seen application beyond Laser-Induced Forward Transfer, except for changes in hydrophobicity using surface structuration as shown in Chapter 4. Since blisters are curved structures made from polymer with high transmission, they may also be useful as microlenses if made with the right dimensions (thickness and radii of curvature) provided that the linear refractive index and absorption properties do not change drastically after irradiation from an ultrafast pulse.

Figure 6.1 shows how a polymer blister can be thought of as a lens, for the simplifying case where surfaces can be considered spherical and for negligible laser penetration into the film of thickness t. For the cross-sectional profiles of blisters that we observed in the earlier focussed ion beam measurements, we see curvatures which face the same direction above and below the film, which match the shape of a meniscus lens. We also observed hollow regions beneath blisters which would be under ambient conditions at steady state, with an index of $n = 1$. The role of refraction from the substrate to the hollow region is neglected in our case, since we will only consider collimated light passed through the substrate into the hollow region for now.

A standard optics textbook such as Hecht's *Optics, Fifth Edition* [39] describes the fo-

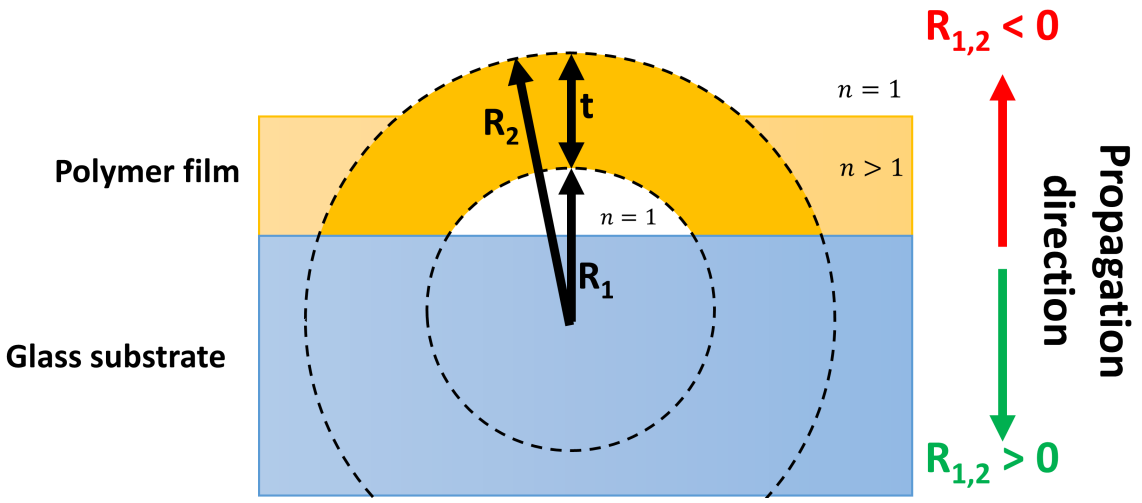

Figure 6.1: An idealized spherical polymer blister may be considered as a thick lens with thickness t, radii of curvature R_1 and R_2, and refractive index $n > 1$. When light is sent through the lens from the substrate side, R_1 and R_2 are negative. When light is sent though the polymer side, R_1 and R_2 are both positive and their subscripts should be exchanged in the above image.

cussing behaviour of a lens with non-negligible thickness with the following equation:

$$\frac{1}{f} = (n-1)\left(\frac{1}{R_1} - \frac{1}{R_2} + \frac{n-1}{n}\frac{t}{R_1 R_2}\right) \tag{6.1}$$

where f is the focal length of the lens, n is the refractive index of the material comprising the lens, R_1 and R_2 are the front and back radii of curvature, respectively, and t is the central thickness of the lens. From inspection of Figure 6.1 and previous FIB studies of blister cross-sections, we see that the curvature of the surface below the polymer film is much sharper than that of the top surface. Hence, it must be the case that R_1 and R_2 are negative due to orientation and $\frac{1}{|R_1|} > \frac{1}{|R_2|}$, meaning that the term $\frac{1}{R_1} - \frac{1}{R_2}$ gives a negative contribution to the focal length. However, the last term, proportional to $\frac{t}{R_1 R_2}$, must always provide a positive contribution to the focal length. As we saw in Chapters 3 and 5, blisters become taller and have greater curvature (i.e., their heights grow much more rapidly than their diameters) as laser pulse energy is increased. If the last term proportional to $\frac{t}{R_1 R_2}$ can dominate at higher overall curvatures, and if $\frac{1}{R_1} - \frac{1}{R_2}$ can be sufficiently small, these structures may act as tightly focussing microlenses. In Chapters 4 and 5, we also saw how laser pulses partially penetrate

the thin film and modify the material beneath the film's surface. We must also be aware that this modifies the thickness of the film comprising the blister, and since our beam is Gaussian, there may also be more penetration at the center of the blister, leading to a larger negative value of R_1. For these reasons, it is difficult to make further predictions without experimental results. Laser modification, which is confined below the film in our case, is also known to increase the refractive index of a polymer. However, it is unlikely that this would play a significant role compared to changes in structure curvature, since typical refractive index changes of this kind are on the order of 10^{-4} to 10^{-2} [117]. In our previous experiments, we noticed that polyimide blister formation with femtosecond pulses resulted in some sub-wavelength-scale debris or nanoparticles trapped beneath the film as shown by focussed ion beam dissection [118, 119]. The extent to which these nanoparticles would affect the optical quality of the microlenses was not considered for this work, but should be examined in a future systematic study.

Generally, micro-optical elements such as lenses, mirrors, gratings, and waveguides, are important for usage in beam shaping and homogenization, fiber optic coupling, wavefront sensing, usage of cameras, and photovoltaic cells [120–125]. Fabrication of such elements is usually done by photolithography, where a photosensitive thin film is exposed to light through a mask, followed by a series of chemical treatment procedures [126–129]. However, the high cost of equipment and the lengthy fabrication process restricts photolithography technology to mass production by foundries and large companies and institutions. Femtosecond Laser Direct Writing, on the other hand, offers advantages over photolithography in terms of its simplicity, lower overall cost, and ease of fabrication of optical elements anywhere in the material [130–135].

Direct writing of microlens and microlens arrays in bulk material has been performed in both polymer and glass. Naessens *et al.* used ultraviolet nanosecond pulses to machine 200-µm-wide microlenses into a polycarbonate substrate [128]. While effective, this was a multistep ablation process requiring exposure of hundreds to thousands of pulses while simultaneously varying the circularly symmetric beam shape projected onto the material.

The microlenses also required a final smoothing step using a larger nanosecond laser beam. Lin *et al.* fabricated 150-µm-wide microlenses into photosensitive glass by exposure to near-infrared femtosecond pulses followed by a hydrofluoric acid etch of the exposed glass and several hours of high-temperature baking [129]. Meunier *et al.* used $\sim 76 \times 10^6$ near-infrared femtosecond pulses from a 76 MHz oscillator focussed into polycarbonate to cause heat accumulation and melting, which caused surface swelling and yielded microlenses with diameters between 50 and 100 µm [136]. The structure sizes were varied by adjusting the depth of the laser focus inside the material, and the resulting diameters were all significantly larger ($\geq$50 µm in diameter) than the beam waist diameter of $\sim$1.3 µm due to the reliance on heat accumulation.

More recently, Surdo *et al.* have adopted an additive approach using laser catapulting of polymer disks followed by thermal reflow [137, 138]. This technique uses single ultraviolet nanosecond pulses to eject intact polymer sections from a donor film onto a substrate. The substrate is then heated, causing the polymer disks melt and reflow into smoothed microlenses. This technique offers flexibility of lens shape (circular, triangular and cylindrical) without lithography and can print lenses onto curved or flexible surfaces, which are useful advancements. However, it is still somewhat complicated since it requires a non-trivial material transfer process and the processing step of thermal reflow. Thermal reflow also necessarily widens the polymer disks as they are shaped into microlenses.

The aforementioned works (with the exception of Meunier *et al.* [136]) require multiple steps and/or active control of the machining assembly while a lens is being formed, which make these techniques time-consuming. All previous works also rely on some form of sustained heating, applied using lasers or external heat sources, which ultimately restricts the limit of microlens sizes that can be realized. In other words, none of the above techniques take full advantage of the inherent heat localization that comes with energy deposited from single femtosecond pulses. If laser-induced blisters made by single femtosecond pulses show adequate lensing behaviour, they could enable convenient and truly on-demand (single-pulse) fabrication of microlenses with no post-processing. As shown in Chapters 3 and 5, the limit-

ing blister diameters we have achieved are smaller than 1 µm (near the diffraction limit) and could likely be made even smaller, which would cover the lower bound of any structure that may be useful as a microlens.

In the work shown ahead, we create blister microlens arrays fabricated in a back-illumination geometry. As in Chapter 3, each blister is made by a single femtosecond pulse forming a blister in a thin polyimide film. We create arrays of blisters with varying pulse energies and focal spot diameters and examine their feasibility as microlenses by direct imaging of a collimated light beam passed through the arrays. This work serves as a proof of concept for the use of blisters as microlenses.

6.1 Experimental Details

6.1.1 Blister Fabrication

For this study, we used a polyimide film coated onto a circular fused silica substrate with a diameter of 50 mm and a thickness of 500 µm. Fused silica was chosen for the substrate due to its larger bandgap (∼9 eV) and higher breakdown threshold (up to $\sim 10^{14}$ W/cm^2) compared to borosilicate glass in earlier studies [139–141]. We first cleaned the substrates by pre-rinsing in acetone, isopropyl alcohol and deionized water and dried them on a hotplate. We then spin-coated the substrate using PI-2555 precursor from HD Microsystems at 3000 revolutions/min for 60 s. This yielded a film thickness of 2.7 ± 0.1 µm as determined with a Bruker Dektak XT contact profilometer. Our earlier linear absorption data of polyimide films [106] showed transparency for wavelengths above approximately 450 nm, so while many other polymers have broader transmission windows, polyimide is still able to pass much of the visible spectrum and is adequate for testing purposes.

For blister fabrication, we used our experimental setup shown in Figure 2.5 with a 10× 0.2 NA microscope objective and followed the procedures outlined in Section 2.2. The estimated beam waist diameter was 6.1 µm and the corresponding Rayleigh length was estimated to be 36 µm, calculated using Equations 2.4 and 2.5. We fabricated 4 × 4 arrays of blisters using

single pulses at each location, with 20-µm center-to-center separations between structures. Each array was made with a different pulse energy (between 210 and 1610 nJ) and distance between the film and the beam waist (between 0 and 250 µm). This allowed us to look for potential microlensing effects across a large variety of structure sizes and induced blister heights and curvatures. Figure 6.2 shows an optical microscope image summarizing the fabrication experiment. The beam waist of our focussed near-infrared pulses was always placed ahead of the sample (denoted by z_{IR} in Figure 6.2) to avoid excessive intensity in the glass substrate, which would otherwise drive optical breakdown as discussed in previous chapters. Further, we take the intensity threshold for polyimide blister formation in this work to match our earlier work ($\sim 3 \times 10^{12}$ W/cm^2 [106], almost two orders of magnitude below the optical breakdown threshold of fused silica [139–141]. In general, substrate absorption did not occur in most cases of interest due to this large disparity in intensity thresholds; we estimate that it would only be significant for pulse energies of 540 nJ and higher for $z_{IR} = 0$ µm. We will concentrate on the structures made using larger off-focus distances ($z_{IR} \geq 225$ µm) as they showed the clearest lensing effects, likely owing to the larger resulting structure diameters and hence better light-gathering power.

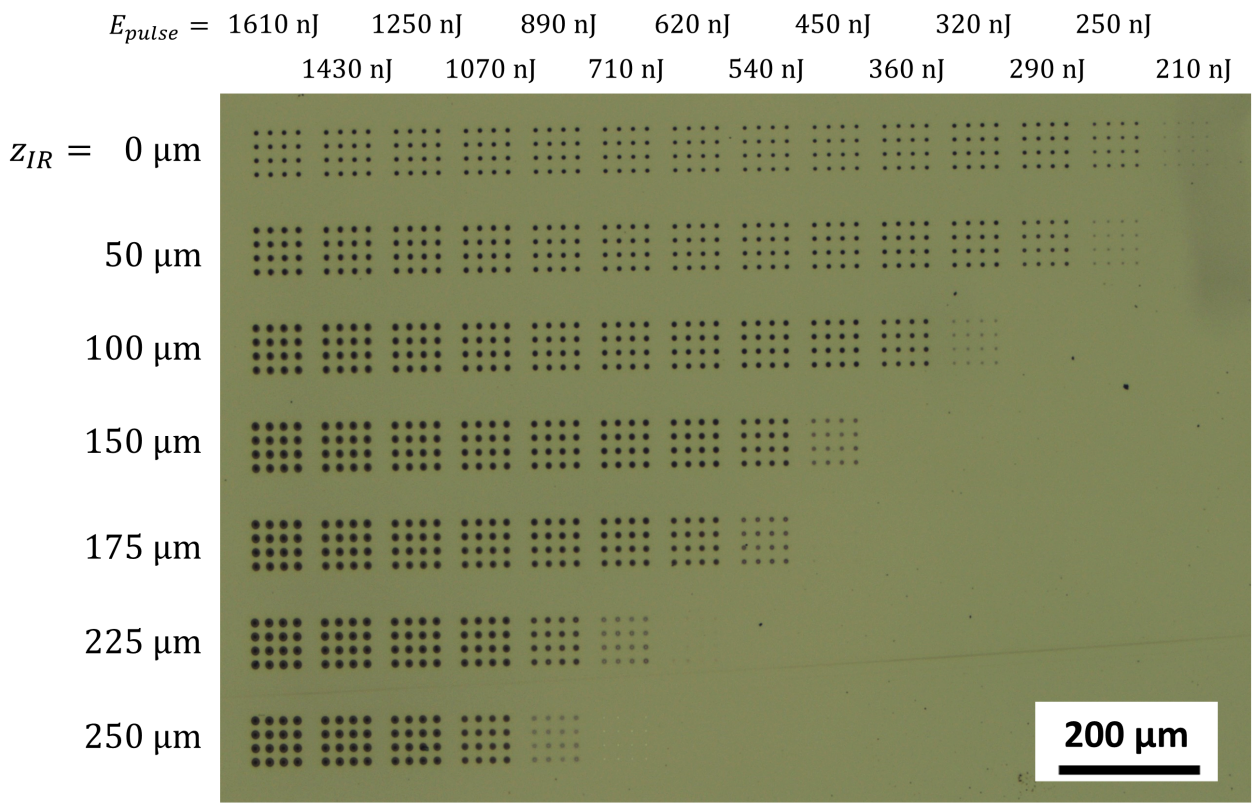

Figure 6.2: An epi-illumination colour microscope image (light introduced and collected from the polyimide side of the sample) showing all blister arrays made in the experiment. The structures made close to the pulse energy threshold in each row (e.g. 710 nJ for $z_{IR} = 250$ µm) are difficult to resolve due to low contrast, but are easier to resolve by optical microscopy with a transmitted-light geometry and by atomic force microscopy shown later. Pulse energies are corrected for all transmission losses in the setup.

6.1.2 Characterization

In addition to *in situ* imaging as detailed in Section 2.2, we performed *ex situ* inspection by taking epi-illumination colour images of the sample with a Zeiss Axio Imager M2.M widefield optical microscope as shown in Figure 6.2. We then characterized the focussing behaviour of blister microlens arrays using a Nikon Eclipse Ni-U upright widefield microscope. We modified the microscope by removing the condenser lens and inserting a vertically oriented Thorlabs CPS532 CW laser diode ($\lambda = 532$ nm, 4.5 mW output power, 3.5 mm beam diameter) which provided collimated back-illumination of our sample. This allowed us to directly image the focussing of a monochromatic beam with an approximately uniform illumination

over each array. A simple schematic of this measurement is shown in Figure 6.3.

The microscope objective used for imaging the transmitted laser light was a Nikon Plan Apo 40× 0.95 NA DIC M N2 microscope objective with a correction collar to compensate for 110 – 230 µm of glass coverslip thickness. However, we imaged the microlenses from the polyimide film side (i.e. through no additional glass) and thus set the correction collar to the minimum correction level to minimize image aberration. Imaging with an NA of 0.95 ensured that virtually all transmitted light was collected. We acquired z-stack images for each array with 151 slices, each slice separated by 1 µm along the optical axis. We post-processed the 3D z-stack image data using Fiji (ImageJ) freeware to extract cross-sectional profiles of the image along the XZ plane for a subset of 4 blisters in each array. The z-position of the film surface ($z = 0$) was estimated by determining the position of the best image focus on the blister structures. At high image magnification, differences of 1 µm in structure height are resolvable in that the top of a blister can appear in focus, while the sample surface is out of focus.

We also performed atomic force microscopy (AFM) characterization of each array using a Bruker Dimension Icon atomic force microscope. This was used to measure blister heights and diameters, and to provide direct confirmation that the polyimide film did not undergo rupture during blister formation, which would greatly diminish the smoothness and surface quality of blisters. Analysis was performed using Gwyddion freeware to extract the heights, diameters and fitted quadratic curvatures (inverse radii of curvature) of blisters.

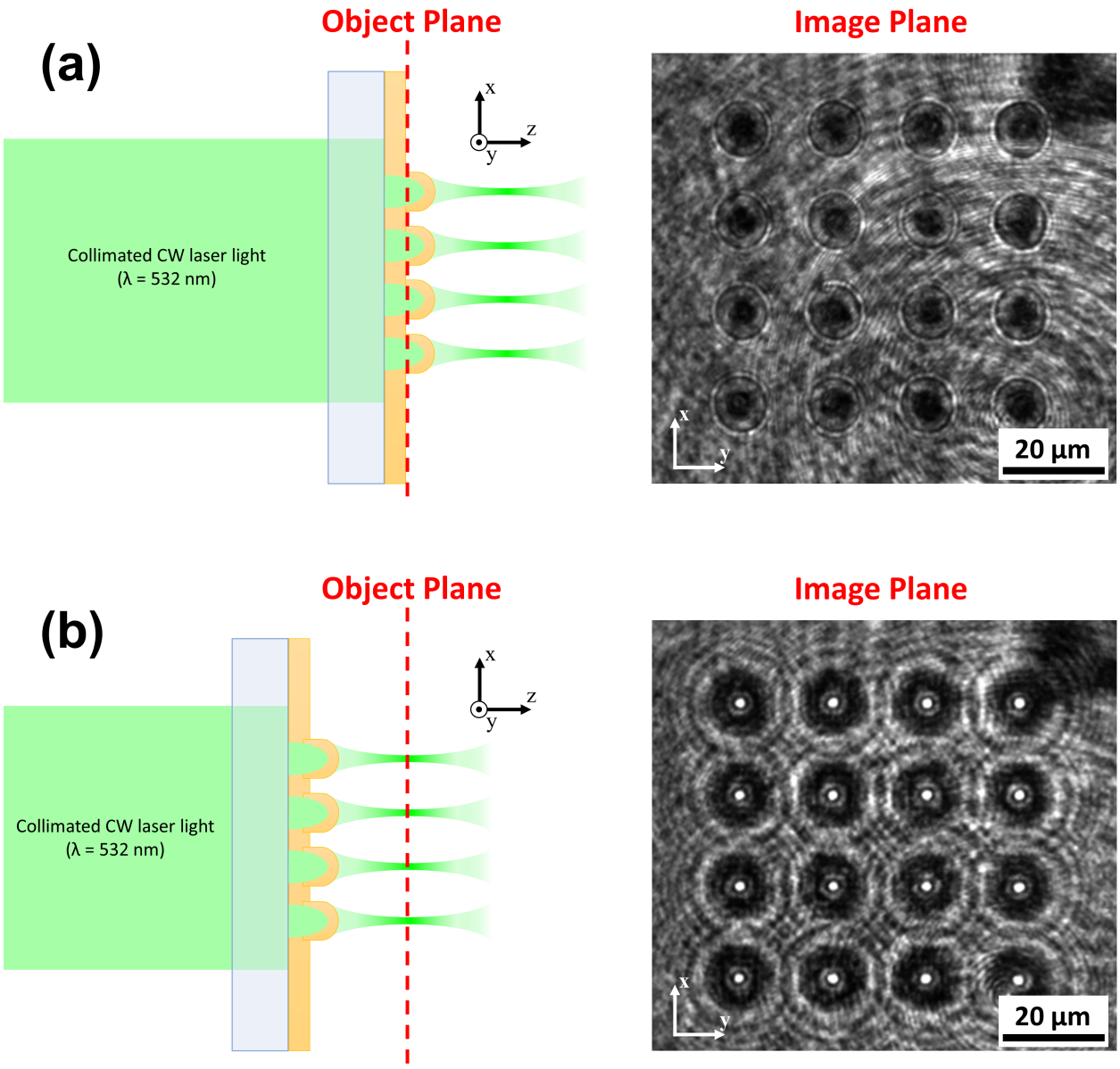

Figure 6.3: **(a)** Schematic of how the polyimide surface containing blister arrays is imaged using the transmitted diode laser beam. The left image is a diagram showing blisters placed in the object plane of the microscope. The green laser beam is sent in the positive z-direction, through the glass substrate and the polyimide blisters. The right image is the microscope image generated at the image plane (on the CCD of the microscope), for blisters made with a pulse energy of 1610 nJ and where the pulsed laser beam waist was placed 250 µm ahead of the polyimide film. **(b)** Same as in (a), but the sample has been retreated 33 µm from the object plane to image the focal spots generated by the blister microlens array. Note the obstruction in the top right corner of the microscope images, which did not appear in other forms of characterization, was due to debris within the Nikon microscope.

6.2 Results and Discussion

Figure 6.4 summarizes the optical and surface characterization of a polyimide blister array made using single pulses with 1610 nJ of pulse energy focussed 250 µm ahead of the polyimide film.

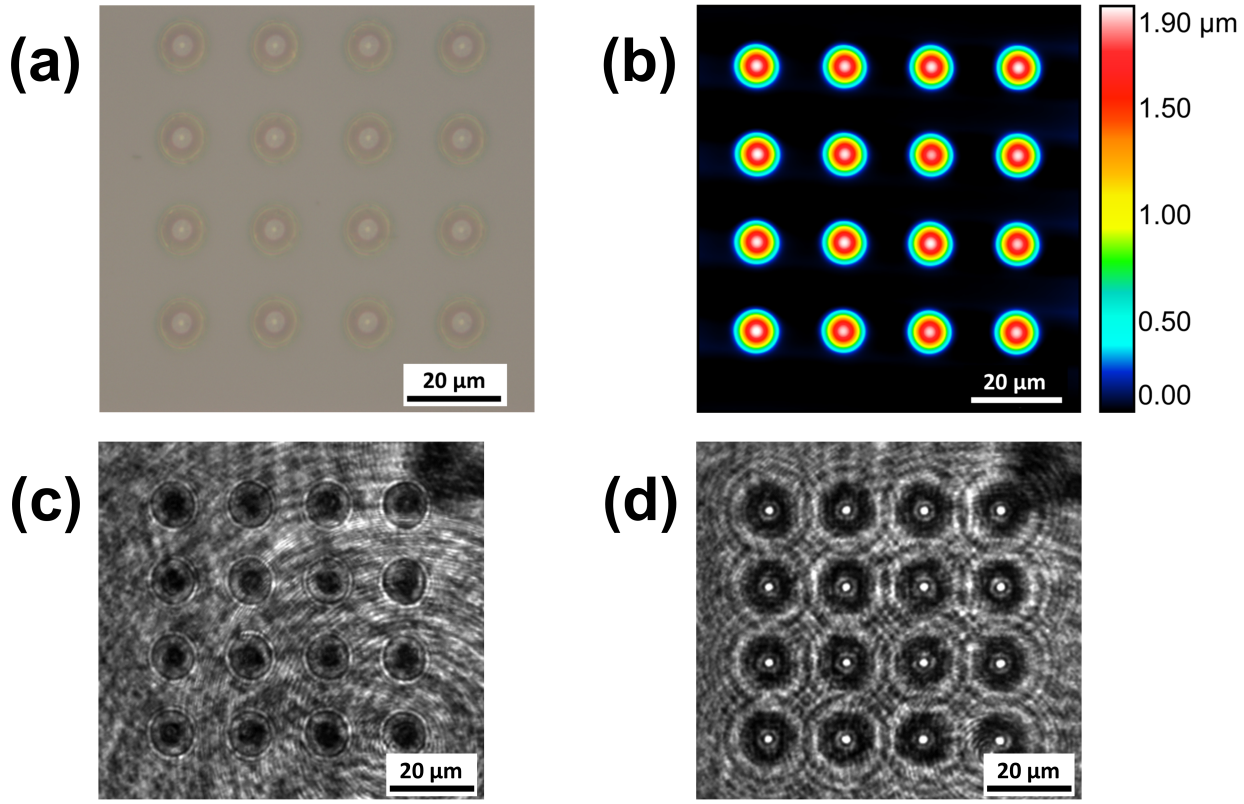

Figure 6.4: Images of a blister array (E_{pulse}=1610 nJ, z_{IR}=250 µm) generated by various forms of optical and surface characterization: **(a)** a colour microscope image (Zeiss Axio Imager), **(b)** a surface height map using AFM (Bruker Dimension Icon), and transmitted light images (modified Nikon Eclipse Ni-U) of **(c)** the polyimide film placed in focus and **(d)** the collection of focal spots generated 33 µm ahead of the film. Note the obstruction in the top right corners of (c) and (d), which are attributed to debris within the Nikon microscope.

In the measurements shown in Figure 6.4, the shot-to-shot repeatability and circularity of the blisters is apparent. The structures appear nearly identical to each other in Figure 6.4(a), with various concentric rings of colour seen in each structure which can be attributing to interference in the thin film. It is likely that this is interference between reflections from the top and bottom of the polyimide film, which would be thinner at the center of the blister due to higher intensity (and thus, penetration) of the Gaussian spatial profile of the laser

beam. However, an additional reflection from the substrate could also occur since the film is delaminated during blister formation. The AFM height map in Figure 6.4(b) shows that the blisters are intact with no signs of cracking or rupture (as discussed in Chapter 3) and have little variation in dimension. The average heights and diameters of the blisters are 1.88 ± 0.02 µm and 10.00 ± 0.02 µm, respectively, where diameters are based on the full width at $1/e^2$ of the maximum height. In Figure 6.4(c), blisters are again imaged using collimated laser illumination, and in Figure 6.4(d), the focal spots generated by these structures are imaged µm ahead of the sample surface.

To further characterize the focussing behaviour of blister microlenses, we explore the cross-sectional view (i.e. XZ slices) of the three-dimensional image data collected using the modified upright Nikon microscope. Figure 6.5 and Figure 6.6 show the XZ slices of the 3D image data for 4 blisters made at various energies for z_{IR} = 225 µm and z_{IR} = 250 µm respectively. At the highest pulse energies (in Figure 6.5(ab) and Figure 6.6(ab)), the blister microlenses focus the laser illumination approximately 33 µm ahead of the film. Asymmetric elongation of the foci is visible in all cases, though this is seen in many works on microlenses [137, 138] as well as in the point spread functions of high-NA microscope objectives. Therefore, though they are worth noting, these deviations from ideal Gaussian focussing are a minor consideration regarding lens performance. Taking the structure base radii to be approximately 5 µm according to the earlier AFM measurements, the numerical aperture of these microlenses is $n_{air}\sin(\theta_{max}) = r/f \approx 0.15$ [39]. In this estimate, f is the focal length and we assume that the blister radius r is also the location of the outermost ray being focussed.

For the lowest pulse energies in Figure 6.5(efg) and Figure 6.6(def), we see virtual foci behind the film, with shorter negative focal lengths at lower pulse energies. This indicates that the blister microlenses transition from being strongly divergent to strongly convergent as pulse energy is increased. The diverging behaviour at lower pulse energies can be explained by Equation 6.1 in the limit of small outer curvature of blister structures. If the laser penetration from the Gaussian pulse creates a much larger inner curvature than that of the top side of the

film ($\frac{1}{|R_1|} \gg \frac{1}{|R_2|}$), meaning that laser energy was deposited without causing significant blister expansion and leaving the top surface nearly flat, Equation 6.1 reduces to $f \approx \frac{R_1}{n-1}$. This focal length is negative since R_1 is always negative. However, as pulse energy is increased and more overall curvature is added to the film, the terms containing R_2 in Equation 6.1 give larger positive contributions and must eventually become larger in magnitude than the negative $\frac{1}{R_1}$ term. At the highest pulse energies, the last term in Equation 6.1 (which is dependant on film thickness and effectively quadratic in the overall curvature of the film) may begin to dominate while the first two terms may become closer in magnitude to one another and lessen the negative contribution to the focal length.

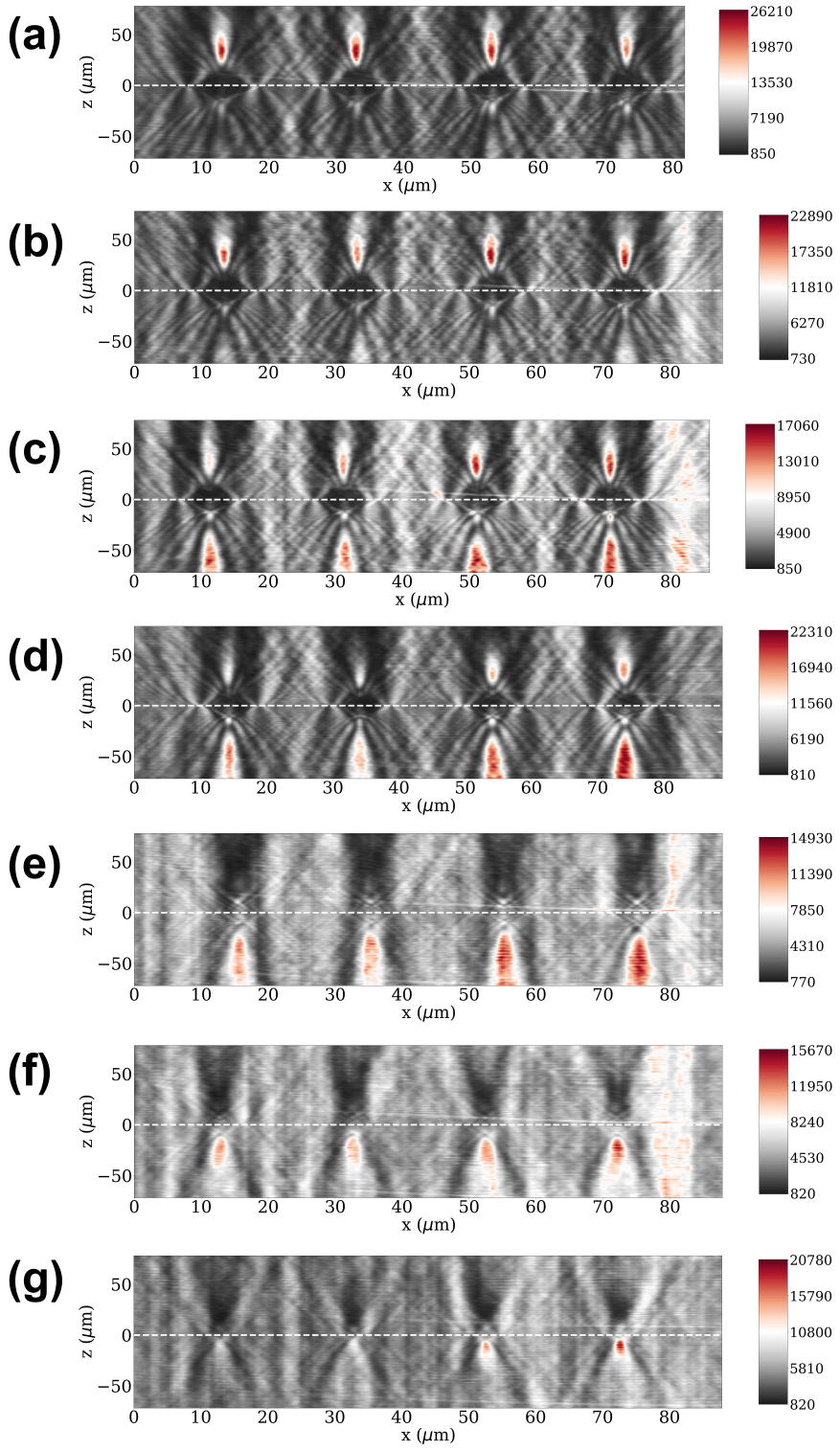

Figure 6.5: XZ cross-sectional images of continuous-wave laser light ($\lambda = 532$ nm) refracted by a row of 4 blister microlenses made using single pulses with energies of **(a)** 1610 nJ, **(b)** 1430 nJ, **(c)** 1250 nJ, **(d)** 1070 nJ, **(e)** 890 nJ, **(f)** 710 nJ and **(g)** 620 nJ for $z_{IR} = 225$ µm. We estimate the peak intensity of the pulses used to fabricate the blisters in (a) to be 7.6 TW/cm^2. Positive values of z denote distances ahead of the polyimide film surface. Bright regions on the right side of some images which are attributed to scattering from debris within the Nikon microscope.

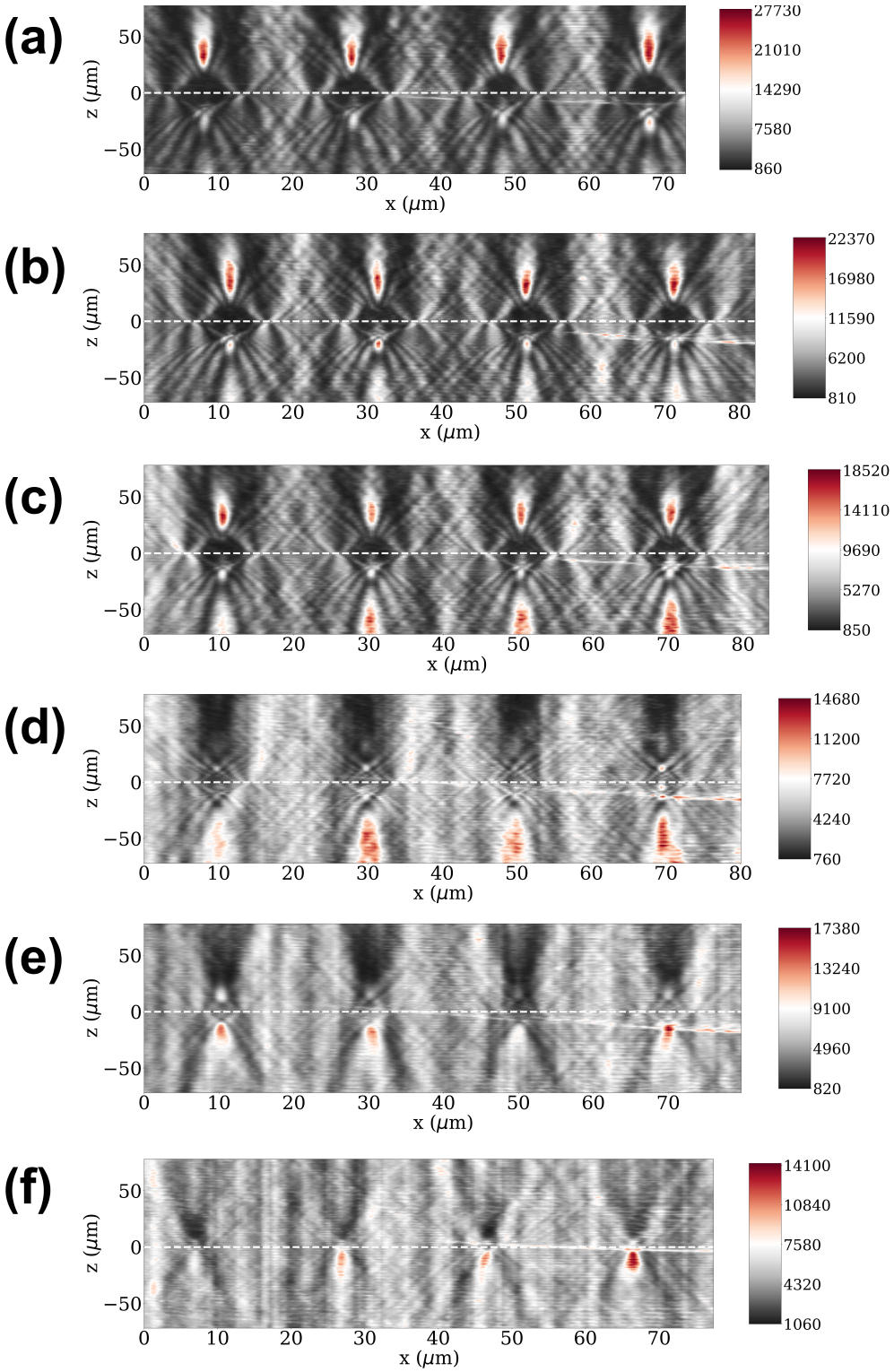

Figure 6.6: XZ cross-sectional images of continuous-wave laser light ($\lambda = 532$ nm) refracted by a row of 4 blister microlenses made using single pulses with energies of **(a)** 1610 nJ, **(b)** 1430 nJ, **(c)** 1250 nJ, **(d)** 1070 nJ, **(e)** 890 nJ, and **(f)** 710 nJ for $z_{IR} = 250$ µm. We estimate the peak intensity of the pulses used to fabricate the blisters in (a) to be 6.2 TW/cm^2. Positive values of z denote distances ahead of the polyimide film surface. Bright regions on the right side of some images which are attributed to scattering from debris within the Nikon microscope.

It also must be noted that there is dual behaviour (both focussing and defocussing of light) in the intermediate cases shown in Figure 6.5 and Figure 6.6. This may be because the shape of the inner and outer blister surfaces may differ enough from ideal quadratic curved surfaces that the focal distance of rays depends on the distance from the center of the microlens. This is spherical aberration, though these structures are in the thick lens regime (i.e. where the third term in Equation 6.1 is not negligible) and so the considerable thickness of these lenses and the center-weighted laser penetration into the film may be the cause of this effect. Thinning of the film at the center of blisters may reduce the positive contribution of the thickness-dependant term in Equation 6.1, allowing for a long negative focal length at the center of blisters in the intermediate pulse energy regime. Dependence on the radial distance from the center of the lens may allow both focussing and defocussing to take place over the same lens in principle. This dual effect could also be caused by the delamination of surrounding parts of the film that were not directly penetrated by the laser, inducing similar curvatures on either side of this boundary but creating a step-like change in thickness. However, further characterization using focussed ion beam dissection may be required to explore these possibilities, and the additional effect of a refractive index change in the melt front beneath the film.

The AFM data shown in Figure 6.7 summarizes the resulting dimensions and average curvatures of blister structures. Using AFM, we observed intact blister formation with no cracking or rupture in all cases. The earlier arguments about the transition from diverging to converging lens behaviour is also supported by the AFM data in Figure 6.7. At lower pulse energies, the heights of blisters are small relative to their diameters, resulting in very small outer curvatures. For this reason, we notice a high degree of correlation between pulse energy and curvature of the top surface of blisters, though it is difficult to make conclusions based on outer curvature alone. As mentioned above, focussed ion beam dissection is necessary to obtain information about the curvature and other modification beneath the film. There was little variation in structure diameter due to the large beam cross-section on the sample, compared to our work in earlier chapters. The maximum outer curvatures for the structures

of interest, observed for $z_{IR} = 225$ µm, were approximately -150 mm^{-1}. However, this represents the average curvature taken over the circle with its circumference at $1/e^2$ of the maximum blister height. This may underestimate the maximum curvature since it includes the bordering region of the blister. This region would have lower curvature since blisters are smooth continuous structures on the initially flat film. Reducing the size of the bounded region for the curvature fit to approximately 60% of the maximum height, we see a higher outer curvature of approximately -175 mm^{-1}, corresponding to a radius of curvature of approximately -5.7 µm. Taking an upper bound estimate using Equation 6.1 with $n = 1.7$, $t \approx 2.7$ µm and $R_1 \approx R_2 \approx -5.7$ µm, the focal length of lenses with these parameters would be approximately $+42$ µm. This estimate agrees reasonably well with our observations in Figure 6.5 and Figure 6.6. It does not account for potential thinning of the film due to laser penetration, but such an effect may also be counteracted by densification of the polymer that has been modified.

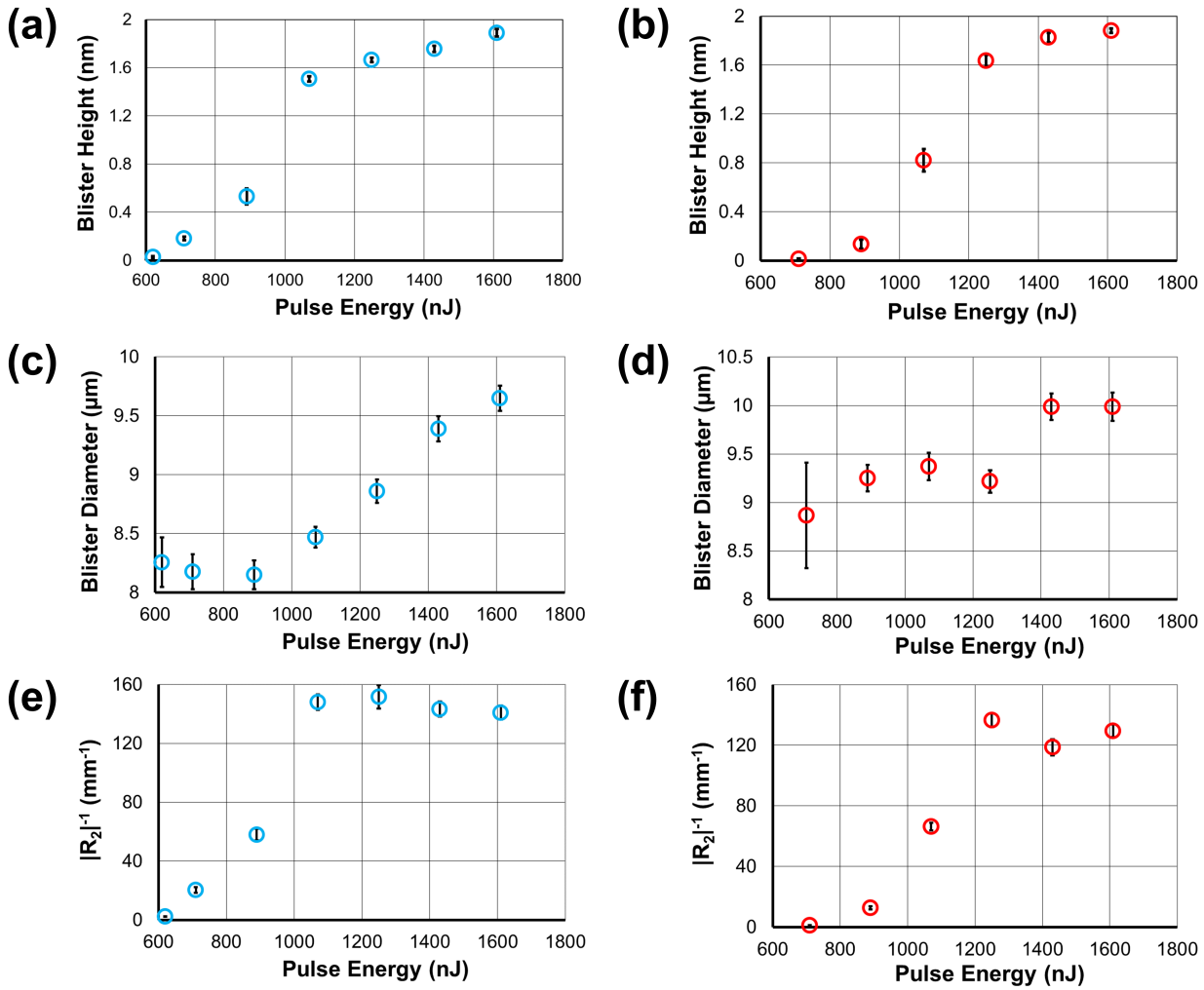

Figure 6.7: Heights of blisters from Figure 6.5 **(a)** and Figure 6.6 **(b)**, $1/e^2$ diameters of blisters from Figure 6.5 **(c)** and Figure 6.6 **(d)**, and average magnitude of the curvature (inverse radius of curvature) of blisters from Figure 6.5 **(e)** and Figure 6.6 **(f)**, as measured by AFM.

6.3 Conclusions and Outlook

Microlenses are a versatile micro-optic used in a variety of technologies, and practical and rapid methods for their fabrication are desirable. In this work, we have demonstrated a novel microlens fabrication method using single femtosecond pulses to form microlenses in a polymer film coated on glass. This process requires a single pulse with no follow-up steps required in many other fabrication methods. The lens behaviour can be made strongly

divergent or convergent depending on the laser penetration into the underside of the film and the overall level of induced curvature from blister formation. In principle, these lenses are easy to fabricate on any surface and could be integrated with other optical elements such as waveguides in micro- and nano-optics.

The use of pulses with Gaussian spatial profiles may have resulted in non-uniform penetration into the film in this work, which would cause variation of the curvature as a function of radial distance from the center of microlenses. This may be mitigated by implementing flat-top beam shaping, pre-focussing in the substrate to flatten the Gaussian intensity profile [87], or thicker polymer films which would lessen the relative extent of laser penetration, ultimately leading to less axial elongation of microlens focal volumes and removal of dual focussing behaviour in the intermediate pulse energy regime. Once this is addressed, it may be interesting to further examine the intermediate behaviour seen in Figure 6.5 and 6.6 to explore focal length tunability.

Further studies would be required to explore how the inner curvature is affected by laser penetration as well as a potential refractive index change in the modified polymer beneath the film. Exploration of blister structures using FIB has proven to be useful in our earlier works and could be used to answer these questions and allow for modelling of blister microlenses by ray tracing. Future optical characterization (using either incoherent white light through a narrow bandpass filter or laser light passed through a polarization scrambler or depolarizer) may be more useful for precise characterization without the appearance of interference fringes. Reduced spatial coherence in the light beam may also aid in having truly uniform illumination of the microlens arrays for clear quantification of shot-to-shot repeatability of structures. Polymers with a wider transparency window than polyimide (such as PMMA or polycarbonate) could also be used, along with multiple wavelengths in optical characterization to assess chromaticity.

Larger microlenses than those shown in our work are still certainly of interest. It may be possible to scale this technique up using thicker films and pulsed lasers with much higher pulse energies. Ultrafast pulsed laser sources reaching up to millijoules of pulse energy are now

commercially available [142–144]. Pulses could also be lengthened to limit peak intensity and peak power, to mitigate self-focussing and substrate breakdown and allow for lenses of larger diameters. Ultraviolet nanosecond lasers, like in the work of Surdo *et al.* [137, 138] and earlier polyimide blister formation work of Arnold's group [69, 93, 116], may also be beneficial for scaling up the size of blister microlenses. Ultraviolet pulses have limited penetration due to strong linear absorption in polymers, and the peak powers and intensities would be sufficiently low that substrate interactions would not be a concern. If blister microlens fabrication is also realized at larger length scales, this method may provide a rapid, industrially viable process for fabricating microlenses and microlens arrays at any size scale required.

Chapter 7

Conclusions and Future Scope

7.1 Conclusions

Femtosecond pulses enable localized energy deposition due to pulse durations far below the thermal relaxation time of most materials and high intensities which enable nonlinear absorption processes. These properties lead to spatial confinement of the deposited energy, enabling laser-induced structure sizes can below the diffraction limit. In this thesis, I have used nonlinear absorption of femtosecond pulses to develop polymer blister formation at the few-micrometer scale and nanoscale. This represents a factor-of-2 improvement on what was achieved in glass films on silicon [82], and a factor-of-10 improvement on what had been shown for back-illuminated polymer films on glass which are relevant to LIFT applications [69].

In Chapter 3, we extended polymer blister formation to the nanoscale using nonlinear absorption of femtosecond pulses. We have made the smallest laser-induced blisters to date to our knowledge (400 nm full width at half-maximum), below both the spot size of the laser and the laser wavelength (800 nm) used. We also accounted for nonlinear absorption that occurs in the substrate as the focussed pulse travels toward the polymer film. We demonstrated a linear relationship between energy deposited in the film and the resulting volume of the laser-induced blister.

In Chapter 4, we explored the resulting changes to chemical composition and surface adhesion when a polymer film is textured using blisters. We provided direct evidence that laser-induced chemical changes are confined beneath the film, and that changes to the surface are purely morphological. We showed that laser-induced blisters offer a way to create superhydrophobic surfaces using inexpensive polymer films without relying on laser-induced chemical changes. This allows for tailoring of film chemistry and structuration independently.

In Chapter 5, we proposed an advanced method for blister formation, a dynamic release mirror structure (DRMS), which can be used for Laser-Induced Forward Transfer (LIFT). It relies on a multi-layer composition where nonlinear absorption can occur in polymer and/or metal layers while also restricting laser penetration using the opacity of the metal layer. This allows the DRMS to be driven by high intensities and fluences while preventing residual intensity below the nonlinear absorption threshold to pass through and modify a sensitive transfer material before it can undergo LIFT. This method combines the advantages of polymers and metals as dynamic release layers for LIFT while mitigating the drawbacks of using the materials individually. Using multiple layers also introduces a new avenue for tunability of the process by thicknesses and material selection. While this work has served as a proof-of-concept, it would be interesting to explore its utility for LIFT in experiment. One could tailor the absorption and intact expansion of the film by choice of film material and thickness. Effects of pulse duration could also be explored. The DRMS approach could be explored for nanosecond and picosecond durations and larger size scales typically used for LIFT, where it may provide more control and flexibility for LIFT processes as well.

In Chapter 6, we used blister formation as a method for direct printing of microlenses into a polymer film. This method is extremely rapid, using single laser pulses with no post-processing steps. In theory, this limits the processing speed to that of the stage motion required for patterning and the laser-pulse repetition rate. Previous works using laser pulses in microlens fabrication required cumbersome fabrication processes, post-processing steps, and/or lengthy laser exposures [127, 129, 136–138]. We characterized the lens behaviour as a function of pulse energy (and thus intensity and fluence) and noted the transition from

diverging to converging lens behaviour as pulse energy was increased. Since we used tightly focussed femtosecond pulses with Gaussian spatial profiles, we suspect that laser penetration at the center of the spatial profile caused appreciable negative curvature on the underside of blisters. This non-uniform laser penetration was also observed directly using focussed ion beam (FIB) measurements in our earlier works. This leads to divergent behaviour at low overall blister curvature, but higher pulse energies give higher overall curvatures that allow the thickness-dependent term in the thick lens equation to dominate, since it is approximately quadratic in overall curvature.

This fabrication technique could be refined in future studies. Perhaps the most important questions left to address are the roles of refractive index change and curvature induced by the penetration of the Gaussian pulse profile. The curvature due to laser penetration could be minimized using either direct flat-top beam shaping or profile flattening from nonlinear substrate absorption [87]. We expect this to minimize the curvature of the underside of blisters, which would minimize the divergence induced by this interface and hence improve focussing power of these microlenses. This may also help to reduce the aberrations of the foci, since we suspect the variation in thickness caused by the laser penetration contributes to this. Polymers such as polymethyl methacrylate and polycarbonate offer greater transparency in the visible spectrum, and hence may be more useful for applications. Earlier works showed that blister formation is possible using UV nanosecond pulses [69, 93, 116]. UV nanosecond pulses would provide a convenient way to scale up the size of microlenses and microlens arrays made using this method while avoiding substrate interactions.

7.2 Future Scope

Femtosecond pulses provide heat localization that make them useful for laser ablation. Ablation, in contrast to the formation of intact blisters shown in this thesis, is the removal of small portions of material from bulk material or a thin film. Blister formation is adjacent to ablation of a thin film; as shown in Chapter 3, if too much energy is deposited into the

film, blisters begin to rupture. For an even thinner film, intact blister formation does not occur, and the laser-irradiated portion of the material is simply removed (i.e. ablated) from the film.

One novel application of laser ablation is in imaging mass spectrometry, where a pulsed laser is fired at various locations on a solid material, and the material ablated from each location is analyzed by mass spectrometry. This technique provides 2D and 3D spatial maps of chemical composition, with resolution determined by the ablation spot size. This is particularly interesting for biological applications, where tissue can be sectioned into slices thinner than 100 nm [145] and each slice can be interrogated independently.

Specialized metal-atom staining techniques can also be used for biological tissue, where hundreds of rare-earth-metal atoms on a polymer chain are attached to an antibody which then binds to target proteins of interest [146]. When the ablated tissue is analyzed with a mass spectrometer, these rare-earth metals provide strong, distinct signals corresponding to specific proteins. Imaging mass spectrometry paired with rare-earth metal staining is called imaging mass cytometry, where metals are measured as a proxy for various proteins. This technique provides direct biological insights which are relevant to cancer research [147, 148], immunology [149], gastroenterology [150, 151], and transplant surgery [152].

One of the leading commercial imaging mass cytometers is the Standard BioTools (formerly Fluidigm) Hyperion+ imaging mass cytometry system [153, 154]. The system consists of a UV nanosecond pulsed laser system (Nd:YAG, $\lambda = 213$ nm) with a spot size of 1 µm. The laser is used to ablate biological tissue samples shot-by-shot, and the plumes of ablated material are caught in an argon gas flow directed parallel to the sample surface. The gas flow leads the ablated material in an inductively coupled plasma (ICP) torch, where it is efficiently digested into singly-ionized atoms. Low-mass ions that are not of interest for imaging mass cytometry (ex. C, H, N, O and other common elements that make up the bulk of biological material) are removed using a quadropole mass filter, and the remaining high-mass ions are measured using a time-of-flight mass spectrometer (TOF-MS). With the variety of staining reagents available, up to 37 distinct metal isotopes from yttrium-89 to bismuth-209 can be

used for imaging simultaneously. These instruments offer sensitive and highly multiplexed imaging that cannot be matched by current fluorescence microscopy techniques [155].

While this technology is already powerful, it is an interesting prospect to further improve the spatial resolution of imaging mass cytometry. If sub-100-nm resolution can be realized, a new level of biological insight at the scale of cell organelles could be obtained. Of course, this idea comes with technical challenges. This problem is a two-dimensional one, at least technologically, because ultramicrotome tissue sectioning can reach thicknesses below 100 nm [145]. Then, to obtain a small ablation spot in a thin film of biological material, a natural step would be to using nonlinear absorption of intense femtosecond pulses at a short wavelength (for example, second or third harmonic of a Ti:sapphire laser), to achieve ablation resolution that is a fraction of the spot size. However, smaller spot sizes provide less material per pixel (where each pixel is from one ablation spot). This introduces two further issues to solve:

1. The time to generate an image of a tissue section will scale inversely with the square of ablation spot diameter.

2. There is less material coming from each pixel, meaning that the number of metal atoms that decreases proportionally to the square of the ablation spot diameter.

The problem with imaging speed could be addressed by adopting a faster ionization scheme than argon gas flow into an ICP torch, which is the rate-limiting step in existing imaging mass spectrometry instruments. The gas flow and ICP torch could be simply removed, but this would greatly limit the ion detection sensitivity of the imaging mass cytometer. Ablation alone does not efficiently break down the material into single ions, and sensitivity becomes even more critical as pixel size is decreased. Hence, an ionization method is still required. A second laser pulse at much higher intensity could be introduced ahead of the sample, to strongly ionize the ablated material and keep the sensitivity of the instrument at a workable level. The second pulse could also be of a longer wavelength, which would provide a larger focal volume in which catch the ablated material. A schematic of this approach is shown in Figure 7.1. An all-optical approach may be a necessary step towards imaging mass

cytometry at sub-diffraction-limit scales and may also provide greater simplicity and speed for current diagnostics.

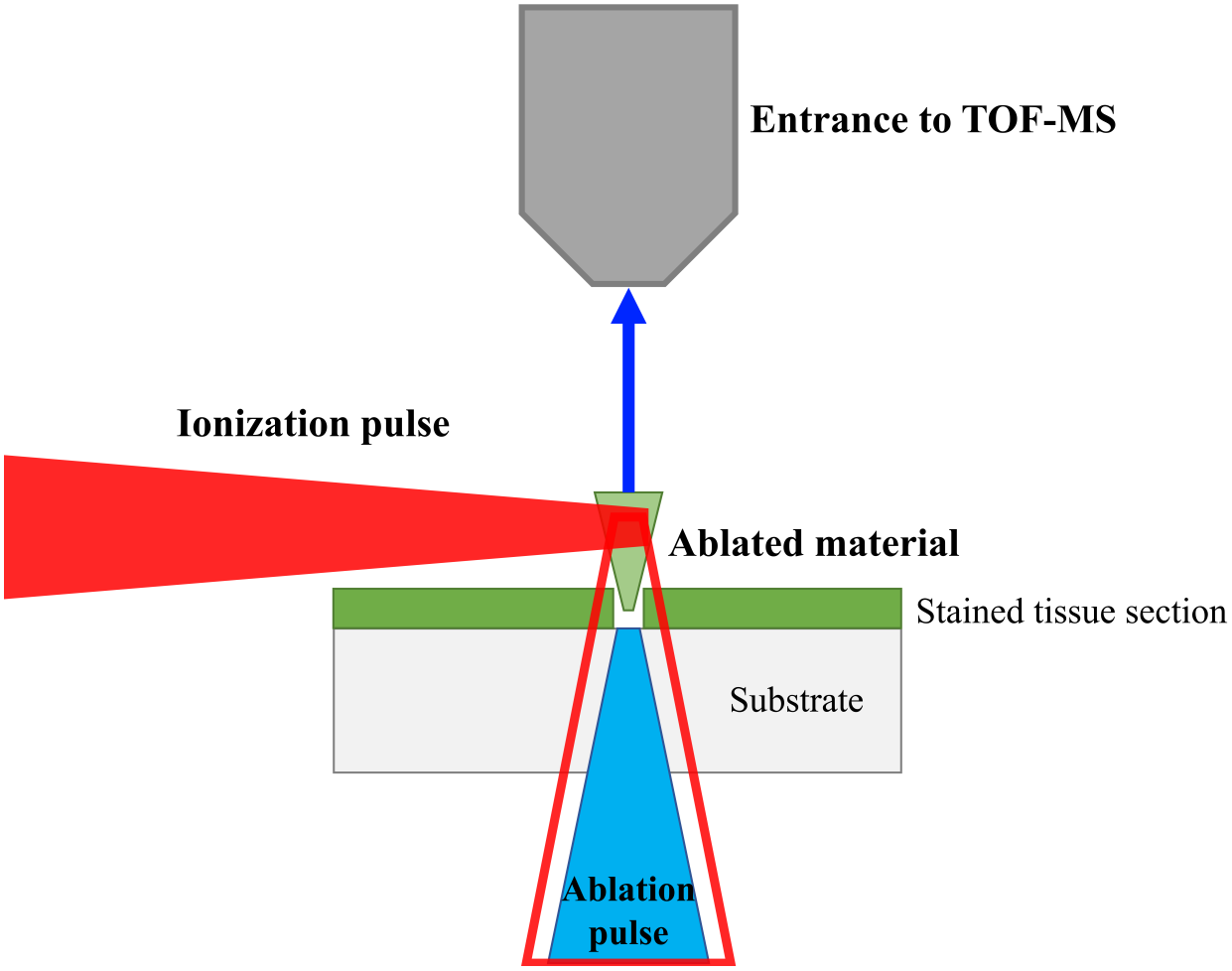

Figure 7.1: Schematic of an all-optical approach to ablation and ionization of tissue sections in imaging mass cytometry. An ablation pulse of a short wavelength could be introduced through a transparent substrate and ablate a small piece of a stained tissue section. Some time later, a second intense pulse could be introduced ahead of the sample to strongly ionize the ablated material. The ionization pulse could be introduced either from beside the sample or collinear with the ablation pulse, so long as the ionization pulse does not cause collateral damage to the tissue sample in the latter case.

These ideas are the basis of our ongoing collaboration project with Standard BioTools. For testing these new ionization schemes, an imaging mass spectrometer with a customizable laser beamline is required. An imaging time-of-flight mass spectrometer using single ultrafast pulses was implemented in our lab and initial tests were performed by Martin Chiasson, whose

work is detailed in a 2016 thesis [56]. This system was the starting point of the system that was developed in Chapter 2 and onward, though many alterations were made to improve optical alignment and automation. The mass spectrometer, made by Kore Technology, will be described briefly here since the deeper details are available in the work by Chiasson. The mass spectrometer is integrated with our vacuum system, with its entrance suspended over the sample stage as shown in Figure 7.1. For simple single-pulse tests of the mass spectrometer, the optical beamline and experimental automation described in Section 2.2 was used. The only difference is that, rather than polymer films, the samples used were indium tin oxide (ITO), a transparent conductive material, coated to a thickness of 70 nm on 170-µm-thick borosilicate coverslips. Laser pulses were focussed through the glass coverslips onto the ITO coating with sufficient intensity and fluence to ablate ITO, and in the process, create ions to be measured by mass spectrometry. Figure 7.2 shows a model of our mass spectrometer built in SIMION mass spectrometer modelling software.

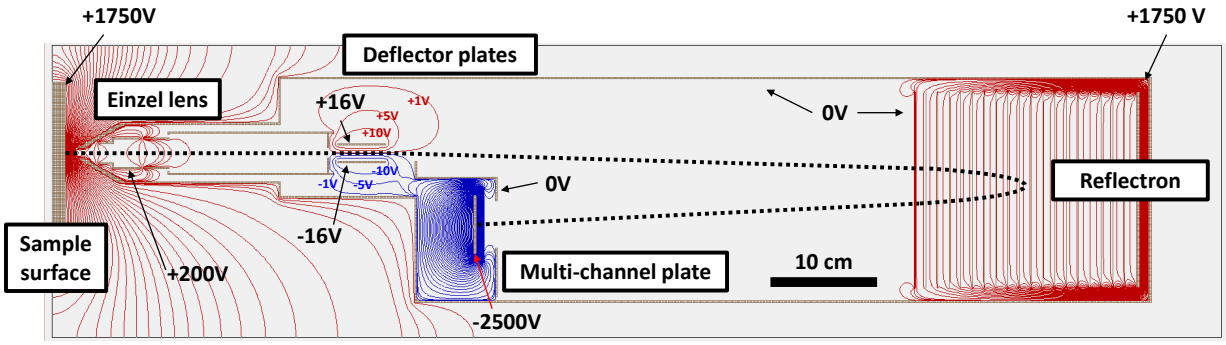

Figure 7.2: A SIMION model of our Kore time-of-flight mass spectrometer. The black dotted line illustrates a typical flight path of a positive ion, from its creation at the biased sample surface to its arrival at the microchannel plate, where it is detected. Equipotential lines are in increments of approximately 52.5 V, except those labelled near the deflector plates. Red equipotential lines are positive and blue equipotential lines are negative. The enclosure of the mass spectrometer, the front of the reflectron, and the housing of the microchannel plate are grounded.

The ITO sample is biased at +1750 V, so that positive ions created at the surface are pushed into the Einzel lens. The Einzel lens is a multi-element ion optic which focusses

a divergent beam of ions; this is useful because ions have a natural kinetic energy spread after being created by the laser. After this, ions travel through deflector plates for a small displacement which will allow them to reach the microchannel plate (MCP). The reflectron uses a voltage gradient to reverse the direction of the ions while correcting the spread in flight time due to the component of initial kinetic energy along the flight axis. The ions then travel to the grounded mesh on the front of the MCP, where ∼90% pass through and are detected.

We optimized and characterized the performance of the mass spectrometer using the ITO-coated glass coverslip as a test sample. First, deflector plate voltages were adjusted so the ion signal on the MCP was maximized. Then, reflectron voltages (set at the midpoint and end of the reflectron) were adjusted to minimize the spread of arrival times for each atomic isotope being measured. Since arrival times directly correspond to mass-to-charge ratio in time-of-flight mass spectrometry, this step optimizes the mass resolution of the mass spectrometer. From these measurements, we determined that the mass spectrometer had a resolution of $\frac{m}{\Delta m} \approx 9000$ and a mass calibration accurate to within 0.003 amu for masses below 250 amu. To estimate the efficiency of ion detection, we measured krypton gas ions. This was done by moving our laser focus ahead of the ITO surface and ionizing krypton gas leaked into the system at a pressure of 10^{-5} Torr. In parallel, we modelled the ionized volume of krypton gas using the Ammosov-Delone-Krainov model for tunneling ionization of krypton [156, 157], approximating the focus of 800-nm pulses through our 0.75 NA microscope objective as a perfect (non-aberrated) Gaussian focus. This model allowed us to predict how many ions are created by each pulse on average. Comparing to the number of Kr ions measured, we determined the ion detection efficiency to be approximately 1%. The maximum expected ion detection efficiency, accounting for 5 passes through 90% transmissive grids in the TOF-MS and the 60% open area ratio of the MCP, is approximately 35%. This lack of detection efficiency was caused by numerous bottlenecks inherent to the Kore system design. Further, this efficiency would become worse taking for ions coming from a solid-density plasma with an average kinetic energy of a few electron volts. Simulations using SIMION indicated that

singly-charged argon-40 ions with a kinetic energy component of 50 meV perpendicular to the TOF-MS flight axis would miss the MCP. This would apply to a small number of gas ions for very low pressures and at room temperature, but would be a problem for ions originating from a solid-density plasma with a kinetic energy spread of a few eV. This becomes a critical issue for observing small numbers of rarely-occurring ions in a dense solid, such as a metals in a stained biological tissue section. Standard BioTools reagents typically contain ∼100 rare earth metals per bonding antibody, and typical direct laser ionization rates they have encountered during ablation is below 1% from their initial estimates. Thus, using as sensitive a detection method as possible is needed.

Fortunately, imaging mass cytometry only requires mass differences of 1 amu to be resolved, and the requirement can be even more relaxed if the rare earth metals in the staining reagents of interest are further apart in mass. This allows us to greatly simplify our mass spectrometer, trading the unneeded mass resolution of the Kore design for increased ion detection efficiencies. By adopting a simple linear TOF-MS design with a much shorter flight path and fewer bottlenecks, we can ensure that even ions with several eV of total initial kinetic energy can reach the MCP for detection.

Figure 7.3 details the simplified TOF-MS design and its implementation. The simplified design truncates the original Kore design at the deflector plates, replacing them with a new MCP (Hamamatsu F13446-11 dual MCP, 27 mm diameter) to catch as many ions as possible. As our SIMION simulations in Figure 7.3(b), in spite of one remaining bottleneck (15 mm diameter) on the vacuum flange before the MCP, we see that ions with initial off-axis kinetic energy components up to 1.8 eV can reach the detector. Hence, the new design accepts ions with off-axis kinetic energy components approximately 40 times larger. The MCP should receive most ions created in a solid plasma with a few eV of average kinetic energy, since the initial orientation of the thermal velocities would be also randomly distributed, and very few would be directed mostly off-axis. However, in case this remains an experimental issue, the original aperture in the Kore vacuum flange could be machined wider, so that the full sensitive area of the MCP is covered. Estimates from SIMION indicate that this would

improve the off-axis kinetic energy acceptance up to 5 eV.

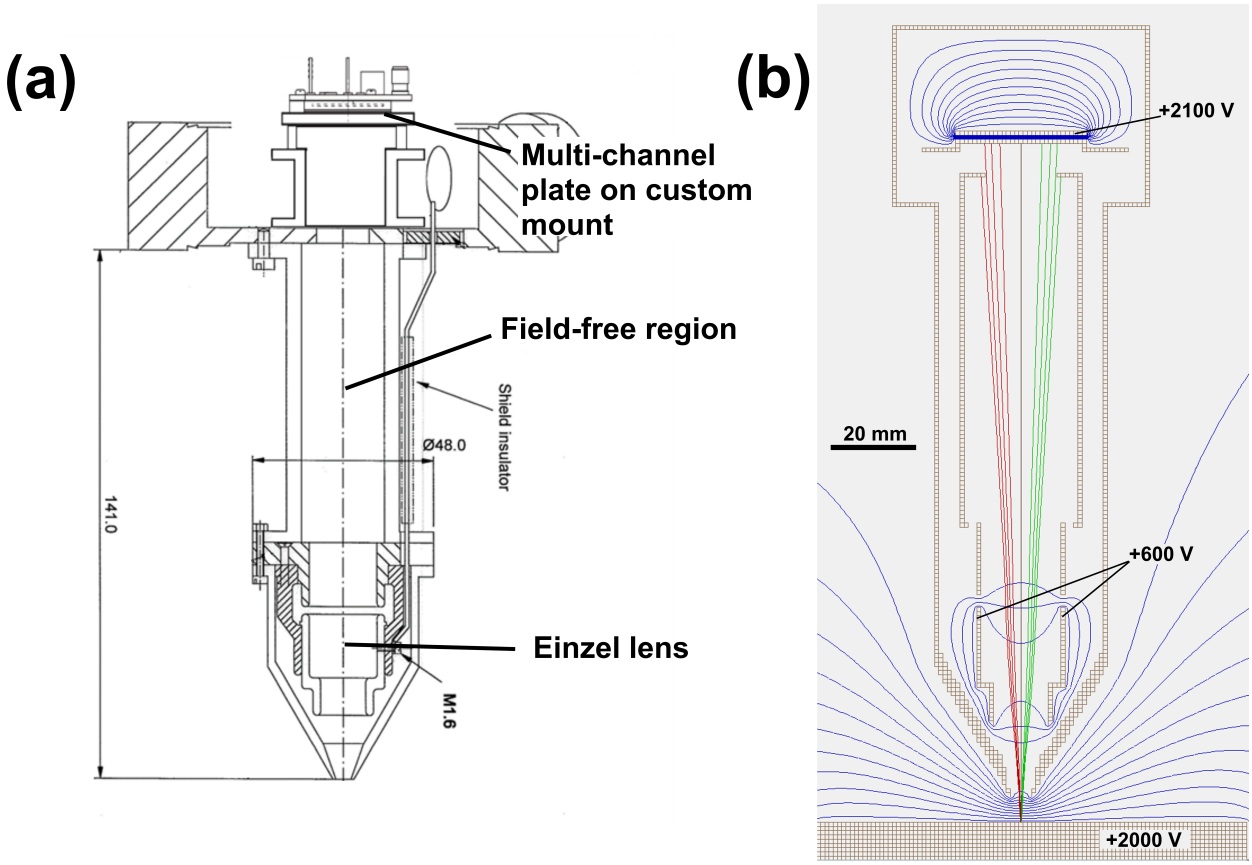

Figure 7.3: **(a)** A schematic of the simplified time-of-flight mass spectrometer. We retained the original Einzel lens and field-free region from the original Kore design. An MCP is placed where the deflector plates were mounted in the original design. Dimensions given are in mm. **(b)** A SIMION simulation of the new design. Apart from the voltages labelled on the sample, Einzel lens and back of the MCP, all other surfaces (including the front of the MCP) are grounded. Equipotential lines are drawn from 0 V to +1925 V in 175 V increments. Ion flight paths are simulated for singly-charged krypton-84 generated 50 µm above the biased ITO surface (bottom), for initial off-axis kinetic energy components of 0 to 2.4 eV in increments of 0.6 eV. The black line represents the path for no off-axis kinetic energy component. Red (green) lines represent paths for ions with increasing off-axis kinetic energy components directed to the left (right). Ions with up to 1.8 eV of off-axis kinetic energy reach the MCP.

We have implemented the simplified TOF-MS design in the lab and performed preliminary krypton gas ionization tests with an accompanying ionization volume modeling as done in the Kore system. These tests suggest our detection efficiency is approximately ∼20% (improved by a factor of 20; presumably much more in solid-state experiments). Our Hamamatsu MCP has an open-area ratio of 70% and a 65% quantum efficiency under our measurement condi-

tions, according to the manufacturer, for an upper limit of 45% on the detection efficiency. Further improvements may be possible, but as-is, the mass spectrometer's performance may already be sufficient for the experiments we wish to perform.

The proposed two-pulse ablation and ionization experiments also require a new optical beamline. For simplicity, we adopt a collinear geometry, where two beams are combined and focussed through the substrate onto the sample. As described earlier, the ionization pulse should be focussed ahead of the ablated region into the ablation plume, which will necessarily require a delay on the second pulse as well. For this purpose, we assembled the beamline shown in Figure 7.4. We begin with the spatially-filtered Gaussian beam from our infrared ($\lambda \sim 800$ nm) femtosecond pulsed laser, as shown in Figure 2.1, with vertical polarization (out of the page). The beam is focussed into a type II second-harmonic generation BBO crystal for approximately 20% conversion without significantly modifying the spatial profile of the infrared beam. The grating compressor in our laser was adjusted to obtain the shortest infrared pulse duration at the BBO crystal to maximize second-harmonic generation efficiency. Our second-harmonic beam ($\lambda \sim 400$ nm) was extracted using two dichroic mirrors (which also remove residual infrared light), collimated, and sent through a variable attenuator consisting of a half-wave plate in a motorized mount and a wire-grid polarizer oriented to transmit vertically-polarized light. The infrared beam was passed through the first dichroic mirror and collimated using a plano-convex lens on a motorized stage. By adjusting the position of this lens along the optical axis, the divergence of the infrared beam can be precisely tuned to focus the infrared beam a specified distance ahead of the sample of interest, as in Figure 7.1. The infrared beam then travels on a physical delay line and through a variable attenuator consisting of a motorized half-wave plate and a vertically-oriented wire grid polarizer. The infrared beam then reflects from a mirror on a motorized rotation mount, which is used to make slight angular adjustments so that the two beams overlap in the focal plane. This ensures that the infrared pulse overlaps with the ablation plume. Lastly, the two beams are combined on another dichroic mirror and are sent into the vacuum window for use in our mass spectrometry system.

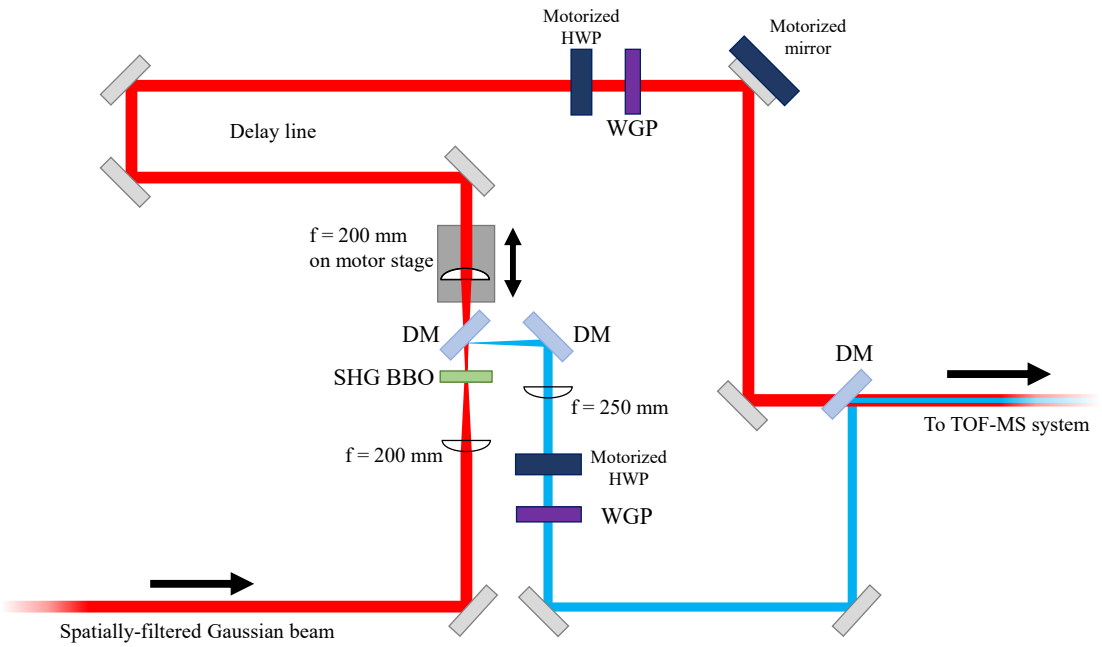

Figure 7.4: A schematic of the optical beamline for two-pulse ablation and ionization. SHG = second-harmonic generation. DM = dichroic mirror. HWP = half-wave plate. WGP wire-grid polarizer. Half-wave plates were selected for the wavelength on each arm.

This beamline has been implemented in the lab and adjusted so that the beams overlap in the focal plane, with the infrared pulse focussed 5 µm ahead of the blue focus at a delay of 5 ns. Pulse energy calibrations have been set up on each arm independently. We are now ready to proceed with the first two-pulse ablation and ionization experiments to demonstrate the feasibility of this approach for future commercial instruments. With this improved laser ionization mass spectrometry system, we hope to prove that femtosecond laser pulses can be used to improve resolution and throughput in imaging mass cytometry. With these improvements, we can provide richer sub-cellular insights in biology.

Appendix A

Peak Power for a Gaussian Pulse

As mentioned in Section 2.1.3, the power profile of a Gaussian temporal pulse is:

$$P(t) = P_0 \cdot 2^{-(2t/\tau)^2} \tag{A.1}$$

It can be determined using an integral table or a resource such as WolframAlpha that the area under a Gaussian curve of this form is:

$$\int_{-\infty}^{\infty} 2^{-q^2} dq = \sqrt{\frac{\pi}{\ln(2)}} \tag{A.2}$$

With this, we can easily integrate Equation A.1. Due to conservation of energy, the left side must give:

$$\int_{-\infty}^{\infty} P(t)dt = E_{pulse} \tag{A.3}$$

Using the substitution $q = 2t/\tau$, integration of the right side of Equation A.1 gives:

$$\int_{-\infty}^{\infty} P_0 \cdot 2^{-(2t/\tau)^2} dt = P_0 \cdot \frac{\tau}{2} \int_{-\infty}^{\infty} 2^{-q^2} dq = P_0 \cdot \frac{\tau}{2} \sqrt{\frac{\pi}{\ln(2)}} \tag{A.4}$$

Combining the results from Equations A.3 and A.4, we arrive at the desired result:

$$P_0 = 2\sqrt{\frac{\ln(2)}{\pi}} \left(\frac{E_{pulse}}{\tau} \right) \approx 0.94 \frac{E_{pulse}}{\tau} \tag{A.5}$$

Bibliography

1. Day, D., Gu, M. & Smallridge, A. Rewritable 3D Bit Optical Data Storage in a PMMA-Based Photorefractive Polymer. *Advanced Materials* **13.** ISSN: 0935-9648. doi:10.1002/1521-4095(200107)13:12/13<1005::AID-ADMA1005>3.0.CO;2-7. http://journals.scholarsportal.info/details/09359648/v13i12-13/1005_r3bodsiappp.xml (2001).
2. Hui, R. *Introduction to Fiber-Optic Communications* (2020). ISBN: 978-0-12-805345-4. doi:10.1016/B978-0-12-805345-4.00001-9. https://www.sciencedirect.com/science/article/pii/B9780128053454000019 (2023).
3. Extreme ultraviolet lithography: A review: Journal of Vacuum Science & Technology B: Microelectronics and Nanometer Structures Processing, Measurement, and Phenomena: Vol 25, No 6. https://avs.scitation.org/doi/full/10.1116/1.2794048 (2023).
4. Modi, A., Bühler, F., Andreasen, J. G. & Haglind, F. A review of solar energy based heat and power generation systems. *Renewable and Sustainable Energy Reviews* **67.** ISSN: 1364-0321. doi:10.1016/j.rser.2016.09.075. https://www.sciencedirect.com/science/article/pii/S1364032116305664 (2023) (2017).
5. Hong, K.-M. & Shin, Y. C. Prospects of laser welding technology in the automotive industry: A review. *Journal of Materials Processing Technology* **245.** ISSN: 0924-0136. doi:10.1016/j.jmatprotec.2017.02.008. https://www.sciencedirect.com/science/article/pii/S0924013617300523 (2023) (2017).
6. Tran, K. & Ryce, A. Laser Refractive Surgery for Vision Correction: A Review of Clinical Effectiveness and Cost-effectiveness. http://www.ncbi.nlm.nih.gov/books/NBK532537/ (2023) (Ottawa (ON), 2018).
7. Webb, R. H. Confocal optical microscopy. *Rep. Prog. Phys.* **59.** ISSN: 0034-4885. doi:10.1088/0034-4885/59/3/003. https://dx.doi.org/10.1088/0034-4885/59/3/003 (2023) (1996).
8. Streets, A. M., Li, A., Chen, T. & Huang, Y. Imaging without Fluorescence: Nonlinear Optical Microscopy for Quantitative Cellular Imaging. *Anal. Chem.* **86.** Publisher: American Chemical Society. ISSN: 0003-2700. doi:10.1021/ac5013706. https://doi.org/10.1021/ac5013706 (2023) (2014).
9. Pallen, S., Shetty, Y., Das, S., Vaz, J. M. & Mazumder, N. Advances in nonlinear optical microscopy techniques for in vivo and in vitro neuroimaging. *Biophys Rev* **13.** ISSN: 1867-2469. doi:10.1007/s12551-021-00832-7. https://doi.org/10.1007/s12551-021-00832-7 (2023) (2021).

10. Kumar, V., Coluccelli, N. & Polli, D. *Molecular and Laser Spectroscopy* (2018). ISBN: 978-0-12-849883-5. doi:10.1016/B978-0-12-849883-5.00005-X. https://www.sciencedirect.com/science/article/pii/B978012849883500005X (2023).

11. High-harmonic generation from solids — Nature Physics. https://www.nature.com/articles/s41567-018-0315-5 (2023).

12. Miziolek, A. W., Palleschi, V. & Schechter, I. Laser Induced Breakdown Spectroscopy. Google-Books-ID: PKJWgvQ6wAYC. ISBN: 978-1-139-45831-3 (2006).

13. Singhal, N., Kumar, M., Kanaujia, P. K. & Virdi, J. S. MALDI-TOF mass spectrometry: an emerging technology for microbial identification and diagnosis. *Frontiers in Microbiology* **6.** ISSN: 1664-302X. https://www.frontiersin.org/articles/10.3389/fmicb.2015.00791 (2023) (2015).

14. Günther, D. & Hattendorf, B. Solid sample analysis using laser ablation inductively coupled plasma mass spectrometry. *TrAC Trends in Analytical Chemistry. Trace-metal analysis* **24.** ISSN: 0165-9936. doi:10.1016/j.trac.2004.11.017. https://www.sciencedirect.com/science/article/pii/S0165993605000117 (2023) (2005).

15. Arnold, C. B., Serra, P. & Piqué, A. Laser Direct-Write Techniques for Printing of Complex Materials. *MRS Bulletin* **32.** ISSN: 1938-1425, 0883-7694. doi:10.1557/mrs2007.11. https://www.cambridge.org/core/journals/mrs-bulletin/article/laser-directwrite-techniques-for-printing-of-complex-materials/35B5BB1230919276AC75F38CB1B448F6 (2007).

16. Serra, P. & Piqué, A. Laser-Induced Forward Transfer: Fundamentals and Applications. *Advanced Materials Technologies* **4.** ISSN: 2365-709X. doi:10.1002/admt.201800099. https://onlinelibrary.wiley.com/doi/abs/10.1002/admt.201800099 (2019).

17. Vorobyev, A. Y. & Guo, C. Direct femtosecond laser surface nano/microstructuring and its applications. *Laser & Photonics Reviews* **7.** _eprint: https://onlinelibrary.wiley.com/doi/pdf/10.10 ISSN: 1863-8899. doi:10.1002/lpor.201200017. https://onlinelibrary.wiley.com/doi/abs/10.1002/lpor.201200017 (2023) (2013).

18. Florian, C., Kirner, S. V., Krüger, J. & Bonse, J. Surface functionalization by laser-induced periodic surface structures. *Journal of Laser Applications* **32.** Publisher: Laser Institute of America. ISSN: 1042-346X. doi:10.2351/7.0000103. https://lia.scitation.org/doi/10.2351/7.0000103 (2023) (2020).

19. Stuart, B. C. *et al.* Nanosecond-to-femtosecond laser-induced breakdown in dielectrics. *Phys. Rev. B* **53.** ISSN: 0163-1829, 1095-3795. doi:10.1103/PhysRevB.53.1749. https://link.aps.org/doi/10.1103/PhysRevB.53.1749 (1996).

20. Maiman, T. H. Stimulated Optical Radiation in Ruby. *Nature* **187.** Number: 4736 Publisher: Nature Publishing Group. ISSN: 1476-4687. doi:10.1038/187493a0. https://www.nature.com/articles/187493a0 (1960).

21. Weiner, A. Ultrafast Optics. ISBN: 978-1-118-21147-2 (2011).

22. McClung, F. J. & Hellwarth, R. W. Giant Optical Pulsations from Ruby. *Journal of Applied Physics* **33.** Publisher: American Institute of Physics. ISSN: 0021-8979. doi:10.1063/1.1777174. https://aip.scitation.org/doi/10.1063/1.1777174 (1962).

23. Ditmire, T. High-power Lasers: The invention of the laser 50 years ago has led to the latest generation of devices, with power bursts thousands of times that of the nation's entire electrical grid. *American Scientist* **98.** Publisher: Sigma Xi, The Scientific Research Society. ISSN: 0003-0996. https://www.jstor.org/stable/27859566 (2010).

24. Treacy, E. B. Compression of picosecond light pulses. *Physics Letters A* **28.** ISSN: 0375-9601. doi:10.1016/0375-9601(68)90584-7. https://www.sciencedirect.com/science/article/pii/0375960168905847 (1968).

25. Treacy, E. Optical pulse compression with diffraction gratings. *IEEE Journal of Quantum Electronics* **5.** Conference Name: IEEE Journal of Quantum Electronics. ISSN: 1558-1713. doi:10.1109/JQE.1969.1076303 (1969).

26. Strickland, D. & Mourou, G. Compression of amplified chirped optical pulses. *Optics Communications* **56.** ISSN: 0030-4018. doi:10.1016/0030-4018(85)90120-8. https://www.sciencedirect.com/science/article/pii/0030401885901208 (1985).

27. Joglekar, A. *et al.* A study of the deterministic character of optical damage by femtosecond laser pulses and applications to nanomachining. *Appl. Phys. B* **77.** ISSN: 1432-0649. doi:10.1007/s00340-003-1246-z. https://doi.org/10.1007/s00340-003-1246-z (2003).

28. Pronko, P. P. *et al.* Machining of sub-micron holes using a femtosecond laser at 800 nm. *Optics Communications* **114.** ISSN: 0030-4018. doi:10.1016/0030-4018(94)00585-I. http://www.sciencedirect.com/science/article/pii/003040189400585I (1995).

29. Sugioka, K. & Cheng, Y. Femtosecond laser three-dimensional micro- and nanofabrication. *Applied Physics Reviews* **1.** Publisher: American Institute of Physics. doi:10.1063/1.4904320. https://aip.scitation.org/doi/10.1063/1.4904320 (2014).

30. Sugioka, K. Progress in ultrafast laser processing and future prospects. *Nanophotonics* **6.** ISSN: 2192-8606. doi:10.1515/nanoph-2016-0004. https://www.degruyter.com/view/j/nanoph.2017.6.issue-2/nanoph-2016-0004/nanoph-2016-0004.xml (2016).

31. Yang, L. *et al.* The Fabrication of Micro/Nano Structures by Laser Machining. *Nanomaterials (Basel)* **9.** ISSN: 2079-4991. doi:10.3390/nano9121789. https://www.ncbi.nlm.nih.gov/pmc/articles/PMC6956144/ (2023) (2019).

32. Ruffino, F. & Grimaldi, M. G. Nanostructuration of Thin Metal Films by Pulsed Laser Irradiations: A Review. *Nanomaterials (Basel)* **9.** ISSN: 2079-4991. doi:10.3390/nano9081133. https://www.ncbi.nlm.nih.gov/pmc/articles/PMC6723593/ (2023) (2019).

33. Sugioka, K. & Cheng, Y. Ultrafast lasers—reliable tools for advanced materials processing. *Light: Science & Applications* **3.** Number: 4 Publisher: Nature Publishing Group. ISSN: 2047-7538. doi:10.1038/lsa.2014.30. https://www.nature.com/articles/lsa201430 (2014).

34. Jeon, H. *et al.* Chemical patterning of ultrathin polymer films by direct-write multiphoton lithography. *J Am Chem Soc* **133.** ISSN: 1520-5126. doi:10.1021/ja200313q. https://europepmc.org/articles/PMC3086137 (2023) (2011).

35. Baum, A. *et al.* Pulse-duration dependency of femtosecond laser refractive index modification in poly(methyl methacrylate). *Opt. Lett., OL* **33.** Publisher: Optica Publishing Group. ISSN: 1539-4794. doi:10.1364/OL.33.000651. https://opg.optica.org/ol/abstract.cfm?uri=ol-33-7-651 (2023) (2008).

36. Taylor, R. S. *et al.* Femtosecond laser fabrication of nanostructures in silica glass. *Opt. Lett., OL* **28.** Publisher: Optica Publishing Group. ISSN: 1539-4794. doi:10.1364/OL.28.001043. https://opg.optica.org/ol/abstract.cfm?uri=ol-28-12-1043 (2003).

37. Kattamis, N. T., McDaniel, N. D., Bernhard, S. & Arnold, C. B. Laser direct write printing of sensitive and robust light emitting organic molecules. *Appl. Phys. Lett.* **94.** Publisher: American Institute of Physics. ISSN: 0003-6951. doi:10.1063/1.3098375. https://aip.scitation.org/doi/10.1063/1.3098375 (2009).

38. Goodfriend, N. T. *et al.* Blister-based-laser-induced-forward-transfer: a non-contact, dry laser-based transfer method for nanomaterials. *Nanotechnology* **29.** ISSN: 0957-4484. doi:10.1088/1361-6528/aaceda. https://doi.org/10.1088%2F1361-6528%2Faaceda (2018).

39. Hecht, E. Optics. ISBN: 978-0-13-397722-6 (2017).

40. Pedrotti, F. L., Pedrotti, L. M. & Pedrotti, L. S. Introduction to Optics. ISBN: 9781108552493 Publisher: Cambridge University Press. doi:10.1017/9781108552493 (2017).

41. Boyd, R. W. Nonlinear Optics - 3rd Edition. ISBN: 978-0-12-369470-6. doi:10.1016/B978-0-12-369470-6.00016-2 (Burlington, 2008).

42. Gaussian Beam Propagation — Edmund Optics. https://www.edmundoptics.com/knowledge-center/application-notes/lasers/gaussian-beam-propagation/ (2022).

43. Gaussian Beam Optics. https://www.newport.com/n/gaussian-beam-optics (2022).

44. Paschotta, D. R. Gaussian Beams. https://www.rp-photonics.com/gaussian_beams.html (2022).

45. Siegman, A. E. How to (Maybe) Measure Laser Beam Quality. *DPSS (Diode Pumped Solid State) Lasers: Applications and Issues (1998), paper MQ1* (1998). doi:10.1364/DLAI.1998.MQ1. https://opg.optica.org/abstract.cfm?uri=DLAI-1998-MQ1.

46. Zalloum, O. H. Y., Parrish, M., Terekhov, A. & Hofmeister, W. On femtosecond micromachining of HPHT single-crystal diamond with direct laser writing using tight focusing. *Opt. Express, OE* **18.** ISSN: 1094-4087. doi:10.1364/OE.18.013122. https://www.osapublishing.org/oe/abstract.cfm?uri=oe-18-12-13122 (2010).

47. Nemoto, S. Nonparaxial Gaussian beams. *Appl. Opt., AO* **29.** Publisher: Optica Publishing Group. ISSN: 2155-3165. doi:10.1364/AO.29.001940. https://opg.optica.org/ao/abstract.cfm?uri=ao-29-13-1940 (2023) (1990).

48. Paschotta, D. R. Gaussian Pulses. https://www.rp-photonics.com/gaussian_pulses.html (2022).

49. Oshina, I. & Spigulis, J. Beer–Lambert law for optical tissue diagnostics: current state of the art and the main limitations. *J Biomed Opt* **26.** ISSN: 1083-3668. doi:10.1117/1.JBO.26.10.100901. https://www.ncbi.nlm.nih.gov/pmc/articles/PMC8553265/ (2021).

50. Boyd, R. W. Nonlinear Optics. Google-Books-ID: 3vHb7WGXmSQC. ISBN: 978-0-08-047975-0 (2003).

51. Parodi, V. *et al.* Nonlinear Optical Microscopy: From Fundamentals to Applications in Live Bioimaging. *Front Bioeng Biotechnol* **8.** ISSN: 2296-4185. doi:10.3389/fbioe.2020.585363. https://www.ncbi.nlm.nih.gov/pmc/articles/PMC7581943/ (2023) (2020).

52. Oheim, M., Michael, D. J., Geisbauer, M., Madsen, D. & Chow, R. H. Principles of two-photon excitation fluorescence microscopy and other nonlinear imaging approaches. *Advanced Drug Delivery Reviews. Multi-Photon Imaging: Diseases and Therapies* **58.** ISSN: 0169-409X. doi:10.1016/j.addr.2006.07.005. https://www.sciencedirect.com/science/article/pii/S0169409X06001207 (2023) (2006).

53. Joglekar, A. P., Liu, H.-h., Meyhöfer, E., Mourou, G. & Hunt, A. J. Optics at critical intensity: Applications to nanomorphing. *Proceedings of the National Academy of Sciences* **101.** Publisher: Proceedings of the National Academy of Sciences. doi:10.1073/pnas.0307470101. https://www.pnas.org/doi/full/10.1073/pnas.0307470101 (2023) (2004).

54. Bonse, J. & Krüger, J. Structuring of thin films by ultrashort laser pulses. *Appl. Phys. A* **129.** ISSN: 1432-0630. doi:10.1007/s00339-022-06229-x. https://doi.org/10.1007/s00339-022-06229-x (2023) (2022).

55. Trebino, R. *et al.* Measuring ultrashort laser pulses in the time-frequency domain using frequency-resolved optical gating. *Review of Scientific Instruments* **68.** Publisher: American Institute of Physics. ISSN: 0034-6748. doi:10.1063/1.1148286. https://aip.scitation.org/doi/abs/10.1063/1.1148286 (1997).

56. Chiasson, M. An Imaging Mass Spectrometer with Ultrashort Laser Pulses as its Ionization Source. Accepted: 2016-03-03T16:55:13Z. Thesis (Université d'Ottawa / University of Ottawa, 2016). doi:10.20381/ruor-5234. http://ruor.uottawa.ca/handle/10393/34343.

57. Laurell Spin Processor - WS-650-23. https://photonics.uottawa.ca/en/laurell-spin-processor-ws-650-23 (2022).

58. Sputtering System - Quorum 150R. https://photonics.uottawa.ca/en/facilities/sputtering-system (2022).

59. Sputter Coating - Angstrom Sciences- Sputter Deposition. https://www.angstromsciences.com/sputter-coating (2022).

60. Profiler – DektakXT. https://photonics.uottawa.ca/en/facilities/profiler-dektak-xt (2022).

61. AFM-Bruker – Dimension Icon. https://photonics.uottawa.ca/en/facilities/AFM-Bruker-Dimension-Icon (2022).

62. Jalili, N. & Laxminarayana, K. A review of atomic force microscopy imaging systems: application to molecular metrology and biological sciences. *Mechatronics* **14.** ISSN: 0957-4158. doi:10.1016/j.mechatronics.2004.04.005. https://www.sciencedirect.com/science/article/pii/S0957415804000455 (2004).

63. Binnig, G., Quate, C. F. & Gerber, C. Atomic Force Microscope. *Phys. Rev. Lett.* **56.** Publisher: American Physical Society. doi:10.1103/PhysRevLett.56.930. https://link.aps.org/doi/10.1103/PhysRevLett.56.930 (1986).

64. Binnig, G., Gerber, C., Stoll, E., Albrecht, T. R. & Quate, C. F. Atomic Resolution with Atomic Force Microscope. *EPL* **3.** Publisher: IOP Publishing. ISSN: 0295-5075. doi:10.1209/0295-5075/3/12/006. https://doi.org/10.1209/0295-5075/3/12/006 (1987).

65. Alexander, S. *et al.* An atomic-resolution atomic-force microscope implemented using an optical lever. *Journal of Applied Physics* **65.** Publisher: American Institute of Physics. ISSN: 0021-8979. doi:10.1063/1.342563. https://aip.scitation.org/doi/abs/10.1063/1.342563 (1989).

66. ORION NanoFab. https://photonics.uottawa.ca/en/facilities/orion-nanofab (2022).

67. Chan, C. M. & Weng, L.-T. Surface Characterization of Polymer Blends by XPS and ToF-SIMS. *Materials* **9.** Number: 8 Publisher: Multidisciplinary Digital Publishing Institute. ISSN: 1996-1944. doi:10.3390/ma9080655. https://www.mdpi.com/1996-1944/9/8/655 (2016).

68. Kattamis, N. T., Purnick, P. E., Weiss, R. & Arnold, C. B. Thick film laser induced forward transfer for deposition of thermally and mechanically sensitive materials. *Appl. Phys. Lett.* **91.** ISSN: 0003-6951. doi:10.1063/1.2799877. https://aip.scitation.org/doi/abs/10.1063/1.2799877 (2007).

69. Brown, M. S., Kattamis, N. T. & Arnold, C. B. Time-resolved study of polyimide absorption layers for blister-actuated laser-induced forward transfer. *Journal of Applied Physics* **107.** ISSN: 0021-8979. doi:10.1063/1.3327432. https://aip.scitation.org/doi/10.1063/1.3327432 (2010).

70. Goodfriend, N. T. *et al.* Laser pulse duration dependence of blister formation on back-radiated Ti thin films for BB-LIFT. *Applied Physics A* **122.** ISSN: 0947-8396, 1432-0630. doi:10.1007/s00339-016-9666-x. http://link.springer.com/10.1007/s00339-016-9666-x (2016).

71. Domke, M., Rapp, S., Schmidt, M. & Huber, H. P. Ultra-fast movies of thin-film laser ablation. *Appl. Phys. A* **109.** ISSN: 1432-0630. doi:10.1007/s00339-012-7072-6. https://doi.org/10.1007/s00339-012-7072-6 (2023) (2012).

72. Domke, M. *et al.* Understanding Thin Film Laser Ablation: The Role of the Effective Penetration Depth and the Film Thickness. *Physics Procedia. 8th International Conference on Laser Assisted Net Shape Engineering LANE 2014* **56.** ISSN: 1875-3892. doi:10.1016/j.phpro.2014.08.012. https://www.sciencedirect.com/science/article/pii/S1875389214001576 (2023) (2014).

73. Rapp, S., Domke, M., Schmidt, M. & Huber, H. P. Physical Mechanisms during fs Laser Ablation of Thin SiO2 Films. *Physics Procedia. Lasers in Manufacturing (LiM 2013)* **41.** ISSN: 1875-3892. doi:10.1016/j.phpro.2013.03.141. https://www.sciencedirect.com/science/article/pii/S1875389213001557 (2023) (2013).

74. Inogamov, N., Zhakhovsky, V. & Migdal, K. Laser-induced spalling of thin metal film from silica substrate followed by inflation of microbump. *Applied Physics A* **122.** doi:10.1007/s00339-016-9942-9 (2016).

75. Tamura, H., Kohama, T., Kondo, K. & Yoshida, M. Femtosecond-laser-induced spallation in aluminum. *Journal of Applied Physics* **89.** Publisher: American Institute of Physics. ISSN: 0021-8979. doi:10.1063/1.1346996. https://aip.scitation.org/doi/abs/10.1063/1.1346996 (2001).

76. Fedorov, A. & De Hosson, J. T. M. Adhesion of polymer coatings studied by laser-induced delamination. *Journal of Applied Physics* **97.** Publisher: American Institute of Physics. ISSN: 0021-8979. doi:10.1063/1.1929858. https://aip.scitation.org/doi/10.1063/1.1929858 (2023) (2005).

77. Bian, J. *et al.* Laser-Induced Interfacial Spallation for Controllable and Versatile Delamination of Flexible Electronics. *ACS Appl. Mater. Interfaces* **12.** ISSN: 1944-8244, 1944-8252. doi:10.1021/acsami.0c18951. https://pubs.acs.org/doi/10.1021/acsami.0c18951 (2023) (2020).

78. Lorenz, P., Ehrhardt, M. & Zimmer, K. Laser Structuring of Thin Layers for Flexible Electronics by a Shock Wave-induced Delamination Process. *Physics Procedia. 8th International Conference on Laser Assisted Net Shape Engineering LANE 2014* **56.** ISSN: 1875-3892. doi:10.1016/j.phpro.2014.08.013. https://www.sciencedirect.com/science/article/pii/S1875389214001588 (2023) (2014).

79. Vella, D., Bico, J., Boudaoud, A., Roman, B. & Reis, P. M. The macroscopic delamination of thin films from elastic substrates. *Proceedings of the National Academy of Sciences* **106.** Publisher: Proceedings of the National Academy of Sciences. doi:10.1073/pnas.0902160106. https://www.pnas.org/doi/10.1073/pnas.0902160106 (2023) (2009).

80. Kim, J.-H., Kil, H.-J., Lee, S., Park, J. & Park, J.-W. Interfacial Delamination at Multilayer Thin Films in Semiconductor Devices. *ACS Omega* **7.** Publisher: American Chemical Society. doi:10.1021/acsomega.2c02122. https://doi.org/10.1021/acsomega.2c02122 (2023) (2022).

81. Alig, I. *et al.* Investigation of delamination mechanisms in polymer coatings by scanning acoustic microscopy. *J. Phys. D: Appl. Phys.* **44.** ISSN: 0022-3727. doi:10.1088/0022-3727/44/3/034009. https://dx.doi.org/10.1088/0022-3727/44/3/034009 (2023) (2010).

82. Serrano, J. R. & Cahill, D. G. Laser-Induced Blistering of Thin SiO2 on Si. *Microscale Thermophysical Engineering* **9.** ISSN: 1089-3954. doi:10.1080/10893950590945030. https://doi.org/10.1080/10893950590945030 (2005).

83. McDonald, J. P. *et al.* Femtosecond-laser-induced delamination and blister formation in thermal oxide films on silicon (100). *Appl. Phys. Lett.* **88.** Publisher: American Institute of Physics. ISSN: 0003-6951. doi:10.1063/1.2193777. https://aip.scitation.org/doi/full/10.1063/1.2193777 (2006).

84. Kumar, K. *et al.* Quantized structuring of transparent films with femtosecond laser interference. *Light Sci Appl* **3.** Number: 3 Publisher: Nature Publishing Group. ISSN: 2047-7538. doi:10.1038/lsa.2014.38. https://www.nature.com/articles/lsa201438 (2023) (2014).

85. Ho, S., Kumar, K., Lee, K. K. C., Li, J. & Herman, P. R. Interferometric femtosecond laser processing for nanostructuring inside thin film. *Advanced Optical Technologies* **3.** Publisher: De Gruyter. ISSN: 2192-8584. doi:10.1515/aot-2014-0047. https://www.degruyter.com/document/doi/10.1515/aot-2014-0047/html (2023) (2014).

86. Roper, D. M., Ho, S., Haque, M., Jha, P. & Herman, P. R. Inhibition and Enhancement of Quantized, Interference-Driven, Ultrafast-Laser Cleaving, and Intrafilm Ejection with Angle and Polarization Control. *Advanced Materials Technologies* **3.** _eprint: https://onlinelibrary.wiley.com/doi/pdf/10.1002/admt.201700234. ISSN: 2365-709X. doi:10.1002/admt.201700234. https://onlinelibrary.wiley.com/doi/abs/10.1002/admt.201700234 (2023) (2018).

87. Rayner, D. M., Naumov, A. & Corkum, P. B. Ultrashort pulse non-linear optical absorption in transparent media. *Opt. Express, OE* **13.** ISSN: 1094-4087. doi:10.1364/OPEX.13.003208. https://www.osapublishing.org/oe/abstract.cfm?uri=oe-13-9-3208 (2005).

88. Ahmed, B. *et al.* Optical and structural study of aromatic polymers irradiated by gamma radiation (2012). https://www.semanticscholar.org/paper/Optical-and-structural-study-of-aromatic-polymers-Ahmed-Raghuvanshi/b1b4b2f95f1aba5c9fa560835b6b5082edd096b8 (2023).

89. Kumar, V., Goyal, P., Gupta, R. & Kumar, S. Tailoring of optical band gap and refractive index of heat treated Kapton-H Polyimide. *Advances in Applied Science Research* (2014).

90. Ebnalwaled, A. A., Yousef, A., Gerges, M. K. & Thabet, A. SYNTHESIS OF NANO-POLYIMIDE FOR MICROELECTRONIC APPLICATIONS. *Journal of Applied Chemical Science International.* ISSN: 2395-3713. https://ikprress.org/index.php/JACSI/article/view/3908 (2023) (2016).

91. Chu, S., Wang, Y., Wang, C., Yang, J. & Zou, Z. Bandgap modulation of polyimide photocatalyst for optimum H2 production activity under visible light irradiation. *International Journal of Hydrogen Energy* **38.** ISSN: 0360-3199. doi:10.1016/j.ijhydene.2013.02.035. https://www.sciencedirect.com/science/article/pii/S0360319913004011 (2023) (2013).

92. Tauc, J. Optical properties and electronic structure of amorphous Ge and Si. *Materials Research Bulletin* **3.** ISSN: 0025-5408. doi:10.1016/0025-5408(68)90023-8. https://www.sciencedirect.com/science/article/pii/0025540868900238 (2023) (1968).

93. Kattamis, N. T., Brown, M. S. & Arnold, C. B. Finite element analysis of blister formation in laser-induced forward transfer. *Journal of Materials Research* **26.** ISSN: 2044-5326, 0884-2914. doi:10.1557/jmr.2011.215. https://www.cambridge.org/core/journals/journal-of-materials-research/article/finite-element-analysis-of-blister-formation-in-laserinduced-forward-transfer/86AD47A7ECD8BA0DC651013D640258AF (2011).

94. Mark, J. E. The effect of strain-induced crystallization on the ultimate properties of an elastomeric polymer network. *Polymer Engineering & Science* **19.** _eprint: https://onlinelibrary.wiley. ISSN: 1548-2634. doi:10.1002/pen.760190608. https://onlinelibrary.wiley.com/doi/abs/10.1002/pen.760190608 (2023) (1979).

95. Cheng, C. *et al.* Bisphenol A Sensors on Polyimide Fabricated by Laser Direct Writing for Onsite River Water Monitoring at Attomolar Concentration. *ACS Appl. Mater. Interfaces* **8.** Publisher: American Chemical Society. ISSN: 1944-8244. doi:10.1021/acsami.6b03743. https://doi.org/10.1021/acsami.6b03743 (2016).

96. Tang, M. Laser Ablation of Metal Substrates for Super-hydrophobic Effect. doi:10.2961/JLMN.2011.01.0002 (2011).

97. Long, J. *et al.* Superhydrophobic Surfaces Fabricated by Femtosecond Laser with Tunable Water Adhesion: From Lotus Leaf to Rose Petal. *ACS Appl. Mater. Interfaces* **7.** Publisher: American Chemical Society. ISSN: 1944-8244. doi:10.1021/acsami.5b01870. https://doi.org/10.1021/acsami.5b01870 (2015).

98. Moradi, S., Kamal, S., Englezos, P. & Hatzikiriakos, S. G. Femtosecond laser irradiation of metallic surfaces: effects of laser parameters on superhydrophobicity. *Nanotechnology* **24.** Publisher: IOP Publishing. ISSN: 0957-4484. doi:10.1088/0957-4484/24/41/415302. https://doi.org/10.1088/0957-4484/24/41/415302 (2013).

99. Hermens, U. *et al.* Mimicking lizard-like surface structures upon ultrashort laser pulse irradiation of inorganic materials. *Applied Surface Science. European Materials Research Society Spring Meeting 2016 – Symposium "Laser – Materials Interactions for Tailoring Future's Applications"* **418.** ISSN: 0169-4332. doi:10.1016/j.apsusc.2016.12.112. https://www.sciencedirect.com/science/article/pii/S0169433216328306 (2017).

100. Lee, B. E. J., Exir, H., Weck, A. & Grandfield, K. Characterization and evaluation of femtosecond laser-induced sub-micron periodic structures generated on titanium to improve osseointegration of implants. *Applied Surface Science* **441.** ISSN: 0169-4332. doi:10.1016/j.apsusc.2018.02.119. https://www.sciencedirect.com/science/article/pii/S016943321830463X (2018).

101. Zuo, M., Takeichi, T., Matsumoto, A. & Tsutsumi, K. Surface characterization of polyimide films. *Colloid Polym Sci* **276.** ISSN: 1435-1536. doi:10.1007/s003960050281. https://doi.org/10.1007/s003960050281 (1998).

102. Wang, Z. K., Zheng, H. Y., Lim, C. P. & Lam, Y. C. Polymer hydrophilicity and hydrophobicity induced by femtosecond laser direct irradiation. *Appl. Phys. Lett.* **95.** Publisher: American Institute of Physics. ISSN: 0003-6951. doi:10.1063/1.3232212. https://aip.scitation.org/doi/10.1063/1.3232212 (2009).

103. Alshehri, A. M. *et al.* Selective cell adhesion on femtosecond laser-microstructured polydimethylsiloxane. *Biomed. Mater.* **11.** Publisher: IOP Publishing. ISSN: 1748-605X. doi:10.1088/1748-6041/11/1/015014. https://doi.org/10.1088/1748-6041/11/1/015014 (2016).

104. Farzam, M., Beitollahpoor, M., Solomon, S. E., Ashbaugh, H. S. & Pesika, N. S. Advances in the Fabrication and Characterization of Superhydrophobic Surfaces Inspired by the Lotus Leaf. *Biomimetics* **7.** Number: 4 Publisher: Multidisciplinary Digital Publishing Institute. ISSN: 2313-7673. doi:10.3390/biomimetics7040196. https://www.mdpi.com/2313-7673/7/4/196 (2023) (2022).

105. Wang, B., Zhang, Y., Shi, L., Li, J. & Guo, Z. Advances in the theory of superhydrophobic surfaces. *J. Mater. Chem.* **22.** Publisher: The Royal Society of Chemistry. ISSN: 1364-5501. doi:10.1039/C2JM32780E. https://pubs.rsc.org/en/content/articlelanding/2012/jm/c2jm32780e (2012).

106. Godfrey, A. T., Kallepalli, D. L., Ratté, J., Zhang, C. & Corkum, P. Femtosecond-Laser-Induced Nanoscale Blisters in Polyimide Thin Films through Nonlinear Absorption. *Phys. Rev. Applied* **14.** Publisher: American Physical Society. doi:10.1103/PhysRevApplied.14.044057. https://link.aps.org/doi/10.1103/PhysRevApplied.14.044057 (2020).

107. Kaur, K. S. *et al.* Shadowgraphic studies of triazene assisted laser-induced forward transfer of ceramic thin films. *Journal of Applied Physics* **105.** Publisher: American Institute of Physics. ISSN: 0021-8979. doi:10.1063/1.3132822. https://aip.scitation.org/doi/full/10.1063/1.3132822 (2009).

108. Ben-Yakar, A. & Byer, R. L. Femtosecond laser ablation properties of borosilicate glass. *Journal of Applied Physics* **96.** ISSN: 0021-8979, 1089-7550. doi:10.1063/1.1787145. http://aip.scitation.org/doi/10.1063/1.1787145 (2004).

109. Krüger, J., Dufft, D., Koter, R. & Hertwig, A. Femtosecond laser-induced damage of gold films. *Applied Surface Science. Photon-Assisted Synthesis and Processing of Functional Materials* **253.** ISSN: 0169-4332. doi:10.1016/j.apsusc.2007.02.164. https://www.sciencedirect.com/science/article/pii/S0169433207003868 (2007).

110. Guay, J.-M. *et al.* Polarization-dependent femtosecond laser ablation of poly-methyl methacrylate. *New J. Phys.* **14.** Publisher: IOP Publishing. ISSN: 1367-2630. doi:10.1088/1367-2630/14/8/085010. https://doi.org/10.1088/1367-2630/14/8/085010 (2012).

111. Baudach, S., Bonse, J., Krüger, J. & Kautek, W. Ultrashort pulse laser ablation of polycarbonate and polymethylmethacrylate. *Applied Surface Science* **154-155.** ISSN: 0169-4332. doi:10.1016/S0169-4332(99)00474-2. https://www.sciencedirect.com/science/article/pii/S0169433299004742 (2000).

112. Chan, W.-L., Averback, R. S. & Cahill, D. G. Nonlinear energy absorption of femtosecond laser pulses in noble metals. *Appl. Phys. A* **97.** ISSN: 1432-0630. doi:10.1007/s00339-009-5383-z. https://doi.org/10.1007/s00339-009-5383-z (2023) (2009).

113. Cheng, K. *et al.* Ultrafast dynamics of single-pulse femtosecond laser-induced periodic ripples on the surface of a gold film. *Phys. Rev. B* **98.** Publisher: American Physical Society. doi:10.1103/PhysRevB.98.184106. https://link.aps.org/doi/10.1103/PhysRevB.98.184106 (2023) (2018).

114. Zywietz, U., Fischer, T., Evlyukhin, A., Reinhardt, C. & Chichkov, B. *Laser Printing of Functional Materials* Section: 11 (2018). ISBN: 978-3-527-80510-5. doi:10.1002/9783527805105.ch11. https://onlinelibrary.wiley.com/doi/abs/10.1002/9783527805105.ch11.

115. Mercadier, L. *et al.* Femtosecond laser desorption of ultrathin polymer films from a dielectric surface. *Appl. Phys. Lett.* **103.** ISSN: 0003-6951. doi:10.1063/1.4817816. https://aip.scitation.org/doi/abs/10.1063/1.4817816 (2013).

116. Brown, M. S., Brasz, C. F., Ventikos, Y. & Arnold, C. B. Impulsively actuated jets from thin liquid films for high-resolution printing applications. *Journal of Fluid Mechanics* **709.** ISSN: 1469-7645, 0022-1120. doi:10.1017/jfm.2012.337. https://www.cambridge.org/core/journals/journal-of-fluid-mechanics/article/impulsively-actuated-jets-from-thin-liquid-films-for-highresolution-printing-applications/8B18A5957DC4317B99B9F4D2134259CC (2012).

117. Ding, L., Blackwell, R., Künzler, J. F. & Knox, W. H. Large refractive index change in silicone-based and non-silicone-based hydrogel polymers induced by femtosecond laser micro-machining. *Opt. Express, OE* **14.** Publisher: Optica Publishing Group. ISSN: 1094-4087. doi:10.1364/OE.14.011901. https://opg.optica.org/oe/abstract.cfm?uri=oe-14-24-11901 (2006).

118. Kallepalli, D. L. N. *et al.* Multiphoton laser-induced confined chemical changes in polymer films. *Opt. Express, OE* **28.** Publisher: Optical Society of America. ISSN: 1094-4087. doi:10.1364/OE.389215. https://www.osapublishing.org/oe/abstract.cfm?uri=oe-28-8-11267 (2020).

119. Kallepalli, D. L. N. *et al.* Surface adhesion of back-illuminated ultrafast laser-treated polymers. *Phys. Rev. Materials* **5.** Publisher: American Physical Society. doi:10.1103/PhysRevMaterials.5.045201. https://link.aps.org/doi/10.1103/PhysRevMaterials.5.045201 (2021).

120. O'Connell, C., Sherlock, R. J. & Glynn, T. J. Fabrication of a reusable microlens array for laser-based structuring. *OE* **49.** Publisher: SPIE. ISSN: 0091-3286, 1560-2303. doi:10.1117/1.3281665. https://www.spiedigitallibrary.org/journals/optical-engineering/volume-49/issue-1/014201/Fabrication-of-a-reusable-microlens-array-for-laser-based-structuring/10.1117/1.3281665.full (2010).

121. Wippermann, F., Zeitner, U.-D., Dannberg, P., Bräuer, A. & Sinzinger, S. Beam homogenizers based on chirped microlens arrays. *Opt. Express, OE* **15.** Publisher: Optica Publishing Group. ISSN: 1094-4087. doi:10.1364/OE.15.006218. https://opg.optica.org/oe/abstract.cfm?uri=oe-15-10-6218 (2007).

122. Smith, P. J. *et al.* Switchable fiber coupling using variable-focal-length microlenses. *Review of Scientific Instruments* **72.** Publisher: American Institute of Physics. ISSN: 0034-6748. doi:10.1063/1.1380391. https://aip.scitation.org/doi/10.1063/1.1380391 (2001).

123. Schlehahn, A. *et al.* A stand-alone fiber-coupled single-photon source. *Sci Rep* **8.** Number: 1 Publisher: Nature Publishing Group. ISSN: 2045-2322. doi:10.1038/s41598-017-19049-4. https://www.nature.com/articles/s41598-017-19049-4 (2018).

124. Domínguez, C., Jost, N., Askins, S., Victoria, M. & Antón, I. A review of the promises and challenges of micro-concentrator photovoltaics. *AIP Conference Proceedings* **1881.** Publisher: American Institute of Physics. ISSN: 0094-243X. doi:10.1063/1.5001441. https://aip.scitation.org/doi/10.1063/1.5001441 (2017).

125. Song, Y. M. *et al.* Digital cameras with designs inspired by the arthropod eye. *Nature* **497.** ISSN: 1476-4687. doi:10.1038/nature12083 (2013).

126. Seisyan, R. P. Nanolithography in microelectronics: A review. *Tech. Phys.* **56.** ISSN: 1090-6525. doi:10.1134/S1063784211080214. https://doi.org/10.1134/S1063784211080214 (2011).

127. Naessens, K., Ottevaere, H., Baets, R., Daele, P. V. & Thienpont, H. Direct writing of microlenses in polycarbonate with excimer laser ablation. *Appl. Opt., AO* **42.** Publisher: Optica Publishing Group. ISSN: 2155-3165. doi:10.1364/AO.42.006349. https://opg.optica.org/ao/abstract.cfm?uri=ao-42-31-6349 (2003).

128. Naessens, K., Ottevaere, H., Van Daele, P. & Baets, R. Flexible fabrication of microlenses in polymer layers with excimer laser ablation. *Applied Surface Science. Physics and Chemistry of Advanced Laser Materials Processing* **208-209.** ISSN: 0169-4332. doi:10.1016/S0169-4332(02)01359-4. https://www.sciencedirect.com/science/article/pii/S0169433202013594 (2003).

129. Lin, C. H. *et al.* Fabrication of microlens arrays in photosensitive glass by femtosecond laser direct writing. *Appl. Phys. A* **97.** ISSN: 1432-0630. doi:10.1007/s00339-009-5350-8. https://doi.org/10.1007/s00339-009-5350-8 (2009).

130. Gattass, R. R. & Mazur, E. Femtosecond laser micromachining in transparent materials. *Nature Photon* **2.** Number: 4 Publisher: Nature Publishing Group. ISSN: 1749-4893. doi:10.1038/nphoton.2008.47. https://www.nature.com/articles/nphoton.2008.47 (2008).

131. Qiu, J., Miura, K. & Hirao, K. Femtosecond laser-induced microfeatures in glasses and their applications. *Journal of Non-Crystalline Solids. Proceedings of the 2005 International Conference on Glass* **354.** ISSN: 0022-3093. doi:10.1016/j.jnoncrysol.2007.02.092. https://www.sciencedirect.com/science/article/pii/S0022309307011611 (2008).

132. Juodkazis, S., Mizeikis, V., Matsuo, S., Ueno, K. & Misawa, H. Three-Dimensional Micro- and Nano-Structuring of Materials by Tightly Focused Laser Radiation. *BCSJ* **81.** Publisher: The Chemical Society of Japan. ISSN: 0009-2673. doi:10.1246/bcsj.81.411. https://www.journal.csj.jp/doi/10.1246/bcsj.81.411 (2008).

133. Juodkazis, S., Mizeikis, V. & Misawa, H. Three-dimensional microfabrication of materials by femtosecond lasers for photonics applications. *Journal of Applied Physics* **106.** Publisher: American Institute of Physics. ISSN: 0021-8979. doi:10.1063/1.3216462. https://aip.scitation.org/doi/10.1063/1.3216462 (2009).

134. Nolte, S., Will, M., Burghoff, J. & Tuennermann, A. Femtosecond waveguide writing: a new avenue to three-dimensional integrated optics. *Appl Phys A* **77.** ISSN: 1432-0630. doi:10.1007/s00339-003-2088-6. https://doi.org/10.1007/s00339-003-2088-6 (2003).

135. Ams, M. *et al.* Investigation of Ultrafast Laser–Photonic Material Interactions: Challenges for Directly Written Glass Photonics. *IEEE Journal of Selected Topics in Quantum Electronics* **14.** Conference Name: IEEE Journal of Selected Topics in Quantum Electronics. ISSN: 1558-4542. doi:10.1109/JSTQE.2008.925809 (2008).

136. Meunier, T., Villafranca, A. B., Bhardwaj, R. & Weck, A. Fabrication of microlens arrays in polycarbonate with nanojoule energy femtosecond laser pulses. *Optics Letters* **37.** ISSN: 0146-9592, 1539-4794. doi:10.1364/OL.37.004266. https://www.osapublishing.org/abstract.cfm?URI=ol-37-20-4266 (2012).

137. Surdo, S., Carzino, R., Diaspro, A. & Duocastella, M. Single-Shot Laser Additive Manufacturing of High Fill-Factor Microlens Arrays. *Advanced Optical Materials* **6.** _eprint: https://onlinelibrary.wiley.com/doi/pdf/10.1002/adom.201701190. ISSN: 2195-1071. doi:10.1002/adom.201701190. https://onlinelibrary.wiley.com/doi/abs/10.1002/adom.201701190 (2018).

138. Surdo, S., Diaspro, A. & Duocastella, M. Geometry-controllable micro-optics with laser catapulting. *Opt. Mater. Express, OME* **9.** ISSN: 2159-3930. doi:10.1364/OME.9.002892. https://www.osapublishing.org/ome/abstract.cfm?uri=ome-9-7-2892 (2019).

139. Lenzner, M. *et al.* Femtosecond Optical Breakdown in Dielectrics. *Phys. Rev. Lett.* **80.** Publisher: American Physical Society. doi:10.1103/PhysRevLett.80.4076. https://link.aps.org/doi/10.1103/PhysRevLett.80.4076 (1998).

140. Li, M., Menon, S., Nibarger, J. P. & Gibson, G. N. Ultrafast Electron Dynamics in Femtosecond Optical Breakdown of Dielectrics. *Phys. Rev. Lett.* **82.** Publisher: American Physical Society. doi:10.1103/PhysRevLett.82.2394. https://link.aps.org/doi/10.1103/PhysRevLett.82.2394 (1999).

141. Nguyen, N. T., Saliminia, A., Liu, W., Chin, S. L. & Vallée, R. Optical breakdown versus filamentation in fused silica by use of femtosecond infrared laser pulses. *Opt. Lett.* **28.** ISSN: 0146-9592, 1539-4794. doi:10.1364/OL.28.001591. https://www.osapublishing.org/abstract.cfm?URI=ol-28-17-1591 (2003).

142. Revolution - High Energy kHz Green Lasers — Coherent. https://www.coherent.com/lasers/amplifiers/revolution (2022).

143. PHAROS Lasers. https://lightcon.com/product/pharos-femtosecond-lasers/ (2022).

144. KMLabs. RAEA Ultrafast Amplifier. https://www.kmlabs.com/raea-high-power (2022).

145. Winey, M., Meehl, J. B., O'Toole, E. T. & Thomas H. Giddings, J. Conventional transmission electron microscopy. *Molecular Biology of the Cell* **25.** Publisher: American Society for Cell Biology. doi:10.1091/mbc.E12-12-0863. https://www.ncbi.nlm.nih.gov/pmc/articles/PMC3907272/ (2014).

146. Fluidigm Corporation. Maxpar Antibody Labeling User Guide. https://www.imc.unibe.ch/unibe/portal/fak_medizin/micro_imc/content/e987276/e988978/MaxparAntibodyLabelingUserGuidePRD002REV14.pdf (2022).

147. Mi, H., Ho, W. J., Yarchoan, M. & Popel, A. S. Multi-Scale Spatial Analysis of the Tumor Microenvironment Reveals Features of Cabozantinib and Nivolumab Efficacy in Hepatocellular Carcinoma. *Frontiers in Immunology* **13.** ISSN: 1664-3224. https://www.frontiersin.org/article/10.3389/fimmu.2022.892250 (2022).

148. Strittmatter, N. *et al.* Multi-modal molecular imaging maps the correlation between tumor microenvironments and nanomedicine distribution. *Theranostics* **12.** ISSN: 1838-7640. doi:10.7150/thno.68000. https://www.thno.org/v12p2162.htm (2022).

149. Iyer, A., Hamers, A. A. J. & Pillai, A. B. CyTOF® for the Masses. *Frontiers in Immunology* **13.** ISSN: 1664-3224. https://www.frontiersin.org/article/10.3389/fimmu.2022.815828 (2022).

150. Lutter, L. *et al.* Compartment-driven imprinting of intestinal CD4 (regulatory) T cells in inflammatory bowel disease and homeostasis. Tech. rep. Section: New Results Type: article (bioRxiv, 2022). doi:10.1101/2022.05.06.490870. https://www.biorxiv.org/content/10.1101/2022.05.06.490870v1.

151. Dieckman, T. *et al.* Single-Cell Analysis of Refractory Celiac Disease Demonstrates Inter- and Intra-Patient Aberrant Cell Heterogeneity. *Cellular and Molecular Gastroenterology and Hepatology* **14.** Publisher: Elsevier. ISSN: 2352-345X. doi:10.1016/j.jcmgh.2022.03.005. https://www.cmghjournal.org/article/S2352-345X(22)00054-6/fulltext (2022).

152. Ung, N. *et al.* Adaptation of Imaging Mass Cytometry to Explore the Single Cell Alloimmune Landscape of Liver Transplant Rejection. *Frontiers in Immunology* **13.** ISSN: 1664-3224. https://www.frontiersin.org/article/10.3389/fimmu.2022.831103 (2022).

153. Fluidigm Corporation. Hyperion Imaging System Brochure. https://fluidigm.my.salesforce.com/sfc/p/#700000009DAw/a/4u0000019d0L/xyd15.0YcHz.ZuCeGsamEqRBBSULWBwT.Q1SVRRAWo0 (2022).

154. Fluidigm Corporation. Hyperion and Hyperion+ Imaging Systems User Guide. https://fluidigm.my.salesforce.com/sfc/p/#700000009DAw/a/4u0000019kK7/pGYy8VUeTSYMrcxhEUcMGXPYK5Klb1MWKhezKatjKAI (2022).

155. Fluidigm Corporation. CyTOF XT. https://www.fluidigm.com/products-services/instruments/cytof-xt (2022).

156. Tong, X. M. & Lin, C. D. Empirical formula for static field ionization rates of atoms and molecules by lasers in the barrier-suppression regime. *J. Phys. B: At. Mol. Opt. Phys.* **38.** Publisher: IOP Publishing. ISSN: 0953-4075. doi:10.1088/0953-4075/38/15/001. https://doi.org/10.1088/0953-4075/38/15/001 (2005).

157. Tong, X. M., Zhao, Z. X. & Lin, C. D. Theory of molecular tunneling ionization. *Phys. Rev. A* **66.** Publisher: American Physical Society. doi:10.1103/PhysRevA.66.033402. https://link.aps.org/doi/10.1103/PhysRevA.66.033402 (2002).